

**SIMULATION BASED OPTIMIZATION OF
INDIGENOUSLY DEVELOPED INORGANIC
SCINTILLATORS AND VARIOUS LIGHT SENSORS
TO DEVELOP GAMMA SPECTROMETER SYSTEMS**

By

PRATIP MITRA

(PHYS01201604022)

Bhabha Atomic Research Centre, Mumbai

A thesis submitted to the

Board of Studies in Physical Sciences

In partial fulfillment of requirements

for the Degree of

DOCTOR OF PHILOSOPHY

of

HOMI BHABHA NATIONAL INSTITUTE



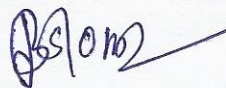
April, 2021

Homi Bhabha National Institute¹

Recommendations of the Viva Voce Committee

As members of the Viva Voce Committee, we certify that we have read the dissertation prepared by **Pratip Mitra** entitled “**Simulation Based Optimization of Indigenously Developed Inorganic Scintillators and Various Light Sensors to Develop Gamma Spectrometer Systems**” and recommend that it may be accepted as fulfilling the thesis requirement for the award of Degree of Doctor of Philosophy.

Chairman – Prof. B. S. Tomar

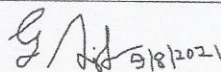


Guide / Convener – Prof. S. C. Gadkari



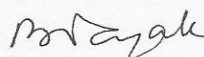
31/07/2021

Examiner – Prof. Ani Kumar Gourishetty

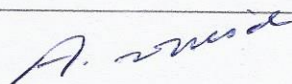


31/07/2021

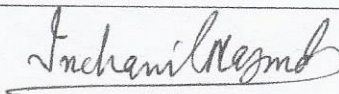
Member 1 – Prof. B. K. Nayak



Member 2 – Prof. A. Vinod Kumar



Member 3 – Prof. Indranil Mazumdar

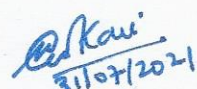


Final approval and acceptance of this thesis is contingent upon the candidate's submission of the final copies of the thesis to HBNI.

I/We hereby certify that I/we have read this thesis prepared under my/our direction and recommend that it may be accepted as fulfilling the thesis requirement.

Date: July 31, 2021

Place: Mumbai



31/07/2021

Signature
Guide

¹ This page is to be included only for final submission after successful completion of viva voce.

STATEMENT BY AUTHOR

This dissertation has been submitted in partial fulfillment of requirements for an advanced degree at Homi Bhabha National Institute (HBNI) and is deposited in the Library to be made available to borrowers under rules of the HBNI.

Brief quotations from this dissertation are allowable without special permission, provided that accurate acknowledgement of source is made. Requests for permission for extended quotation from or reproduction of this manuscript in whole or in part may be granted by the Competent Authority of HBNI when in his or her judgment the proposed use of the material is in the interests of scholarship. In all other instances, however, permission must be obtained from the author.



(Pratip Mitra)

DECLARATION

I hereby declare that the investigation presented in the thesis has been carried out by me. The work is original and has not been submitted earlier as a whole or in part for a degree/diploma at this or any other Institution/University.



(Pratip Mitra)

List of Publications arising from the thesis

Journal

[1] “Optimization of Parameters for a CsI(Tl) Scintillator Detector Using GEANT4-Based Monte Carlo Simulation Including Optical Photon Transport”, **Pratip Mitra**, Mohit Tyagi, R. G. Thomas, A. Vinod Kumar, and S. C. Gadkari, *IEEE Transactions on Nuclear Science*, **2019**, 66(7), 1870-1878.

[2] “Development of a silicon photodiode-based compact gamma spectrometer using a Gd₃Ga₃Al₂O₁₂:Ce,B single crystal scintillator”, **Pratip Mitra**, Saurabh Srivastava, Mohit Tyagi, A Vinod Kumar and S C Gadkari, *Bulletin of Materials Science*, **2019**, 42(6), <https://doi.org/10.1007/s12034-019-1942-x>.

[3] “An environmental gamma spectrometry system with CsI(Tl) scintillator and FPGA based MCA for open field deployment”, **Pratip Mitra**, Ashutosh Gupta, G. Priyanka Reddy, Saurabh Srivastava, Mohit Tyagi, M.K. Sharma, S.C. Gadkari, Probal Chaudhury, A. Vinod Kumar, *Applied Radiation and Isotopes*, **2021**, 172, <https://doi.org/10.1016/j.apradiso.2021.109677>.

Conferences

[1] “⁴¹Ar Monitoring by using an Indigenously Developed Portable Spectrometer based on in-house grown Crystal Scintillator”, **Pratip Mitra**, Mohit Tyagi, Amit K. Verma, D. G. Desai, S. Sen, S. G. Singh, S. Anilkumar, A. Vinod Kumar, S. C. Gadkari, *33rd IARP International Conference, Developments towards Improvements of Radiological Surveillance at Nuclear Facilities and Environment (IARPIC-2018)*, **2018**, P-1.

[2] “A Compact Gamma Spectrometer Based on a Gd₃Ga₃Al₂O₁₂:Ce,B Single Crystal Scintillator Coupled to a Silicon Photodiode”, **Pratip Mitra**, Saurabh Srivastava, Mohit

Tyagi, A. Vinod Kumar and S. C. Gadkari, *Materials & Technologies for Energy Conversion and Storage (M-TECS 2018)*, **2018**.

[3] “Size dependence for $Gd_3Ga_3Al_2O_{12}:Ce,B$ single crystal scintillator on pulse-height spectra generated by GEANT4 simulation with optical photon transport”, **Pratip Mitra**, R. G. Thomas, Mohit Tyagi, A. Vinod Kumar, and S. C. Gadkari, *Proceedings of the 63rd DAE Symposium on Nuclear Physics*, **2018**, 1050-1051, Available online at www.sympnp.org/proceedings.

[4] “Dependence of gamma spectra from a CsI(Tl) scintillator on the quantum efficiency of the coupled photodetector: A GEANT4-based study”, **Pratip Mitra**, R. G. Thomas, Mohit Tyagi, A. Vinod Kumar, and S. C. Gadkari, *Proceedings of the 64th DAE Symposium on Nuclear Physics*, **2019**, 878-879, Available online at www.sympnp.org/snp2019.



(Pratip Mitra)

Dedicated

to

My Parents

(Mrs. Palu Mitra and Mr. Pradip Kumar Mitra)

ACKNOWLEDGEMENTS

I express my deep sense of gratitude to my guide **Prof. S. C. Gadkari**, Raja Ramanna Fellow, TPD, BARC for his invaluable suggestions, expert advice and support throughout the course of this study.

I owe many thanks to **Dr. Mohit Tyagi**, TPD, BARC for sharing his knowledge and expertise and for his continuous mentoring which has helped me learn a lot.

I am deeply indebted to **Dr. R. G. Thomas**, NPD, BARC for his continuous support and kind help without which this research work would not have been possible.

The critical review of this work by the Doctoral Committee consisting of **Prof. B. S. Tomar**, Raja Ramanna Fellow, HBNI (Chairman), **Prof. B. K. Nayak**, Ex-head, NPD, BARC (Member), **Prof. A. Vinod Kumar**, Head, EMAD, BARC (Member) and **Prof. Indranil Mazumdar**, TIFR (Member) is gratefully acknowledged.

Special thanks are due to **Dr. Shashwati Sen Yeram**, Head, CTS, TPD, BARC and all members of CTS, TPD, BARC, especially **Dr. Babita Tiwari, Dr. S. G. Singh, Dr. G. D. Patra, Dr. M. G. Ghosh, Dr. Shreyas S. Pitale, Dr. A. K. Singh, Shri D. G. Desai, Shri A. N. Patil** and **Shri J. Loganathan** for their continuous help and co-operation in this work.

I wish to thank my colleagues of ESNG, EMAD, BARC, namely **Shri S. Garg, Shri Saurabh Srivastava, Smt. G. Priyanka Reddy, Shri T. Mukundan, Shri M. P. Ratheesh, Shri S. G. Gavas, Shri P. R. Ninawe, Shri S. S. Salunkhe, Shri A. V. L. Narayana** and **Smt. Anisha Gupta** for their constant support.

Special thanks are due to **Shri Probal Chaudhury**, Head, RSSD, BARC, **Shri M. K. Sharma**, Head, RMS&DS, RSSD, BARC and **Shri Ashutosh Gupta**, RMS&DS, RSSD, BARC for their help and co-operation.

I would like to thank **Dr. S. Anilkumar**, Head, NFS, RSSD, BARC, **Shri Amar Dutt Pant** and **Shri Amit Kumar Verma** of NFS, RSSD, BARC, and **Shri M. S. Prakasha**, RMP for their help and support during the initial studies on EGSS.

Thanks are also due to **Shri M. B. Pote** and **Shri R. N. Khanderao** of RMS&DS, RSSD, BARC and **all members of HS&EG workshop, BARC** for their help in designing and fabricating the various mechanical assemblies.

I also wish to thank **Shri V. Sathian**, Head, RSS, RSSD, BARC and **Dr. S. K. Singh, Shri S. M. Tripathi** and **Smt. Liji Shaiju** of RSS, RSSD, BARC for their help and support in the calibration work carried out.

Last but not the least; I am forever indebted to my **family, relatives, friends, teachers and well-wishers** for everything that they have given me.

CONTENTS

LIST OF ABBREVIATIONS	x
LIST OF FIGURES	xi
LIST OF TABLES	xv
CHAPTER 1: INTRODUCTION	1
1.1 Radiation and its detection	1
1.2 Photodetectors	15
1.3 Gamma spectrometry	27
1.4 Scope and aim of the thesis	42
CHAPTER 2: THEORY AND EXPERIMENTAL METHODS	46
2.1 Growth of single crystals	46
2.2 Measurement of emission spectra of CsI(Tl) and GGAG:Ce,B by radioluminescence	55
2.3 Monte Carlo simulation for radiation detection	58
CHAPTER 3: SIMULATION STUDIES ON CsI(Tl)	72
3.1 Introduction	72
3.2 Simulation methodology	74
3.3 Energy calibration by simulation	81
3.4 Experimental measurements	81
3.5 Experimental energy calibration	83
3.6 Experimental validation of the simulation model	87
3.7 Effect of variation of simulation parameters	87
3.8 Conclusion	103
CHAPTER 4: SIMULATION STUDIES ON GGAG:Ce AND GGAG:Ce,B	105
4.1 Introduction	105
4.2 Simulation studies on a 2" $\phi \times 2$ " L GGAG:Ce scintillator	107
4.3 Simulation studies on small GGAG:Ce,B scintillators	113
4.4 Conclusion	118
CHAPTER 5: SIMULATION STUDIES ON LIGHT GUIDES	119
5.1 Introduction	119
5.2 Simulation studies on trapezoidal PMMA light guides	120
5.3 Simulation studies on trapezoidal CsI(Tl) scintillators	126
5.4 Simulation studies on the impact of presence <i>vis-a-vis</i> absence of light guide	129
5.5 Conclusion	132
CHAPTER 6: DEVELOPMENT OF GAMMA SPECTROMETRY SYSTEMS	133
6.1 CsI(Tl) based environmental gamma spectrometry system (EGSS)	133
6.2 Compact gamma spectrometer with a GGAG:Ce,B scintillator coupled to a photodiode	151
CHAPTER 7: CONCLUSION AND SCOPE FOR FUTURE WORK	164
7.1 Conclusion	164
7.2 Scope for future work	165
REFERENCES	167

LIST OF ABBREVIATIONS

VIS	Visible light	IR	Infrared
MSV	Mean square voltage	GM	Geiger-Mueller
PSD	Pulse shape discrimination	UV	Ultraviolet
LN₂	Liquid nitrogen	PMT	Photomultiplier tube
BGO	Bi ₄ Ge ₃ O ₁₂	CMS	Compact Muon Solenoid
YSO:Ce	Y ₂ (SiO ₄)O:Ce	GSO:Ce	Gd ₂ (SiO ₄)O:Ce
LSO:Ce	Lu ₂ (SiO ₄)O:Ce	LGSO:Ce	Lu _x Gd _{2-x} (SiO ₄)O:Ce
LYSO:Ce	Lu _x Y _{2-x} (SiO ₄)O:Ce	GPS:Ce	Gd ₂ Si ₂ O ₇ :Ce
LPS:Ce	Lu ₂ Si ₂ O ₇ :Ce	YAP:Ce	YAlO ₃ :Ce
LuAP:Ce	LuAlO ₃ :Ce	LuYAP:Ce	Lu _x Y _{1-x} AlO ₃ :Ce
YAG:Ce	Y ₃ Al ₅ O ₁₂ :Ce	LuAG:Ce	Lu ₃ Al ₅ O ₁₂ :Ce
GGAG:Ce	Gd ₃ Ga ₃ Al ₂ O ₁₂ :Ce	GGAG:Ce,B	Gd ₃ Ga ₃ Al ₂ O ₁₂ :Ce,B
GYAG:Ce	(Y,Gd) ₃ Al ₅ O ₁₂ (Ce)	HPGe	High purity germanium
CZT	Cd _{1-x} Zn _x Te	NIR	Near infrared
APD	Avalanche photodiode	SiPM	Silicon photomultiplier
SNR	Signal to noise ratio	HV	High voltage
NEA	Negative electron affinity	QE	Quantum efficiency
EWQE	Emission weighted quantum efficiency	CT	Computed tomography
JFET	Junction field-effect transistor	MPPC	Multi-pixel photon counter
MCA	Multichannel analyzer	EGSS	Environmental gamma spectrometry system
USB	Universal serial bus	CZ	Czochralski
RF	Radiofrequency	MP	Melting point
CCD	Charge coupled device	LY	Light yield
P	Polished	G	Ground
PFP	Polished front painted	GFP	Ground front painted
PBP	Polished back painted	GBP	Ground back painted
SS	Specular spike	SL	Specular lobe
L	Lambertian	BS	Backscatter
PPH	Peak-pulse-height	ROI	Region-of-interest
DPP	Digital pulse processing	DAQ	Data acquisition
PMMA	Poly(methyl methacrylate)	PC	Personal computer
FPGA	Field programmable gate array	GSM	Global system for mobile communications
SMS	Short message service	UART	Universal asynchronous receiver-transmitter
RS-232	Recommended serial communication standard	CMOS	Complimentary metal-oxide-semiconductor
ERM	Environmental radiation monitor	TTL	Transistor-transistor-logic
PDU	Protocol description unit	SMF	Sealed maintenance free
MDA	Minimum detectable amount	NIM	Nuclear instrument module
IC	Integrated circuit		

LIST OF FIGURES

1.1	Electronic band diagram of an activated inorganic crystal scintillator	4
1.2	Basic construction of a PMT	16
1.3	Basic configuration of a silicon photodiode	22
1.4	Simplified pulse-height spectrum for monoenergetic gamma rays with 100% photoelectric absorption	28
1.5	Simplified pulse-height spectrum for monoenergetic gamma rays with 100% Compton scattering	29
1.6	Simplified pulse-height spectrum for monoenergetic gamma rays with 100% pair production	30
1.7	Predicted pulse-height spectrum for a small detector that stops all secondary charged particles but cannot stop any secondary gamma photons	31
1.8	Predicted pulse-height spectrum for a large detector that stops all secondary radiation	32
1.9	Predicted pulse-height spectrum for an intermediate size detector that partially stops secondary gamma photons	32
1.10	Influence of the surrounding materials to the otherwise expected (dashed) pulse-height spectrum	34
1.11	Simplified block diagram of an inorganic scintillator based gamma spectrometer	38
1.12	Simplified block diagram of an HPGe based gamma spectrometer	42
2.1	Simplified schematic diagram of the Czochralski growth process	48
2.2	Photograph of the CZ crystal puller system (Oxypuller, Cyberstar)	51
2.3	As-grown GGAG:Ce,B single crystal ingot ($\sim 25 \text{ mm } \phi \times 60 \text{ mm L}$) under UV illumination	52
2.4	Simplified schematic diagram of the Bridgman-Stockbarger growth process	53
2.5	Photograph of the vertical Bridgman-Stockbarger crystal growth system used to grow CsI(Tl) single crystals	54
2.6	As-grown CsI(Tl) single crystal ingot ($\sim 55 \text{ mm } \phi \times 60 \text{ mm L}$)	56
2.7	Setup for measurement of emission spectra	56
2.8	Emission spectrum of CsI(Tl)	57
2.9	Emission spectrum of GGAG:Ce,B	57
2.10	(a) Emission spectra of GGAG:Ce,B for various HV settings of the X-ray tube (tube current fixed at 30 mA), (b) Dependence of the integrated areas under the emission spectra of (a) on the X-ray tube HV	58
2.11	(a) Emission spectra of GGAG:Ce,B for various values of the X-ray tube current (HV fixed at 40 kV), (b) Dependence of the integrated areas under the emission spectra of (a) on the X-ray tube current	59
2.12	Sketch showing the modeling of a ground surface consisting of micro facets	68
2.13	(a) Specular spike reflection from a perfectly smooth surface, (b) Specular lobe reflection from a slightly rough surface, (c) Lambertian reflection from a diffuse surface, (d) Backscatter reflection from a very rough surface	69
3.1	Schematic diagram of the xz plane cross-section of the simulation geometry consisting of a $50.8 \text{ mm } \phi \times 50.8 \text{ mm L}$ cylindrical CsI(Tl) scintillator crystal, along with the reference coordinate system (Figure not to scale)	75
3.2	Normalized emission spectrum of CsI(Tl)	77
3.3	Normalized emission spectrum of CsI(Tl) as a function of photon energy	77

3.4	(a) Simulated spectrum for a 50.8 mm $\phi \times$ 50.8 mm L cylindrical CsI(Tl) scintillator using the source at serial number 1 of Table 3.1, along with the derived energy calibration, (b) The same spectrum converted to energy scale	82
3.5	(a) Experimentally acquired spectrum of $^{137}\text{Cs} + ^{60}\text{Co}$ source with a 50.8 mm $\phi \times$ 50.8 mm L cylindrical CsI(Tl) scintillator, along with the derived energy calibration, (b) The same spectrum converted to energy scale	84
3.6	Comparison of experimental and simulated spectra of ^{137}Cs for a 50.8 mm $\phi \times$ 50.8 mm L cylindrical CsI(Tl) scintillator	85
3.7	(a) Simulated spectrum of ^{41}Ar for a 50.8 mm $\phi \times$ 50.8 mm L cylindrical CsI(Tl) scintillator, (b) Experimental spectrum of ^{41}Ar containing air filled in a Marinelli beaker	86
3.8	(a) Simulated spectra of ^{137}Cs for efficiency, $\eta = 0.05$ (typical of PMT) and (b) efficiency, $\eta = 0.8267$ (typical of photodiode). In both cases, the gain (G) of the photodetector is taken to be 2.7×10^5 , which is typical of PMT	88
3.9	Variation of the energy resolution at 662 keV and the corresponding peak-pulse-height with efficiency (η) of the photodetector	90
3.10	Simulated spectra of ^{137}Cs for different values of reflectivity (R) of the scintillator-reflector interface	93
3.11	Variation of the energy resolution at 662 keV and the corresponding peak-pulse-height with reflectivity (R) of the scintillator-reflector interface	94
3.12	Simulated pulse-height spectra with ^{137}Cs for different values of the parameter resolution scale. The full-energy peak broadens as this parameter increases, whereas the centroid of the peak remains unchanged	98
3.13	Variation of the energy resolution at 662 keV and the corresponding peak-pulse-height with the parameter resolution scale	99
3.14	Simulated spectra of ^{137}Cs for different values of scintillation yield (N (photons/MeV)) of the scintillator	100
3.15	Variation of the energy resolution at 662 keV and the corresponding peak-pulse-height with scintillation yield (N) of the scintillator	100
3.16	Comparison of simulated spectra with ^{137}Cs for 25.4 mm $\phi \times$ 25.4 mm L, 50.8 mm $\phi \times$ 50.8 mm L and 76.2 mm $\phi \times$ 76.2 mm L cylindrical CsI(Tl) scintillators	101
3.17	Comparison of simulated spectra with ^{208}Tl for 25.4 mm $\phi \times$ 25.4 mm L, 50.8 mm $\phi \times$ 50.8 mm L and 76.2 mm $\phi \times$ 76.2 mm L cylindrical CsI(Tl) scintillators	103
4.1	(a) Simulated spectrum for a 50.8 mm $\phi \times$ 50.8 mm L cylindrical GGAG:Ce scintillator using the source at serial number 1 of Table 3.1, along with the derived energy calibration, (b) The same spectrum converted to energy scale	110
4.2	(a) Experimentally acquired spectrum of $^{137}\text{Cs} + ^{60}\text{Co}$ source with a 50.8 mm $\phi \times$ 50.8 mm L cylindrical GGAG:Ce scintillator, along with the derived energy calibration, (b) The same spectrum converted to energy scale	112
4.3	Comparison of experimental and simulated spectra of ^{137}Cs for a 50.8 mm $\phi \times$ 50.8 mm L cylindrical GGAG:Ce scintillator	113
4.4	Schematic diagram of the yz plane cross-section of the simulation geometry consisting of a $10 \times 10 \times 10 \text{ mm}^3$ cubic GGAG:Ce,B scintillator crystal, along with the reference coordinate system (Figure not to scale)	114
4.5	Normalized emission spectrum of GGAG:Ce,B	115
4.6	Normalized emission spectrum of GGAG:Ce,B as a function of photon energy	115
4.7	Comparison of simulated spectra with ^{137}Cs for $10 \times 10 \times 10$, $18 \times 18 \times 10$, $18 \times 18 \times 18$, and $18 \times 18 \times 25 \text{ mm}^3$ GGAG:Ce,B scintillators	116

5.1	Schematic diagram of the simulation geometry consisting of a $50.8 \times 50.8 \times 50.8$ mm ³ cuboid shaped CsI(Tl) scintillator crystal, coupled to a $10 \times 10 \times 0.3$ or $18 \times 18 \times 0.3$ mm ³ photodetector through a trapezoidal PMMA light guide. The Teflon reflector and the outer aluminum enclosure are not shown for clarity (Figure not to scale)	121
5.2	Comparison of the simulated spectra with ¹³⁷ Cs for different heights (10, 20 and 30 mm) of the light guide and the $10 \times 10 \times 0.3$ mm ³ photodetector	123
5.3	Representative light paths for different heights (10, 20 and 30 mm) of the light guide	124
5.4	Comparison of the simulated spectra with ¹³⁷ Cs for different heights (10, 20 and 30 mm) of the light guide and the $18 \times 18 \times 0.3$ mm ³ photodetector	125
5.5	Schematic diagram of the simulation geometry consisting of a trapezoidal CsI(Tl) scintillator crystal, coupled directly to a $10 \times 10 \times 0.3$ or $18 \times 18 \times 0.3$ mm ³ photodetector. The Teflon reflector and the outer aluminum enclosure are not shown for clarity (Figure not to scale)	127
5.6	Comparison of the simulated spectra with ¹³⁷ Cs for different heights (25.4, 38.1 or 50.8 mm) of the trapezoidal CsI(Tl) scintillator and the $10 \times 10 \times 0.3$ mm ³ photodetector	128
5.7	Comparison of the simulated spectra with ¹³⁷ Cs for different heights (25.4, 38.1 or 50.8 mm) of the trapezoidal CsI(Tl) scintillator and the $18 \times 18 \times 0.3$ mm ³ photodetector	128
5.8	Schematic diagram of the simulation geometry consisting of a trapezoidal CsI(Tl) scintillator crystal, coupled (a) directly to a $18 \times 18 \times 0.3$ mm ³ photodetector and (b) through a cuboid shaped PMMA light guide to the same photodetector. The Teflon reflectors and the outer aluminum enclosures in both the geometries are not shown for clarity (Figures not to scale)	130
5.9	Comparison of the simulated spectra with ¹³⁷ Cs with and without a 10 mm long cuboid shaped PMMA light guide in between a trapezoidal CsI(Tl) scintillator and a $18 \times 18 \times 0.3$ mm ³ photodetector	131
6.1	Block diagram of the GM counter based ERM	136
6.2	Dose rate response of the GM counter based ERM for ⁶⁰ Co source	137
6.3	Functional block diagram of EGSS	140
6.4	Photograph of EGSS (height: 92 cm, base area: 35×35 cm ² , weight: 28 kg)	141
6.5	A screenshot of a spectrum displayed at the central receiving station. The spectrum was recorded by the system upon triggering-on by introduction of a ¹³⁷ Cs test source	142
6.6	A typical pulse-height spectrum recorded by EGSS when a ¹³⁷ Cs test source was introduced	146
6.7	(a) Pulse-height spectrum recorded by EGSS when a ¹³⁷ Cs and a ⁶⁰ Co test source were introduced together, along with the derived energy calibration, (b) the same spectrum converted to energy scale	147
6.8	Pulse-height spectrum recorded during passing of ⁴¹ Ar containing plume over EGSS	148
6.9	Four consecutive 1 h spectra recorded by EGSS during passing of ⁴¹ Ar containing plume	150
6.10	Comparison of four consecutive 5 min spectra of ¹³⁷ Cs recorded with a $10 \times 10 \times 10$ mm ³ GGAG:Ce,B scintillator (with Spectralon reflector) coupled to a PMT, after exposure to visible light	154

6.11	Comparison of pulse-height spectra of ^{137}Cs for different reflectors on a $10 \times 10 \times 10 \text{ mm}^3$ GGAG:Ce,B scintillator coupled to a PMT	154
6.12	The pulse processing circuit of the compact gamma spectrometer with a GGAG:Ce,B scintillator coupled to a photodiode	157
6.13	Energy resolution of the GGAG:Ce,B-photodiode based gamma spectrometer as a function of reverse bias voltage of the photodiode	158
6.14	Pulse-height spectra of ^{137}Cs measured with a GGAG:Ce,B-photodiode based gamma spectrometer for different shaping times: (a) 1, (b) 2 and (c) 4 μs	160
6.15	Energy calibration of the GGAG:Ce,B-photodiode based gamma spectrometer	161
6.16	Photograph of the developed USB based compact ($137 \times 86 \times 84 \text{ mm}^3$) gamma spectrometer with a $10 \times 10 \times 10 \text{ mm}^3$ GGAG:Ce,B scintillator coupled to a $10 \times 10 \text{ mm}^2$ photodiode	162

LIST OF TABLES

1.1	Properties of common inorganic scintillators used for gamma spectrometry	37
2.1	Values of optimized growth parameters used for growth of GGAG:Ce and GGAG:Ce,B single crystals	51
3.1	Various source configurations used in simulation	75
3.2	Values of energy resolution at 662 keV for six simulated spectra with different choices of surface finish of the scintillator-reflector interface. In all the six cases, $\sigma_\alpha = 0^\circ$	95
3.3	Values of energy resolution at 662 keV for two different values of surface roughness (σ_α) of the scintillator-reflector interface with two different surface finish G and GFP	96
3.4	Values of energy resolution at 662 keV for different combinations of the four reflection types with two different surface finishes G and GFP	97
3.5	Values of energy resolution at 662 keV and 2614 keV for different dimensions of the CsI(Tl) scintillator	103
4.1	Some parameters of the GGAG:Ce scintillator (Make: Epic Crystals) used for experiments and modeled in simulation	107
4.2	Energy resolution and <i>PPH</i> at 662 keV for different dimensions of the GGAG:Ce,B scintillator	117

INTRODUCTION

1.1 Radiation and its detection

1.1.1 Classification of radiation

Radiation is the quantized emission of energy in the form of particles, or, equivalently, waves. It can be broadly categorized as either (i) non-ionizing or (ii) ionizing. Ionizing radiation carries enough energy to ionize matter, whereas non-ionizing radiation, e.g., photons of visible light (VIS), infrared (IR), microwave, radiofrequency, etc., does not have sufficient energy to cause ionization. Ionizing radiation can be further subdivided into two broad categories depending on how they ionize matter, viz. (i) directly ionizing or charged particulate radiation and (ii) indirectly ionizing or uncharged radiation. Directly ionizing radiation consists of either (i) fast electrons, e.g., beta particles (β^-/e^-) or positrons (β^+/e^+) having nuclear origin or high energy electrons produced by other processes, or (ii) heavy charged particles, e.g., alpha particles (α), protons (p), fission fragments or any other heavy ions. Indirectly ionizing radiation can be categorized into (i) electromagnetic radiation, e.g., X-rays and gamma (γ) rays and (ii) (fast or slow) neutrons (n) [1]–[3].

1.1.2 Interaction of radiation with matter

Directly ionizing radiation causes ionization or excitation via Coulomb force interactions with the electrons of the interacting matter. Fast electrons, in addition to the above, may lose their energy via radiative losses (Bremsstrahlung). Electromagnetic radiation interacts with matter via Rayleigh (elastic) scattering, photoelectric effect, Compton (inelastic) scattering and pair production. Neutrons interact via scattering (elastic and inelastic) and nuclear reactions, e.g., (n, α), (n, p), (n, γ), (n, f) etc. [1]–[3]. The net result of interaction of any ionizing radiation with matter is ionization (and excitation, which may be followed by

secondary ionization) of atoms or molecules of the matter, and the collection of these ion pairs forms the basis of any radiation detector [1].

1.1.3 Modes of detector operation

Radiation detectors are normally used in three different modes, namely, (i) pulse mode, (ii) current mode and (iii) mean square voltage (MSV or Campbelling [4]) mode [1]. In pulse mode, each radiation quantum interacting with the detector is recorded. This mode is used for radiation spectroscopy or pulse counting. In current mode, the time-averaged current from the detector is measured. This mode is useful for very high event rates where pulse counting becomes inapplicable due to pulse pile-up. In the MSV mode, the recorded signal is proportional to the product of the event rate and the square of the charge produced in each event. This mode is useful for measurements in radiation fields containing more than one type of radiation [1].

1.1.4 Types of radiation detectors

Radiation detectors are broadly classified in terms of the nature of the detection medium as (i) gas-filled detectors, (ii) scintillation detectors and (iii) semiconductor diode detectors [1].

1.1.4.1 Gas-filled detectors

Gas-filled detectors rely on the interaction of ionizing radiation with gas molecules [1] and are further categorized based on the region of operation into (i) ionization chambers [5]–[8], (ii) proportional counters [5]–[8] and (iii) Geiger-Mueller (GM) counters [6]–[9]. In ionization chambers, all the ion pairs formed in primary ionization are collected. They are used in current mode in radiation survey instruments, radiation source calibrators, measurement of radioactive gases, remote sensing of ionization, etc. and in pulse mode for charged particle spectroscopy. Secondary ionization is allowed in proportional counters, keeping the gas multiplication factor constant. Proportional counters are used for α , β and fission fragment counting (gas flow type), neutron counting (^3He or BF_3 filled), detection and

spectroscopy of soft X-rays (end window type) and γ -rays with Xe or Kr filling, dosimetry (tissue equivalent proportional counters), position sensing, etc. In GM counters, the entire gas volume is ionized for each primary event, irrespective of the energy of the primary. Therefore, they can be used only for pulse counting because the energy information is lost. The pulse amplitudes from these detectors is large and normally do not require any external amplification, unlike the ionization chambers and the proportional counters. Therefore, the GM counters are simple, low cost and easy to operate. They are typically used in radiation survey meters, counting of active samples etc. [1].

1.1.4.2 Scintillation detectors

Scintillator materials, upon excitation by ionizing radiation and the subsequent relaxation, gives rise to scintillation photons. These photons are sensed by a coupled photodetector that results in the required electrical signal. An ideal scintillator should have high conversion efficiency of ionizing radiation energy into scintillation photons. The light yield should be proportional to the deposited energy. The scintillating medium should be transparent to its own emission and its refractive index should be near to that of glass, i.e., 1.5. The decay time should be short. Further, the scintillation material should be of good optical quality and available in large sizes [1], [10].

1.1.4.2.1 Organic scintillators

Organic scintillators scintillate owing to their π -electron structure. These are typically fast scintillators and are capable of pulse shape discrimination (PSD) between different types of ionizing radiation owing to their decay times that are dependent on the type of the exciting radiation. Some of the examples of this class of detectors are (i) pure organic crystals, e.g., Anthracene, Stilbene, (ii) solutions of organic scintillators in appropriate solvents, e.g., liquid scintillators for α or β counting, (iii) plastic scintillators, (iv) thin film scintillators, (v) high

atomic number (high Z) loaded organic scintillators for gamma detection or $GdNO_3$ loaded organic scintillators for neutron detection [1], [10].

1.1.4.2.2 Inorganic scintillators

The electronic band structure of inorganic scintillators, arising due to their crystalline structure, determines their scintillation mechanism. Upon absorption of energy from ionizing particles, electrons get excited from the valence band to the conduction band. Their return to the valence band leads to the emission of scintillation photons. There are, however, other competing processes for this de-excitation that make the scintillation process rather inefficient. Also, the band gap may be such that the emitted photons are often in the ultraviolet (UV) regime. These two limitations are usually taken care of by intentionally adding small concentrations of dopants to the pure inorganic scintillator crystal. Addition of these dopants creates electronic energy levels (called activator states) in the otherwise forbidden region of the pure crystal. Electronic de-excitation through these activator states increases the probability of visible light emission [1], [10], [11]. Figure 1.1 shows the energy band diagram of an activated scintillator [1].

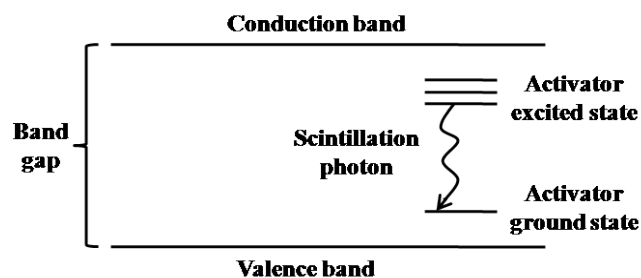


Figure 1.1: Electronic band diagram of an activated inorganic crystal scintillator [1].

No inorganic scintillator simultaneously has all the ideal properties required for a particular application. There is always a tradeoff and the particular scintillator with the most favorable properties for the application needs to be chosen [1].

1.1.4.2.2.1 Alkali halides

Among inorganic scintillators, the alkali halide NaI(Tl) is the oldest [12] and the most widely used even today [1], [13]–[16], largely due to its high effective atomic number (Z_{eff}), high light yield and availability in large sizes at relatively low cost. It has a high light yield which is significantly nonproportional at low energies [1], [11], [17]. The light yield decreases at elevated temperatures [18]–[20]. The decay time of NaI(Tl) is slow and may limit its applicability at high count rate situations [1]. NaI(Tl) is hygroscopic, and, hence, needs to be encapsulated in an airtight container [1], [10]. NaI(Tl) crystals are fragile. Polycrystalline NaI(Tl), made by recrystallizing small single crystal ingots under heat and pressure, are found to have equivalent scintillation properties as single crystal NaI(Tl), but are more rugged and therefore, can be used for harsh environments where thermal and mechanical shocks are likely to be encountered [21], [22]. Li co-doped NaI(Tl) can detect gammas as well as neutrons with very good PSD capabilities [23]. Pure NaI is a fast scintillator but its light yield is very poor. The light yield improves significantly at liquid nitrogen (LN_2) temperature (77 K) [1], [24].

CsI(Tl) [25] is another popular alkali halide scintillator. It offers compactness due to its higher Z_{eff} . It is less brittle and less hygroscopic than NaI(Tl). Its light yield is higher than that of NaI(Tl) [1], [16], [26]. But its scintillation emission spectrum, peaking at the green region, does not match well with the spectral response of conventional photomultiplier tubes (PMTs) with bi-alkali photocathodes, and hence, results in lower pulse-heights when coupled with them. However, the emission spectrum matches well with the spectral response of silicon based photodetectors, resulting in compact, low voltage spectrometry devices, eliminating the need of conventional PMTs [1]. It is a very slow scintillator compared to NaI(Tl) [27]. However, its decay time is dependent on the type of exciting radiation, and as a result, it has good PSD capabilities [28]–[33]. CsI(Na) has a higher light yield than NaI(Tl)

and its emission spectrum is similar to that of NaI(Tl), but its decay is very slow [34] and it is hygroscopic [1].

The alkali halide LiI(Eu) is important for neutron detection owing to the ${}^6\text{Li}$ (n, α) reaction [1], [35], [36].

1.1.4.2.2.2 Other slow inorganic scintillators

$\text{Bi}_4\text{Ge}_3\text{O}_{12}$ (BGO) is an intrinsic (undoped) scintillator which has the highest photoelectric absorption cross-section per unit volume among common inorganic scintillators, owing to its very high density and high Z_{eff} [1]. It is also available in large sizes but its low light yield, high refractive index and slow decay time make it a poor scintillator as far as energy and time resolution are concerned [37]. CdWO_4 and CaWO_4 also have high density, high Z_{eff} , as well as greater light yield as compared to BGO, but are extremely slow [38]–[43]. This means that their use in pulse mode for spectrometry is limited to small counting rate applications only. They are mostly used in current mode for X-ray detection and radiography. $\text{ZnS}(\text{Ag})$ is a polycrystalline (powder) scintillator with high scintillation efficiency, used as thin screens for α and heavy ion detection [1], [44]. $\text{CaF}_2(\text{Eu})$ is an inert scintillator used at severe environmental conditions. It has a good light yield but a very long decay time [1], [45], [46]. $\text{SrI}_2(\text{Eu})$ is a newly identified scintillator with an excellent light yield and, consequently, a very good energy resolution [47], [48]. It is free from intrinsic radioactive contamination and is found to have low nonproportionality. However, it has a slow decay time that limits its application to high counting rate applications [1].

1.1.4.2.2.3 Undoped fast inorganic scintillators with low light yield

BaF_2 is a pure scintillator with high Z_{eff} and high density but a low light yield [49]–[51]. It has a fast component [52]–[55] of the scintillation decay that emits UV photons. The energy resolution achievable with this scintillator is usually poor and the slow component of the decay poses a few problems in timing applications involving high counting rates [1]. Pure CsI

has a low light yield and a complex emission spectrum with a mixture of fast and slow components [1], [56]–[58]. When cooled to LN₂ temperature, its scintillation properties improve a lot [1], [59]. CeBr₃ is a new scintillator with high density and high Z_{eff} , excellent light yield, sharp rise time and fast decay time [1], [60], [61]. Therefore, it offers excellent timing resolution as well as energy resolution, and consequently, may become a popular choice in high counting rate coincidence measurements. PbWO₄ is a pure scintillator with a fast decay time but an extremely low light yield [1], [62]. It has been especially developed for the electromagnetic calorimeter of the Compact Muon Solenoid (CMS) facility [1], [63].

1.1.4.2.2.4 Ce-activated fast inorganic scintillators

Rare earth (Y, La, Gd and Lu) halides and some of the rare earth oxides, when activated with Ce, usually result in very good light yield due to the electronic transition from the 5d to the 4f states of the Ce activator. The decay time of this transition is usually intermediate between the fast organic scintillators and the typically slow inorganics [64]. The high Z_{eff} and high density of this class of scintillators is also extremely useful for gamma spectrometry. In addition, the presence of ¹⁵⁷Gd (which has a very high neutron absorption cross-section) in Gd-based scintillators means that they have the potential to be used as efficient neutron detectors [1].

1.1.4.2.2.5 Rare earth oxyorthosilicates

Rare earth oxyorthosilicates, namely, Y₂(SiO₄)O:Ce (YSO:Ce), Gd₂(SiO₄)O:Ce (GSO:Ce), Lu₂(SiO₄)O:Ce (LSO:Ce), Lu_xGd_{2-x}(SiO₄)O:Ce (LGSO:Ce) and Lu_xY_{2-x}(SiO₄)O:Ce (LYSO:Ce) are useful in various applications [1]. YSO:Ce has a moderate light yield [65], a good energy resolution [66], and a fast decay time [67] but its relatively low Z_{eff} and low density [68] compared to other scintillators in this class limits its applicability to gamma spectrometry. GSO:Ce [69], [70] overcomes these problems and also offers very good radiation hardness [71]. Doping concentration and co-doping are found to have significant

effects on its scintillation properties [1], [72]. LSO:Ce offers high Z_{eff} and high density combined with a high light yield and a short decay time [73], but the nonproportionality of light yield [74] and the presence of ^{176}Lu that adds a significant amount of internal radioactivity are the major drawbacks of this scintillator [1]. LGSO:Ce has lower afterglow than LSO:Ce and also offers better energy resolution than LSO:Ce and LYSO:Ce. LYSO:Ce, with various proportions of Lu and Y, blends the favorable properties of LSO:Ce with those of YSO:Ce [75].

1.1.4.2.2.6 Rare earth pyrosilicates

Rare earth pyrosilicates, namely, $\text{Gd}_2\text{Si}_2\text{O}_7:\text{Ce}$ (GPS:Ce) and $\text{Lu}_2\text{Si}_2\text{O}_7:\text{Ce}$ (LPS:Ce) have good combination of scintillation and stopping power properties [1]. The former has issues related to growth of its single crystals [76], whereas the latter has nonproportionality related problems [77], [78].

1.1.4.2.2.7 Rare earth aluminum perovskites

Rare earth aluminum perovskites, namely, $\text{YAlO}_3:\text{Ce}$ (YAP:Ce), $\text{LuAlO}_3:\text{Ce}$ (LuAP:Ce) and the composite $\text{Lu}_x\text{Y}_{1-x}\text{AlO}_3:\text{Ce}$ (LuYAP:Ce) have some very good scintillation properties [1], [79]. YAP:Ce has a very good light yield that is remarkably free from nonproportionality [80], a very fast decay time, and an excellent combination of mechanical and chemical properties like hardness, inertness and strength that result in very good energy resolution and timing resolution as well as ease in crystal growth and handling [1]. The light yield and the energy resolution are, however, seen to deteriorate with increase in crystal dimensions [79], [81]. Substituting Lu for Y results in very high stopping power for gamma rays as well as scintillation properties very similar or even better to those of YAP:Ce [1], [82]. The internal contamination due to ^{176}Lu , the self-absorption of scintillation emission by the crystal, and the challenges associated with the growth of large single crystals, however, pose significant

difficulties at present with the development of LuAP:Ce [1], [83]. LuYAP:Ce is easier to manufacture but the self-absorption is increased with respect to LuAP:Ce [1].

1.1.4.2.2.8 Rare earth aluminum garnets

Rare earth aluminum garnets, namely, $Y_3Al_5O_{12}:Ce$ (YAG:Ce) [84], [85] and $Lu_3Al_5O_{12}:Ce$ (LuAG:Ce) [86]–[88] are non-hygroscopic and offer good light yield and fast decay times. Their emission spectra are similar to that of CsI(Tl), resulting in the development of gamma spectrometers with silicon based photodetectors [1]. The relative intensities of the fast and the slow components of the scintillation decay depend on the type of ionizing radiation. This results in good PSD properties of these crystals. LuAG:Ce, by virtue of its high mechanical and chemical stability, can be machined into various shapes and sizes as per requirement. Another rare earth composite aluminum garnet that has recently been discovered is $Gd_3Ga_3Al_2O_{12}:Ce$ (GGAG:Ce) [89], [90]. It has high Z_{eff} , high density, high light yield, fast decay time, good energy resolution [91] as well as good PSD capabilities [92]. It is also non-hygroscopic and its emission peaks at the green region, like that of CsI(Tl). Therefore, it has the potential to be coupled with silicon based photodetectors in order to develop compact spectrometric devices [93]. Co-doping GGAG:Ce results in modifications of its scintillation, optical and timing characteristics. GGAG:Ce, co-doped with B (GGAG:Ce,B) is the brightest single crystal oxide scintillator [92]–[98].

1.1.4.2.2.9 Lanthanum halides

$LaCl_3(Ce)$ [101] and $LaBr_3(Ce)$ [102] are the most attractive modern alternatives to NaI(Tl) owing to their higher Z_{eff} and higher densities, higher light yield, much faster decay times, emission wavelengths well matched to conventional photocathodes, and much better energy resolution [103], [104]. $LaBr_3(Ce)$ is commercially available nowadays [105], [106] with dimensions good enough for gamma spectrometry and offer better energy resolution compared to its competitive scintillator materials. The energy resolution achievable with

LaBr₃(Ce) is as low as approaching the Poisson statistical limit. This is due to the extremely low nonproportionality of the scintillation response of this material. Its characteristics are also well suited for applications involving high count rates. The two major shortcomings of this scintillators are (i) the presence of internal contamination from ¹³⁸La and ²²⁷Ac (Ac is a chemical analogue of La) [107]–[113] and (ii) the hexagonal crystal structure that leads to anisotropic thermal expansion resulting in internal stresses and, consequently, cracking of the crystals when they are cooled after growth [1]. LaBr₃(Ce) is even more hygroscopic than NaI(Tl), leading to further difficulties in the growth process. As a consequence, LaBr₃(Ce), at present, is significantly more costly compared to NaI(Tl). Although the ²²⁷Ac concentration has been suppressed with advancement in crystal growth technologies, ¹³⁸La is naturally present and results in a signature background spectrum. This limits the applicability of LaBr₃(Ce) to low counting rate scenarios, e.g., environmental gamma spectrometry. LaBr₃(Ce), in addition, shows good radiation hardness [114], [115] and its light yield and energy resolution are more or less constant over a wide temperature range [116]. However, its PSD capabilities are poor [117]. Sr co-doped LaBr₃(Ce) retains most of the scintillation properties of LaBr₃(Ce), while improving the energy resolution [106]. LaBr_{3-x}Cl_x(Ce) has better mechanical properties and similar scintillation characteristics to those of LaBr₃(Ce) [118].

1.1.4.2.2.10 Lutetium halides

Lutetium halides, specifically LuI₃(Ce) and LuBr₃(Ce), are promising scintillator materials [119], [120]. LuI₃(Ce) has a very good light yield, fast decay time and a good energy resolution achievable [121], [122]. However, growth of its crystals with large enough dimensions continues to be an issue. LuBr₃(Ce) has inferior properties compared to those of LuI₃(Ce). The intrinsic background due to ¹⁷⁶Lu remains a problem in these two crystals [1].

1.1.4.2.2.11 Other halides

GdI₃(Ce) [119] and YI₃(Ce) [122] have very high light yield, fast decay times and are free from internal radioactivity. In fact, their light yield are greater than that of LaBr₃(Ce) and the nonproportionality is also found to be lesser. At present, however, their crystal qualities are not good enough to result in energy resolution better than LaBr₃(Ce) [1].

1.1.4.2.2.12 Elpasolites

Elpasolites are compounds having the chemical formula A₂DEX₆(Ce) (where A: Cs, Rb or K; D: Li or Na or a mixture thereof; E: La, Ce, Gd, Y, Lu or a mixture thereof; X: Cl, Br, I or a mixture thereof). Two of them are of particular interest, namely, Cs₂LiLaBr₆(Ce) and Cs₂NaLaI₆(Ce). They are cubic in crystal structure and, therefore, easy to fabricate, rugged, hygroscopic, and have generally high light yield and fast decay times [1]. Cs₂LiLaBr₆(Ce) can be used for simultaneous gamma and neutron detection and offer good PSD [123]. They have very good light yield proportionality and consequently result in very good energy resolution comparable to that of LaBr₃(Ce). Cs₂LiLaBr_{6-x}Cl_x(Ce) offers good energy resolution as well as good PSD capabilities. Cs₂LiYCl₆(Ce) and Rb₂LiYBr₆(Ce), owing to the presence of ⁶Li, are good candidates for neutron detection. The former has different decay times for n and γ, and, consequently, achieves n/γ discrimination by PSD [124]. The latter, on the other hand, does this by virtue of having different light yield, and, consequently, different pulse amplitudes, for n and γ [125].

1.1.4.2.2.13 Transparent ceramic scintillators

Growth of large volume single crystal scintillators is often a very demanding and sometimes even an impossible process. An alternative is to develop transparent ceramics by sintering a powdered material into a polycrystalline solid. Some success has been achieved with YAG(Ce) and LuAG(Ce). These ceramics are found to have better light output than their single crystal counterparts [126], [127]. Ceramic (Y,Gd)₃Al₅O₁₂(Ce) (GYAG:Ce) has also

been produced to increase the Z_{eff} and density over YAG(Ce) [128]. In ceramic development, addition of higher concentrations of activator, co-doping, stoichiometry control, etc. are generally easier than in the growth of single crystals. However, loss of optical photons due to scattering at the grain boundaries reduces the transparency of the ceramics. This limits the suitability of ceramics production with only those materials that have cubic crystal structures and no birefringence [1].

1.1.4.2.2.14 Scintillating glasses

Ce activated silicate glasses with Li or B loading are used for neutron detection [129]. Light output of the Li loaded glasses is much higher than that of the B loaded glasses. The emission is due to the electronic transitions between the Ce^{3+} activator states. Although their light output is much lower than conventional scintillators, these glasses are used in severe environmental conditions, e.g., when the scintillator must be exposed to corrosive chemicals or exposed to very high temperatures. Glasses are also available in a wide variety of physical forms, e.g., in the form of thin fibers or as a powder containing small spheres, among others. For neutron detection, usually Li enriched in 6Li is used, whereas for beta or gamma counting, the enrichment is not required. For small count rate applications just above the background, care must be taken to eliminate the naturally radioactive Th and K from the glasses [1]. Tb activated glasses are another class of glass scintillators that offer a much higher light output [130] with a very slow decay time that peaks around the green region. They are useful in X-ray imaging applications.

1.1.4.2.2.15 Noble gas scintillators

When ionizing radiation passes through a pressurized volume of noble gases, molecular excitation occurs. The subsequent de-excitation gives rise to UV scintillation photons that are directly sensed by photodetectors with extended response in the UV region or, alternatively, are converted to visible photons by adding a secondary gas like N_2 that absorbs UV and re-

radiates in the visible region. The decay times are quite fast and the light yield is also quite high, but the loss of photons during conversion to visible light limits the effective light output. There are no constraint in the available shapes and sizes of noble gas scintillators. They have been widely used for heavy ion spectroscopy [1], [10].

1.1.4.2.2.16 Cryogenic liquid and solid scintillators

The noble gas He can be condensed into liquid [131], whereas Ar, Kr and Xe can be condensed into liquids as well as solids [132] at cryogenic temperatures. These cryogenic liquids and solids generally have good light yield [133] with fast decay times that peaks in the UV region. In order to efficiently collect the scintillation photons at the photodetectors, the latter must also be maintained at cryogenic temperatures so that the density fluctuations in the scintillator due to temperature gradients near the photodetector do not lead to loss of the photons by virtue of scattering. Xe is the most suitable choice for gamma ray detection owing to its high Z. Ar is a low cost alternative that is used in large volume scintillators [1].

1.1.4.2.2.17 Scintillating fibers

Some inorganic scintillators, e.g., Ce activated glasses loaded with Li, BGO, LSO:Ce, LYSO:Ce, YAP(Ce), YAG(Ce), LuAG(Ce), can be made in the form of thin fibers with scintillation photons travelling through them by virtue of total internal reflection [134], [135]. The fiber core is usually surrounded by a clad with a lower refractive index. Light may be sensed at both ends of the fiber. Light collection efficiency, however, depends on the losses of optical photons due to absorption in the bulk of the scintillator as well as on the losses during reflection at the core-clad interface [1].

1.1.4.3 Semiconductor diode detectors

Semiconductor diode detectors offer solid detection media that are typically of the order of 1000 times denser than gases. This results to compactness over gas-filled detectors. They also offer the best energy resolution among all types of detectors, owing to the lowest energy

(about 3 eV) required to generate an information carrier, compared to that required for a gas (typically of the order of 30 eV) or a scintillator (typically of the order of 100 eV or more). Semiconductors also offer fast timing characteristics. However, they are generally more susceptible to radiation damage than other types of detectors. A semiconductor diode detector is usually made by using a detector grade highly pure semiconductor with high resistivity and then forming *p*- and *n*-type contacts on its opposite ends. Highly pure semiconductors may be available only in small sizes, thereby limiting the achievable detector dimensions. Semiconductors usually have a band gap of nearly 1 eV. Electron-hole pairs are generated upon the passage of ionizing radiation through the detector. A reverse bias is applied across the *p-n* junction in order to suppress the leakage current and to collect the radiation-induced charge carriers at the opposite electrodes. This forms the basic electrical signal.

Among natural semiconductor materials, Si has a band gap of 1.1 eV at room temperature (300 K) which is larger than that of Ge (0.7 eV). Therefore, the thermally generated leakage current in Ge is higher than that in Si at room temperature. Si diodes can be used at room temperature (although their performance generally improves with cooling) but Ge detectors need to be operated at LN₂ temperature. Si diodes are primarily used for charged particle and X-ray spectroscopy as well as for personnel monitoring. They can also be used in the photovoltaic mode that does not require the application of a reverse bias and the charge carriers are simply collected by the contact potential existing across the junction. Depletion layer thicknesses of Si diodes are limited to typically less than a few millimeters. Thicker detectors with required high resistivity, however, may be formed by Li-ion drifting, resulting in Si(Li) detectors, that are used for low energy photon spectroscopy and electron spectroscopy.

Similar configuration existed for Ge detectors, namely the Ge(Li) detectors, before the high purity germanium (HPGe) configuration was realized by the zone-refining technique.

While Si(Li) and Ge(Li) detectors must be continuously maintained at LN₂ temperature during operation as well as storage in order to prevent the Li ion redistribution, HPGe detectors can be stored under room temperature between operations. HPGe detectors offer the best energy resolution among all detectors for gamma spectrometry and are available as large volume detectors. The higher Z of Ge (32) is also an advantage over Si ($Z = 14$) when it comes to gamma spectrometry.

Compound semiconductors, namely, CdTe, HgI₂, Cd_{1-x}Zn_xTe (CZT) etc. have high Z_{eff} , high density and large band gap, permit room temperature operation, but offer energy resolution values that are typically one order of magnitude poorer than that achievable with HPGe, and are available in much smaller sizes compared to HPGe [1].

1.2 Photodetectors

1.2.1 An overview

Photodetectors are photon sensors that convert photons into a measurable electrical signal whose amplitude is proportional to the photon intensity. They can be sensitive to UV, VIS or near IR (NIR) photons and are, therefore, useful in various fields like optical spectroscopy, laser related measurements, astronomy, etc. When coupled to scintillators, they convert the scintillation photons into a proportional electrical signal, thereby making it possible to perform radiation detection and spectroscopy with scintillators. There are generally two types of photodetectors, namely, (i) PMTs and (ii) silicon based solid state photodetectors. The latter can be subdivided into three categories: (i) silicon photodiodes, (ii) avalanche photodiodes (APDs) and (iii) silicon photomultipliers (SiPMs). PMTs are the oldest and the most widely used even today, performing remarkably well in converting the weak light signals from scintillators into amplified electrical signals without introducing much noise. Silicon based photodetectors, on the other hand, are relatively new developments. They offer advantages like compactness, low power and low voltage operation, ruggedness and

insensitivity to magnetic fields. However, the signal to noise ratio (SNR) provided by them remains a concern [1].

1.2.2 Photomultiplier tubes (PMTs)

1.2.2.1 Construction

A simplified structure of a PMT [136], [137] is depicted in Figure 1.2.

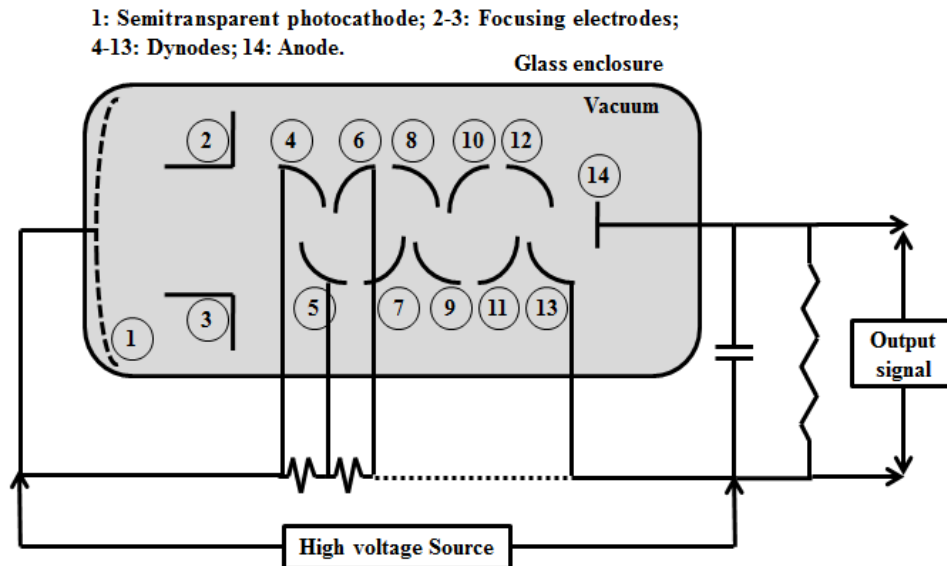


Figure 1.2: Basic construction of a PMT.

It is basically a vacuum tube with a glass enclosure, having (i) a photocathode that absorbs photons and emits photoelectrons, (ii) focusing electrodes for efficiently collecting the photoelectrons at the first dynode, (iii) a coupled electron multiplication structure consisting of multiple dynodes maintained at progressively increasing voltages, thereby providing amplification of the photoelectron signal, and (iv) an anode for collecting the amplified signal. A high voltage (HV) source and a resistive voltage divider network are also included in the design for proper biasing of the photocathode and each successive dynode up to the anode. Either the photocathode is grounded and a positive HV is applied to the anode, or, alternatively, the anode is grounded and a negative HV is applied to the photocathode. As the electron trajectories inside the PMT are extremely sensitive to magnetic fields, usually a magnetic shield made up of a mu-metal, maintained at the photocathode potential, is also

provided outside the glass enclosure. The amplitudes of the output pulses at the anode remain largely proportional to the number of photons incident on the photocathode. Much of the timing information of the incident light pulses are also preserved in the output anode pulses [1].

1.2.2.2 The photocathode

1.2.2.2.1 The photoemission process

Conversion of photons to electrons in the photocathode is a three step process. In the first step, a photon is absorbed and its energy is transferred to an electron of the photocathode. Next, this electron migrates to the photocathode surface. Finally, it escapes from the surface. The maximum initial photoelectron energy is theoretically equal to the photon energy, which, for typical scintillation photons, is $h\nu \cong 3$ eV. Some of this energy is lost in the migration process. The balance energy of the photoelectron must be enough to overcome the work function of the photocathode material in order for it to escape from the surface. Therefore, a minimum photon energy is required in order to make it energetically possible for the photoelectrons to escape the photocathode surface. This imposes a long wavelength cutoff which is typically in the red or the near IR region. Further, the work function as well as the rate of energy loss by the photoelectrons during their migration should be as low as possible in order to maximize the number of escaping photoelectrons. The energy loss during migration always imposes a maximum escape depth. Photoelectrons originating beyond this depth inside the surface cannot escape. The escape depth in metals is only a few nm, whereas the same for semiconductors is about 25 nm. Photocathodes this thin are, however, semitransparent for visible scintillation photons. Therefore, there is also a high energy (low wavelength) cutoff, beyond which the process of conversion of photons to photoelectrons becomes extremely inefficient.

In semiconductor photocathodes, electrons are elevated from the valence band to the conduction band upon absorbing photons having an energy greater than the band gap. These electrons end up at the bottom of the conduction band within usually a picosecond by losing their energy through phonon interactions. The electron affinity is defined as the difference between the values of electron potential at vacuum and at the bottom of the conduction band. For semiconductors, it is usually positive, and hence the electrons must reach the surface very rapidly, even before phonon interactions can reduce their energies to the bottom of the conduction band. For materials with negative electron affinity (NEA), however, the electrons that have dropped to the bottom of the conduction band can also escape [1].

1.2.2.2 Thermionic noise

Normal conduction electrons, in the absence of incident light photons, are in thermal equilibrium having energies distributed about a mean of about 0.025 eV at room temperature. The electrons near the high-end extreme of this distribution may possess energies above the surface potential barrier, and therefore, have a finite escape probability from the surface. This gives rise to a thermionic noise which is higher for materials with lower potential barrier. Hence, higher photosensitivity of semiconductors relative to metals is achieved at the cost of a greater thermionic noise. The thermionic noise increases with temperature [1].

1.2.2.3 Photocathode designs

Photocathodes can be either opaque or semitransparent. Opaque photocathodes have thicknesses greater than the maximum escape depth and are deposited on a thick backing. Photoelectrons are collected from the same surface on which the photons are incident. Semitransparent photocathodes, on the other hand, are thinner than the maximum escape depth and are deposited on a thin transparent backing, often the glass end window of the PMT. Photoelectrons are collected from the opposite surface to the one on which the photons are incident. Semitransparent photocathodes are more commonly used for applications

involving scintillators. Any variation in the uniformity of the thickness of the photocathode over its entire area results in variations of its sensitivity, and can contribute to deterioration of energy resolution in scintillation based spectrometers [1].

1.2.2.2.4 Quantum efficiency and spectral response

The quantum efficiency (QE) of the photocathode is defined as [1],

$$QE = \frac{\text{number of photoelectrons emitted}}{\text{number of photons incident}} \quad (1.1)$$

For typical photocathodes, it is limited to a maximum value of 0.2-0.3 and drops at high and low values of wavelengths due to reasons described in Section 1.2.2.2.1. It is highly dependent on the wavelength of the incident photons. A plot of QE as a function of the wavelength is called the spectral response of the photocathode. The effective QE when a particular scintillator is coupled to a PMT is determined by averaging the spectral response curve of the photocathode over the emission spectrum of the scintillator. This averaged QE is called emission weighted quantum efficiency ($EWQE$) [138].

1.2.2.2.5 Photocathode materials

Presently available photocathode materials include (i) Cs-activated Na_2KSb , also called multialkali photocathodes, offering QE of up to 0.3 in the blue region, (ii) O and Cs-activated K_2CsSb , also called bialkali photocathodes, offering higher QE than the multialkali photocathodes in the blue region and also resulting in lower thermionic noise [1].

There are various techniques to increase the QE of bialkali photocathodes to as high as 0.45 in the blue region. Reducing reflection of photons from the photocathode by introducing an anti-reflective coating [139], reflecting back some of the photons that have passed through the semitransparent photocathode by introducing nearby reflective structures [140], [141], avoiding electron traps by using ultra-pure materials [139], etc. are some of these techniques [1].

1.2.2.3 Electron multiplication

1.2.2.3.1 Secondary electron emission

The photoelectrons escaping the photocathode surface, having energies of the order of 1 eV or less, are focused towards the first dynode by focusing electrodes. The first dynode is kept at a positive potential of several hundred volts. Therefore, photoelectrons can gain kinetic energies of the order of several hundred eV before reaching the first dynode. Here, they can cause electronic excitation from the valence band to the conduction band of the dynode, the band gap being only 2-3 eV, and each photoelectron can create of the order of 30 excited electrons. These excited electrons have random directions of motion and many of them do not make it to the surface of the dynode. Among those which reach the surface, only a small fraction will have a kinetic energy greater than the surface barrier. Therefore, the net effect is the emission of just a few secondary electrons per photoelectron from the same surface of the first dynode in which the photoelectron strikes. The multiplication factor (δ) of a single dynode is defined as [1],

$$\delta = \frac{\text{number of secondary electrons emitted}}{\text{number of photoelectrons incident}} \quad (1.2)$$

It is strongly dependent on the photoelectron energy. It is low for low energy photoelectrons owing to the low number of electrons that they excite into the conduction band. It also falls for high energy photoelectrons because they create excited electrons at greater average depths into the dynode and many of these electrons cannot reach the surface. The value of δ is maximum at an intermediate photoelectron energy. For conventional dynode materials like BeO, MgO and Cs₃Sb, its maximum value of about 10 is reached at photoelectron energies of about 1 keV. Typical values of δ are, however, 4-6 for conventional interdynode voltages of a few hundred volts [1].

1.2.2.3.2 Materials with negative electron affinity

As per arguments presented in Section 1.2.2.2.1, δ can be significantly increased by using NEA materials, e.g., GaP heavily doped with Zn and with a nearly monatomic layer of Cs applied to one of the surfaces [142]. Electrons that have fallen to the bottom of the conduction band can also escape from the surface. δ continues to increase up to very high photoelectron energies. Therefore, achievable values of δ become about 50-60 with interdynode voltages of about 1000 V, and even higher values may be obtained if the design of the PMT permits application of higher interdynode voltages [1].

1.2.2.3.3 Multiple stages of multiplication

For a dynode structure with N stages, each having a multiplication factor δ , the overall gain of the PMT becomes [1],

$$\text{Overall gain} = \alpha\delta^N \quad (1.3)$$

where α is the fraction of produced photoelectrons at each stage that is collected by the subsequent stage. For suitably designed PMTs, it is very close to unity. For typical dynodes with $\delta \sim 5$, ten stages result in an overall gain of 5^{10} , i.e., about 10^7 . The overall gain is also strongly dependent on the interdynode voltage.

In reality, however, the emission of secondary electrons is a statistical process, and therefore, δ fluctuates about a mean value from event to event. This fluctuation of δ contributes to deterioration of energy resolution from scintillator based spectrometers [1].

1.2.3 Silicon based solid state photodetectors

1.2.3.1 Silicon photodiodes

1.2.3.1.1 Basic operation

These are silicon diodes with the PIN configuration (as shown in Figure 1.3 [1]), having a high resistivity near intrinsic (i) region of thickness of the order of 200-500 μm sandwiched between a very thin (typically $< 1 \mu\text{m}$) highly doped p -type region and a very thin (typically

1-2 μm) highly doped n -type region. Scintillation photons enter the active (i) region of the photodiode through the very thin p -type entrance window and generate electron-hole pairs upon absorption. These electron-hole pairs are collected by applying a reverse bias. The collected charge is processed at a connected preamplifier which produces the output signal [1], [143].

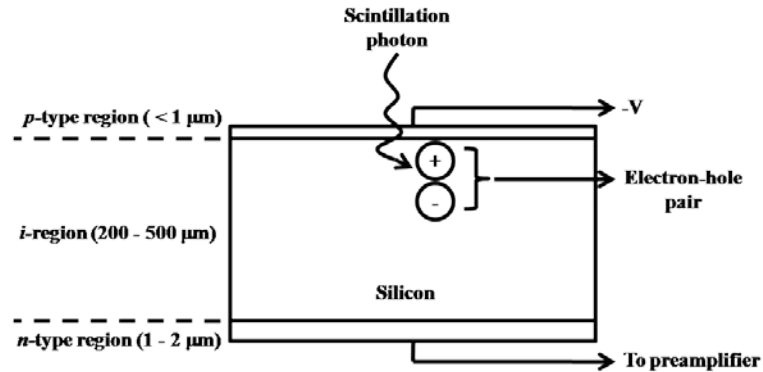


Figure 1.3: Basic configuration of a silicon photodiode [1].

1.2.3.1.2 Quantum efficiency and spectral response

Unlike PMTs, the charge carriers need not escape from the surface, and therefore, the maximum QE achievable with photodiodes can be much higher. The spectral response is also much broader, extending way into the long wavelength region and resulting in much higher values of $EWQE$ when photodiodes are coupled with scintillators, especially those which have high scintillation yield at long wavelengths, e.g., CsI(Tl), GGAG:Ce, BGO, etc. [1].

1.2.3.1.3 Noise in photodiodes

As there is no amplification of the generated charge, the output signal from a photodiode is orders of magnitude smaller than that from a PMT. Due to this small signal amplitude, electronic noise is a major problem when photodiodes are operated in pulse mode. The electronic noise increases with increasing surface area of the diode due to the corresponding increase in dark current and capacitance. The SNR decreases with decreasing energy of the ionizing radiation [1]. When scintillators are coupled with photodiodes for gamma spectrometry, energy resolution values achievable are usually always inferior to those cases

in which scintillators are coupled with PMTs [144]. When used in current mode, however, at high event rates, as in X-ray computed tomography (CT) applications, the SNR increases and the photodiodes perform exceedingly well [145].

There are broadly two sources of noise in photodiodes: (i) capacitance related series noise originating at the input stage of the preamplifier, and (ii) leakage current related parallel noise originating due to fluctuations in the leakage current of the photodiode. The first of these noises decreases with increasing thicknesses of the photodiodes, whereas the second increases. Thicknesses of about 200-500 μm usually give an optimum noise value. On the other hand, both the types of noise increase with increasing surface area of the photodiode, and therefore, photodiode areas are usually limited to only a few cm^2 [1].

The shaping time constant of the pulse shaping electronics also determines the relative importance of the two types of noise. Longer shaping times reduce series noise but increase parallel noise. An optimum shaping time must be chosen that minimizes the overall noise. On the other hand, the shaping time must be longer than the scintillation decay time in order to ensure complete charge collection in each scintillation event, and at the same time, short enough to avoid pulse pile-up at high event rates [1].

Cooling of a photodiode reduces its dark current and thereby the associated noise. On the other hand, increase in dark current and the associated noise with increasing temperature usually forbids their operation at elevated temperatures. Use of wider band gap compound semiconductors, e.g., HgI_2 , decreases dark current. Attainable energy resolution values with this photodiode may be superior to those obtainable with PMTs [146]. By incorporating the input junction field-effect transistor (JFET) stage of the preamplifier on the same chip as the silicon photodiode, the overall stray capacitance of the connection between the photodiode and the preamplifier may be avoided. Thus the overall capacitance and the associated noise can be greatly reduced [1].

Although the charge collection time for semiconductors is only of the order of a few nanoseconds, the timing resolution achievable with photodiodes is usually deteriorated by the fluctuations in the noise level [1].

The surface areas of photodiodes are limited from noise considerations. This poses problems for collecting scintillation light from large area scintillators. Covering the scintillator with multiple photodiodes and adding up their signals increases the signal as well as the noise by the same factor. Therefore, the SNR does not increase [1].

In addition to scintillation photons, ionizing radiation can themselves directly penetrate into the photodiode and create electron-hole pairs. In order to minimize this effect, the photodiodes should be kept as thin as possible. However, thin photodiodes have a greater capacitance and therefore a higher series noise [1].

1.2.3.2 Avalanche photodiodes (APDs)

At high applied voltages typically somewhat below the breakdown voltage, the charge carriers can be accelerated enough between collisions in order to create secondary ionization, a process called avalanche. This internal gain (typically a few hundred) helps to increase the SNR for APDs as compared to photodiodes, especially for pulse mode operation with low energy ionizing radiation. The gain, however, is an exponential function of the applied voltage. Therefore, well-regulated HV supplies are required for biasing of APDs. Also, the gain dependence of APDs on temperature (decreasing by about 2% per °C increase in temperature) is even stronger than that for PMTs. Therefore, automatic gain compensation schemes need to be incorporated when APDs are operated under varying temperature conditions. For current mode applications, the more stable photodiodes are generally preferred over APDs. APDs generally have good timing properties because the carrier drift time in semiconductors is usually of the order of less than a nanosecond.

As the APDs have much lower gain than the PMTs, this gain is subject to higher statistical fluctuations. This gain fluctuation, along with the series and the parallel noise which are also present in the APDs as in the photodiodes, deteriorate the achievable energy resolution when APDs are coupled with scintillators, as compared to when PMTs are coupled with scintillators. This deterioration is more severe for low energy ionizing radiation. The higher quantum efficiency of the APDs somewhat offsets the deterioration of obtainable energy resolution, an effect that is especially significant for scintillators having high light yield at longer wavelengths, e.g., CsI(Tl), GGAG:Ce, BGO, etc. APDs are available only with small surface areas that are similar to photodiodes, and therefore, efficient collection of scintillation photons from large size scintillators remains an area of concern [1].

1.2.3.3 Silicon photomultipliers (SiPMs)

When the voltage to an APD is increased above the breakdown voltage, the avalanche process runs away and the diode enters a Geiger mode in which the initial charges produced by the interaction of an ionizing particle are multiplied to a level beyond control. Therefore, the Geiger mode APD produces a large output pulse from even a single radiation event. The Geiger mode avalanche is usually quenched by employing a high resistance in series which produces a voltage drop when the avalanche current passes through it, thereby lowering the voltage across the diode to below the breakdown voltage. The quenching time is equal to the product of the diode capacitance and the quenching resistance. A two dimensional array of a large number of such small APD cells working in the Geiger mode (each quenched by a series resistor) and connected in parallel is called a SiPM or a multi-pixel photon counter (MPPC). The SiPM is realized on a single silicon chip. Each cell has typical dimensions of only tens of microns and there are usually of the order of 10^4 cells or more in an array, so that the probability of one cell being hit by more than one scintillation photon during a radiation event is usually very low. Under this condition, the number of cells producing avalanche is

proportional to the number of scintillation photons reaching the SiPM. Also, the output of each cell is nearly identical by virtue of the uniformity of each cell and its quenching resistor. Therefore, by connecting the individual cells in parallel and adding their outputs, an output signal obtained which is proportional to the number of detected scintillation photons.

The thermally excited electrons lead to spurious avalanches which add randomly as a noise to the actual scintillation signal. These thermally generated electrons, however, usually fire a single cell at a time. For situations in which each pulse results from a very large number of scintillation photons, the thermal events can be discarded by setting a discrimination level suitably so as to register only those pulses that result from simultaneous firing of multiple cells. Also, by cooling the SiPM, the dark noise can be reduced. Impurities in silicon can act as trap centers and release trapped electrons afterwards, thereby initiating delayed avalanches, a phenomenon called afterpulsing. Also, photons may be emitted by a cell upon carrier recombination. These photons may travel to neighboring cells directly or upon reflections inside the coupled scintillator, and trigger avalanches. This process is called optical cross-talk.

The photon detection efficiency of SiPMs is typically higher than the PMTs, and depends on the geometric fill factor, the quantum efficiency, and the avalanche initiation probability. For stable operation of SiPMs, stable biasing circuitry and gain compensation schemes need to be implemented. Also, SiPM surface areas are restricted due to dark noise considerations, and therefore, efficient collection of photons from large scintillators remains an issue. It is to be noted that SiPMs have a response which is inherently nonlinear with scintillation light intensity. For increasing light intensities, more and more photons are incident on a single cell within its recovery time, and therefore, more and more photons go undetected [1].

1.3 Gamma spectrometry

Gamma spectrometry is the branch of radiation detection that deals with the acquisition of energy spectra of gamma ray sources by using gamma spectrometers and the subsequent analysis of the acquired spectra in order to identify and/or quantify the radionuclides present in the gamma sources. It is extensively used in the fields of nuclear physics and engineering, geochemical exploration, astrophysical sciences, environmental radioactivity monitoring, nuclear medicine, nuclear forensics, material science and engineering, homeland security, health physics, etc.

1.3.1 Gamma ray interactions

Three processes, namely, photoelectric absorption, Compton scattering and pair production, lead to energy loss of gamma photons in detector media. Photoelectric absorption is predominant for gamma rays with energies up to several hundred keV, pair production predominates at very high energies (above 5-10 MeV), and Compton scattering is the most probable process in between. Photoelectric interaction probability varies roughly as $Z^{4.5}$, where Z is the atomic number of the interacting medium. On the other hand, the probabilities of Compton scattering and pair production varies as Z and Z^2 , respectively. Therefore, high Z materials are chosen as detector materials for gamma spectrometry in order to increase the gamma ray interaction probability [1].

1.3.1.1 Photoelectric absorption

In this process, a photoelectron is ejected from one of the electronic shells (predominantly the innermost shell for typical gamma energies) of the interacting atom upon absorption of a gamma photon having energy $h\nu$. The ejected electron carries a kinetic energy (E_{e^-}) equal to $h\nu$ minus the binding energy (E_b) of the electron in its shell. Subsequent rapid electronic rearrangement fills the vacancy in the electronic shell and emits either a characteristic X-ray photon or an Auger electron. If the photoelectron as well as the characteristic X-ray photon or

the Auger electron are all absorbed in the detector medium, the result for a series of such photoelectric absorptions is a single peak at energy $h\nu$ in the pulse-height spectrum, as shown in Figure 1.4 [1].

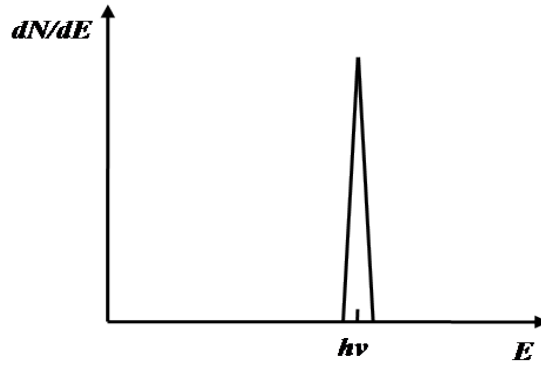


Figure 1.4: Simplified pulse-height spectrum for monoenergetic gamma rays with 100% photoelectric absorption [1].

1.3.1.2 Compton scattering

This inelastic scattering process of the original gamma photon (energy $h\nu$) results in a scattered photon (energy $h\nu'$) and a recoil electron (kinetic energy E_{e^-}), where,

$$h\nu' = \frac{h\nu}{1 + \frac{h\nu}{m_0c^2}(1 - \cos\theta)} \quad (1.4)$$

and

$$E_{e^-} = h\nu - h\nu' = h\nu \frac{\frac{h\nu}{m_0c^2}(1 - \cos\theta)}{1 + \frac{h\nu}{m_0c^2}(1 - \cos\theta)} \quad (1.5)$$

m_0c^2 being the rest mass energy of the electron (511 keV) and θ being the scattering angle.

As $\theta \cong 0$, $h\nu' \cong h\nu$ and $E_{e^-} \cong 0$. On the other hand, as $\theta \cong \pi$,

$$h\nu' /_{\theta=\pi} = \frac{h\nu}{1 + \frac{2h\nu}{m_0c^2}} \quad (1.6)$$

and

$$E_{e^-/\theta=\pi} = h\nu \frac{\frac{2h\nu}{m_0c^2}}{1 + \frac{2h\nu}{m_0c^2}} \quad (1.7)$$

Therefore, E_{e^-} can range continuously between 0 and that predicted by Equation (1.7), depending on the distribution of θ that follows the Klein-Nishina formula. For a series of monoenergetic gamma rays interacting purely via Compton scattering, the pulse-height spectrum takes the simplified shape as shown in Figure 1.5 [1].

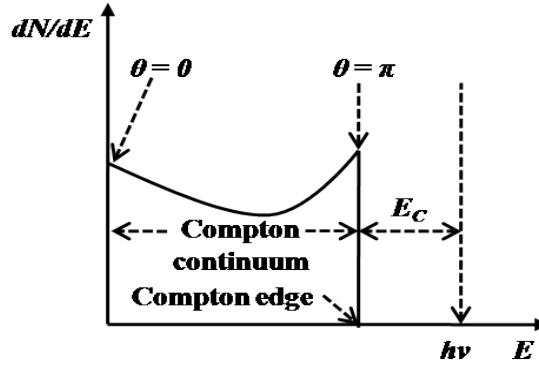


Figure 1.5: Simplified pulse-height spectrum for monoenergetic gamma rays with 100% Compton scattering [1].

The gap between the Compton edge ($E_{e^-/\theta=\pi}$) and the primary gamma energy ($h\nu$) is given by,

$$E_C = h\nu - E_{e^-/\theta=\pi} = \frac{h\nu}{1 + \frac{2h\nu}{m_0c^2}} \quad (1.8)$$

which, in the limit as $h\nu \gg \frac{m_0c^2}{2}$, takes the constant value,

$$E_C \cong \frac{m_0c^2}{2} (= 256 \text{ keV}) \quad (1.9)$$

Equations (1.4) to (1.9) are simplified formulae which assume scattering by free electrons. The small binding energies of the electrons in practical detector materials typically result in rounding off of the rise near the Compton edge and the introduction of a finite slope to its

abrupt drop. The finite momenta of bound electrons also affect the shape of the Compton continuum [1].

1.3.1.3 Pair production

This process occurs under the influence of the nuclei of the absorbing medium and results in the formation of an e^-e^+ pair and complete disappearance of the incident gamma photon. The energy of the gamma photon in excess of $2m_0c^2$ ($= 1.02$ MeV) is equally shared as the kinetic energies between the resulting e^-e^+ pair. If all e^-e^+ pairs are absorbed in a series of pair production interactions, the result is the simplified pulse-height spectrum with a single peak at energy $(h\nu-2m_0c^2)$, as shown in Figure 1.6 [1].

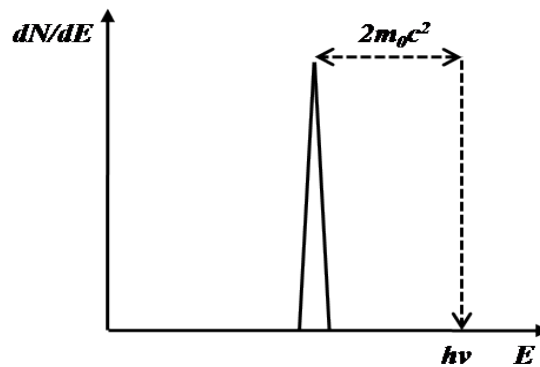


Figure 1.6: Simplified pulse-height spectrum for monoenergetic gamma rays with 100% pair production [1].

The pair production process is often followed by positron annihilation, in which it combines with an electron of the absorber. This results in the generation of two annihilation photons directed opposite to each other, and carrying equal energies of $(511 \text{ keV} + 0.5E_{e^+})$, where, E_{e^+} is the remaining kinetic energy of the positron just before annihilation, which is most often 0 except for in-flight annihilation. The annihilation process complicates the energy spectrum due to secondary interactions that the annihilation photons may undergo [1].

1.3.2 Features of gamma ray pulse-height spectra

1.3.2.1 Small detectors

For detector dimensions that are small compared to the mean free path of the secondary gamma photons but sufficient to stop all secondary charged particles, the pulse-height spectrum should consist of a photopeak at energy $h\nu$, a Compton continuum, and a double escape peak (because only the kinetic energy of the e^-e^+ pair gets deposited and both the annihilation photons escape) at energy $(h\nu - 2m_0c^2)$, as shown in Figure 1.7 [1]. Further, the last of these would disappear for gamma energies that are below the values for which pair production becomes significant [1].

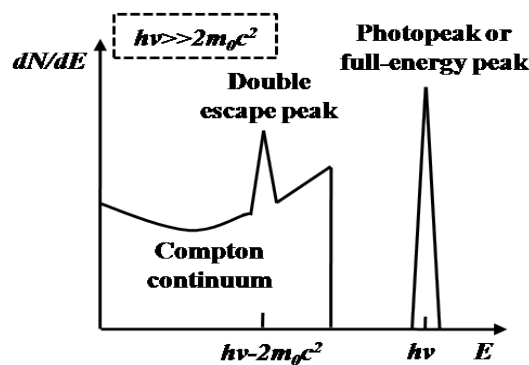


Figure 1.7: Predicted pulse-height spectrum for a small detector that stops all secondary charged particles but cannot stop any secondary gamma photons [1].

1.3.2.2 Large detectors

For detector dimensions that are large enough to stop all primary and secondary radiation, the entire primary gamma photon energy is deposited inside the detector in each interaction. The result of a series of such interactions is a single full-energy peak at energy $h\nu$ of the pulse-height spectrum, as shown in Figure 1.8 [1]. It is important to note that no matter how complex the interaction history of the primary gamma photon is, the pulse-height spectrum is such that it looks like it has undergone a single photoelectric absorption. Therefore, the terms photopeak and full-energy peak are used interchangeably [1].

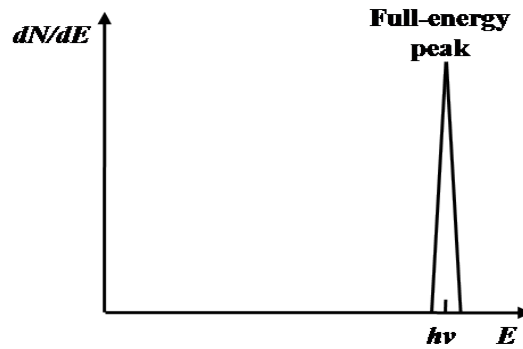


Figure 1.8: Predicted pulse-height spectrum for a large detector that stops all secondary radiation [1].

1.3.2.3 Intermediate size detectors

For practical detector dimensions that are between the two abovementioned extremes, the pulse-height spectra are usually complicated due to partial energy deposition by the secondary photons. Here, a single escape peak may also appear in addition to the double escape peak due to events in which one of the annihilation photons gets stopped inside the detector volume, whereas the other escapes. Further, events with multiple Compton scattering followed by escape of the final scattered photon lead to partial filling of the otherwise empty region between the Compton edge and the photopeak. This also distorts the shape of the Compton continuum that would result only from single scattering events. Figure 1.9 [1] shows the pulse-height spectrum that displays these features.

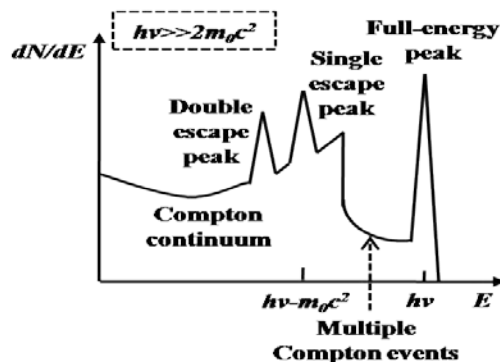


Figure 1.9: Predicted pulse-height spectrum for an intermediate size detector that partially stops secondary gamma photons [1].

1.3.2.4 Factors complicating pulse-height spectra

For high gamma energies, the average energies of the secondary electrons will tend to increase. As a result, a significant fraction of secondary electrons may escape from the detector. This would result in loss of some events from the photopeak and a skewing of the Compton continuum towards lower energies. Further, as the energies of the secondary electrons and the Z_{eff} of the detector medium increase, production of Bremsstrahlung increases. The escape of a fraction of these Bremsstrahlung photons results in similar alterations to the pulse-height spectrum as described above for secondary electron escape. Furthermore, Events in which the characteristic X-ray photon, resulting from the redistribution of electrons among the electronic shells subsequent to a photoelectron emission, escapes the detector volume, lead to a new peak at an energy $h\nu$ minus the characteristic X-ray energy. These peaks are called X-ray escape peaks and are most prominent for low energy gamma rays for which the photoelectric absorption near the detector's surface is predominant, thereby facilitating the escape of the characteristic X-rays, as well as for detectors with high surface area-to-volume ratios. For practical gamma energies, the photoelectron emission from the K-shell is most probable, and, therefore, the characteristic X-rays have energies equal to the K-shell binding energy. X-ray escape peaks at positions corresponding to higher electronic shells are less probable and are usually not resolvable.

Detectors are always surrounded by other materials, e.g., detector encapsulation to protect from moisture, light, shock, etc., shielding materials to suppress the natural background radiation, detector's support and ancillary equipment, etc. Gamma photons, upon scattering from these surrounding materials, often reach the detector to create a backscatter peak near 0.25 MeV, following the arguments presented in Equation (1.9). The peak is created because Compton scattered photons have a nearly identical energy of about 0.25 MeV for large scattering angles (hence the name backscattering) above nearly $110-120^\circ$ (see

Equation (1.4)). Further, characteristic X-ray photons may be created in the surrounding materials subsequent to photoelectric absorption in them. These photons may reach the detector and create an additional X-ray peak. This peak is more evident when the detector is surrounded by high Z materials. Furthermore, at high gamma energies, pair production and the subsequent positron annihilation may give rise to annihilation photons. These photons may present themselves as an annihilation peak at 511 keV. There are chances of confusing this peak with a genuine peak appearing due to a positron emitting source. Figure 1.10 [1] shows the simplified pulse-height spectrum that shows the influence of the surrounding materials.

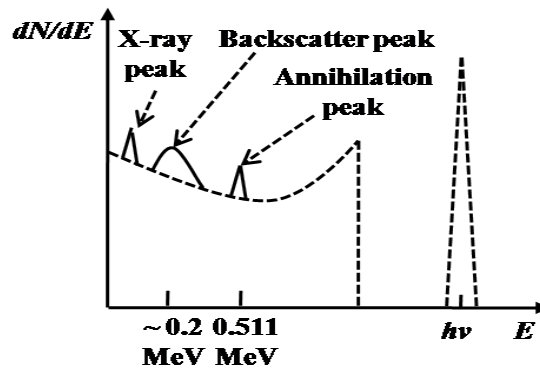


Figure 1.10: Influence of the surrounding materials to the otherwise expected (dashed) pulse-height spectrum [1].

The pulse-height spectrum may be further complicated when the source is not a pure gamma emitter. For example, annihilation peak may appear at 511 keV when the source emits positrons which are subsequently annihilated within the source or its encapsulation. If both annihilation photons can be simultaneously detected, as in a well type detector, a peak at 1.022 MeV may appear. Further, β^- emitting sources can lead to the generation of Bremsstrahlung via radiative energy losses of the β^- particles at the source encapsulation or at the external absorbers used to stop the β^- particles from unnecessarily complicating the gamma spectrum. These Bremsstrahlung photons may add a continuum onto which the entire gamma spectrum is superimposed. The Bremsstrahlung contribution cannot be simply

subtracted as a background, and, therefore, leads to errors in calculations of areas under the gamma spectrum.

Detection of two or more gamma photons in coincidence often leads to summation peaks in the recorded spectra. This becomes evident with sources that emit more than one gamma photons in cascade decay.

It is, however, difficult to observe all the features discussed so far in a single recorded spectrum [1].

1.3.3 Detectors used for gamma spectrometry

1.3.3.1 General considerations

Gases usually have low stopping power for gamma rays of typical energies, largely due to their very low densities. Therefore, gas-filled detectors are usually not employed for gamma spectrometry. Organic scintillators, owing to their low Z_{eff} and low densities, are also not typically suitable for this application. Si ($Z=14$) diode detectors, although used for low energy photon spectrometry, also have low Z_{eff} and low density, and, therefore, are not good choices for spectrometry of gamma rays with energies beyond a few hundreds of keV. The two major remaining types of detectors, namely, inorganic scintillators and HPGe detectors, are, therefore, used for most gamma spectrometry applications. Another modern detector worthy of a mention for this application is the compound semiconductor, CZT.

Further, it is useful to mention here that all spectrometry measurement must be carried out in pulse mode in order to retain the pulse-height (and, proportionately, energy) information of individual radiation interaction events within the detector. It is also worth a mention that in all of gamma spectrometry applications, typically the differential pulse-height spectra are recorded, which are plots of $\frac{dN}{dH}$ versus H , where H is the pulse-height (or, proportionately, energy) and $\frac{dN}{dH}$ is the ratio of the differential number of pulses dN observed to have a pulse-height within the differential pulse-height interval dH . The number of pulses

between two pulse-height values can be obtained by integrating the differential pulse-height spectrum between these two abscissa values [1].

1.3.3.2 Inorganic scintillators as gamma spectrometers

Inorganic scintillators optically coupled with photodetectors (PMTs, silicon photodiodes, APDs or SiPMs) are extensively used as detectors for gamma spectrometry. Table 1.1 provides an overall summary of properties of common inorganic scintillators that are used for gamma spectrometry, whereas Figure 1.11 shows a simplified block diagram of an inorganic scintillator based gamma spectrometer.

Upon interaction with a gamma photon, the inorganic scintillator produces many scintillation photons, as described in detail in Section 1.1.4.2. These scintillation photons travel to the coupled photodetector, where they are converted to a current pulse whose amplitude is proportional to the energy deposited by the incident gamma photon in the scintillator, as detailed in Section 1.2. The output pulse from the photodetector is sent to a preamplifier, which produces a proportional voltage step with a sharp rise time and a slow decay time, often called a tail pulse. The tail pulse is then shaped and amplified by the amplifier. Many such shaped and amplified pulses are fed to the multichannel analyzer (MCA) which measures the amplitude of each pulse and subsequently assigns each pulse to a particular channel according to the height of the pulse. When a pulse is assigned to a particular channel, a counter corresponding to that particular channel is incremented by one. This process generates a histogram which is nothing but the differential pulse-height spectrum, as discussed in Section 1.3.3.1.

1.3.3.2.1 Energy resolution of an inorganic scintillator based gamma spectrometer

The energy resolution R is defined as, [1]

$$R = \frac{FWHM}{H_0} \times 100\% \quad (1.10)$$

Table 1.1: Properties of common inorganic scintillators used for gamma spectrometry [1], [11].

Inorganic scintillator	Density (g/cm ³)	Wavelength of maximum emission (nm)	Refractive index	Decay time (μs)	Absolute Light yield (photons/MeV)	Pulse-height relative to NaI(Tl) using bialkali PMT	Hygroscopic
Alkali halides							
NaI(Tl)	3.67	415	1.85	0.23	38,000	1.00	Yes
CsI(Tl)	4.51	540	1.79	0.70 (57%), 3.50 (43%)	65,000	0.49	Slightly
CsI(Na)	4.51	420	1.84	0.46, 4.18	39,000	1.10	Yes
Other slow inorganic scintillators							
BGO	7.13	480	2.15	0.30	8,200	0.13	No
CdWO ₄	7.90	470	2.3	1.1 (40%), 14.5 (60%)	15,000	0.4	No
CaWO ₄	6.1	420	1.94	8	15,000		No
CaF ₂ (Eu)	3.17	435	1.47	0.9	24,000	0.5	No
SrI ₂ (Eu)	4.6	435	2.05	1.2	85,000	1.3	Yes
Undoped fast inorganic scintillators with low light yield							
BaF ₂ (fast component)	4.89	220	1.54	0.0006	1,400	0.03	Slightly
BaF ₂ (slow component)	4.89	310	1.56	0.63	9,500	0.2	Slightly
CsI (fast component)	4.51	305	1.80	0.002 (35%), 0.02 (65%)	2,000	0.05	Slightly
CsI (slow component)	4.51	450	1.80	Multiple, up to several μs	Varies	Varies	Slightly
CeF ₃	6.16	310, 340	1.68	0.005, 0.027	4,400	0.04 to 0.05	No
CeBr ₃	5.2	380	2.09	0.017	68,000	1.22	Yes

Table 1.1 (Continued)

Ce-activated fast inorganic scintillators							
YSO:Ce	4.54	420	1.8	0.07	24,000	1.2	No
GSO:Ce	6.71	440	1.85	0.056 (90%), 0.4 (10%)	9,000	0.2	No
LSO:Ce	7.4	420	1.82	0.047	25,000	0.75	No
LYSO:Ce	7.4	428	1.82	~0.04	28,000	0.25	No
GPS:Ce	5.5	372, 394		0.04	19,000		No
LPS:Ce	6.2	385		0.038	26,000		No
YAP:Ce	5.37	370	1.95	0.027 (90%), 10 (10%)	18,000	0.45	No
LuAP:Ce	8.4	365	1.94	0.017	17,000	0.3	No
YAG:Ce	4.56	550	1.82	0.088 (72%), 0.302 (28%)	17,000	0.5	No
LuAG:Ce	6.7	520	1.84	0.06	25,000	0.2	No
GGAG:Ce	6.67	550	1.9	0.055	46,000	~0.4	No
GGAG:Ce,B	6.67	550	1.9	0.055	54,000	~0.4	No
LaCl ₃ (Ce)	3.85	350	~1.9	0.028	49,000	0.7-0.9	Yes
LaBr ₃ (Ce)	5.08	380	~1.9	0.016	63,000	1.65	Yes
LaBr ₃ (Ce,Sr)	5.08	385	~2.0	0.025	73,000	1.9	Yes

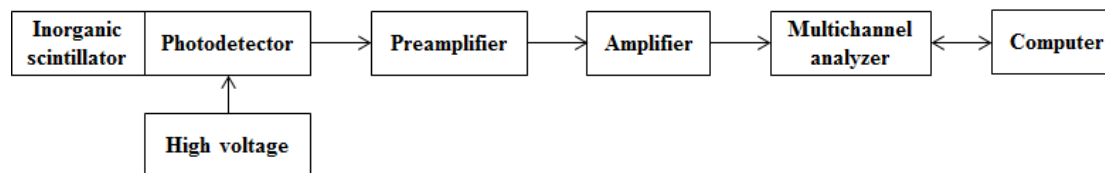


Figure 1.11: Simplified block diagram of an inorganic scintillator based gamma spectrometer.

where, $FWHM$ = full width at half maximum of the full-energy peak, and H_0 = mean pulse-height corresponding to the same peak. Unlike the theoretically predicted spectra presented in Figures 1.4 to 1.9, the measured pulse-height spectra show broadened peaks due to the finite energy resolution.

Among all detectors generally employed in gamma spectrometry, inorganic scintillators offer the poorest energy resolution. The finite energy resolution in them originates from the following factors [1], [11], [14]: (i) Inherent statistical fluctuations in the number of information carriers, (ii) nonproportionality of light yield of the scintillator with deposited gamma energy, (iii) nonuniformity of light yield over the volume of the scintillator, (iv) nonuniform light collection at the coupled photodetector from scintillation events occurring at different parts of the scintillator volume, (v) imperfect optical coupling of the scintillator and the photodetector, (vi) nonuniformity of response of the photodetector over its active area, (vii) fluctuations of gain of the photodetector from event to event, (viii) electronic noise, and (ix) drifts in operating parameters over the course of measurement, e.g., variations in HV supply to the photodetector, temperature fluctuations, large changes in the event rate, etc. Factors (ii) to (iv) are due to the scintillator crystal itself and are together called the intrinsic crystal resolution [1], [14].

The first of these factors is the most dominant for well standardized detector systems, for which the other factors are already minimized. This factor is determined by the fluctuations in the number of the information carriers at the point where it is minimum, i.e., in the number of photoelectrons (n_{ph}). In an ideal scenario where all the other factors could be neglected, then, assuming Poisson statistics, the energy resolution due to only the statistical fluctuations in the number of photoelectrons would become,

$$R/Poisson\ statistical = \frac{FWHM}{H_0} \times 100\% = \frac{2.35C\sqrt{n_{ph}}}{Cn_{ph}} \times 100\% = \frac{2.35}{\sqrt{n_{ph}}} \times 100\% \quad (1.11)$$

where C is a proportionality constant. Also, in this case, the dependence of R on energy (E) of the gamma photons can be simply predicted by noting that $FWHM \propto \sqrt{E}$ and $H_0 \propto E$:

$$R/Poisson\ statistical = \frac{FWHM}{H_0} \times 100\% = \frac{K'\sqrt{E}}{K''E} \times 100\% = \frac{K}{\sqrt{E}} \times 100\% \quad (1.12)$$

where K' and K'' are proportionality constants and $K = K'/K''$. Energy resolution values are conventionally quoted at the energy of gamma rays from ^{137}Cs (662 keV), and can be calculated at other energies by Equation (1.12) if the above assumptions hold [1]. In most practical cases, however, these assumptions do not hold because the other factors also contribute to energy resolution.

Even a monoenergetic beam of gamma photons, in principle, can create secondary electrons with a broad distribution of energies within a scintillator. This electronic energy distribution also depends on the size of the scintillator and the energy of the beam. Since the light yield is nonproportional to electron energy [17], [147], the total light output will vary from event to event, even for this monoenergetic beam. This nonproportional response may become a significant contributor to energy resolution, and therefore, scintillators with larger nonproportionality would always yield poorer energy resolution.

Nonuniformity of light yield over the volume of the scintillator due to inhomogeneities in the properties of the scintillator crystal, e.g., nonuniform doping, etc. can worsen the energy resolution. For well standardized crystals, this factor is usually negligible, whereas for newly developed scintillator materials, this can be significant.

Nonuniform light collection from different portions of the scintillator can be significant if the reflection conditions at its surfaces are not uniform throughout and if there is significant absorption of the scintillation photons within the bulk of the crystal. This factor is especially important for large scintillators with complicated shapes.

The optical coupling between the scintillator and the photodetector must be of good quality so that minimum optical photons are lost at the scintillator-photodetector interface. An optical coupling agent is usually applied to this interface for refractive index matching. Care should be taken in order to avoid air bubbles that can severely impact the light collection at the photodetector due to refractive index mismatch.

Nonuniform deposition thickness of the photocathode as well as nonuniform photoelectron collection from different parts of it on the first dynode also contributes to resolution loss.

Statistical fluctuation of gain of the photodetector can be a significant source of resolution deterioration. Statistical fluctuations of electron multiplication in PMTs as well as gain fluctuations in APDs are included in this category.

Electronic noise for PMT based designs usually may be neglected, but for silicon based photodetectors, especially for photodiodes with low SNR, it becomes significant, and requires the use of special low noise electronics. Instabilities in bias supply and variations in temperature can also add to the electronic noise for the silicon based photodetectors.

Drifts in operating parameters during the course of measurement can lead to significant broadening of peaks for spectra recorded over long acquisition times. Temperature related light yield variations of the scintillator as well as gain fluctuations of the photodetector and the other electronic components, drifts in bias voltages, etc. can contribute to this. Gain stabilization methods usually need to be implemented when spectra must be acquired over long times [1], [11].

1.3.3.3 HPGe detectors as gamma spectrometers

HPGe detectors must be operated at LN₂ temperature and are, therefore, always accompanied by an insulated dewar containing an LN₂ filled reservoir. The detector is kept in thermal contact with the LN₂. It is housed in an evacuated cryostat in order to thermally insulate it

from the surroundings [1]. Figure 1.12 shows a simplified block diagram of an HPGe based gamma spectrometer. HPGe detectors provide the best energy resolution for gamma spectrometry among any detectors.

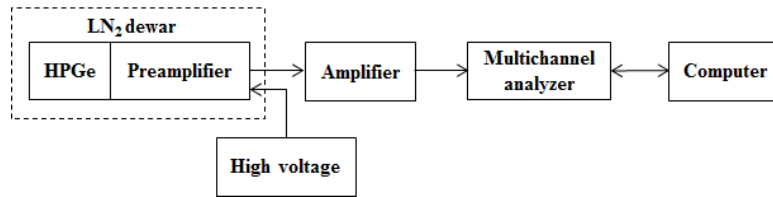


Figure 1.12: Simplified block diagram of an HPGe based gamma spectrometer.

It is important to mention that although HPGe offers far superior energy resolution than scintillators, it is less efficient because of its lower Z_{eff} [1], [148], [149]. Therefore, small scintillators can yield spectra that are similar in statistic to those acquired with much larger volumes of HPGe, provided the acquisition time is same for both.

1.3.3.4 CZT detectors as gamma spectrometers

This compound semiconductor material offers the most suitable semiconductor based alternative to HPGe for gamma spectrometry [150], [151]. Furthermore, owing to its high band gap, it can be operated as a room temperature detector, unlike HPGe. The same cause restricts its energy resolution to much inferior values than those achievable with HPGe. However, energy resolution offered by CZT is superior to those offered by NaI(Tl) and LaBr₃(Ce). CZT crystals are presently available in volumes of up to a few cubic centimeters. Consequently, their detection efficiencies are lower than large volume HPGe detectors. Photoelectric absorption cross-section, however, is higher for CZT than that of HPGe, owing to the higher Z_{eff} of the former [1].

1.4 Scope and aim of the thesis

Gamma spectrometry with single crystal inorganic scintillators optically coupled with photodetectors has many important applications in various fields of science [152]–[158]. Research in this field is growing continuously in order to (i) identify new inorganic

scintillator materials, (ii) improve performance of existing conventional scintillators by material engineering, (iii) grow single crystal inorganic scintillators with sizes appropriate for gamma spectrometry, (iv) characterize the grown single crystals, (v) optimize their properties for various required gamma spectrometry applications by systematic theoretical and experimental investigation, (vi) develop gamma spectrometry systems suitable for various applications by optically coupling the scintillators with appropriate photodetectors and by developing and optimizing the appropriate electronics and the suitable instrumentation [158].

Thallium doped cesium iodide, CsI(Tl), is a widely used single crystal scintillator while cerium doped gadolinium gallium aluminum garnet, GGAG:Ce, (as well as GGAG:Ce co-doped with boron, i.e., GGAG:Ce,B) is a recently developed scintillator which has shown promising properties and a wide scope to improve the performance of various detection devices using this crystal. Therefore, indigenously developed CsI(Tl) [159]–[161] and GGAG:Ce (also GGAG:Ce,B) [157] have been selected for the present research work. Both these scintillators have high light yield as well as high gamma ray absorption cross-section and high photofraction owing to their high values of densities and Z_{eff} . Their emission spectra, peaking around 550 nm, match well with the spectral response of silicon based photodetectors. This enables the design of compact photodiode- or SiPM-based spectrometers operating at lower voltages than the typically used bulkier and more fragile PMT-based systems that operate at much higher voltages. The Tl-doped alkali halide scintillator CsI(Tl) offers economic synthesis in large sizes and is only slightly hygroscopic. Therefore, it is easy to obtain as well as easy to handle. GGAG:Ce is a Ce-activated fast rare earth oxide scintillator with garnet structure. It is non-hygroscopic and has very good physical and chemical properties. As a result, it can be used in extreme environmental conditions.

Theoretical simulations are necessary to design and set up a radiation detector having the best performance. For a realistic modeling of the complete detector setup, the

transportation of scintillation photons up to the optical sensor also needs to be simulated along with radiation transport. Therefore, Monte Carlo simulation has been used to theoretically model the physics processes involved in the detection of gamma photons by both the selected scintillators. Radiation transport calculations have been performed for determination of energy deposition in the scintillators by gamma photons. Optical (scintillation) photons have been generated and transported inside the scintillator in order to understand the effect of scintillation, optical, physical and surface properties on the resulting gamma ray pulse-height spectra. The Monte Carlo simulation toolkit GEANT4 [162]–[165] has been used for creating the complete detector model that includes both radiation transport and optical photon generation and transport. The simulation model has been experimentally validated for both the scintillators. Simulation based parametric investigation has been carried out in order to identify the important factors that influence the performance of the detector setups under design [166]–[168].

Various experimental characterization studies have been performed with the two selected scintillators. They have been tested in conjuncture with conventional PMTs as well as silicon photodiodes. A complete environmental gamma spectrometry system (EGSS) has been designed and developed using a CsI(Tl) scintillator optically coupled with a bialkali PMT. This developed system is a standalone, solar-powered unit with online real-time spectral data communication, suitably designed for continuous operation in open environmental conditions. The system has been field-tested and detection and identification of a dispersing ^{41}Ar containing plume have been successfully carried out [16]. Another gamma spectrometer system has been designed and developed using a GGAG:Ce,B scintillator optically coupled with a silicon photodiode [93]. This compact, low voltage spectrometer can be conveniently connected through a universal serial bus (USB) to a computer for its operation.

In the current work, the simulation studies and the development of gamma spectrometry systems have been successfully carried out for two scintillators. The work can be extended to various conventional and advanced single crystal scintillators in order to design and develop gamma spectrometry systems for various applications.

THEORY AND EXPERIMENTAL METHODS

2.1 Growth of single crystals

2.1.1 Fundamental aspects

Crystalline solids are those solid materials whose fundamental constituent units (atoms, molecules or ions) are arranged in a periodic manner. Single crystals are solid material samples which have an unbroken periodicity extending throughout their entirety and do not involve any grain boundaries. Polycrystalline materials are those that are composed of many single crystals with different sizes and orientations, separated by grain boundaries.

A single crystal of a material can be grown by slowly and gradually solidifying it from its melt, precipitating it from a solution, depositing it from a vapor, re-crystallizing it from its solid phase, etc. under a controlled environment. In the process of crystallization, the constituent units of the material lose their randomness and ultimately achieve long range order typical of crystalline solids [160], [169]. From the point of view of thermodynamics, crystallization is always associated with a lowering of the Gibbs free energy.

Some degree of supercooling (for growth from melt) or supersaturation (for growth from solution) is required as a driving force to initiate the crystallization process. Crystallization is a first order phase transition involving two steps: (i) nucleation and (ii) growth. Nucleation is a slow process in which one or more small nuclei of the newly forming crystal appear when a small number of constituent units (atoms, molecules or ions) place themselves with a particular periodicity and correct orientation. Nucleation can be heterogeneous or homogeneous depending on whether or not it is influenced by foreign solid particles. Heterogeneous nucleation is comparatively faster, results in higher success rates, and facilitated by residual solid particulate impurities, cuts or scratches in the glassware,

introduction of a seed crystal, etc., all of which typically provide nucleation sites. After successful nucleation, more and more free constituent units get added to the nuclei, thereby gradually increasing their sizes. This outward propagation of the crystalline structure is called growth and is a much faster process than nucleation. It is important to note that the various initially appearing nuclei may have different crystallographic orientations, and therefore, to grow a single crystal, one has to allow the subsequent growth process around only one of these nuclei and kill all others. This is done by controlling the growth parameters and the environment.

2.1.2 Various crystal growth techniques

Crystal growth techniques can be classified into three basic categories depending on the type of the phase transition that is involved: (i) solid-solid, (ii) liquid-solid, and (iii) gas-solid. Liquid-solid processes are the most extensively used among the three and can be further subdivided into five categories: (i) growth from melt, (ii) growth from solution, (iii) growth from gel, (iv) growth from flux, and (v) hydrothermal growth. Growth from melt, achievable for only those materials which melt congruently without undergoing any structural changes, contributes to nearly 80% of all crystals grown worldwide [160], [169], [170]. The lion's share of these grown crystals is those of Si and is consumed in the semiconductor industry. Other large-scale crystal fabrication facilities also typically employ this method, the majority of the grown crystals being scintillators, optical and acousto-optic materials, materials used for lasers, and artificial gemstones.

There exist various techniques to grow single crystals from melt: (i) Czochralski technique [171], (ii) Bridgman-Stockbarger technique [172], (iii) Verneuil technique, (iv) Kyropoulos technique, and (v) Float-zone technique. Choice of a crystal growth technique for growth of single crystals of a particular material from its melt depend on various considerations, e.g., requirement of size and quality of the grown crystal, melting temperature,

melting behavior, viscosity of the melt, chemical properties, thermal expansion and thermal conductivity, vapor pressure, etc. The two single crystal scintillators that are studied in this thesis, namely, CsI(Tl) and GGAG:Ce (as well as GGAG:Ce with B co-doping, i.e., GGAG:Ce,B), were both grown from melt. CsI(Tl) was grown by the Bridgman-Stockbarger technique [159]–[161], whereas GGAG:Ce (as well as GGAG:Ce,B) was grown by the Czochralski technique [157]. These two techniques are discussed below.

2.1.3 Czochralski technique

2.1.3.1 Method

The Czochralski (CZ) technique [171] is extensively used for growth of large single crystal ingots of semiconductors, metals, and various oxide materials. Figure 2.1 shows a simplified schematic diagram of the CZ growth process [160], [169].

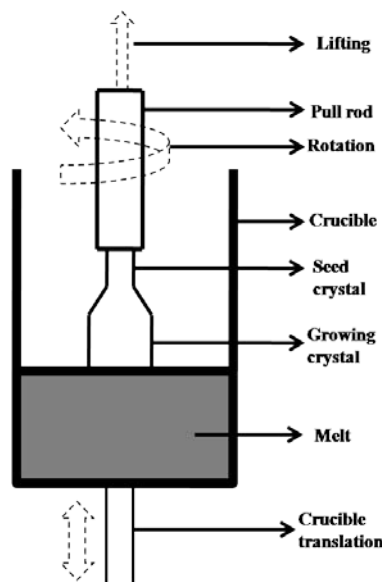


Figure 2.1: Simplified schematic diagram of the Czochralski growth process [160], [169].

The starting material is a stoichiometric mixture of the constituents of the single crystal to be grown, polycrystalline samples of the material, or a pre-synthesized powder of the same. This starting material is loaded into a crucible and melted by inductive, resistive or arc heating. Heat losses from the crucible are minimized by thermally insulating it from the environment. Subsequently, a small seed crystal of the same material whose crystal is being grown,

attached to a rod, is slowly lowered into the centre of the crucible until it comes into contact with the free surface of the melt. A thermal equilibrium is then established between the seed and the melt by controlling the temperature of the latter. Thereafter, the rod is slowly rotated (speed of rotation 5-25 rpm) as well as pulled upwards (pulling rate 0.2-5 mm/h) in a controlled manner. The pulling rate is chosen to be slower than, or at the most equal to, the crystallization rate around the seed, ensuring a dynamic equilibrium between the melt and the crystal being grown. In this way, the crystal slowly grows around the seed and the final shape of the grown single crystal ingot is nearly cylindrical. The diameter of the grown ingot can be controlled and maintained by controlling the temperature of the melt as well as the pulling rate and the speed of rotation of the seed. After growing the single crystal ingot with the desired length, the growth is terminated by rapidly lifting the grown ingot from the melt or by increasing the melt temperature. Then the grown ingot is usually kept near the melt surface and slowly cooled to room temperature at a rate suitable for the particular material.

2.1.3.2 Advantages and limitations

The main advantage of this technique lies in the fact that the various growth parameters can be conveniently controlled. Also, the introduction of the seed crystal facilitates in heterogeneous nucleation and the grown crystal does not come in direct contact with the crucible. Choice of a suitable nonreactive, easily cleanable and easily fabricable crucible with high temperature withstanding capacity is crucial for the CZ growth technique. Materials which have a low vapor pressure and those having a high thermal conductivity can be favorably grown by this technique. Requirement of a seed crystal of the same material that is being grown limits the use of this technique for synthesis of new materials.

2.1.3.3 Crystal growth system

The CZ crystal growth system (CZ crystal puller) consists of a radiofrequency (RF) heating coil with its associated power supply. This provides induction heating which melts the

contents of the crucible and maintains the required high temperature. The temperature gradients can be easily controlled by controlling the power to the heater. A growth station contains the crucible and thermally insulates the same from the surroundings. An outer, double walled, water cooled, closed growth chamber houses the growth station and provides the mechanism for insertion of the pull rod. It also has gas inlets through which gases of choice may be introduced into the chamber, thereby making it possible to grow single crystals in suitable environments, as required. View ports are also available on the growth chamber for observing the crystal growth process. Mechanisms for pulling and rotation as well as devices for measurement of crystal mass are also provided. The entire system is computer controlled. The growth rate (solidified mass per h) is calculated by the crystal weighing device and a feedback signal is generated based on its difference from the previously optimized (reference) growth rate. This feedback signal is used to correct for the growth rate and keep it constant at the reference growth rate by automatically controlling the heater power and/or the pull rate and rotation speed. Provisions may be there for automatic vertical translation of the crucible in order to keep the solid-melt interface at a fixed vertical position as the crystal grows, and thereby, the melt level decreases [160], [169].

2.1.3.4 Growth of GGAG:Ce and GGAG:Ce,B single crystals

The CZ crystal growth system used in the present work for growing the GGAG:Ce and GGAG:Ce,B single crystals was an automatic diameter controlled crystal puller (Model: Oxypuller, Make: Cyberstar, France) with a 50 kW, 8-20 kHz induction supply, a 6 kg weighing head capacity with 1 mg accuracy, and a total crystal translation of 600 mm with 0.01 mm positioning accuracy. A photograph of the system is shown in Figure 2.2 [160], [169]. The starting material was a stoichiometric mixture of Gd_2O_3 , Al_2O_3 and Ga_2O_3 with 0.2 at% Ce doping with respect to Gd (for GGAG:Ce) or 0.2 at% Ce as well as 0.2 at% B doping, both with respect to Gd (for GGAG:Ce,B).

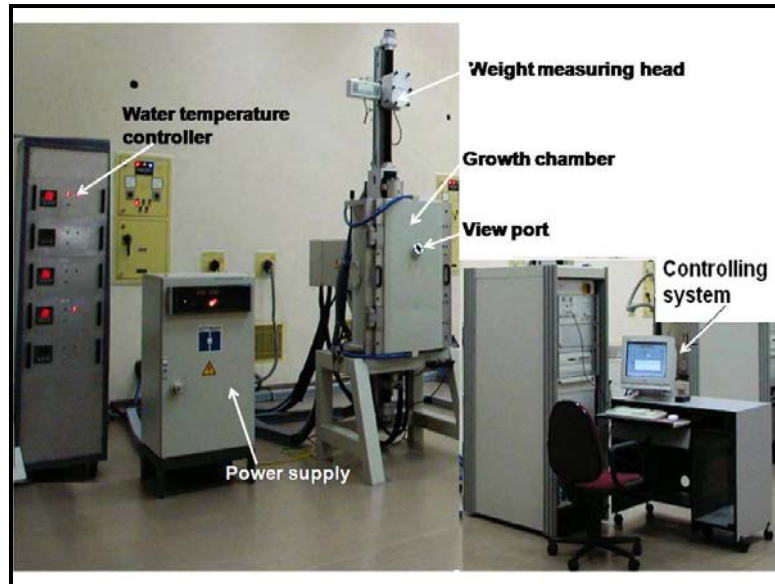


Figure 2.2: Photograph of the CZ crystal puller system (Oxypuller, Cyberstar) [160], [169].

Solid state sintering of this mixture was carried out in a box furnace at 1400 °C. After confirming the formation of a single phase compound by X-ray powder diffraction technique, the sintered material, in the form of pellets, was loaded in a suitable crucible and heated to 50 °C above its melting point for homogenizing the melt. A small previously grown single crystal seed (not oriented in any specific direction) was used in the crystal growth process. A continuous flow of Ar gas was maintained through the growth chamber. The optimized values [157] of the growth parameters, used in the growth process, are listed in Table 2.1.

Table 2.1: Values of optimized growth parameters used for growth of GGAG:Ce and GGAG:Ce,B single crystals [157].

Parameter	Value
Melting temperature	1850 °C
Pulling rate	1 mm/h
Speed of rotation	10-20 rpm
Cooling rate	20-30 °C/h
Temperature gradient	30-50 °C/cm
Initial chamber pressure	10 ⁻⁵ mbar
Ar gas pressure	1100 mbar
Doping concentration for GGAG:Ce	0.2 at% of Ce w.r.t. Gd
Doping concentration for GGAG:Ce,B	0.2 at% of Ce and 0.2 at% of B, both w.r.t. Gd

Single crystal ingots with dimensions of approximately 25 mm ϕ \times 60 mm L could be grown in this method. Figure 2.3 shows a photograph of an as-grown GGAG:Ce,B single crystal ingot under UV illumination [93].

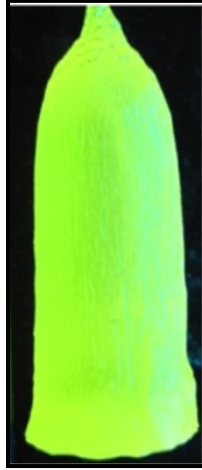


Figure 2.3: As-grown GGAG:Ce,B single crystal ingot (\sim 25 mm ϕ \times 60 mm L) under UV illumination [93].

2.1.4 Bridgman-Stockbarger technique

2.1.4.1 Method

The Bridgman-Stockbarger technique [172] is used to grow small to medium size single crystal ingots of certain semiconductors, synthetic gemstones and other technologically important materials like laser hosts, alkali halide scintillators, etc. The principle of this technique is relatively simple and is illustrated in the schematic diagram of Figure 2.4 [160], [161]. The process undergoes in a specially designed furnace consisting of two independently controlled heating zones having temperatures above (zone I) and below (zone II) the melting point (MP) of the material whose single crystal is being grown, thermally insulated from each other by an adiabatic separator. Polycrystalline material is loaded into a crucible and the material is melted in zone I. Subsequently, the crucible is slowly introduced into zone II. This causes slow progress of single crystal formation along the length of the crucible until finally

the entire melt in the crucible becomes a single crystal. The process can be performed either in vertical or horizontal direction, depending on the design of the furnace.

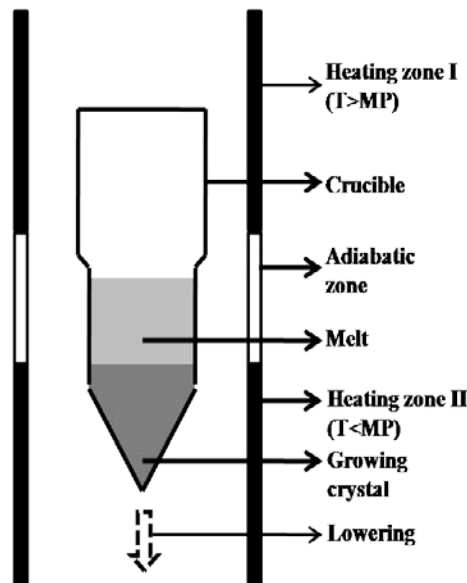


Figure 2.4: Simplified schematic diagram of the Bridgman-Stockbarger growth process [160], [161].

2.1.4.2 Advantages and limitations

The main advantages of the Bridgman-Stockbarger technique are that it is a low cost and technologically simple process. Further, a single crystal of a particular diameter can be grown by choosing a crucible with the same internal diameter. However, the stress that the grown crystal is subjected to when the crucible cools (and therefore contracts itself) can lead to dislocations in the crystals. Further, the contact of the melt with the inner walls of the crucible can lead to unwanted nucleation. Also, the grown crystal is in contact with the inner walls of the crucible. This may lead to sticking of the crystal to the crucible and the process of its recovery may result in significant thermal and/or mechanical stresses to the grown crystal. Therefore, choice of the appropriate crucible material, its proper designing to facilitate the recovery of the grown crystal, and standardization of the growth and the recovery process are of paramount importance.

2.1.4.3 Growth of CsI(Tl) single crystals

The crystal growth system (shown in Figure 2.5 [160], [161]) used to grow the CsI(Tl) single crystals that are the subject of the present study consists of a modified vertical furnace having four separately controlled resistive heating elements, two each for the upper and the lower isothermal heating zones. The two zones are separated by a 50 mm thick adiabatic separator. The maximum temperature gradient provided by the adiabatic material is 20 °C/cm. Four temperature controllers are used to set and control the temperature profile inside the furnace. Four temperature monitors are installed to monitor the temperature profile. There are provisions for lowering the crucible into the furnace. The furnace can also be rotated about a horizontal axis passing through its centre. While rotating the furnace, the crucible can be locked at its position.



Figure 2.5: Photograph of the vertical Bridgman-Stockbarger crystal growth system used to grow CsI(Tl) single crystals [160], [161].

The crucible is specially designed, as shown in Figure 2.4 [160], [161]. The material of the crucible is fused silica with its inner wall coated with carbon. The upper part of the crucible has a slightly higher internal diameter than the lower part. The crystal is grown in the lower part.

High purity CsI is loaded into a crucible and dehydrated by heating the crucible in an evacuated oven. After cooling the dehydrated material, it is mixed with 0.15 mole% of TlI (0.15 at% of Tl with respect to Cs) and again dehydrated. Then the crucible is sealed in Ar environment. The sealed crucible is introduced to zone I of the furnace, kept at (MP + 50 °C). The material is completely melt and thermalized. Then the crucible is slowly lowered into zone II of the furnace, maintained at (MP - 50 °C). The lowering rate is 0.5-2 mm/h. After the entire melt solidifies into a single crystal, the temperature of zone I is reduced to (MP - 50 °C). Then the crucible is locked at its position and the furnace is rotated upside down. Thereafter, the temperature of the zone containing the crystal is elevated from (MP - 50 °C) to slightly above MP. In this way, the grown crystal detaches from the inner wall of the crucible and slides down to the larger part of the crucible. The temperature of this zone is then quickly lowered to (MP - 50 °C) and the grown crystal is annealed at this temperature. Thereafter, the furnace is cooled down to room temperature at a cooling rate of 30 °C/h. The crucible is finally cut open to retrieve the grown single crystal [160], [161]. Single crystal ingots with dimensions of approximately 55 mm ϕ \times 60 mm L were grown. Figure 2.6 shows a photograph of an as-grown CsI(Tl) single crystal [16].

2.2 Measurement of emission spectra of CsI(Tl) and GGAG:Ce,B by radioluminescence

Radioluminescence is the emission of light from certain materials, called luminescence materials, upon irradiation with ionizing radiation. The intensity distribution of the emitted light as a function of its wavelength is called the radioluminescence emission spectrum. In the present study, 10 \times 10 \times 10 mm³ samples were saw-cut from both CsI(Tl) and GGAG:Ce,B single crystal ingots. One surface of each sample was polished with appropriate sand papers to clear optical finish. All other surfaces were ground. The emission spectra of the samples were measured by using the setup shown in Figure 2.7.

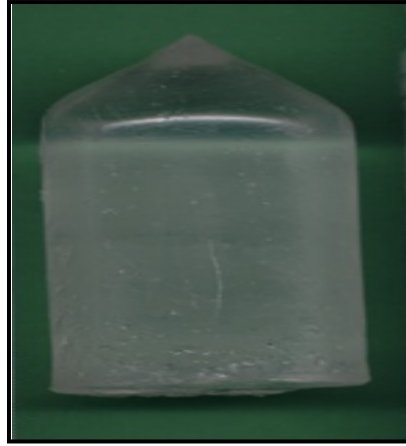


Figure 2.6: As-grown CsI(Tl) single crystal ingot ($\sim 55 \text{ mm } \phi \times 60 \text{ mm L}$) [16].

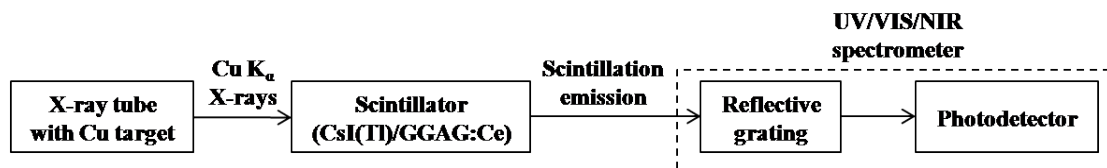


Figure 2.7: Setup for measurement of emission spectra.

An X-ray tube with Cu target was used as the source. The HV and current of the X-ray tube were set at 40 kV and 30 mA, respectively. Cu K_{α} lines (8.04 keV) irradiated the samples. Light emitted from the polished surface of the samples was measured by a high resolution UV/VIS/NIR spectrometer (Make: Avantes) having a reflective grating and a linear CCD (charge coupled device) pixelated array based photodetector. Figures 2.8 and 2.9 show the measured emission spectra of CsI(Tl) and GGAG:Ce,B, respectively [93], [166].

It can be seen from Figures 2.8 and 2.9 that the emission spectra of CsI(Tl) and GGAG:Ce,B peak in the green region, at nearly 540 nm and 530 nm, respectively. This ensures that the emission spectra are characteristic of the intentionally added activators for both the scintillators, and not of some unwanted impurities. Also, these two emission spectra match well with the spectral response of silicon based photodetectors. This encourages the development of solid state photodetector based gamma spectrometry systems with these two scintillators.

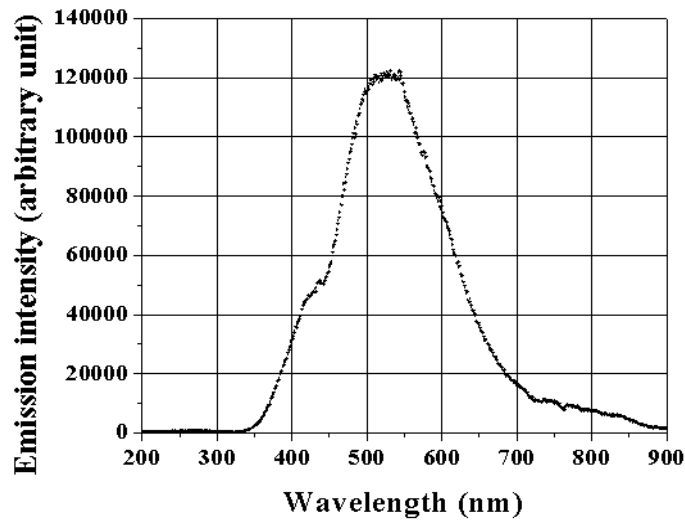


Figure 2.8: Emission spectrum of CsI(Tl) [166].

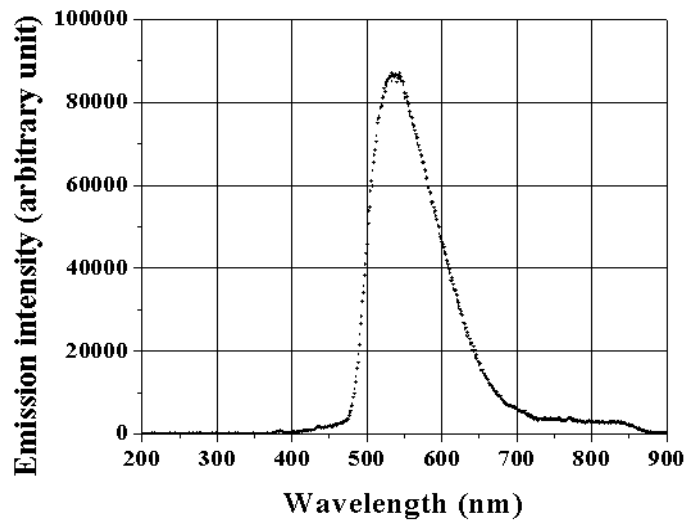


Figure 2.9: Emission spectrum of GGAG:Ce,B [93].

The effect of variation of HV of the X-ray tube on the emission spectra of GGAG:Ce,B was studied by varying the HV in the range 10-40 kV, keeping the tube current fixed at 30mA. Figure 2.10 (a) shows the emission spectra of GGAG:Ce,B recorded for various HV settings, whereas Figure 2.10 (b) shows the dependence of the integrated areas under the emission spectra as a function of the HV, with a straight line also fitted to the dependence. This linear dependence indicates that the total intensity of scintillation emission increases linearly with the intensity of the incident X-ray beam.

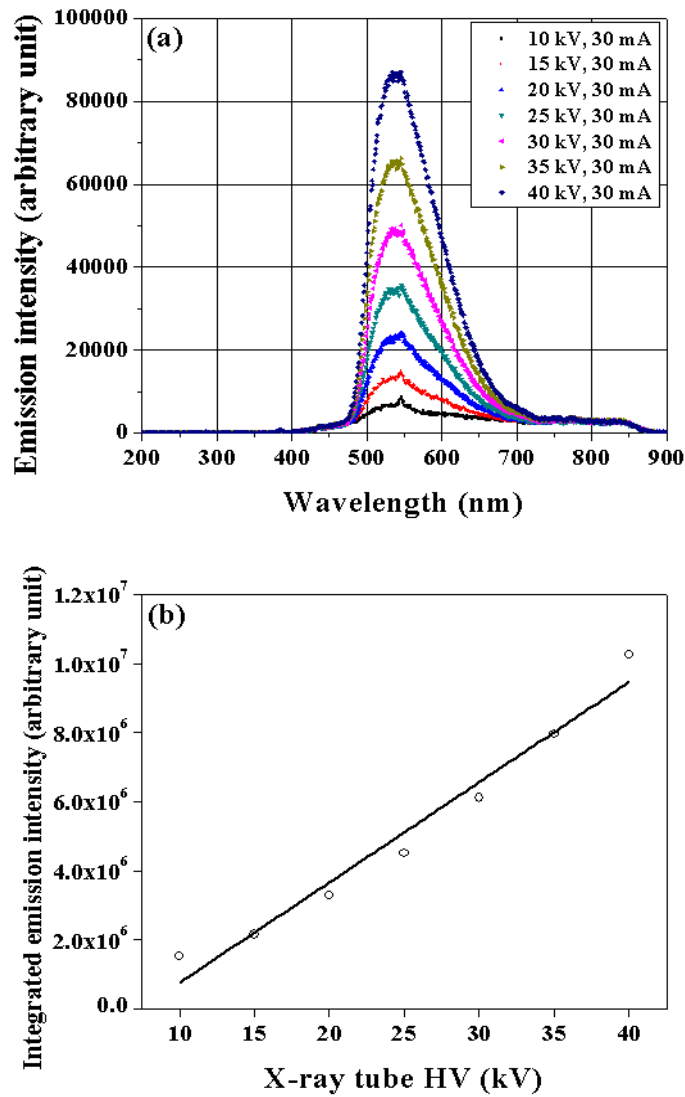


Figure 2.10: (a) Emission spectra of GGAG:Ce,B for various HV settings of the X-ray tube (tube current fixed at 30 mA), (b) Dependence of the integrated areas under the emission spectra of (a) on the X-ray tube HV.

The effect of variation of current of the X-ray tube on the emission spectra of GGAG:Ce,B was also studied by varying the current in the range 2-30 mA, while keeping the HV fixed at 40 kV. The results are shown in Figures 2.11 (a) and (b).

2.3 Monte Carlo simulation for radiation detection

2.3.1 Introduction

Monte Carlo is a numerical technique that uses random numbers to solve problems [173]. Its

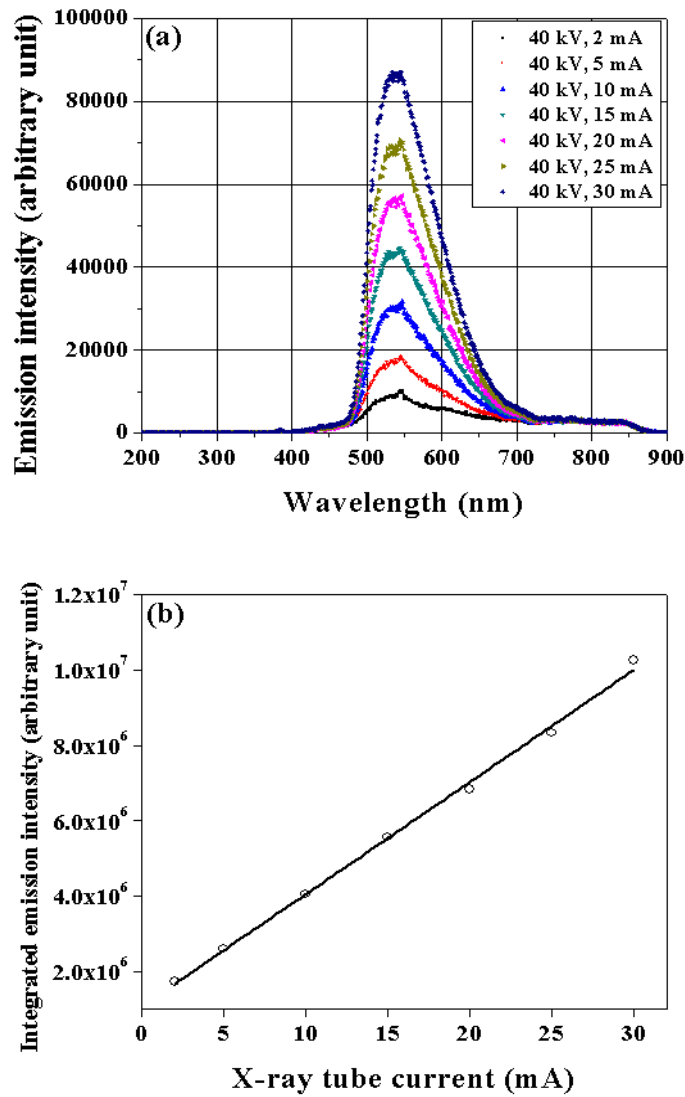


Figure 2.11: (a) Emission spectra of GGAG:Ce,B for various values of the X-ray tube current (HV fixed at 40 kV), (b) Dependence of the integrated areas under the emission spectra of (a) on the X-ray tube current.

versatility lies in its diverse fields of applicability, e.g., physical and mathematical sciences, various disciplines of engineering, environmental sciences, chemistry, biology, computer science and engineering, economics, law, and many more. In physical sciences, there application extends to statistical and computational physics, quantum physics, nuclear and particle physics, radiation transport and dosimetry calculations, astrophysics, atmospheric science, and beyond. In nuclear and particle physics, Monte Carlo methods are used for

design of detector models, their experimental validation and design optimization. This also involves ionizing radiation transport calculations. In radiation transport theory, analytically solving the transport equation gives an overall picture of the spatial and temporal behavior of the particle fluence, and subsequently, all other quantities of interest can be derived from it. However, solving the transport equation analytically is possible only in a very few simple cases. In all other cases that are of practical importance, approximate numerical solutions are targeted. These are called deterministic methods, wherein the phase space of the problem is usually discretized and certain simplifying approximations are made. Various computer codes have been developed and validated against experiments, and are extensively used by a large community of scientists for solving various radiation transport problems.

Deterministic methods of solution often become computationally very challenging and expensive, especially for cases involving complex geometries. In these situations, Monte Carlo methods seem to be the only way out. In Monte Carlo methods, phase space discretization and simplifying approximations are not employed. Instead, each primary particle is tracked until it escapes from the volume of interest or gets absorbed within it, thereby generating various secondary particles. Subsequently, these secondaries are individually tracked in a similar way as the primary. Quantities of interest are scored for each particle history. Average of scores for a large number of such particle-tracking histories give the statistical estimate of that particular quantity. In this way, three dimensional problems are solved with little more effort than one dimensional problems, and therefore, Monte Carlo methods are well suited for complex geometries.

There are various general purpose Monte Carlo radiation transport packages, e.g., MCNP [174], EGS [175], FLUKA [176], [177], PENELOPE [178], GEANT4 [162]–[165], etc., that are used by many researchers for detector simulations, shielding calculations, reactor physics simulations, dosimetry applications, etc. A wide assortment of particles from

the standard model is usually available in these packages for simulation. However, most of the packages are developed for high energy particle physics applications, and may lack the capability to simulate low energy processes including optical photon simulations. Monte Carlo ray-tracing software packages, on the other hand, are good for optical photon transport, but lack the capability of production of optical photons by radiation transport leading to scintillation [179]. GEANT4 is capable of accurate radiation transport and optical photon transport simulations, and is, therefore, ideal for simulation of scintillators.

For scintillator based spectrometry of gamma radiation with energies up to a few MeV, which is the subject of this thesis, the only secondary ionizing particles that can be generated upon interaction of the primary gamma photons with scintillators are gamma- or X-ray photons and electrons of both charges (e^- and e^+). These, together with the optical photons that are generated in the scintillation process, are therefore, the only types of particles needed to be handled in simulation.

2.3.2 GEANT4 simulation of scintillators

GEANT4 [162]–[165] is an open source, general purpose, object oriented Monte Carlo simulation toolkit, written in the C++ programming language, for simulating the transport of particles through matter. It utilizes classes and objects. The user can assemble a simulation program for a specific application by using classes available from the toolkit and modifying or extending them, as needed. The toolkit enables the user to build the required geometrical model with various components having different shapes and materials, initiate the required primary particles, choose appropriate physics processes from a comprehensive set provided, score different quantities of interest, and visualize the geometry and particle tracks. The simulation of scintillators in GEANT4 involves gamma and electron transport followed by optical photon transport.

2.3.2.1 Gamma and electron transport

Primary gamma photons are generated by sampling from user-provided distributions in terms of energy, point of production and initial direction. They are transported in discrete steps between interactions. Energy dependent probabilities of various types of interaction at each step are sampled according to the interaction cross-section values. After each interaction, the energy loss, the final state of the particle, and the path length before the next interaction are also sampled. The photon processes that are relevant for modeling of a scintillator for gamma spectrometry include photoelectric effect, Compton scattering, pair production and Rayleigh scattering, whereas the electron and positron processes include Coulomb scattering, ionization and delta (δ) ray production, Bremsstrahlung and positron annihilation.

2.3.2.2 Optical photon transport

2.3.2.2.1 Introduction

In GEANT4, optical photons are defined as those photons whose wavelengths are much greater compared to the typical atomic spacing [164]. They are treated as a special class of particles which are distinctly different from X-ray or γ -ray photons, without a smooth transition as a function of energy between the two classes of particles. Physics processes that are typical of wavelike behavior of electromagnetic radiation are incorporated for optical photons, whereas for higher energy X-ray or γ -ray photons, the set of physics processes are entirely different (as described in Section 2.3.2.1). Physics processes for optical photons include bulk absorption, Rayleigh scattering, Mie scattering, and reflection, refraction and absorption at medium boundaries [164], [165].

When optical photons and their physics processes are enabled in GEANT4, optical photons are produced when charged particles travel through (i) a scintillator (scintillation process), (ii) a dielectric medium with velocities above the phase velocity of light in that medium (Cherenkov effect) or (iii) inhomogeneous media, e.g., boundary between two

different media (transition radiation) [165]. Therefore, GEANT4 provides the unique capability to initiate a simulation with an ionizing radiation particle and completing it with the detection of the resulting optical photons at a photodetector, entirely within the same event loop. This makes it a perfect toolkit for modeling the behavior of scintillation and Cherenkov detectors as well as any associated light guides. Optical photons generated as secondaries have linear polarization by default in GEANT4. For simulations involving optical photons as primaries, however, the user has to set linear polarization in order for the simulation to work correctly. It is also to be noted that optical photons are produced in GEANT4 without energy conversion. Therefore, their energy must not be tallied as part of the energy balance in an event.

The optical properties of the media that are required to implement the physics processes of optical photons must be stored by the user as entries in a material properties table, and linked to the material in question. These properties can be constants or stored as functions of the wavelength (or equivalently, energy) of the optical photons as key-value pairs. In the latter case, values at intermediate points between two successive keys are determined by suitable interpolation [164].

2.3.2.2.2 Generation of optical photons in scintillators

The following material properties need to be supplied as input parameters by the user in order to define each scintillating material and generate optical photons in them [164], [179], [180]:

(i) Scintillation yield: It is the characteristic light yield (photons/MeV) of the scintillator (LY). The mean number of optical photons (N) generated in a step in which a total energy E_{dep} is deposited is given by $N = (LY \times E_{dep})$.

(ii) Resolution scale: It is the intrinsic resolution of the scintillator which usually broadens the statistical distribution of the number of generated scintillation photons. This broadening is due to the impurities in doped scintillators. On the other hand, when the Fano factor plays a

role, there can be narrowing of this statistical distribution. The actual number of optical photons produced in a step fluctuates about its mean number N with a Gaussian distribution having a standard deviation given by $\sigma = (\textit{Resolution scale} \times N^{1/2})$. Therefore, $\sigma = N^{1/2}$ for *Resolution scale* = 1. The fluctuation is broadened for *Resolution scale* > 1, whereas for *Resolution scale* = 0, there is no fluctuation. For steps resulting in $N \leq 10$, however, the distribution is considered to be Poisson having a mean N .

(iii) Fast and slow time constants: These are the fast and the slow exponential decay time constants of the scintillator.

(iv) Yield ratio: It is the relative strength of the fast component as a fraction of the total scintillation yield. If it is defined to be 1, then there is no slow component. On the other hand, if it is 0.5, then the relative contributions of the each component is 50%.

(v) Emission spectrum: Both the fast and the slow decay components have their intrinsic emission spectrum. The overall emission spectrum of the scintillator as a function of the optical photon wavelength needs to be normalized, converted into a function of optical photon energy, separated into fast and slow components, and incorporated into the code. Energy of each generated optical photon is sampled from this spectrum.

(vi) Birks' constant: It is the adjustable parameter in the Birks' formula [1], [10] that expresses the nonproportionality of the scintillation yield due to quenching.

Optical photons are generated evenly along the track segment involved in the step and emitted uniformly over 4π solid angle with random linear polarization perpendicular to the emission direction and at times determined by the parameters mentioned above in (iii) and (iv).

For those scintillators whose scintillation yield and/or yield ratio depend on the type of exciting particle, different scintillation processes may be separately defined for each exciting particle.

2.3.2.2.3 Tracking of optical photons in scintillators

2.3.2.2.3.1 Bulk processes

The following material properties, supplied by the user as functions of the optical photon wavelength, control the optical photon transport within the bulk of materials [164], [179], [180]:

(i) Absorption length: It is the mean distance traveled by the optical photons before being bulk absorbed. The particles are simply killed after they get absorbed. For scintillator dimensions (of the order of centimeters) that are typical of gamma spectrometry applications, the transparency of the scintillators for their own scintillation emission ensures that most of the optical photons escape bulk absorption.

(ii) Rayleigh scattering length: It is the mean distance traveled by the optical photons before being Rayleigh scattered. Rayleigh scattering is an elastic scattering process in which the optical photons only get deflected, but do not lose energy. Mean free path corresponding to this process for optical photons of typical wavelengths is of the order of meters in crystalline scintillation media. Therefore, Rayleigh scattering becomes unimportant for scintillators having much smaller dimensions that are typically used for gamma spectrometry. For large volume liquid detection media that are typically employed for neutrino detection, however, Rayleigh scattering becomes important. If the Rayleigh scattering length is not specified by the user, its value is defaulted to that for liquid water at 10 °C.

(iii) Mie scattering length: This is the mean distance before the optical photons undergo Mie scattering. Mie scattering is the analytical solution of Maxwell's equations in the case of scattering of optical photons by spherical scattering centers. It is important only when the radii (r) of the spherical particles are comparable in size with the wavelength (λ) of the photons, which is not the case for transport of optical photons through scintillators, where $\lambda \gg r$.

(iv) Refractive index: Refractive indices of all the materials through which optical photons traverse need to be specified.

2.3.2.2.3.2 Surface processes

When optical photons arrive at an interface between two media, they can get reflected, refracted or absorbed. There are two ways of implementing a surface in GEANT4. The first implementation, called a border surface, is defined as the interface between an ordered pair of volumes that are placed adjacent to each other. In the second implementation, called a skin surface, a volume is assumed to be completely surrounded by a surface. The first implementation allows the definition of different parameters to the different surfaces of the same volume. Also, since these types of surfaces are defined as interfaces between ordered pairs of volumes, the same surface can have different properties for optical photons that are incident from opposite directions. The second implementation, on the other hand, may be useful when a scintillator is wrapped by a reflector and is placed into many different mother volumes. However, all the surfaces of this scintillator must have the same properties in this case [164], [180].

In a dedicated material properties table for each particular surface defined in the program, the following surface parameters need to be specified by the user in order to control the physics processes undergone by optical photons when they reach this surface [164], [165], [179], [180]:

(i) Surface model: There are two models available in GEANT4 for modeling an optical surface, namely, the UNIFIED model [181] and the GLISUR [182] model. The UNIFIED model has been used to perform all the simulations reported in this study. This model is more comprehensive than the GLISUR model and provides more flexibility to the user for defining various surface properties. The parameters mentioned below are available to be specified

when the UNIFIED model is used. If no model is specified, however, the program defaults to the GLISUR model.

(ii) Surface type: It defines the nature of the two media on either sides of the surface. The following surface types (ordered pairs) are available in the UNIFIED model:

(a) Dielectric-dielectric: It is a surface between two dielectric media. An optical photon incident on it can undergo total internal reflection, refraction or absorption depending on the angle of incidence, refractive indices of the two media, reflectivity of the surface, wavelength of the photon and its state of linear polarization.

(b) Dielectric-metal: It is a surface between a dielectric medium and a metallic medium. An optical photon incident on it from the dielectric medium can be either reflected back into the same medium or get absorbed by the metal. If the photon is absorbed by the metal, it can be detected with a probability equal to the quantum efficiency of the metal.

(c) Dielectric-black: A black medium is that for which the user has not set any optical properties. A photon incident from the dielectric medium immediately gets absorbed in the black medium without being detected.

(iii) Surface finish: This parameter defines the microscopic structure of a surface. A perfectly smooth surface is called polished (P), whereas a rough surface is called ground (G). A front painted surface represents the polished or ground surface of a volume that is coated with a paint, e.g., a polished or ground scintillator coated with a reflector. Therefore, there can be two types of front painted surfaces, either polished front painted (PFP) or ground front painted (GFP). A back painted surface represents the polished or ground surface of a volume that is coated with a reflector with a gap in between, e.g., a polished or ground scintillator coated imperfectly with a reflector, leaving an air gap in between. Therefore, there may be two types of back painted surfaces, namely, polished back painted (PBP) and ground back painted (GBP). Overall, there are six available types of surface finish in the UNIFIED model

for a dielectric-dielectric surface, namely, P, G, PFP, GFP, PBP and GBP. For a dielectric-metal surface, however, only the P and G surface finish are available. If no surface finish is specified by the user, the finish P is taken by default. In the GLISUR model, on the other hand, no matter what the surface type is, only P and G surface finish are available.

(iv) Surface roughness (σ_α): This parameter defines the degree of roughness of a surface. A rough surface is modeled to be consisting of micro facets, as shown in Figure 2.12 [179], [180], [183]. The angle (α) between the average surface normal and a micro facet normal is sampled randomly from a normal distribution with mean zero and standard deviation σ_α . Higher the value of σ_α , rougher the surface.

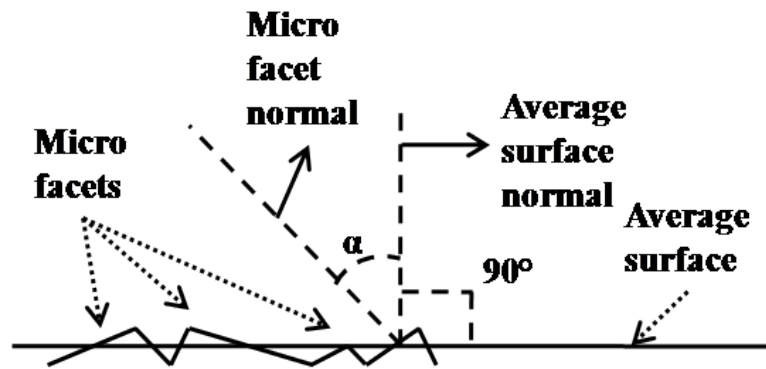


Figure 2.12: Sketch showing the modeling of a ground surface consisting of micro facets [179], [180], [183].

(v) Surface refractive index: This parameter needs to be supplied by the user only for back painted (PBP and GBP) surfaces, e.g., polished or ground scintillators coated imperfectly with a reflector, leaving an air gap in between. The surface refractive index is that of the material in the gap, and must not be confused with the material refractive indices mentioned in Section 2.3.2.2.3.1.

(vi) Reflectivity (R): It is the wavelength dependent probability of reflection of optical photons at a surface. It has to be supplied by the user as a function of photon energy. For $R = 0$, all optical photons are absorbed by the surface, whereas for $R = 1$, all are reflected. If an optical photon is not absorbed, Snell's law is applied according to the refractive indices of

the materials on either side of the surface. This is equivalent to applying Fresnel's equations of reflection and refraction at the surface. As per Maxwell's equations, Fresnel's reflection and refraction are not treated separately. These two processes, along with total internal reflection, are treated as processes having relative probabilities adding up to unity. In case the user does not define it, the default reflectivity for a dielectric-metal surface is set to be unity.

(vii) Reflection type: There are four types of reflection, namely, specular spike (SS), specular lobe (SL), Lambertian (L) and backscatter (BS). Probabilities for each type have to be set by the user, keeping the sum of the probabilities unity. If these probabilities are not set, reflection type is defaulted to L by the program.

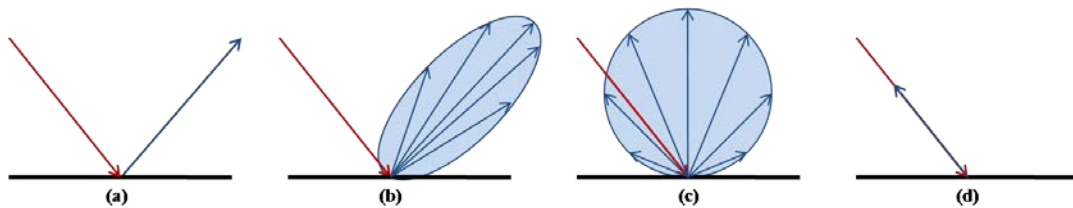


Figure 2.13: (a) Specular spike reflection from a perfectly smooth surface, (b) Specular lobe reflection from a slightly rough surface, (c) Lambertian reflection from a diffuse surface, (d) Backscatter reflection from a very rough surface [183].

Figure 2.13 [183] shows the SS, SL, L and BS types of reflection schematically. It is important to mention that the laws of reflection always hold at the microscopic level for each pair of incident and reflected rays. For a perfectly smooth surface (see Figure 2.13 (a)), it may be assumed that all the micro facets are aligned on a straight line and the average surface normal is parallel to each micro facet normal, i.e., $\sigma_\alpha = 0^\circ$. In this case, the only possible type of reflection is SS against the average surface normal, and the laws of reflection hold on the macroscopic level as well. In the opposite extreme, i.e., for a highly rough surface (called a diffuse surface) with a large σ_α (see Figure 2.13 (c)), an incident parallel beam of light will be reflected in various directions, although still obeying the laws of reflection at the microscopic level. At the macroscopic level, however, the intensity of the reflected beam at a

particular angle (θ) between the observer's line of sight and the average surface normal will be proportional to $\cos \theta$, as per Lambert's cosine law. This is called Lambertian (L) reflection. Practical surfaces exhibit a reflection behavior between these two extremes. Therefore, the individual probabilities of the various reflection types need to be provided. SL is a reflection against a micro facet normal (see Figure 2.13 (b)) and is typical of slightly rough surfaces. In this case, the distribution of the angle of reflection is nonzero but very limited. In the BS type of reflection, an optical photon is reflected back to the incident direction as a result of multiple reflections within the micro facets (see Figure 2.13 (d)).

(viii) Efficiency (η): It is the probability that an optical photon absorbed at a surface is detected and is equivalent to the wavelength dependent QE of the surface, i.e., the probability of conversion of an optical photon to a photoelectron. The user has to specify this parameter as a function of optical photon energy. In case the user does not specify it, it defaults to zero. For $R = 1$, all photons are reflected from a dielectric-metal surface, and, therefore, none can be detected. On the other hand, for $R = 0$, all are absorbed and the detection probability becomes equal to η .

The two following case studies enumerate the different possibilities arising due to various combinations of choices of the above surface parameters [180]:

Case I: Surface type: dielectric-dielectric

(a) Surface finish P: It defines a perfectly smooth surface. Optical photons are reflected/refracted with probability R and absorbed with probability $(1-R)$. Snell's law is applied in case they are not absorbed. Reflection type is SS.

(b) Surface finish G: It defines a rough surface with roughness σ_α . Optical photons are reflected/refracted with probability R and absorbed with probability $(1-R)$. In case photons are not absorbed, α is sampled and Snell's law is applied. Reflection types will be according to the user defined probabilities of SS, SL, L and BS.

(c) Surface finish PFP or GFP: These define volumes perfectly coated with reflectors, where R is the reflectivity of the reflector. Optical photons are reflected with probability R and absorbed with probability $(1-R)$. There is no chance of refraction. So, Snell's law is not applied. Reflection type is SS for PFP and L for GFP.

(d) Surface finish PBP or GBP: These define volumes imperfectly coated with reflectors, leaving a gap in between. R is the reflectivity of the reflector. Refractive index of the material in the gap must be given by the user as a surface parameter. When optical photons reach the interface between the volume and the gap, Snell's law is applied according to the refractive indices of the materials in the volume and the gap. In case of refraction, the photons reach the interface between the gap and the reflector. Here they are reflected with probability R and absorbed with probability $(1-R)$. There is no chance of refraction. So, Snell's law is not applied. Reflection type is SS for PBP and L for GBP. If reflected, the photons can again reach the interface between the gap and the volume, this time from the opposite direction. Here Snell's law is applied. The photons can now be either reflected back to the gap or refracted into the volume.

Case II: Surface type: dielectric-metal

(a) Surface finish P: It defines a perfectly smooth surface. Optical photons are reflected with probability R and absorbed with probability $(1-R)$. Snell's law is not applied because refraction is not possible. In case the optical photons are reflected reflection type is SS. In case they are absorbed, they are detected with a probability η .

(b) Surface finish G: It defines a rough surface with roughness σ_α . Optical photons are reflected with probability R and absorbed with probability $(1-R)$. Snell's law is not applied because refraction is not possible. In case optical photons are reflected, α is sampled. Reflection types will be according to the user defined probabilities of SS, SL, L and BS. In case optical photons are absorbed, they are detected with a probability η .

SIMULATION STUDIES ON CsI(Tl)

3.1 Introduction

The Tl-activated CsI single crystal (CsI(Tl)), despite being one of the earlier discoveries in the field of inorganic scintillators [184], continue to be the chosen scintillator for many applications even today. The properties of CsI(Tl) that are favorable for gamma spectrometry may be picked out from Table 1.1. It has high stopping power for gamma radiation due to its moderately high density (4.51 g/cm^3) and high Z_{eff} (54) [27], [185], [186]. It is also one of the brightest scintillators, having a high light yield of nearly 65,000 photons/MeV [1], [27], [187], [188]. Besides, it has a broad scintillation emission spectrum that peaks at about 540 nm, as measured experimentally and reported in Section 2.2. Although the quantum efficiency of the traditional alkali PMTs is very low (only about 5%) [138], [189], [190] near the peak emission wavelength of CsI(Tl), that of silicon based photodetectors is very high (nearly 90%) in this regime [191]. Therefore, if coupled with the suitable photodetector, CsI(Tl) can potentially outperform many other scintillators in terms of scintillation efficiency. On the other hand, these suitable photodetectors also offer compact, low voltage and magnetically insusceptible solid state spectrometer designs that are preferred in many situations. Last but not the least, CsI(Tl) is only slightly hygroscopic, not very brittle, has good mechanical and chemical properties that are favorable for crystal growth and processing, and its single crystals can be grown in large sizes quite economically, all of which are valuable additions to its list of advantages [1].

Gamma ray pulse-height spectra of scintillators can be generated through Monte Carlo simulation by simulating the transport of gamma photons and their secondary ionizing particles (electrons, positrons, and X/ γ ray photons). However, since the complete physics

process behind the generation of pulse-height spectra also depends on the generation and transport of the scintillation photons in the scintillator, a Monte Carlo model that additionally includes these processes offers more insight and enables the investigation of the parameters which affect the physics processes of optical photons. It is important to note here that these physics processes are entirely different from those of the gamma photons, as discussed in Section 2.3.2.2, and therefore, need separate understanding in order to implement them in simulation [166].

If optical photon generation and transport are not taken into account and the pulse-height spectra are generated by simulating only the energy deposition of the gamma photons and their ionizing secondary particles in the scintillator, the full-energy peaks would have no broadening. They can still be broadened during post processing though, by fitting experimentally obtained resolution versus energy functions to the full-energy peaks [192]–[195]. However, such simulated spectra that are broadened with experimental knowledge, although matching well with experimentally acquired spectra, cannot be used for studying the effect of scintillation, optical, physical and surface properties of the scintillator which affect the pulse-height spectra by affecting the optical processes. Also, *a priori* simulation based optimization of the abovementioned properties is not possible with these spectra. On the other hand, by building a Monte Carlo model that generates the pulse-height spectra by simulating radiation transport as well as optical transport, and subsequently validating the model for an easy to conceive experimental setting, one can utilize these spectra to optimize the abovementioned properties for new and more complicated settings, without resorting to experiments [166].

As described in Section 2.3.2.2, the Monte Carlo simulation toolkit GEANT4 was chosen for building the simulation model because it is capable of treating gamma photons and

optical photons as completely different classes of particles. Separate physics processes for the two classes can also be accurately implemented.

The following sections of this chapter describe the development of a GEANT4-based simulation model for CsI(Tl) and its experimental validation. This model includes radiation transport as well as optical transport and is subsequently utilized to investigate the effect of various simulation parameters on the generated pulse-height spectra.

3.2 Simulation methodology

3.2.1 Detector geometry

A cylindrical CsI(Tl) scintillator crystal with nominal dimensions of $2'' \phi \times 2'' L$ (50.8 mm $\phi \times 50.8$ mm L) was modeled in GEANT4. Figure 3.1 shows a schematic diagram of the xz plane cross-section of the simulation geometry along with the reference coordinate system [166].

The scintillator was coupled to a 50.8 mm $\phi \times 10$ mm L photodetector. The length of the photodetector was taken arbitrarily. This does not affect the simulation results, however, owing to the fact that the optical photons are transported only up to the interface between the scintillator and the photodetector, as mentioned later in Section 3.2.5, and therefore, only the properties of this interface are important for the purpose of detecting the optical photons at this interface [166]. The scintillator-photodetector assembly was coated with a 1 mm thick reflector. The outer enclosure to this assembly was made up of aluminum that had a thickness of 0.5 mm at the front surface and 1 mm elsewhere. The entire assembly shown in Figure 3.1 was assumed to be placed in air. A point source was modeled on the axis of the cylinder at a distance of 300 mm from the front surface of the assembly towards the negative z direction. A divergent beam of gamma photons originating from this point source was modeled to be completely illuminating the front surface. All the dimensions mentioned here were unchanged for all simulations, unless otherwise specified. The energy of the gamma photons

was chosen to be different for different cases. The various sources used for the simulations and their gamma energies and corresponding yields are summarized in Table 3.1. The first source represents equal activities of ^{137}Cs and ^{60}Co , whereas the second and the third are typical of the decays of ^{137}Cs , ^{41}Ar and ^{208}Tl , respectively [166].

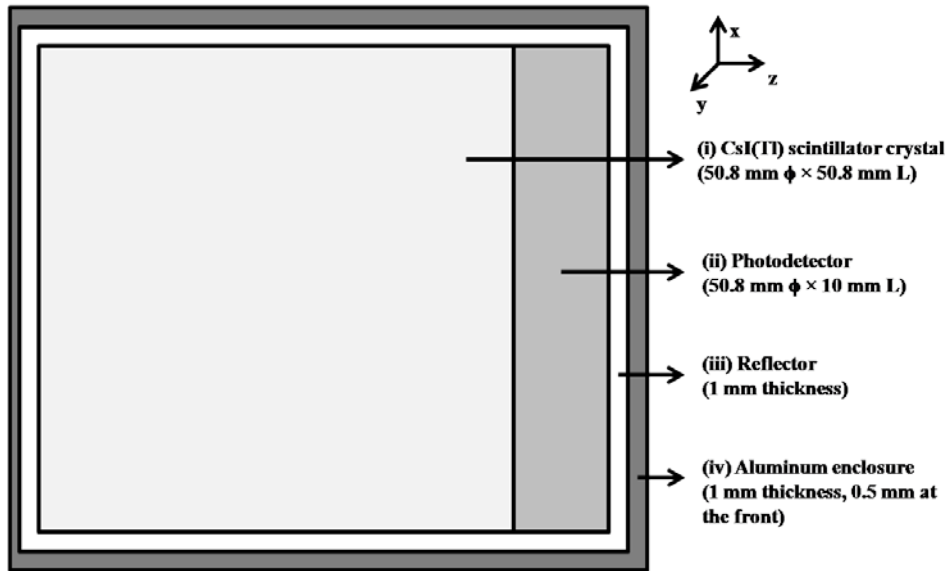


Figure 3.1: Schematic diagram of the xz plane cross-section of the simulation geometry consisting of a 50.8 mm ϕ \times 50.8 mm L cylindrical CsI(Tl) scintillator crystal, along with the reference coordinate system (Figure not to scale) [166].

Table 3.1: Various source configurations used in simulation [166].

Sl. No.	Source name	Source composition
1	$^{137}\text{Cs} + ^{60}\text{Co}$	662 keV (50%), 1173 keV (25%), 1332 keV (25%)
2	^{137}Cs	32 keV (6%), 36 keV (1%), 662 keV (85%)
3	^{41}Ar	1293 keV (100%)
4	^{208}Tl	2614 keV (100%)

3.2.2 Material properties

The CsI(Tl) material, assigned to the scintillator crystal of region (i) in Figure 3.1, had a Tl doping concentration of 0.15 at% (= 0.15 mol%) with respect to Cs, as is typical for the CsI(Tl) crystals indigenously grown by the Bridgman-Stockbarger technique, described in Section 2.1.4.3. Its density was taken to be 4.51 g/cm³, as mentioned in Table 1.1. The material assigned to the photodetector (region (ii) of Figure 3.1) was same as that assigned to

region (i) but its scintillation yield was taken to be zero, as described later in Section 3.2.3. This choice, however, does not affect the simulation results because the optical photons are transported up to the scintillator-photodetector interface, as described later in Section 3.2.5, and as long as the parameters of this interface are correctly incorporated, the modeling remains accurate. The material assigned to the reflector (region (iii) of Figure 3.1) was Teflon with the chemical formula C_2F_4 . Its density was taken to be 2.2 g/cm^3 [196]. It is worth a mention here that only the surface parameters of the reflector are enough for accurate optical transport calculations, but radiation transport calculations become more accurate when the composition and density of the reflector are accurately modeled. This is because the incident gamma photons can, in principle, deposit finite amount of their energies within the reflector. Finally, the overall enclosure (region (iv) of Figure 3.1) was modeled to be made up of the element aluminum [166].

3.2.3 Scintillation and optical properties

The experimentally measured scintillation emission spectrum of CsI(Tl), as shown in Figure 2.8, was first normalized, i.e., the emission intensity corresponding to each channel was divided by the integrated area under the curve. This normalized emission intensity was plotted as a function of wavelength, as shown in Figure 3.2.

Subsequently, the abscissa of the emission spectrum was converted from wavelength (λ) to photon energy (E) by using the formula $E = hc/\lambda$. Figure 3.3 shows the emission spectrum converted to energy scale.

In order to incorporate the energy (or, equivalently, wavelength) dependent parameters into the Monte Carlo simulation program, the energy scale corresponding to the wavelength range 200-900 nm was converted to 32 points. These points were used as the keys for storing the energy dependent parameters' values.

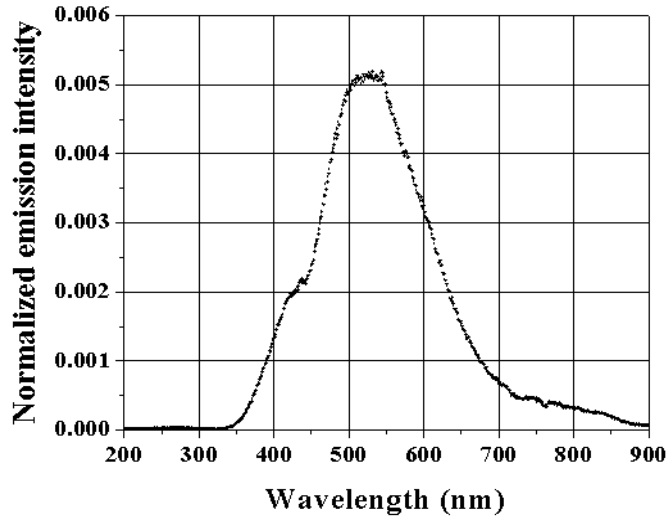


Figure 3.2: Normalized emission spectrum of CsI(Tl).

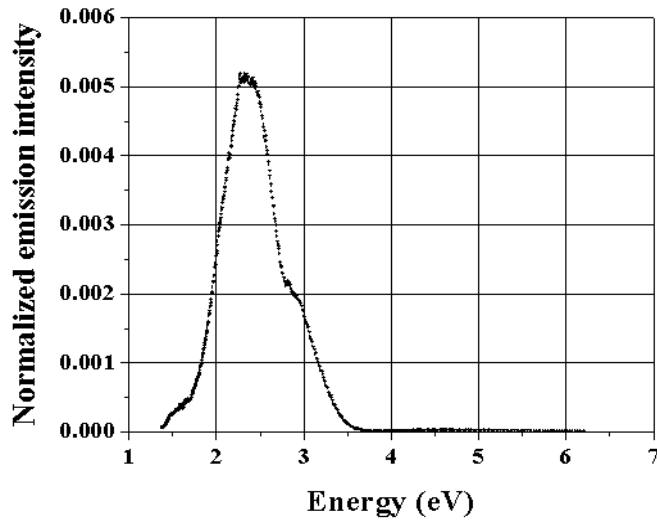


Figure 3.3: Normalized emission spectrum of CsI(Tl) as a function of photon energy.

The scintillation decay curve of CsI(Tl) for gamma excitation consists of a fast and a slow component, and can be modeled as [91], [92],

$$I(t) = A_0 + A_1 e^{-t/\tau_1} + A_2 e^{-t/\tau_2} \quad (3.1)$$

where $I(t)$ is the total pulse intensity as a function of time (t), τ_1 and τ_2 are the fast and the slow decay time constants, respectively, A_1 and A_2 are the relative contributions of the fast and the slow components in the total pulse intensity, respectively, and A_0 is a fitting constant. By fitting Equation (3.1) to the experimentally obtained plot of $I(t)$ versus t , one can estimate

all of these parameters. The relative intensities of the fast and the slow decay components are respectively given by [91], [92],

$$Q_1 = \frac{A_1\tau_1}{A_1\tau_1 + A_2\tau_2} \quad (3.2)$$

and,

$$Q_2 = \frac{A_2\tau_2}{A_1\tau_1 + A_2\tau_2} \quad (3.3)$$

For the CsI(Tl) crystals indigenously grown by the Bridgman-Stockbarger technique, described in Section 2.1.4.3, the values of τ_1 , τ_2 , A_1 and A_2 were experimentally determined and reported in [92]. These values are $\tau_1 = 700$ ns, $\tau_2 = 3500$ ns, $A_1 = 0.57$ and $A_2 = 0.43$. Using these, Q_1 and Q_2 were calculated from Equations (3.1) and (3.2), respectively. Subsequently, each of the 32 normalized emission intensities corresponding to the 32 energy points was divided into the fast and the slow components according to the ratio Q_1/Q_2 . This completed the implementation of the emission spectrum of CsI(Tl) into the simulation code.

The material CsI(Tl) was assigned a refractive index of 1.79 at all the 32 energy points, i.e., throughout its own emission wavelength regime [186]. The (bulk) absorption length as well as the Rayleigh scattering length for CsI(Tl) have not been reported in published literature. Hence both were assumed to be equal to 5 m at all the 32 energy points. This value is much larger than the largest dimension (of the order of centimeters) of the scintillator. As mentioned in Section 2.3.2.2.3.1, this choice for the (bulk) absorption length ensures good optical transparency of the scintillator throughout the range of its own emission wavelength. It is important to note, however, that optical photons can still be lost via interactions at the surfaces. Also, as mentioned in Section 2.3.2.2.3.1, this value for the Rayleigh scattering length is justified because firstly, it is of the order of meters in crystalline scintillators, and secondly, as long as the largest dimension of the scintillator remains much smaller than it, the process of Rayleigh scattering itself becomes unimportant. The

scintillation yield of CsI(Tl) was taken to be 65,000 photons/MeV. Its fast and slow time constants were taken to be 700 ns and 3500 ns, respectively, and the yield ratio was taken to be 0.57 [92]. It is needed to be mentioned that the time constants and the yield ratio do not affect the simulation results because no timing related study is attempted. They are incorporated just for completion. The Mie scattering length was arbitrarily assumed to be 500 m at all the 32 energy points. As mentioned in Section 2.3.2.2.3.1, the Mie scattering process is unimportant for the scattering of the optical photons by the CsI molecules, because the former have wavelengths in the range of a few hundred nanometers, whereas the latter have sizes only of the order of less than a nanometer. Hence, the arbitrary choice does not affect the simulation results [166]. The Birks' constant and the resolution scale for CsI(Tl) were taken to be 1.52×10^{-3} mm/MeV [197] and 1, respectively.

All the above properties for the photodetector were taken to be identical to those of the scintillator, but for its scintillation yield, which was set to be zero because the photodetector does not generate optical photons [166]. The refractive index of Teflon was set equal to 1.35 [198].

All the scintillation and optical properties mentioned in this section were unchanged for all simulations, unless otherwise specified.

3.2.4 Surface properties

As mentioned in Section 2.3.2.2.3.2, the UNIFIED model [181] was used to model the optical surfaces. The scintillator-reflector interface was modeled to be a dielectric-dielectric type of surface with surface finish GFP, surface roughness, $\sigma_\alpha = 0^\circ$ (implicit), reflectivity, $R = 0.98$ [199], reflection type = L [199], and efficiency, $\eta = 0$. On the other hand, the scintillator-photodetector interface was modeled to be a dielectric-metal type of surface with surface finish P, surface roughness, $\sigma_\alpha = 0^\circ$ (implicit), reflectivity, $R = 0$, reflection type = SL [180] (for the surface finish P, SL is equivalent to SS, but as $R = 0$, the reflection type does not

matter) and efficiency, $\eta = 0.05$, i.e., 5%. This value of η is equal to the *EWQE* of the bialkali photocathode of the Hamamatsu R1306 PMT [200] when it is coupled to CsI(Tl) [138]. All the surface properties mentioned here were unchanged for all simulations, unless otherwise specified.

3.2.5 Scoring

Each primary gamma photon as well as all its ionizing secondary particles were transported in the detector. The energy deposited inside the scintillator volume was scored for each primary gamma ray event. As mentioned in Section 2.3.2.2.2, for each energy deposition step of the secondary electrons (or positrons) inside the scintillator, optical photons were generated evenly along the track segment involved in the step and emitted isotropically over 4π solid angle. They were then transported through the scintillator up to the scintillator-photodetector interface. At this interface, they were detected with a probability η of the interface [164], [180]. The number of detected optical photons at this interface (n_{ph}) is equivalent to the number of photoelectrons produced at the photocathode of the coupled PMT. This number was scored for each primary gamma ray event and then converted to an arbitrary pulse-height by using the formula [166],

$$Pulse\ height\ (V) = \frac{n_{ph} \times e \times G}{C} \quad (3.4)$$

where, e ($= 1.602 \times 10^{-19}$ C) is the electronic charge, G is the overall gain (see Equation (1.3)) of the photodetector ($= 2.7 \times 10^5$ for the Hamamatsu R1306 PMT), and C is the overall capacitance of the electronic circuit ($= 1$ nF, taken arbitrarily).

All the simulations were carried out for a total of 7×10^4 primary gamma ray histories. The simulation job was run in parallel on 7 cores of a workstation that had an octa-core processor, with each core handling a total of 10^4 histories. Results from the individual cores were merged by a user-written program. A tally was generated with the pulse-height

values for each primary event. Finally, this tally was used to draw a pulse-height histogram using ROOT [201]. This histogram represents the simulated pulse-height spectrum [166].

3.3 Energy calibration by simulation

Pulse-height spectrum was generated by simulation using the source at serial no. 1 of Table 3.1. This spectrum is shown in Figure 3.4 (a). Each full-energy peak in this spectrum was fitted using a Gaussian function. The pulse-height value corresponding to the centroid of each of the three full-energy peaks was also plotted in Figure 3.4 (a) versus the corresponding gamma energy. A straight line was then fitted to this plot. The equation of this fitted straight line was used to convert the pulse-height scale to the energy scale. The simulated spectrum of Figure 3.4 (a), converted to energy scale, is shown in Figure 3.4 (b). This procedure is similar to the experimental energy calibration of a gamma spectrometer with a ^{137}Cs and a ^{60}Co source, both having the same activity [166].

3.4 Experimental measurements

A 2" $\phi \times$ 2" L cylindrical sample was cut from a CsI(Tl) single crystal ingot that was grown in-house [159]–[161] by the Bridgman-Stockbarger technique, as described in Section 2.1.4.3. One of the flat surfaces of the sample was hand polished with suitable sand papers to clear optical finish, whereas all other surfaces were ground. The polished surface was optically coupled to a Hamamatsu R1306 PMT using a transparent optical grease (Dow corning). The scintillator was tightly wrapped with at least ten layers of Teflon tape (thickness = 3.5 mils = 0.0889 mm per layer [202]), which acts as a diffuse reflector. Care was taken to perfectly coat the scintillator with the reflector so as to avoid formation of any air pockets between the two and also to avoid any light leakage from the scintillator. The anode pulse of the PMT was fed to single board integrated module (DP5G, Amptek [203]) consisting of a preamplifier, a shaping amplifier, and a USB based 4k MCA. The preamplifier, amplifier and the MCA were all integrated in a single PCB. Power to the entire

electronics as well as the HV to the PMT were supplied by a single USB port of the MCA by employing necessary DC-DC converters [166].

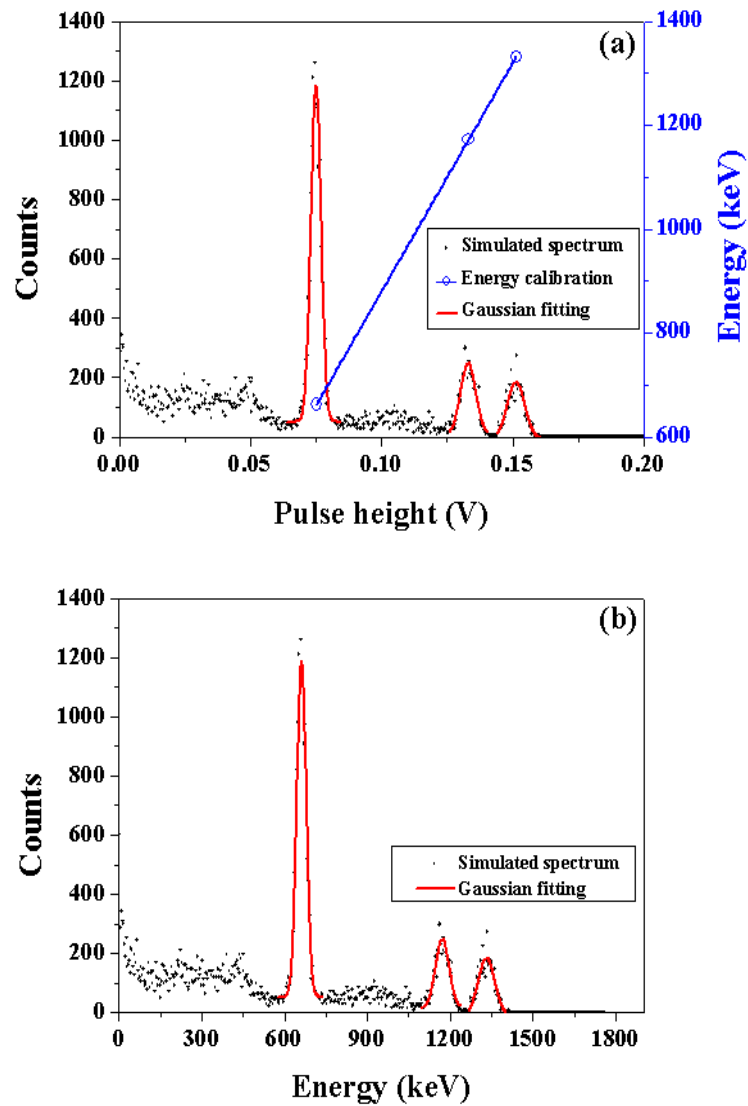


Figure 3.4: (a) Simulated spectrum for a 50.8 mm $\phi \times$ 50.8 mm L cylindrical CsI(Tl) scintillator using the source at serial number 1 of Table 3.1, along with the derived energy calibration, (b) The same spectrum converted to energy scale [166].

In order to prevent light leakage, the whole assembly was sealed in an aluminum enclosure of thickness 1 mm all around, except at the front surface of the scintillator where it was 0.5 mm. The simulation and the experimental assembly were built to match each other.

Firstly, a ^{137}Cs and a ^{60}Co test source were placed together at a distance of 300 mm from the front surface of the aluminum enclosure. Pulse-height spectrum was recorded for an acquisition time of 30 s.

Then, a ^{137}Cs test source was placed at a distance of 300 mm from the front surface of the aluminum enclosure. Pulse-height spectrum was recorded for an acquisition time of 300 s. Background spectrum was also recorded for 300 s by removing the source. The background spectrum was then subtracted from the spectrum recorded with the source in order to get the spectrum due to the source.

Subsequently, a Marinelli beaker filled with ^{41}Ar containing air was placed at a distance of 300 mm from the front surface of the aluminum enclosure. Pulse-height spectra were acquired with this source as well as for background, both for 300 s. The background spectrum was then subtracted from the spectrum with source.

3.5 Experimental energy calibration

Figure 3.5 (a) shows the experimentally acquired pulse-height spectrum for the $^{137}\text{Cs} + ^{60}\text{Co}$ source. Gaussian functions were fitted to the three full-energy peaks of Figure 3.5 (a). The values of the centroid of the three Gaussian functions were also plotted as a function of the channel number. A straight line was fitted to this plot. The equation of this straight line was used to convert the channel number scale to the energy scale. This energy calibration was used for all the experimental spectra. The spectrum of Figure 3.5 (a), converted to the energy scale, is shown in Figure 3.5 (b).

3.6 Experimental validation of the simulation model

3.6.1 Validation for ^{137}Cs

The simulated spectrum with the ^{137}Cs source and the background subtracted experimental spectrum, recorded with the setup described at Section 3.4 and the ^{137}Cs test source, are presented and compared in Figure 3.6.

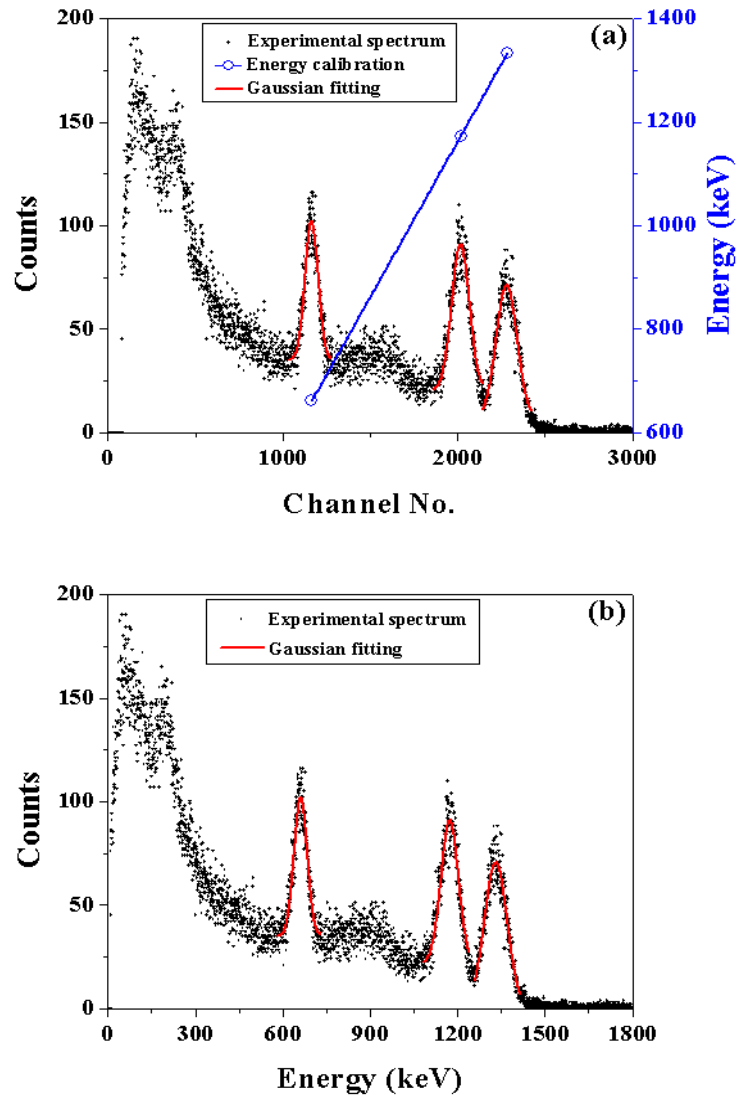


Figure 3.5: (a) Experimentally acquired spectrum of $^{137}\text{Cs} + ^{60}\text{Co}$ source with a 50.8 mm $\phi \times$ 50.8 mm L cylindrical CsI(Tl) scintillator, along with the derived energy calibration, (b) The same spectrum converted to energy scale.

The values of energy resolution at 662 keV for the two spectra, calculated using Equation (1.10), are also shown in Figure 3.6. Good matching between the two spectra near the full-energy peak region is evident from Figure 3.6. The mismatch of the energy resolution may be inferred to be due to the fact that the simulated spectrum does not include some of the factors that are responsible for additional broadening of the experimental spectrum, as described in Section 1.3.3.2.1. For example, factors like nonuniformity of light yield over the volume of

the scintillator, fluctuations of gain of the PMT from event to event, electronic noise, drifts in operating parameters over the course of measurement, etc. are not included in the simulation model. On the other hand, it is also visible from Figure 3.6 that there is a systematic underestimation in the simulated spectrum compared to the experimental spectrum. This may be due to the fact that the surrounding materials, detector's ancillary equipment, etc. which were present in the laboratory during the experimental measurement, may have resulted in a significant amount of scattered radiation, which was not modeled in simulation. Further, the evident mismatch near the 32 keV peak between the simulated and the experimental spectra, also visible in Figure 3.6, may be due to the fact that CsI(Tl) has some nonproportionality of light yield at this low energy region. Therefore, the linear relationship between pulse-height and energy, as shown in Figures 3.4 (a) and 3.5 (a), although being accurate at the calibration energy regime (662-1332 keV), does not hold near the 32 keV peak region [166].

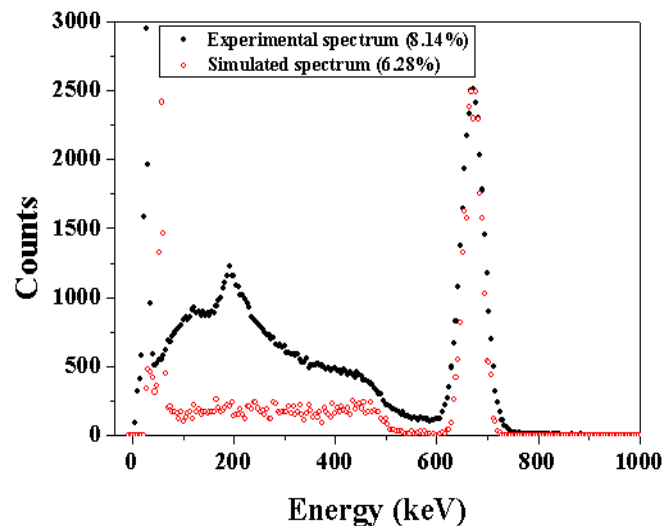


Figure 3.6: Comparison of experimental and simulated spectra of ^{137}Cs for a 50.8 mm $\phi \times$ 50.8 mm L cylindrical CsI(Tl) scintillator [166].

3.6.2 Validation for ^{41}Ar

The simulated spectrum with the ^{41}Ar source and the background subtracted experimental spectrum, recorded with the ^{41}Ar containing Marinelli beaker, are presented and compared in

Figure 3.7. The values of energy resolution at 1293 keV for the two spectra, calculated by fitting Gaussian functions to the full-energy peaks (also shown) and using Equation (1.10), are also presented in Figure 3.7.

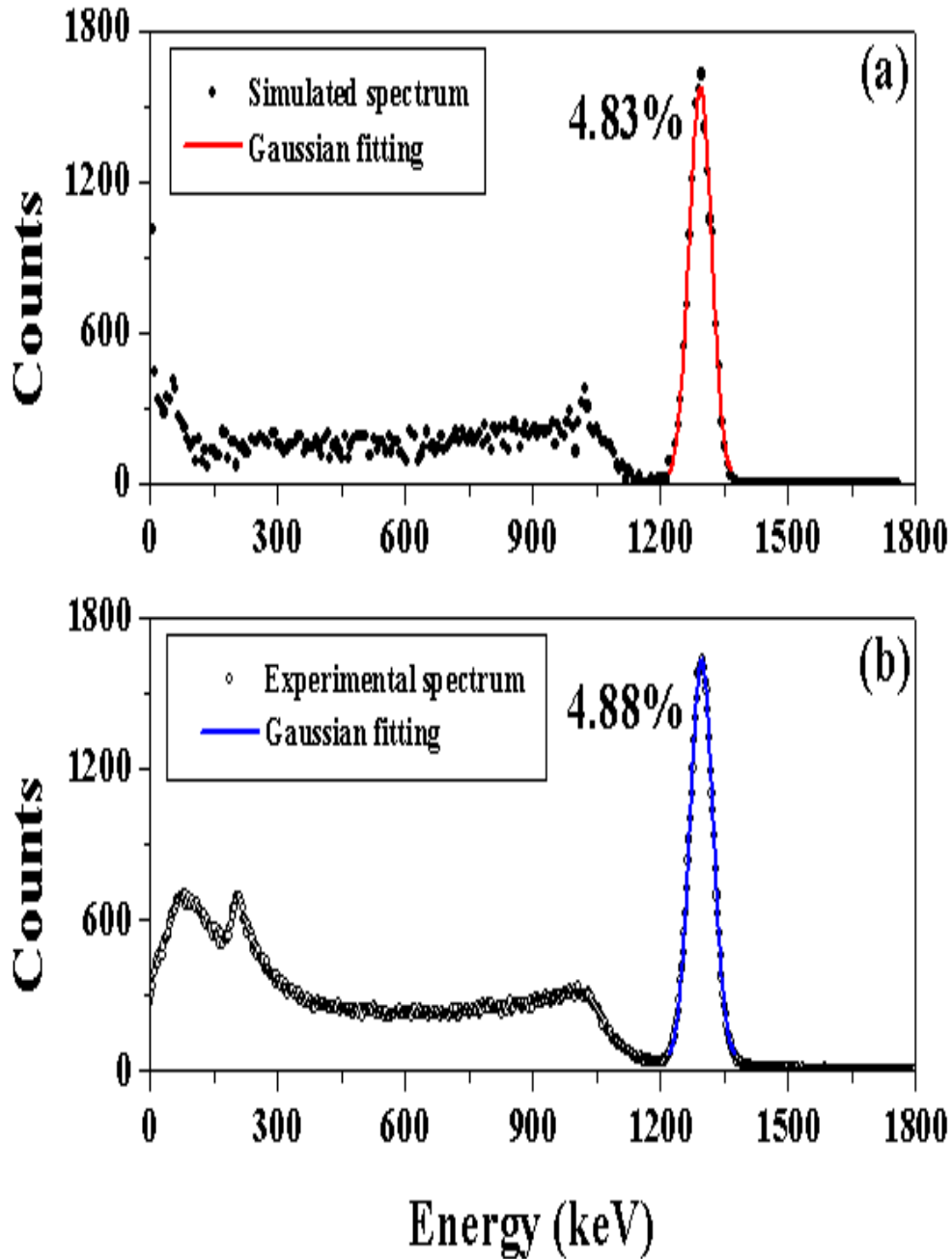


Figure 3.7: (a) Simulated spectrum of ^{41}Ar for a 50.8 mm $\phi \times$ 50.8 mm L cylindrical CsI(Tl) scintillator, (b) Experimental spectrum of ^{41}Ar containing air filled in a Marinelli beaker.

Similar to Figure 3.6, it can be seen from Figure 3.7 that there is good matching between the simulated and the experimental spectra in the 1293 keV full-energy peak region.

The mismatch of energy resolution between the two spectra is also lesser at 1293 keV than that at 662 keV. This may be due to the better SNR at the higher energy of 1293 keV than that at 662 keV, thereby resulting in reduction of electronic noise. The backscatter region is still missing in the simulated spectrum, however, which may be due to the same reason as pointed out in Section 3.6.1.

The matching of the simulated and the experimental spectra near the full-energy peak regions of both the Figures 3.7 and 3.8, however, ensures that the simulation parameters may be optimized by observing the effects of their variation on the simulated spectrum [166].

3.7 Effect of variation of simulation parameters

3.7.1 Efficiency of the photodetector (η)

As mentioned in Section 2.3.2.2.3.2, η is equivalent to the QE of the photodetector coupled to the scintillator. When CsI(Tl) is coupled to the Hamamatsu R1306 PMT, the $EWQE$ is only 0.05, i.e., 5%, as mentioned in Section 3.2.4 [138]. On the other hand, when CsI(Tl) is coupled to the Hamamatsu S3590-08 silicon photodiode which has a photosensitivity, $R_\lambda = 0.36 A/W$ at $\lambda = 540$ nm [191], the quantum efficiency at this wavelength becomes [166],

$$QE_\lambda = \frac{R_\lambda}{\lambda} \times \frac{hc}{e} \approx \frac{R_\lambda \left(\frac{A}{W}\right)}{\lambda (nm)} \times 1240 \left(\frac{W \cdot nm}{A}\right) = \frac{0.36}{540} \times 1240 = 0.8267 \quad (3.5)$$

where h ($= 6.626 \times 10^{-34}$ J.s) is the Planck's constant, c ($= 3 \times 10^8$ m/s) is the speed of light in vacuum, and e ($= 1.602 \times 10^{-19}$ C) is the electronic charge.

Therefore, simulated spectra were generated with ^{137}Cs source for $\eta = 0.05$ and $\eta = 0.8267$, keeping all other parameters unchanged. The two simulated spectra (in pulse-height scale) are shown in Figure 3.8. It can be seen from Figure 3.8 that the energy resolution drastically improves when the CsI(Tl) scintillator is coupled to a photodiode with a much higher QE , with respect to the case when it is coupled to a PMT.

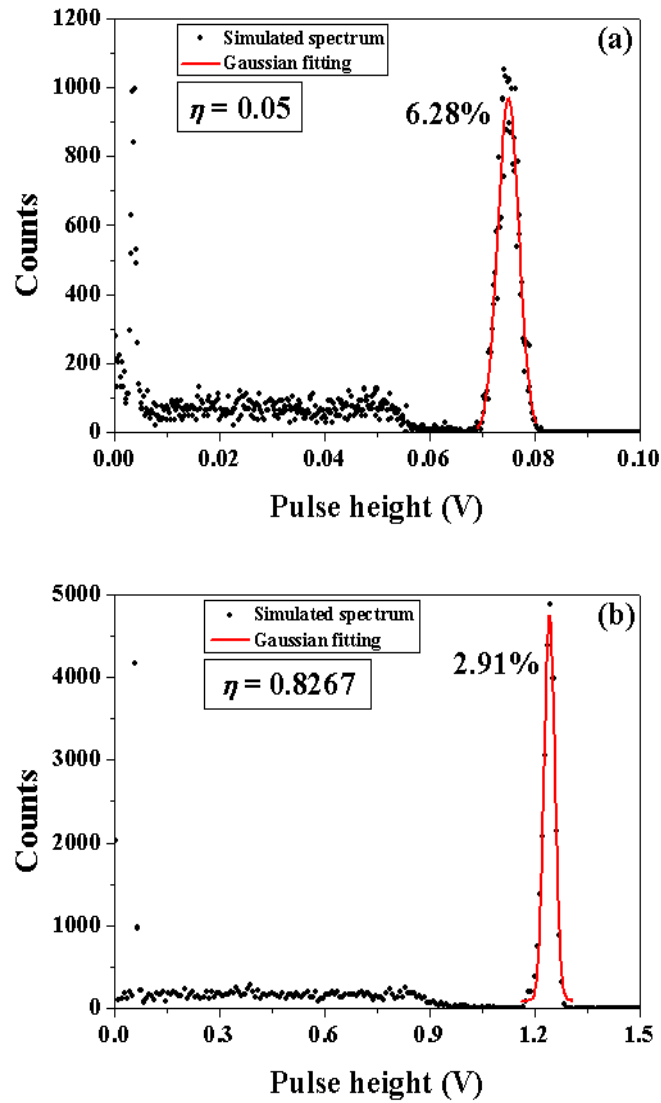


Figure 3.8: (a) Simulated spectra of ^{137}Cs for efficiency, $\eta = 0.05$ (typical of PMT) and (b) efficiency, $\eta = 0.8267$ (typical of photodiode). In both cases, the gain (G) of the photodetector is taken to be 2.7×10^5 , which is typical of PMT [166].

However, it is difficult to experimentally achieve this theoretical limit of energy resolution of nearly 3% when CsI(Tl) is coupled to a photodiode. It is to be noted that only the value of η has been changed for the two cases, keeping another practically important factor, i.e., the gain (G of Equation (3.4)) of the photodetector unchanged. The photodiode only has a gain (G) of unity. As a result, the SNR is much lower than that achievable with a PMT, and therefore, the energy resolution worsens, as described in Section 1.2.3.1.3. On the

other hand, due to the high gain (G) of the PMT, the SNR improves very much, and therefore, the theoretically predicted energy resolution values are closely achievable when the experimental assembly consists of the CsI(Tl) scintillator coupled to a PMT. Also, the surface area of the photodetector is taken to be the same in both the cases. However, photodiodes are practically available with much lower surface areas, as mentioned in Section 1.2.3.1.3. It is also to be mentioned here that the effect of nonproportionality of light yield on the energy resolution is not considered here because the resolution scale is taken to be 1, as mentioned in Section 3.2.3. If this effect is considered, the energy resolution as low as 2.91% may not be achievable [166].

It can also be seen from Figure 3.8 that the pulse-height, as calculated from Equation (3.4), is much higher in Figure 3.8 (b) than in Figure 3.8 (a). This only signifies that the pulse-height would have been much higher with the photodiode had it have the same gain as the PMT but its own (much higher) QE . It is also to be mentioned that the values of pulse-height in Figure 3.8 are completely arbitrary because they are calculated from Equation (3.4) by taking an arbitrary value for C . The value of G also varies for each photodetector. Therefore, for each practical detector system, the absolute pulse-height would change.

In a practical detector system consisting of a scintillator coupled to a PMT, the mismatch of refractive indices between the scintillator and the glass entrance window of the PMT, as well as that between the glass and the deposited photocathode material, may decrease the QE due to reflection losses. When an optical grease is used to couple the scintillator to the PMT, this effect can be greatly reduced as the grease minimizes the refractive index mismatch. This effect is therefore not considered in simulation where the material of the photodetector is taken to be the same as that of the scintillator. Also, the values of η considered for simulation are taken from the experimentally measured and

reported values for the mentioned photodetectors [191], [200]. This measurements already take care of the reflection losses, if any [166].

Subsequent to this, simulated spectra were also generated with ^{137}Cs for several additional values of η , keeping all other parameters unchanged, in order to see the quantitative dependence of the simulated spectra on this parameter. Gaussian functions were fitted to the 662 keV full-energy peak of each simulated spectrum. The energy resolution values at 662 keV were calculated using Equation (1.10). These, and the peak-pulse-height values (*PPH*) at 662 keV are shown as functions of η in Figure 3.9.

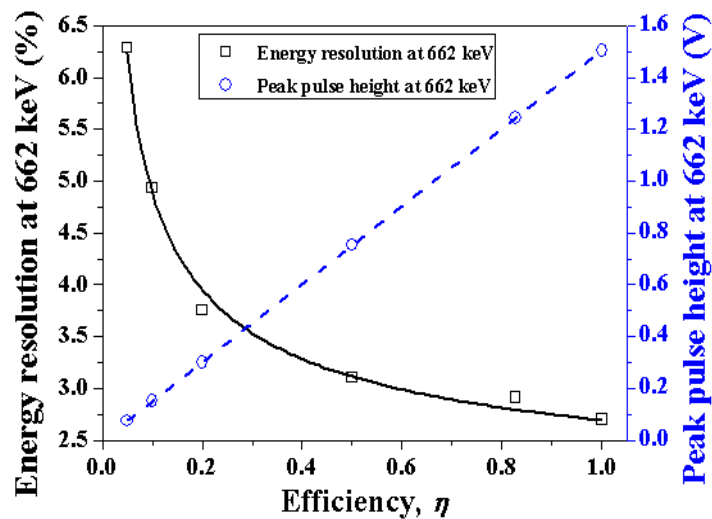


Figure 3.9: Variation of the energy resolution at 662 keV and the corresponding peak-pulse-height with efficiency (η) of the photodetector [167].

The equation of the best-fit curve between energy resolution at 662 keV and η is found to be [167],

$$Resolution (\%) = 1.66872 + \frac{1.02041}{\sqrt{\eta}} \quad (3.6)$$

It is known that energy resolution is inversely proportional to the square root of n_{ph} (see Equation (1.11)). On the other hand, n_{ph} is directly proportional to η because the optical photons are detected with a probability η at the scintillator-photodetector interface. Therefore,

energy resolution should also be proportional to the square root of η , as is predicted by Equation (3.6).

The equation of the best-fit straight line between PPH at 662 keV and η is found to be [167],

$$PPH (V) = 1.5041 \times \eta - 2.47152 \times 10^{-4} \quad (3.7)$$

As PPH is proportional to n_{ph} which, in turn, is proportional to η , the result presented in Equation (3.7) is justified.

Equations (3.6) and (3.7) present the quantitative behavior of energy resolution and PPH at 662 keV, respectively. For this scintillator-photodetector assembly, therefore, values of energy resolution and PPH at 662 keV can be predicted *a priori* from these equations for any arbitrary value of η that might be encountered while working with a new photodetector, provided η is known for the same [167].

It is to be mentioned here that the values of PPH presented in Figure 3.8 and Equation (3.7) are arbitrary, since they are calculated from Equation (3.4) with arbitrary values of C . Also, the value of G should be unique for each photodetector. Therefore, actual values of PPH would be different for practical detectors. The values of the constant parameters in Equation (3.7) should also vary for each particular setting of the constants C and G . However, the functional relationship would be the same.

3.7.2 Gain of the photodetector (G)

The Hamamatsu S3590-08 silicon photodiode has a gain, $G = 1$ and efficiency, $\eta = 0.8267$ [191], whereas all simulations reported in Section 3.7.1 were performed with $G = 2.7 \times 10^5$, which is the gain of the Hamamatsu R1306 PMT [200]. Therefore, the simulation was repeated with ^{137}Cs for the combination ($G = 1, \eta = 0.8267$). For this case, it was seen that the pulse-height of the simulated spectrum was scaled down by a constant factor of 2.7×10^5 relative to the simulated spectrum with the combination ($G = 2.7 \times 10^5, \eta = 0.8267$), whereas

the energy resolution at 662 keV was unchanged. This is straightforward because the pulse-height is calculated using Equation (3.4), where n_{ph} has not changed between these two simulations since η has remained unchanged. Only the constant G has been changed, and therefore, the pulse-height has been appropriately scaled down. This result, however, more importantly indicates that in the hypothetical scenario where gain could be increased without introducing additional electronic noise, the CsI(Tl)-photodiode assembly would offer improved energy resolution compared to the CsI(Tl)-PMT assembly [166].

3.7.3 Capacitance of the electronic circuit (C)

The simulation was repeated with ^{137}Cs for $C = 1$ pF instead of $C = 1$ nF, keeping $G = 2.7 \times 10^5$ and $\eta = 0.05$ (typical for the Hamamatsu R1306 PMT). It was seen that the pulse-height of the simulated spectrum simply got scaled up by a factor of 10^3 ($= 1$ nF/1 pF) with respect to the simulated spectrum presented at Figure 3.8 (a), whereas the energy resolution at 662 keV remained unchanged. This is due to the fact that n_{ph} did not change between these two simulations because η remained unchanged. Only the constant C of Equation (3.4) was decreased, and therefore, the pulse-height was appropriately scaled up [166].

3.7.4 Reflectivity of the scintillator-reflector interface (R)

The impact of R on the energy spectrum of a plastic scintillator based system has been reported earlier in [180]. Here the impact of R on the energy spectrum of a CsI(Tl) scintillator based system is investigated. Typical reflector materials used to coat scintillators have a reflectivity (R) in the range 0.7-1.0 [147]. Therefore, simulated spectra were generated with ^{137}Cs for several values of R in this range, keeping all other parameters unchanged from those mentioned in Section 3.2. Figure 3.10 shows the simulated spectra for different values of R . It is evident from Figure 3.10 that as R increases, the energy resolution improves and the pulse-height increases. The marked improvement in the spectra for only a nominal 1% increase in R shows how important this parameter is. Therefore, for aluminum foil, which is a

commonly used reflector having a notably low reflectivity [204], the pulse-height spectra are expected to have much poorer energy resolution than when other reflectors with higher reflectivity are used [166].

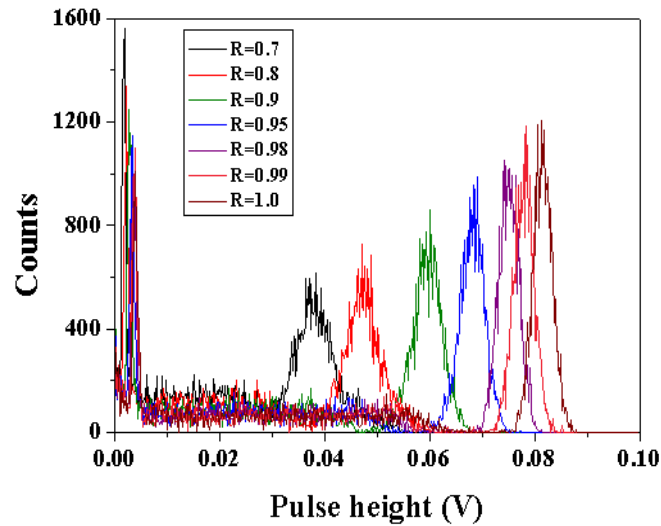


Figure 3.10: Simulated spectra of ^{137}Cs for different values of reflectivity (R) of the scintillator-reflector interface [166].

The values of energy resolution at 662 keV and the corresponding PPH values, obtained by fitting Gaussian functions to the full-energy peaks of Figure 3.10, are shown as functions of R in Figure 3.11. The equation of the best-fit straight line between energy resolution at 662 keV and R is found to be [166],

$$Resolution (\%) = -45.55904 \times R + 50.99045 \quad (3.8)$$

The negative sign of the coefficient of R in Equation (3.8) ensures that resolution decreases (i.e., improves) when R increases. It is known, on the other hand, that $Resolution \propto 1/\sqrt{n_{ph}}$. Therefore, it can be inferred from Equation (3.8) that n_{ph} increases as a quadratic function of R .

The equation of the best-fit curve between PPH at 662 keV and R is found to be [166],

$$PPH (V) = 0.16154 - 0.39728 \times R + 0.31596 \times R^2 \quad (3.9)$$

As PPH is directly proportional to n_{ph} , it can be inferred from Equation (3.9) that n_{ph} increases as a 2nd order polynomial of R [166].

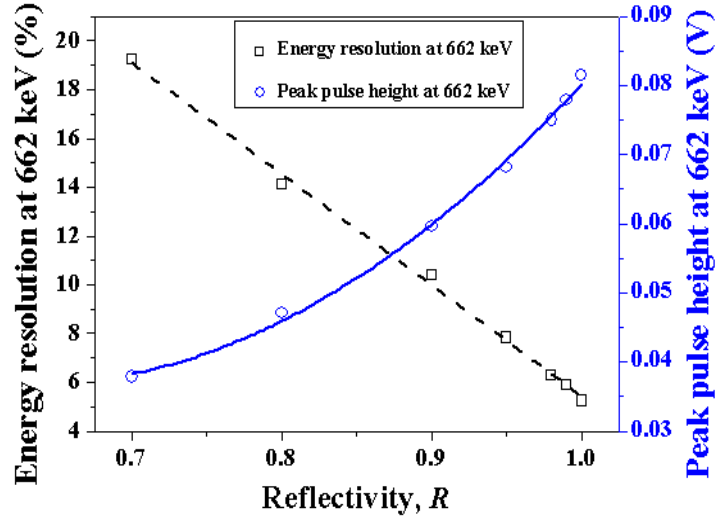


Figure 3.11: Variation of the energy resolution at 662 keV and the corresponding peak-pulse-height with reflectivity (R) of the scintillator-reflector interface [166].

3.7.5 Surface finish of the scintillator-reflector interface

As described in Section 2.3.2.2.3.2, there are overall six types of surface finish (P, G, PFP, GFP, PBP and GBP) available for a dielectric-dielectric surface in the UNIFIED model of GEANT4. Simulated spectra were generated with ^{137}Cs for all these six types of surface finish of the scintillator-reflector surface, keeping the surface roughness, $\sigma_\alpha = 0^\circ$. The six simulated spectra were seen to be nearly indistinguishable from one another. This indicates that the parameter surface finish does not affect the pulse-height spectra much for the specific scintillator-reflector combination studied here. The values of energy resolution at 662 keV for the six simulated spectra are presented in Table 3.2. It is evident from Table 3.2 that the values of energy resolution at 662 keV for the six simulated spectra are almost identical, barring some small differences. These small differences may be due to the slight differences

in choosing the region-of-interest (ROI) near the full-energy peaks for fitting the Gaussian functions, as well as the slight inaccuracies of fitting [166].

Table 3.2: Values of energy resolution at 662 keV for six simulated spectra with different choices of surface finish of the scintillator-reflector interface. In all the six cases, $\sigma_\alpha = 0^\circ$ [166].

Surface finish	Energy resolution (%) at 662 keV
G	6.7
GFP	6.29
GBP	6.27
P	6.12
PFP	7.85
PBP	6.28

It needs to be mentioned here that the possibility of an imperfectly coated scintillator was not considered in simulation, i.e., no air gap was introduced between the scintillator and the reflector. For an imperfectly coated scintillator, however, the pulse-height spectra may get significantly deteriorated due to loss of some of the optical photons resulting from refractive index mismatch at the scintillator-air and the air-reflector interfaces [166].

3.7.6 Surface roughness of the scintillator-reflector interface (σ_α)

In order to see the impact of σ_α on the simulated spectra, simulations were performed with ^{137}Cs for two different values of this parameter, 0° and 12° , for two different types of surface finish, G and GFP of the scintillator-reflector interface. The lower and the higher values of σ_α resemble a perfectly polished scintillator and a very rough scintillator, respectively [180], [183]. The simulated spectra in the four cases were found to be nearly indistinguishable from one another. Table 3.3 depicts the values of energy resolution at 662 keV for the four cases. It is seen from Table 3.3 that the parameter surface roughness (σ_α) does not affect the simulated spectra significantly for the studied scintillator-reflector combination [166].

Table 3.3: Values of energy resolution at 662 keV for two different values of surface roughness (σ_α) of the scintillator-reflector interface with two different surface finish G and GFP [166].

Surface roughness, σ_α	Energy resolution (%) at 662 keV	
	G	GFP
0°	6.7	6.29
12°	6.2	6.33

3.7.7 Reflection type

There are a total of four types (SS, SL, L and BS) of reflection in the UNIFIED model of GEANT4 for a dielectric-dielectric interface. For a practical reflector material, the reflection type is a function of the incident angle of the optical photons. Therefore, for those reflectors which exhibit a combination of different types of reflection, the fraction of each type also depends on the incidence angle. For example, the fraction of specular and Lambertian reflection types as a function of the incidence angle is presented in [205]. For two different types of surface finish, G and GFP, simulated spectra were generated with ^{137}Cs for different combinations of the four reflection types, SS, SL, L and BS. All the simulated spectra were nearly indistinguishable from one another. Therefore, it may be inferred that the parameter reflection type does not impact the simulated spectra much for the particular scintillator-reflector combination studied herein. The values of energy resolution at 662 keV for all these simulated spectra are presented in Table 3.4, wherein it is evident that the energy resolution is fairly constant in all the cases [166].

3.7.8 Resolution scale

As defined in Section 2.3.2.2.1, if the resolution scale is greater than unity, there would be broadening of the full-energy peaks due to nonproportionality of light yield. For all the simulations reported so far, the resolution scale was taken to be unity. Therefore, light yield nonproportionality was not considered.

Table 3.4: Values of energy resolution at 662 keV for different combinations of the four reflection types with two different surface finishes G and GFP [166].

Reflection type	Energy resolution (%) at 662 keV	
	GFP	G
L = 1.0	6.29	6.7
SL = 0.9, L = 0.1	5.97	6.37
SL = 0.8, L = 0.2	6.52	6.87
SL = 0.9, BS = 0.1	6.10	6.21
SL = 0.8, BS = 0.2	6.43	6.31
SL = 0.9, SS = 0.1	6.23	6.50
SL = 0.8, SS = 0.2	6.79	5.97
SL = 1.0	6.02	6.13

This parameter, which represents the extent of nonproportionality of light yield in a scintillator, can be tuned in order to match the energy resolution values of the experimental and the simulated spectra. Resolution scale is closely related to the photon Fano factor, which may be significantly greater than unity for doped scintillators like CsI(Tl). Its exact value is not reported in literature for CsI(Tl), but it is available for some other scintillators in [206]. Therefore, simulations were performed with ^{137}Cs for various values of resolution scale. Figure 3.12 shows the individual simulated spectra for different values of the parameter resolution scale. It can be seen from Figure 3.12 that the energy resolution of the 662 keV peak gradually deteriorates as resolution scale increases, whereas the corresponding peak-pulse-height remains almost unaltered. The energy resolution at 662 keV and the corresponding peak-pulse-height were also plotted as functions of resolution scale and the same is shown in Figure 3.13. It is seen from Figure 3.13 that the energy resolution at 662 keV increases (worsens) linearly as resolution scale increases, whereas the peak-pulse-height remains constant. Therefore, due to a higher degree of nonproportionality of light yield in CsI(Tl), it should be expected that the energy resolution would deteriorate but the pulse-height would be unchanged [166].

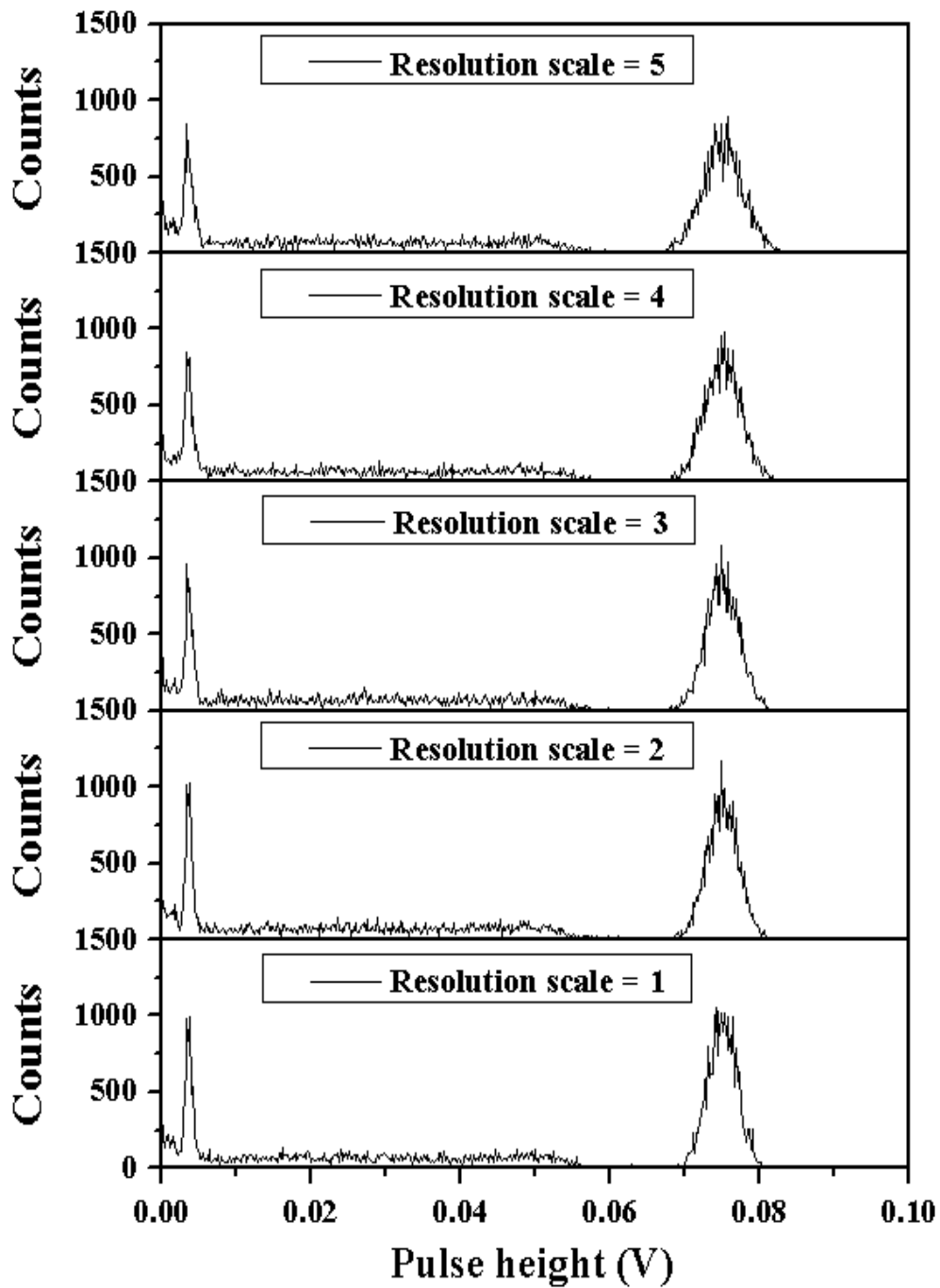


Figure 3.12: Simulated pulse-height spectra with ^{137}Cs for different values of the parameter resolution scale. The full-energy peak broadens as this parameter increases, whereas the centroid of the peak remains unchanged.

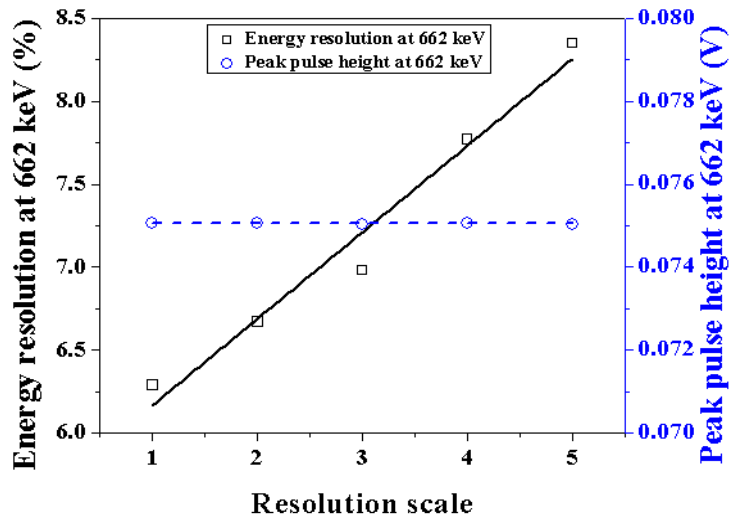


Figure 3.13: Variation of the energy resolution at 662 keV and the corresponding peak-pulse-height with the parameter resolution scale.

3.7.9 Scintillation yield (N)

Each scintillator has a characteristic scintillation yield (N), e.g., for CsI(Tl) it was taken to be 65,000 photons/MeV for all simulations reported so far. However, this parameter may vary from one sample to another due to variation in doping concentration and/or co-doping, if any, residual impurity concentration, etc. The scintillation yield also depends on the energy of the incident gamma photons. Simulations were, therefore, performed with ^{137}Cs for various hypothetical values of N in order to see the effect of this parameter on the simulated spectra. Figure 3.14 shows the simulated spectra for different values of N . It is clear from Figure 3.14 that as N increases, the energy resolution improves and the pulse-height increases [166]. The values of energy resolution at 662 keV and the corresponding PPH values are shown as functions of N in Figure 3.15. The equation of the best-fit curve between energy resolution at 662 keV and N is found to be [166],

$$Resolution (\%) = 0.76714 + \frac{1418.29898}{\sqrt{N} (\text{photons/MeV})} \quad (3.10)$$

On the other hand, the equation of the best-fit straight line between PPH at 662 keV and N is found to be [166],

$$PPH (V) = 1.15273 \times 10^{-6} \times N \left(\frac{\text{photons}}{\text{MeV}} \right) + 1.05333 \times 10^{-4} \quad (3.11)$$

It is known that $Resolution \propto 1/\sqrt{n_{ph}}$ and $PPH \propto n_{ph}$. On the other hand, n_{ph} is directly proportional to N . This justifies the functional relationships presented in Equations (3.10) and (3.11) [166].

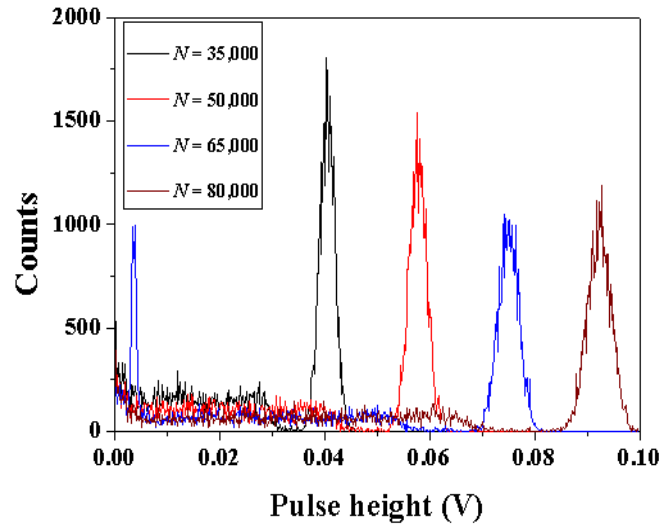


Figure 3.14: Simulated spectra of ^{137}Cs for different values of scintillation yield (N (photons/MeV)) of the scintillator [166].

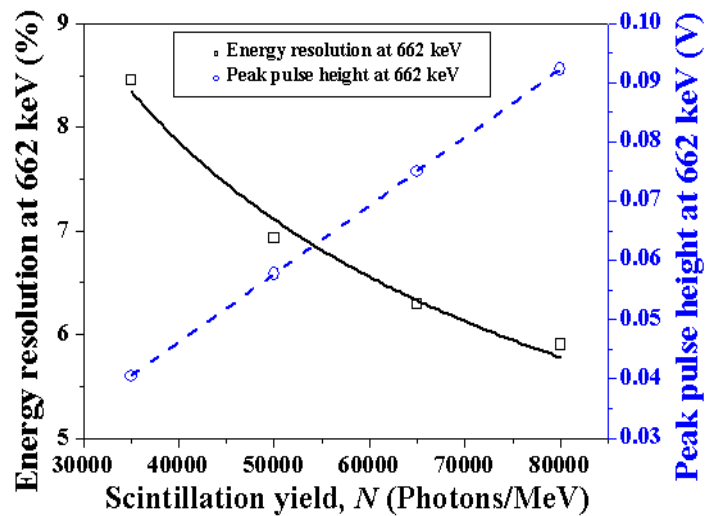


Figure 3.15: Variation of the energy resolution at 662 keV and the corresponding peak-pulse-height with scintillation yield (N) of the scintillator [166].

3.7.10 Size of the scintillator

Simulated spectra were generated with ^{137}Cs for different sizes of the cylindrical CsI(Tl) scintillator, keeping all simulation parameters unchanged from those mentioned in Section 3.2. The studied scintillator sizes were 1" $\phi \times$ 1" L (25.4 mm $\phi \times$ 25.4 mm L), 2" $\phi \times$ 2" L (50.8 mm $\phi \times$ 50.8 mm L) and 3" $\phi \times$ 3" L (76.2 mm $\phi \times$ 76.2 mm L). In each case, the diameter of the photodetector was taken to be same as that of the scintillator, keeping its length fixed at 10 mm. The comparison of the three simulated spectra is shown in Figure 3.16, wherein it is evident that as the size of the scintillator increases, the photopeak efficiency increases but the *PPH* slightly decreases.

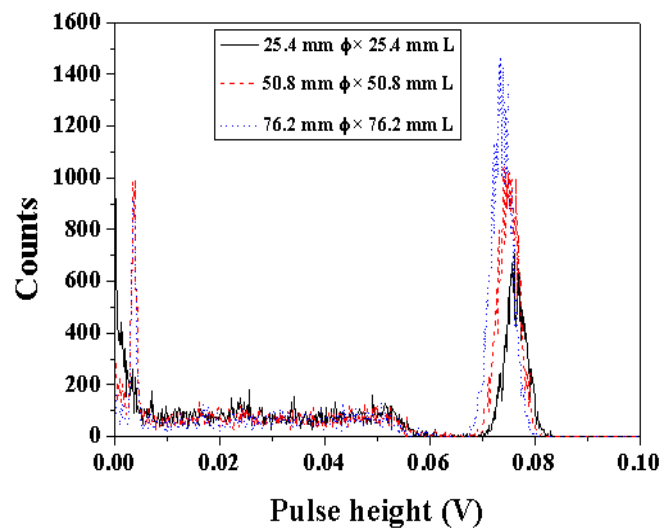


Figure 3.16: Comparison of simulated spectra with ^{137}Cs for 25.4 mm $\phi \times$ 25.4 mm L, 50.8 mm $\phi \times$ 50.8 mm L and 76.2 mm $\phi \times$ 76.2 mm L cylindrical CsI(Tl) scintillators [166].

The first of these is because with an increase of the volume of the scintillator, the energy deposition by the incident gamma photons increases, and therefore, there is a better chance of full-energy deposition. On the other hand, the gamma photons are incident on the front surface of the scintillator, and therefore, the optical photons are predominantly generated near this surface. For a longer scintillator, these generated optical photons have to travel longer distances through the scintillator, and therefore, undergo more number of reflections at the

scintillator-reflector interface, before they can reach the coupled photodetector. Because of the greater extent of loss of optical photons due to reflections for a longer scintillator, therefore, the light collection at the photodetector becomes correspondingly poorer. This explains why the *PPH* slightly decreases with increasing size of the scintillator. It is important to mention here that the bulk absorption of optical photons within the scintillator was not considered in simulation. In fact, the bulk absorption length was taken to be 5 m, which is much larger than the largest dimension of the scintillator, as mentioned in Section 3.2.3. For even larger dimensions of scintillator, however, the bulk absorption may play an important role in reducing the number of optical photons reaching the photodetector, and, consequently, the *PPH*. The impact of the shape of the scintillator on the pulse-height spectrum may be an useful further study [166].

Subsequently, in order to see the effect of the size of the scintillator on the simulated spectra for a higher gamma energy, spectra were generated by simulation with the source at serial number 4 of Table 3.1 (^{208}Tl). ^{208}Tl is a naturally occurring radioisotope of Tl with a gamma energy of 2614 keV, and a progeny of the ^{232}Th decay series. The comparison of the simulated spectra with ^{208}Tl for the three sizes of the scintillator is presented in Figure 3.17. It is clear from Figure 3.17 that the 2614 keV photopeak efficiency is considerably less for the 25.4 mm $\phi \times 25.4$ mm L scintillator, as compared to the other two. This is because the 25.4 mm $\phi \times 25.4$ mm L scintillator is too small to offer good enough photoelectric absorption probability at 2614 keV. It can also be seen from Figure 3.17 that the *PPH* at 2614 keV decreases slightly as the size of the scintillator increases. This behavior is similar to that at 662 keV.

Table 3.5 presents the values of energy resolution at 662 keV and 2614 keV for the three sizes of the scintillator. It is clear from Table 3.5 that the energy resolution at both the energies is more or less independent of the size of the scintillator. It is to be noted, however,

that if the dimensions of the scintillator are increased so much that the bulk absorption of optical photons within the scintillator can no longer be neglected, or if the reflectivity of the scintillator-reflector interface is reduced, or if the shape of the scintillator is changed so as to make the light collection geometry more complex, the energy resolution may vary considerably with size of the scintillator [166].

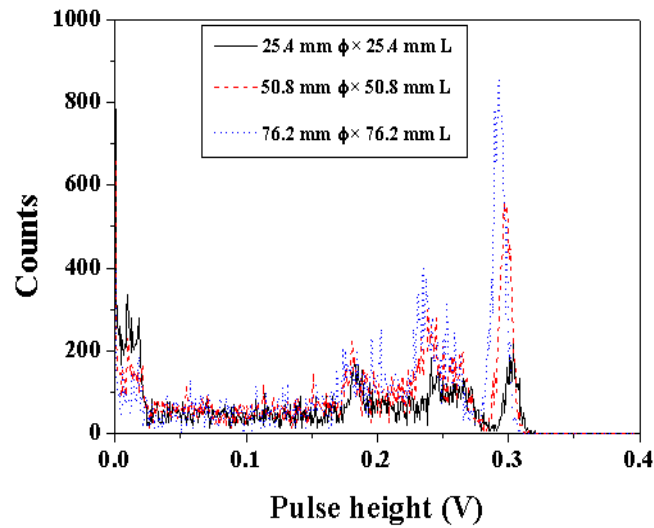


Figure 3.17: Comparison of simulated spectra with ^{208}Tl for 25.4 mm $\phi \times$ 25.4 mm L, 50.8 mm $\phi \times$ 50.8 mm L and 76.2 mm $\phi \times$ 76.2 mm L cylindrical CsI(Tl) scintillators [166].

Table 3.5: Values of energy resolution at 662 keV and 2614 keV for different dimensions of the CsI(Tl) scintillator [166].

Scintillator dimension	Energy resolution (%)	
	662 keV	2614 keV
25.4 mm $\phi \times$ 25.4 mm L	6.31	3.60
50.8 mm $\phi \times$ 50.8 mm L	6.29	3.44
76.2 mm $\phi \times$ 76.2 mm L	6.35	3.73

3.8 Conclusion

In this chapter, it was shown how Monte Carlo simulation including optical photon transport could provide valuable information about the parameters that influence the pulse-height spectra from scintillator based gamma spectrometers. For the studied scintillator-photodetector assembly, it was observed that the scintillation yield and the resolution scale of

the scintillator, the reflectivity of the scintillator-reflector interface and the efficiency of the photodetector were the most impactful parameters. Useful analytical relationships between these simulation parameters and the energy resolution as well as the peak-pulse-height of the simulated spectra were also obtained. On the other hand, parameters such as surface finish, surface roughness and reflection type were found to have relatively lesser impacts on the pulse-height spectra.

These results are likely to facilitate the design of scintillator based gamma spectrometers by acting as a guide to choose the favorable properties of the scintillator-photodetector assembly for the particular application under consideration. Although developed and experimentally validated for CsI(Tl), the simulation model is quite generic and can be extended to another scintillator by substituting appropriate parameters for the specific scintillator and thereafter validating the model experimentally [166].

SIMULATION STUDIES ON GGAG:Ce AND GGAG:Ce,B

4.1 Introduction

The Ce-activated $\text{Gd}_3\text{Ga}_3\text{Al}_2\text{O}_{12}$ single crystal (GGAG:Ce) is a new scintillator material, reported for the first time in the year 2011 [89], [207]. It belongs to the class of the Ce-doped rare earth aluminum garnets, which are typically characterized by a high scintillation yield combined with a fast decay time, owing to the allowed 5d-4f electronic transitions within the Ce-activator states. Besides, this scintillator has a high gamma ray absorption coefficient due to its high density (6.67 g/cm^3 [94]) and high Z_{eff} (55) [92], [100], [208]. It is also rugged, non-hygroscopic, has high radiation hardness and is free from internal radioactive contamination [209]. It has a scintillation emission spectrum that peaks at nearly 530 nm, as measured experimentally and presented in Section 2.2, and also reported in [91], [157], [207], [210], [211]. Therefore, like CsI(Tl), GGAG:Ce can also be coupled with silicon based photodetectors for improved performance than with PMTs.

Since the discovery of GGAG:Ce by Kamada *et al.* [89], [90], [207], [210], [212], several groups of researchers have reported many of its properties and applications. Its scintillation yield has been variously reported in the range 33,000-55,000 photons/MeV [89], [91], [92], [94], [157], [207], [208], [210], [212]. The decay times for gamma irradiation also have been shown to vary in the range 42-127 ns (fast component) and 158-595 ns (slow component) [89], [91], [92], [157], [211]–[213]. It is understood that as the Ce-doping concentration increases beyond 1 at% with respect to Gd, the light yield decreases due to concentration quenching of Ce. Due to the same reason, the decay times, on the other hand, also decreases [89]. Crystals with a nominal Ce concentration of 0.2 at% with respect to Gd have been most widely grown and studied, for which a scintillation yield of about 46,000

photons/MeV and decay times of about 52 ns (fast, nearly 73%) and 282 ns (slow, nearly 27%) are more or less agreed upon [89], [207]. It can be mentioned, however, that the ambiguities in the values of the scintillation yield and the decay times are still present, and generally varies from one sample to another.

Co-doping GGAG:Ce with B^{3+} and Ca^{2+} ions has resulted in crystals with varied properties. For example, it has been observed that B^{3+} co-doping increases the scintillation yield but also increases the decay times [94], [98]. On the other hand, Ca^{2+} co-doping decreases both [94]–[96], [98]. For gamma spectrometry applications, therefore, where the requirement of a superior energy resolution is at a premium, the boron co-doped scintillator should be preferred. On the other hand, for fast timing and/or high counting rate applications, the calcium co-doped scintillator could be a better choice.

Further, post growth annealing at oxidizing environment has shown to increase the scintillation yield and decrease the decay times of these scintillators due to the elimination of the oxygen vacancies that result from the crystals being grown in an inert atmosphere [98], [157]. Further, if these crystals are kept in dark for long times, their scintillation yield decreases due to emptying of room temperature trap centers. Heating the scintillators also results in the same behavior. Exposure to ambient light increases the scintillation yield [98].

Monte Carlo simulation based optimization may help in the planning of future experiments as well as in the design of gamma spectrometers based on these relatively new versatile scintillators. However, Not many Monte Carlo based studies have been carried out for this scintillator so far, apart from the efficiency studies as reported in [208]. Therefore, in the present study, the development of a GEANT4 based Monte Carlo simulation model for these crystals including optical transport has been attempted. The following sections of this chapter describe the details of the simulation studies and their results.

4.2 Simulation studies on a 2" ϕ \times 2" L GGAG:Ce scintillator

4.2.1 Simulation methodology

The simulation methodology presented here is similar to that reported in Section 3.2 for CsI(Tl). Therefore, only those parameters which are different for GGAG:Ce are discussed in detail.

The simulation model was built to match the experimental assembly consisting of a GGAG:Ce cylindrical single crystal scintillator with nominal dimensions 2" ϕ \times 2" L (50.8 mm ϕ \times 50.8 mm L) (Make: Epic Crystals [209]). Some of the parameters of the scintillator, available from the manufacturer's website, are summarized in Table 4.1.

Table 4.1: Some parameters of the GGAG:Ce scintillator (Make: Epic Crystals [209]) used for experiments and modeled in simulation.

Parameter	Value
Density	6.6 g/cm ³
Refractive index	1.9
Scintillation yield	42,000 photons/MeV
Decay time	90 ns
Emission wavelength (max)	530 nm
Hygroscopic	No
Self radiation	No

The simulation geometry was same as that depicted in Figure 3.1, except for the fact that the CsI(Tl) scintillator crystal would be replaced by GGAG:Ce. Only the sources at serial numbers 1 and 2 of Table 3.1 were used for the simulations reported herein.

The modeled scintillator crystal was Gd₃Ga₃Al₂O₁₂:Ce with a Ce-doping concentration of 0.2 at% with respect to Gd. The actual Ce concentration of the scintillator used for experiments was not mentioned by the manufacturer. The approximate Ce concentration was therefore taken to be equal to that of the in-house grown crystals, i.e., 0.2 at% (see Table 2.1). The Ce-doping concentration affects the scintillation yield and the decay times of the scintillator, as described in Section 4.1. However, as long as these parameters are accurately incorporated into the simulation, uncertainties in modeling the doping concentration should not

affect the results. The doping concentration may, on the other hand, influence the radiation transport calculations. However, the associated error should be negligible as long as the modeled Ce concentration is of the same order of magnitude as the actual Ce concentration. The density of the scintillator was taken to be 6.6 g/cm^3 , as per Table 4.1. The photodetector, reflector, and the detector enclosure were modeled exactly like those mentioned in Section 3.2.2.

As the scintillation emission spectrum of the GGAG:Ce scintillator was not available from the manufacturer, the experimentally measured emission spectrum of GGAG:Ce,B, presented in Figure 2.9, was incorporated into the program after normalizing and converting it into the energy scale, and finally storing 32 normalized intensity values against the 32 photon energy values, as per the scheme suggested in Section 3.2.3. This assumption could be made because Tyagi *et al.* [98] have shown that boron co-doping does not alter the emission spectrum of GGAG:Ce. As only one decay time constant was mentioned by the manufacturer, the emission spectrum was not separated into the fast and the slow components. Rather, it was implemented as a single (fast) component with a decay time of 90 ns (see Table 4.1) and yield ratio 1 (see Section 2.3.2.2.2). The refractive index of GGAG:Ce was taken to be 1.91 at all the 32 energy points, as per Table 4.1. The values of the (bulk) absorption length, Rayleigh scattering length and Mie scattering length were taken to be same as those of CsI(Tl). The scintillation yield of GGAG:Ce was taken to be 42,000 photons/MeV, as per Table 4.1. The resolution scale was taken to be 1. Scintillation and optical properties of the photodetector and the reflector were same as mentioned in Section 3.2.3.

The value of the Birks' constant for GGAG:Ce is not available in literature. Avdeichikov *et al.* [197] have reported the values of this parameter for CsI(Tl), GSO:Ce and BGO, which are 1.52×10^{-3} , 5.25×10^{-3} and $6.50 \times 10^{-3} \text{ mm/MeV}$, respectively. Balcerzyk *et al.* [66] have shown that the nonproportionality characteristics of the oxyorthosilicates,

namely, YSO:Ce, LSO:Ce and GSO:Ce, are similar and the scintillation response of these crystals is known to be rather nonproportional [1]. It is shown in [1] that the nonproportionality behavior of GSO:Ce and BGO are nearly identical, whereas the scintillation response of LSO:Ce is further nonlinear at low energies. On the other hand, Iwanowska *et al.* [91] have shown that the nonproportionality characteristics of GGAG:Ce is similar to that of LSO:Ce at energies above 100 keV, whereas at lower energies the light output of GGAG:Ce is slightly less nonproportional than LSO:Ce. Also, it is evident from the data presented in [214] that the values of Birks' constant for undoped crystalline inorganic scintillators is generally higher than those for the doped ones. Therefore, it can be expected that the value of Birks' constant is somewhere close to that of GSO:Ce. This parameter was varied from 1.52×10^{-3} (equal to that of CsI(Tl)) to 1.52×10^{-2} mm/MeV (typical of a highly nonproportional scintillator) but there was no observable change in the simulated spectra. Therefore, the value of 1.52×10^{-3} mm/MeV (same as that of CsI(Tl)) was chosen for GGAG:Ce.

All the surface properties mentioned in Section 3.2.4 were unchanged, including the efficiency of the scintillator-photodetector interface, which was taken to be, $\eta = 0.05$, because the emission spectra of both CsI(Tl) and GGAG:Ce (or, for that matter, GGAG:Ce,B) peak at nearly the same wavelength, as can be seen from Figures 2.8 and 2.9.

The procedure for scoring and generation of simulated spectra were same as those mentioned in 3.2.5.

4.2.2 Energy calibration by simulation

The procedure for energy calibration was identical to that presented in Section 3.3. Figure 4.1 (a) shows the simulated spectrum in pulse-height scale (according to Equation (3.4)) with the source at serial number 1 of Table 3.1, along with the derived energy calibration. Figure 4.1 (b) shows the same spectrum converted to energy scale.

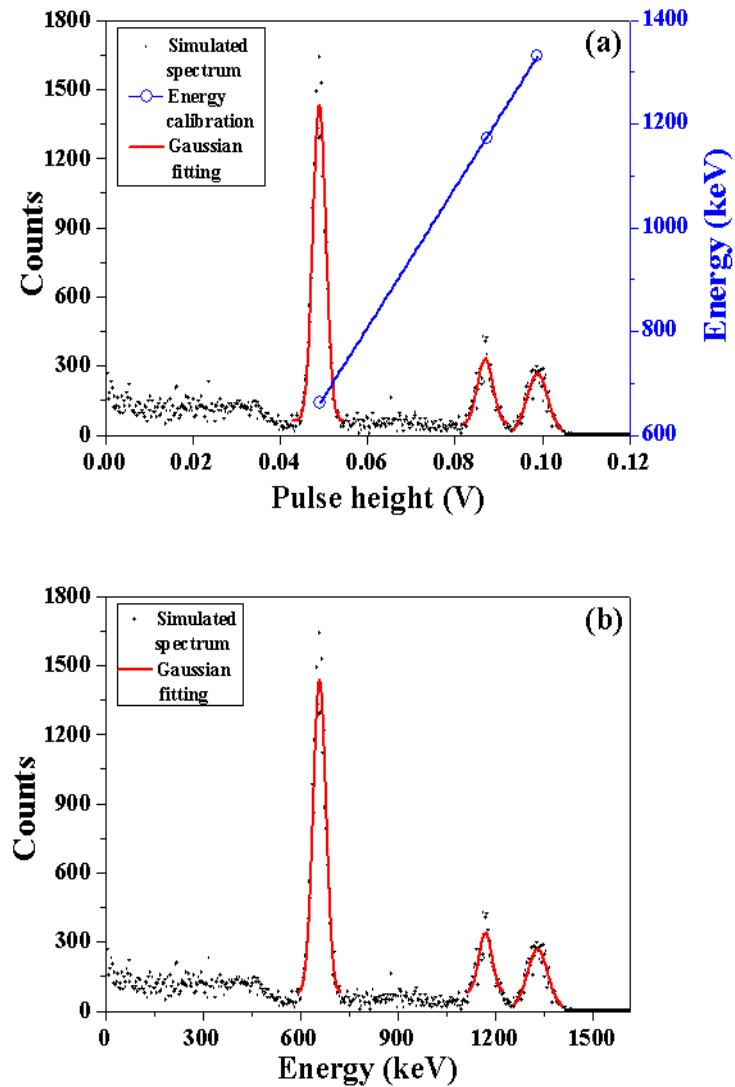


Figure 4.1: (a) Simulated spectrum for a 50.8 mm $\phi \times$ 50.8 mm L cylindrical GGAG:Ce scintillator using the source at serial number 1 of Table 3.1, along with the derived energy calibration, (b) The same spectrum converted to energy scale.

4.2.3 Experimental measurements

One of the flat surfaces of the 2" $\phi \times$ 2" L cylindrical GGAG:Ce scintillator crystal (Make: Epic Crystals [209]) was hand-polished with suitable sand-papers to clear optical finish, whereas all other surfaces were ground. The polished surface was optically coupled to a 2" ϕ Hamamatsu R1306 PMT [200] by using a transparent optical grease (Dow Corning). Wrapping

with Teflon reflector was done similarly as described in Section 3.4. The scintillator-PMT assembly was enclosed in the same light-tight aluminum casing as described in Section 3.4.

The anode pulse of the PMT was fed to a CAEN DT5790M dual digital pulse analyzer [215]. HV of 1000 V was also provided to the PMT from DT5790M. Energy spectra were generated by digital pulse processing (DPP) and acquired on a desktop via the data acquisition (DAQ) software CoMPASS [216].

^{137}Cs and ^{60}Co test sources were used for the experiments. During all the experiments, the sources were placed at a distance of 300 mm from the front surface of the aluminum casing. All spectra, including those of background, were recorded for an acquisition time of 100 s.

4.2.4 Experimental energy calibration

Background subtracted experimental spectrum acquired with $^{137}\text{Cs} + ^{60}\text{Co}$ test sources is shown in Figure 4.2 (a). Using similar procedure as described in Section 3.5, experimental energy calibration was carried out. The spectrum of Figure 4.2 (a), converted to energy scale, is shown in Figure 4.2 (b).

4.2.5 Experimental validation of the simulation model

Figure 4.3 presents the comparison of the spectrum generated by simulation using the ^{137}Cs source of Table 3.1 and the background subtracted experimentally recorded spectrum with the ^{137}Cs test source. The values of energy resolution at 662 keV for the two spectra, calculated using Equation (1.10), are also shown in Figure 4.3. It can be seen from Figure 4.3 that there is a good matching between the two spectra near the 662 keV full-energy peak regions.

The mismatch of the energy resolution values between the simulated and the experimental spectra, as well as the systematic underestimation by the simulation model in the Compton and backscatter regions, compared to those regions of the simulated spectrum, may be due to the factors described in Section 3.6.1.

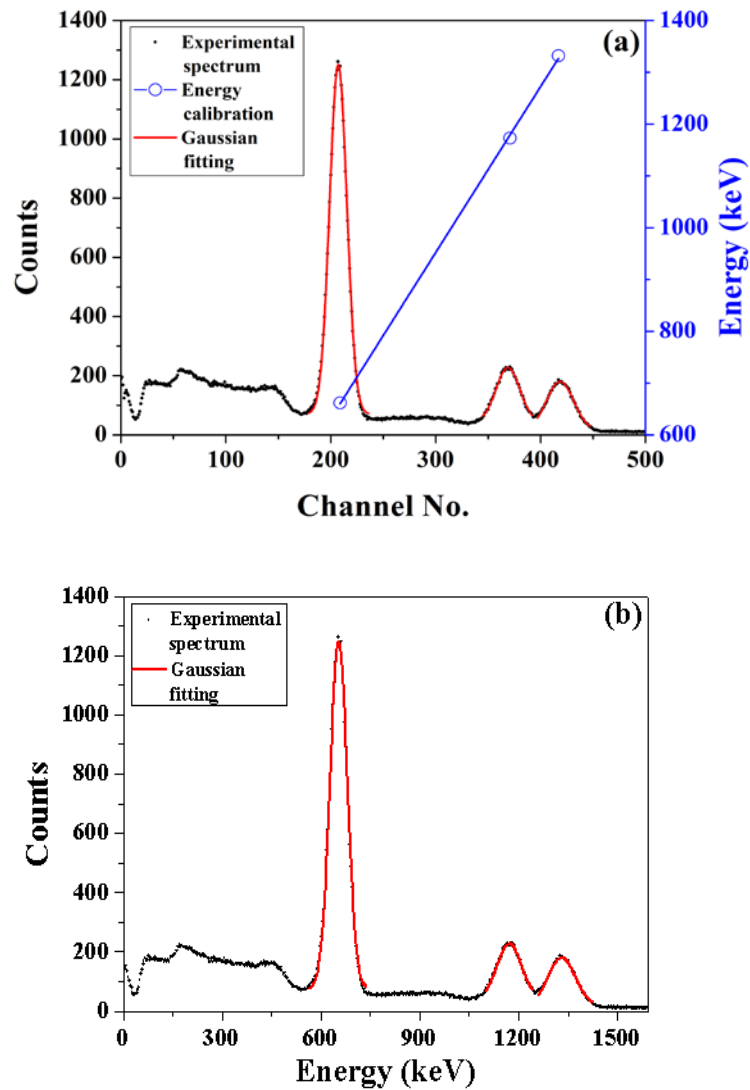


Figure 4.2: (a) Experimentally acquired spectrum of $^{137}\text{Cs} + ^{60}\text{Co}$ source with a 50.8 mm $\phi \times$ 50.8 mm L cylindrical GGAG:Ce scintillator, along with the derived energy calibration, (b) The same spectrum converted to energy scale.

The matching of the simulated and the experimental spectra near the full-energy peak regions of Figure 4.3, however, ensures that the simulation model can be used to find the optimized design of future GGAG:Ce-photodetector assemblies by investigating the effect of the various scintillation, optical, physical and surface parameters on the simulated spectra.

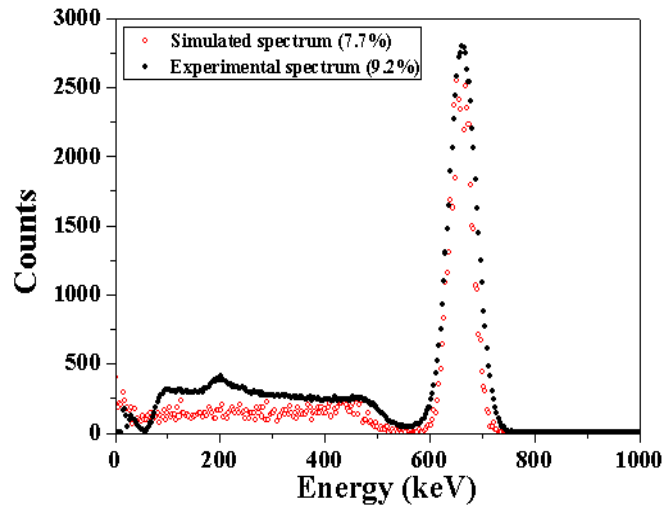


Figure 4.3: Comparison of experimental and simulated spectra of ^{137}Cs for a 50.8 mm $\phi \times$ 50.8 mm L cylindrical GGAG:Ce scintillator.

4.3 Simulation studies on small GGAG:Ce,B scintillators

4.3.1 Simulation methodology

A cubic GGAG:Ce,B scintillator crystal with dimensions of $10 \times 10 \times 10 \text{ mm}^3$ was modeled in GEANT4. Figure 4.4 shows a schematic diagram of the yz plane cross-section of the simulation geometry along with the reference coordinate system [168]. The scintillator was coupled to a photodetector with active area of $10 \times 10 \text{ mm}^2$ and thickness 0.3 mm. These are the typical dimensions of a silicon photodiode. The scintillator-photodetector assembly was coated with a 1 mm thick reflector.

The size of the scintillator was subsequently changed to $18 \times 18 \times 10$, $18 \times 18 \times 18$, and $18 \times 18 \times 25 \text{ mm}^3$, keeping the active area of the photodetector always equal to the surface area of the scintillator. A parallel beam of gamma photons was modeled to be incident on the top surface of the scintillator along the negative z-direction and always entirely covering this surface. The energies of the incident gamma photons were sampled according to the source at serial number 2 (^{137}Cs) of Table 3.1.

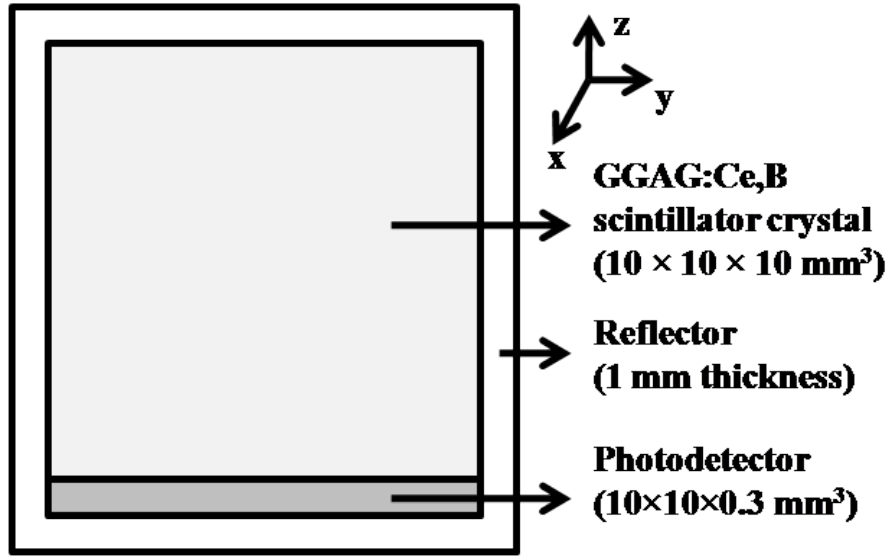


Figure 4.4: Schematic diagram of the yz plane cross-section of the simulation geometry consisting of a $10 \times 10 \times 10 \text{ mm}^3$ cubic GGAG:Ce,B scintillator crystal, along with the reference coordinate system (Figure not to scale) [168].

The GGAG:Ce,B material, assigned to the scintillator crystal in Figure 4.4, had Ce and B doping concentrations of 0.2 at% each with respect to Gd, as is typical for the GGAG:Ce,B single crystals grown in-house by the CZ technique (see Table 2.1). Its density was taken to be 6.67 g/cm^3 , as mentioned in [94]. The materials assigned to the photodetector and the reflector were same as those described in Section 3.2.2.

The experimentally measured emission spectrum of GGAG:Ce,B (see Figure 2.9) was implemented into the program in a way similar to that described in Section 3.2.3. The normalized emission intensity as a function of wavelength is shown in Figure 4.5, whereas Figure 4.6 shows the same as a function of energy. The energy scale corresponding to the wavelength range 200-900 nm was converted to 32 points. For the GGAG:Ce,B crystals grown in-house by the CZ technique, described in Section 2.1.3.4, the values of τ_1 , τ_2 , A_1 and A_2 of Equation (3.1) were experimentally determined and reported in [92]. These values are $\tau_1 = 61 \text{ ns}$, $\tau_2 = 488 \text{ ns}$, $A_1 = 0.77$ and $A_2 = 0.23$. Using these, Q_1 and Q_2 of Equations (3.2) and (3.3) were calculated. Subsequently, each of the 32 normalized emission intensities

corresponding to the 32 energy points was divided into the fast and the slow components according to the ratio Q_1/Q_2 .

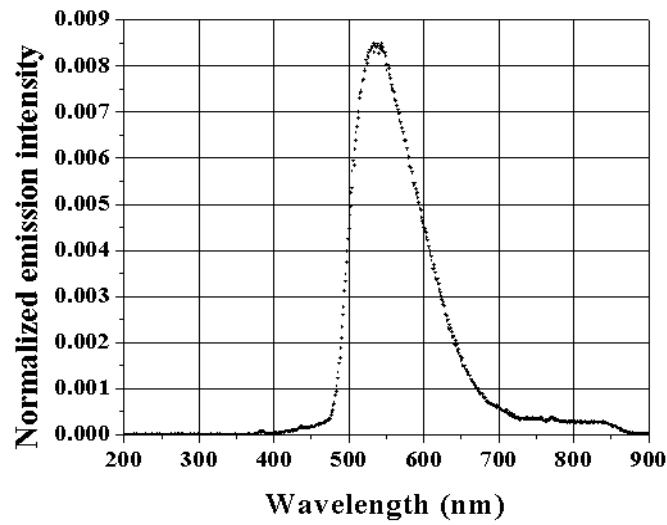


Figure 4.5: Normalized emission spectrum of GGAG:Ce,B.

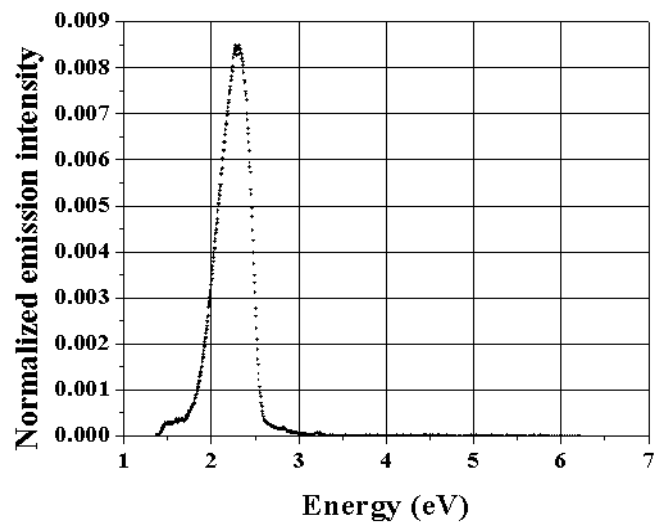


Figure 4.6: Normalized emission spectrum of GGAG:Ce,B as a function of photon energy.

The material GGAG:Ce,B was assigned a refractive index of 1.9 at all the 32 energy points, i.e., throughout its own emission wavelength regime. The values of the (bulk) absorption length, Rayleigh scattering length and Mie scattering length were taken to be same as that of CsI(Tl). The scintillation yield of GGAG:Ce,B was taken to be 46,000

photons/MeV. The resolution scale was taken to be 1. Scintillation and optical properties of the photodetector and the reflector were same as mentioned in Section 3.2.3.

The value of the Birks' constant for GGAG:Ce,B was taken to be 1.52×10^{-3} mm/MeV due to the same reasons as described in Section 4.2.1. All the surface properties mentioned in Section 3.2.4 were unchanged, except for the efficiency of the scintillator-photodetector interface, which was taken to be $\eta = 0.90$, which is close to the typical value for a silicon photodiode. The procedure for scoring and generation of simulated spectra were same as those mentioned in Section 3.2.5, except for the fact that the value of the gain of the photodetector (G) in Equation (3.4) was taken to be equal to that of a photodiode, i.e., unity.

4.3.2 Impact of size of the scintillator on simulated spectra

Figure 4.7 [168] shows the comparison of the simulated spectra with ^{137}Cs for the four sizes of the scintillator, as mentioned in Section in 4.3.1. The values of energy resolution at 662 keV and the corresponding PPH of the scintillators of different sizes, derived from Figure 4.7, are presented in Table 4.2.

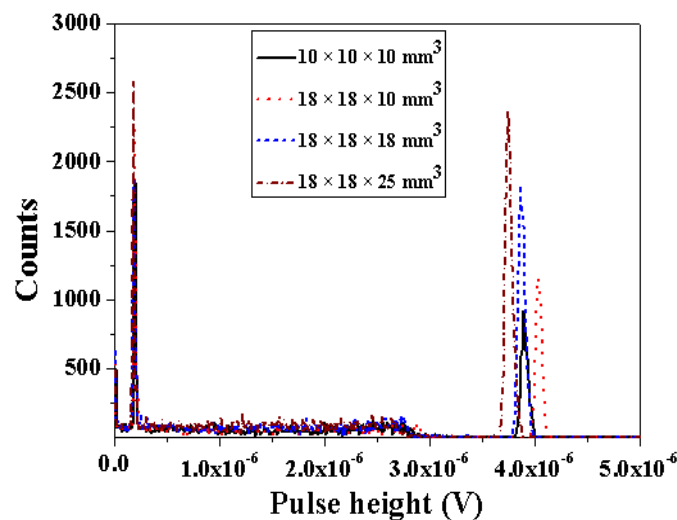


Figure 4.7: Comparison of simulated spectra with ^{137}Cs for $10 \times 10 \times 10$, $18 \times 18 \times 10$, $18 \times 18 \times 18$, and $18 \times 18 \times 25$ mm³ GGAG:Ce,B scintillators [168].

Table 4.2: Energy resolution and *PPH* at 662 keV for different dimensions of the GGAG:Ce,B scintillator.

Size (mm ³)	Energy resolution (%) at 662 keV	<i>PPH</i> (V) at 662 keV
10 × 10 × 10	2.02	3.90290 × 10 ⁻⁶
18 × 18 × 10	1.70	4.04409 × 10 ⁻⁶
18 × 18 × 18	2.01	3.87998 × 10 ⁻⁶
18 × 18 × 25	2.02	3.75495 × 10 ⁻⁶

It is evident from Figure 4.7 as well as Table 4.2 that the *PPH* at 662 keV is higher for the 18 × 18 × 10 mm³ scintillator compared to the 10 × 10 × 10 mm³ scintillator. This is because of the fact that the higher detection volume of the former results in higher average energy deposition by the incident gamma photons, and consequently, higher *PPH*. It is also visible from Figure 4.7 that the photopeak efficiency of the former is also slightly higher. This is because with an increase in the volume of the scintillator, there is also a better chance of full-energy deposition by the incident gamma photons.

On the other hand, among the three scintillators having a top surface area of 18 × 18 mm², the *PPH* is highest for the shortest scintillator, i.e., the one with dimensions 18 × 18 × 10 mm³. For a longer scintillator, the optical photons have to travel longer distances through the scintillator, and therefore, undergo more number of reflections at the scintillator-reflector interface, before they can reach the coupled photodetector. Because of the greater extent of loss of optical photons due to reflections for a longer scintillator, therefore, the light collection at the photodetector becomes correspondingly poorer. This explains why the *PPH* decreases with increasing height of the scintillator. The *PPH* is expected to decrease even more if the reflectivity of the scintillator-reflector interface decreases. It is important to mention here that the bulk absorption of optical photons within the scintillator was not considered in simulation. In fact, the bulk absorption length was taken to be 5 m, which is much larger than the largest dimension of the scintillator.

It is also clear from Table 4.2 that the energy resolution deteriorates as the height of the scintillator increases. This is due to increasingly poorer light collection for the longer scintillators. Comparing the spectra from the $10 \times 10 \times 10 \text{ mm}^3$ and the $18 \times 18 \times 18 \text{ mm}^3$ scintillators, it is clear that the increase in size increases the photopeak efficiency, without significantly affecting the energy resolution or the *PPH* at 662 keV.

It is, however, important to note that the values of energy resolution presented in Table 4.2 may not be experimentally realizable if the scintillator is coupled to a photodiode. This is due to the additional factors that contribute to the broadening of the peaks in an experimental spectra (see Section 1.3.3.2.1), especially the noise in the photodiode that reduces the SNR significantly (see Section 1.2.3.1.3 and Section 3.7.1) [168].

4.4 Conclusion

In this chapter, a Monte Carlo simulation model including optical transport was built and experimentally validated for a commercially available GGAG:Ce scintillator. This model can be used for studying the influence of various parameters on the resulting pulse-height spectra, as was done in Chapter 3 for the CsI(Tl) scintillator. Being a new scintillator, however, some of the parameters for GGAG:Ce are not available from literature and some other parameters also have a lot of ambiguity in their reported values. In the present study, therefore, the values of these debatable parameters were approximated. The developed simulation model may be improved by incorporating more accurate parameter values as and when they are available.

The model was also extended to accommodate small GGAG:Ce,B scintillators. The impact of the size of the scintillator on simulated spectra was also investigated. It was observed that an increase in the height-to-surface area ratio of cuboid shaped scintillators generally resulted in poorer spectra due to less efficient light collection at the photodetector in case of longer scintillators.

SIMULATION STUDIES ON LIGHT GUIDES

5.1 Introduction

A light guide is usually employed between a scintillator and a photodetector when the former cannot be directly coupled to the latter. For example, when the size and/or shape of the scintillator does not match with those of the photodetector, or, in the particular case of PMTs, when the scintillator must be placed in a magnetic field but the PMT has to be kept away in order to shield it from the magnetic field, or when the light from a thin scintillator must be dispersed throughout the photocathode in order to avoid degradation of energy resolution arising from local fluctuations of the photocathode deposition thickness, a light guide becomes a useful component of the scintillator based detector assembly [1].

Light guides are optically transparent solids with polished surfaces and are usually coated with reflectors [1]. Their design usually promotes total internal reflection of light photons. A good light guide material has to have (i) good optical clarity, (ii) good mechanical properties so that it can be easily made in different shapes and sizes, and (iii) very little natural scintillation response of its own to ionizing radiation [217]. Poly(methyl methacrylate), or PMMA [218], also referred to as Acrylic and having different trade names like Lucite, Perspex, Plexiglas, Rohaglas, etc., is the most widely used light guide material. It is a transparent plastic with a refractive index of 1.49-1.51 [1], [217] and can be easily manufactured in complex shapes in order to provide a smooth transition between surfaces of scintillators and those of photodetectors. Another popular light guide material is quartz, which also has similar properties.

It must be remembered that any light guide which has a larger cross-sectional area on the scintillator end than on the photodetector end must result in some loss of optical

photons. This is due to the fact that the flux of optical photons per unit area per unit solid angle at any point inside the light guide can never be greater than that at its input [1]. For an unchanged cross-sectional area of the light guide throughout its length, however, it is theoretically possible to collect all the photons from a scintillator to a photodetector of equal or larger cross-sectional area.

A suitably designed light guide can help in efficient light collection from a larger scintillator to a smaller photodetector. With this motivation, a GEANT4 based Monte Carlo simulation model was developed to study the impact of incorporation of light guides between larger scintillators and smaller photodetectors on the resulting gamma ray pulse-height spectra. For the scintillators CsI(Tl) and GGAG:Ce, whose emission spectra are better matched with silicon based photodetectors than with PMTs, this study can be useful because the silicon based photodetectors are limited to sizes of only up to a few cm², whereas scintillators with much bigger sizes are usually required for gamma spectrometry.

5.2 Simulation studies on trapezoidal PMMA light guides

5.2.1 Simulation methodology

5.2.1.1 Detector geometry

Figure 5.1 depicts a simplified schematic diagram of the simulation geometry. A cuboid shaped CsI(Tl) single crystal scintillator with dimensions 2" × 2" × 2" (50.8 × 50.8 × 50.8 mm³) was coupled to a trapezoidal PMMA light guide, which, in turn, was coupled to a photodetector with dimensions 10 × 10 × 0.3 or 18 × 18 × 0.3 mm³. These are the dimensions of the Hamamatsu S3590-08 [191] and S3204-08 [219] silicon photodiodes, respectively. The cross-sectional area of the surface of the light guide that was coupled to the scintillator was equal to that of the scintillator surface area, i.e., 50.8 × 50.8 mm², whereas that of the surface coupled to the photodetector was always equal to surface area of the photodetector, i.e., 10 × 10 or 18 × 18 mm². The height of the light guide was varied (10, 20 or 30 mm) in order to see

its effect on the simulated spectra. The entire assembly shown in Figure 5.1 was coated with a 1 mm thick Teflon reflector. The outer enclosure to this assembly was made up of aluminum that had a thickness of 0.5 mm at the bottom surface and 1 mm elsewhere. The reflector and the aluminum enclosure are not shown in Figure 5.1 for clarity.

The whole assembly was placed in air. A parallel beam of gamma photons was modeled to be incident perpendicularly on the bottom surface of the scintillator and entirely covering this surface. The energies of the incident gamma photons were sampled according to the source at serial number 2 (^{137}Cs) of Table 3.1.

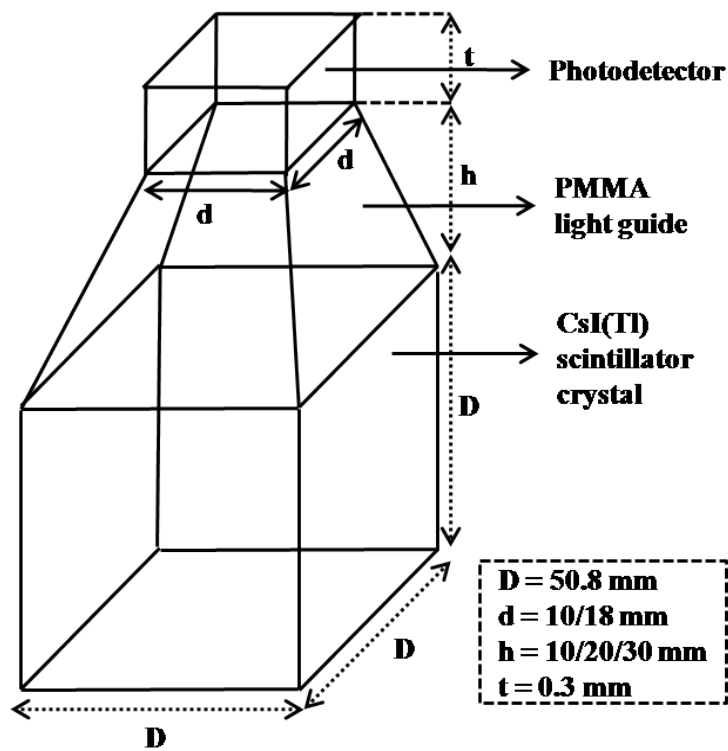


Figure 5.1: Schematic diagram of the simulation geometry consisting of a $50.8 \times 50.8 \times 50.8$ mm³ cuboid shaped CsI(Tl) scintillator crystal, coupled to a $10 \times 10 \times 0.3$ or $18 \times 18 \times 0.3$ mm³ photodetector through a trapezoidal PMMA light guide. The Teflon reflector and the outer aluminum enclosure are not shown for clarity (Figure not to scale).

5.2.1.2 Material properties

All properties of the materials CsI(Tl), Teflon, photodetector and aluminum were same as those presented in Section 3.2.2. The PMMA light guide region of Figure 5.1 was assigned the material Plexiglas, available in GEANT4. This material has an assigned density of 1.19 g/cm^3 [164], which also matches that of commercially available PMMA light guides [217].

5.2.1.3 Scintillation and optical properties

Scintillation and optical properties of all materials except PMMA were identical to those mentioned in Section 3.2.3. At each of the 32 energy points, the refractive index of PMMA was calculated from [220] and implemented into the program. The values of the (bulk) absorption length, Rayleigh scattering length and Mie scattering length were taken to be same as those of CsI(Tl).

5.2.1.4 Surface properties

The scintillator-reflector interface was modeled exactly as that described in Section 3.2.4. The scintillator-light guide interface was modeled to be a dielectric-dielectric type of surface with surface finish P, surface roughness, $\sigma_\alpha = 0^\circ$ (implicit), reflectivity, $R = 0$, reflection type = L (implicit), and efficiency, $\eta = 0$. It is to be noted that as $R = 0$, there is no reflection from this surface and therefore, the reflection type becomes unimportant. The light guide-reflector interface was modeled to be a dielectric-dielectric type of surface with surface finish PFP, surface roughness, $\sigma_\alpha = 0^\circ$ (implicit), reflectivity, $R = 0.98$ [199], reflection type = SL, and efficiency, $\eta = 0$. The light guide-photodetector interface was modeled to be a dielectric-metal type of surface with surface finish P, surface roughness, $\sigma_\alpha = 0^\circ$ (implicit), reflectivity, $R = 0$ reflection type = SL [180] (for the surface finish P, SL is equivalent to SS, but as $R = 0$, the reflection type does not matter) and efficiency, $\eta = 0.8267$. This value of η is equal to the *QE* of the Hamamatsu S3590-08 [191] and S3204-08 [219] silicon photodiodes at $\lambda = 540 \text{ nm}$.

5.2.1.5 Scoring

The procedure for scoring and generation of simulated spectra were same as those mentioned in Section 3.2.5, except for the facts that the optical photons generated in the scintillator were now transported up to the light guide-photodetector interface and the number of optical photons detected at this interface (n_{ph}) was treated as the pulse-height with arbitrary units.

5.2.2 Impact of surface area of the photodetector and height of the light guide on simulated spectra

The comparison of the simulated spectra with ^{137}Cs for the different heights of the light guide and the $10 \times 10 \times 0.3 \text{ mm}^2$ photodetector is presented in Figure 5.2. Figure 5.2 shows that the best spectrum, both in terms of energy resolution and *PPH* at 662 keV, is obtained for $h = 20$ mm. Therefore, when a scintillator with a specific exit surface area needs to be coupled with a photodetector with a specific area through a light guide, the best results are obtained for an optimum height of the light guide. This optimum height maximizes the light collection and increases the pulse-height as well as improves the energy resolution.

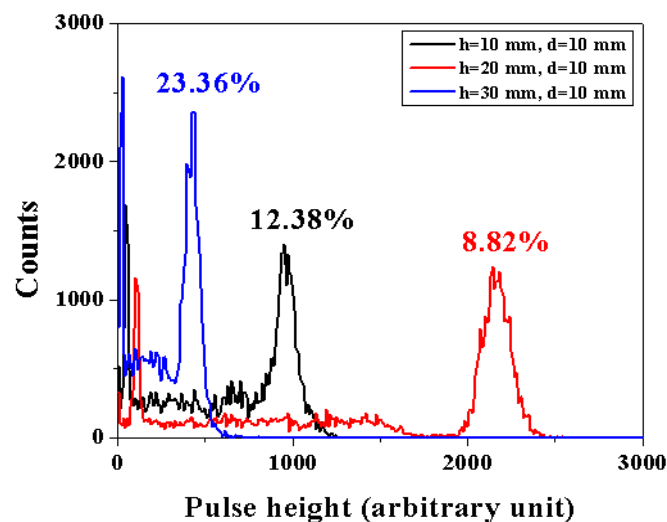


Figure 5.2: Comparison of the simulated spectra with ^{137}Cs for different heights (10, 20 and 30 mm) of the light guide and the $10 \times 10 \times 0.3 \text{ mm}^3$ photodetector.

The fact that the best spectrum is obtained with $h = 20$ mm may be explained with the help of Figure 5.3.

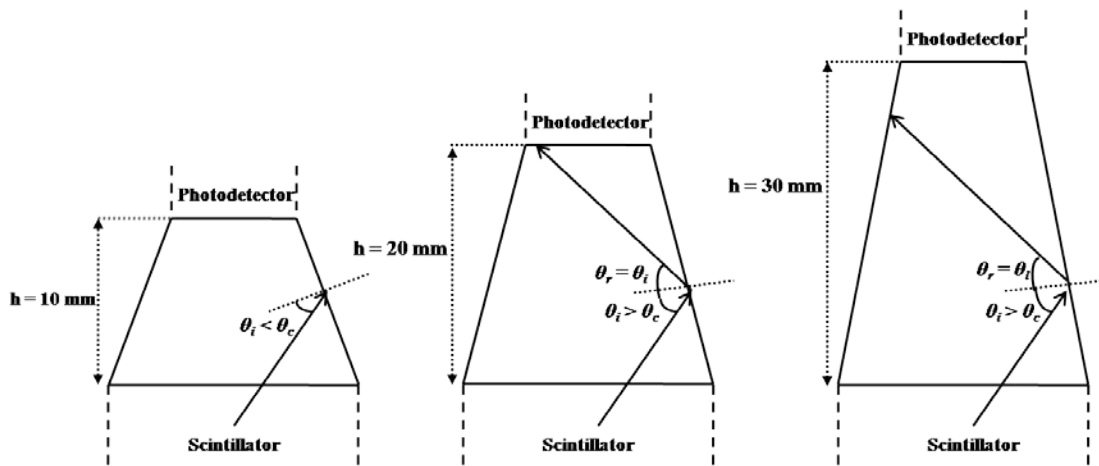


Figure 5.3: Representative light paths for different heights (10, 20 and 30 mm) of the light guide.

As h increases, the transverse inner surfaces of the light guide become flatter. Therefore, the angle of incidence (θ_i) of a sample ray emitted from the scintillator increases with increasing h . So, the probability for θ_i becoming greater than the critical angle, θ_c , also increases. Consequently, chances of total internal reflection also increase. The angle of reflection, θ_r is equal to θ_i . Hence, the reflected ray can propagate directly to the photodetector. However, for even higher values of h , the reflected ray must additionally undergo multiple reflections before reaching the photodetector. Not necessarily all of these reflections are total internal reflection, because the transverse surfaces of the trapezoid are not parallel. Some rays are Fresnel reflected, wherein the associated losses, due to the fact that the reflectivity of the light guide-reflector surface is less than unity, reduces the number of optical photons finally reaching the photodetector. Hence, n_{ph} increases up to an intermediate value of h , beyond which it starts to decrease. As energy resolution is inversely proportional to the square root of n_{ph} , whereas PPH is equal to n_{ph} , the best spectrum is obtained for an intermediate value of h .

Figure 5.4 shows the comparison of the simulated spectra with ^{137}Cs for the different heights of the light guide and the $18 \times 18 \times 0.3 \text{ mm}^3$ photodetector. Clearly, the best spectrum is again obtained for $h = 20 \text{ mm}$. This is due to the same reason as described above. By looking at the abscissa values of Figures 5.2 and 5.4, it is evident that for each value of h , the pulse-height is higher for the larger photodetector. This is because a larger photodetector area results in more optical photons reaching it. Also, larger the photodetector, flatter are the transverse surfaces of the light guide, and therefore, the optical photons can, in principle, reach the photodetector after a lesser number of reflections on these surfaces. On the other hand, it is seen from Figure 5.4 that the spectra with $h = 10 \text{ mm}$ and $h = 20 \text{ mm}$ are not very different. This is due to the different inclination angles of the transverse surfaces of the trapezoidal light guide for $d = 18 \text{ mm}$ and $d = 10 \text{ mm}$, which result in different optimum values of h in the two cases. It is important to mention that the optimized values of h can be fine-tuned in both the cases by repeating the analysis for various intermediate values of h .

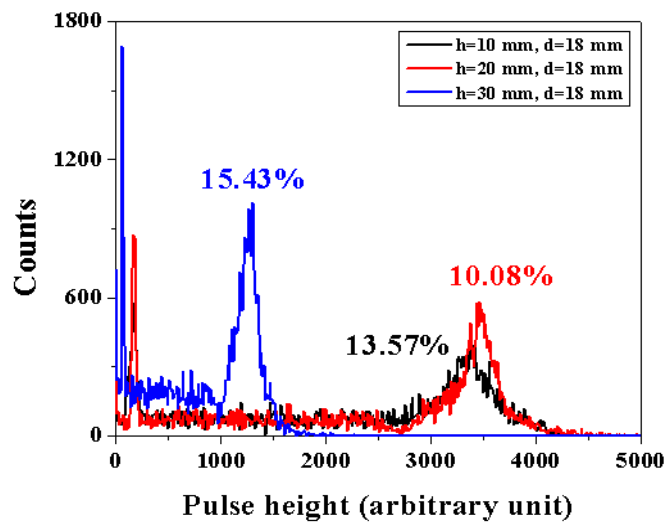


Figure 5.4: Comparison of the simulated spectra with ^{137}Cs for different heights (10, 20 and 30 mm) of the light guide and the $18 \times 18 \times 0.3 \text{ mm}^3$ photodetector.

The presented simulation model did not take into account the bulk absorption of optical photons within the scintillator and the light guide. In fact, the bulk absorption length

was taken to be 5 m for both, which is much larger than the largest dimensions considered in the simulations. Also, all the surface parameters were kept unchanged. The results presented here are likely to vary if bulk absorption becomes significant and/or the reflection conditions change at the surfaces.

5.3 Simulation studies on trapezoidal CsI(Tl) scintillators

The light guide can be eliminated by cutting the scintillator crystal in the shape of a trapezoid and coupling it directly to the photodetector. In order to see the impact of this operation on the pulse-height spectra, simulation based studies were carried out.

5.3.1 Simulation methodology

A trapezoidal CsI(Tl) scintillator, as shown in Figure 5.5, was modeled in GEANT4. The area of the larger flat surface of the trapezoid was $2'' \times 2''$ ($50.8 \times 50.8 \text{ mm}^2$), whereas that of the smaller flat surface was 10×10 or $18 \times 18 \text{ mm}^2$. The height of the trapezoid was varied ($1''$, $1.5''$ or $2''$, i.e., 25.4, 38.1 or 50.8 mm) in order to see its effect on the simulated spectra. The entire assembly shown in Figure 5.5 was coated with a 1 mm thick Teflon reflector. The outer enclosure to this assembly was made up of aluminum that had a thickness of 0.5 mm at the bottom surface and 1 mm elsewhere. The reflector and the aluminum enclosure are not shown in Figure 5.5 for clarity. The whole assembly was placed in air. A parallel beam of gamma photons was modeled to be incident perpendicularly on the larger surface of the trapezoid and entirely covering this surface. The energies of the incident gamma photons were sampled according to the source at serial number 2 (^{137}Cs) of Table 3.1.

All material properties, scintillation and optical properties and surface properties were same as those mentioned in Sections 3.2.2, 3.2.3 and 3.2.4, respectively. The procedure for scoring and generation of simulated spectra were same as those mentioned in Section 3.2.5, except for the fact that the number of optical photons detected at the scintillator-photodetector interface (n_{ph}) was treated as the pulse-height with arbitrary units.

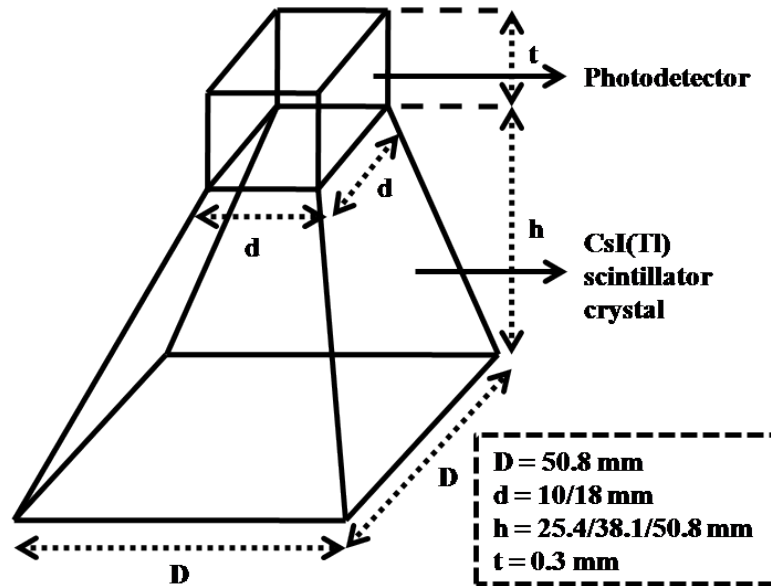


Figure 5.5: Schematic diagram of the simulation geometry consisting of a trapezoidal CsI(Tl) scintillator crystal, coupled directly to a $10 \times 10 \times 0.3$ or $18 \times 18 \times 0.3$ mm³ photodetector. The Teflon reflector and the outer aluminum enclosure are not shown for clarity (Figure not to scale).

5.3.2 Impact of surface area of the photodetector and height of the trapezoidal scintillator on simulated spectra

The comparison of the simulated spectra with ¹³⁷Cs for the different heights of the trapezoidal scintillator and the $10 \times 10 \times 0.3$ mm³ photodetector is presented in Figure 5.6, wherein it is evident that the best spectrum is obtained for the shortest scintillator, i.e., for $h = 25.4$ mm. It is to be noted that as the height of the scintillator increases, so does its volume. Therefore, it may be inferred that for this geometry and, in particular, for these dimensions, the effect of the decrease in light collection efficiency with the increase of the height of the scintillator is not compensated by the effect of the increase in the number of optical photons generated in the longer (and therefore, larger) scintillators.

Figure 5.7 shows the comparison of the simulated spectra with ¹³⁷Cs for the different heights of the trapezoidal scintillator and the $18 \times 18 \times 0.3$ mm³ photodetector, wherein it is

evident that the best spectrum is obtained for $h = 25.4$ mm, due to the same reason as described above.

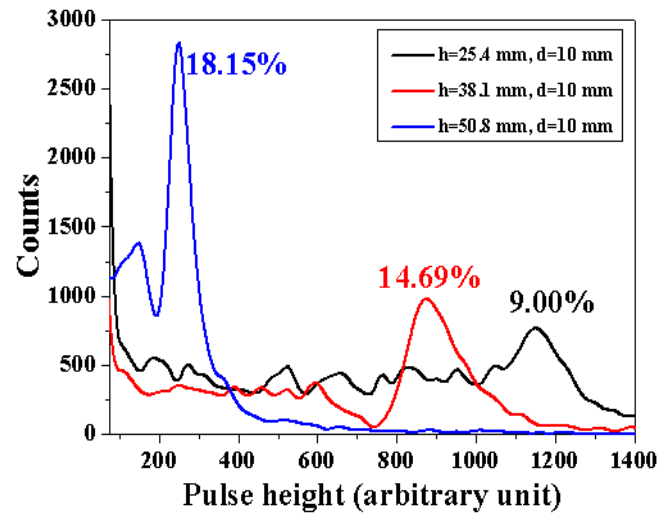


Figure 5.6: Comparison of the simulated spectra with ^{137}Cs for different heights (25.4, 38.1 or 50.8 mm) of the trapezoidal CsI(Tl) scintillator and the $10 \times 10 \times 0.3$ mm³ photodetector.

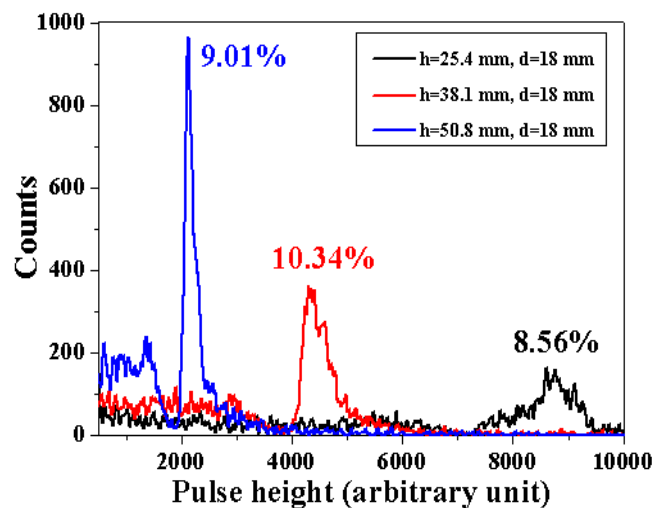


Figure 5.7: Comparison of the simulated spectra with ^{137}Cs for different heights (25.4, 38.1 or 50.8 mm) of the trapezoidal CsI(Tl) scintillator and the $18 \times 18 \times 0.3$ mm³ photodetector.

By looking at the abscissa values of Figures 5.6 and 5.7, it is also evident that for each value of h , the pulse-height is higher for the larger photodetector. This is because a larger photodetector area results in more optical photons reaching it. Also, for a fixed h , the

transverse surfaces of the trapezoidal scintillator become flatter for the larger photodetector, and therefore, the optical photons can, on the average, reach the photodetector after a lesser number of reflections at the transverse inner surfaces. Lastly, the volume of the scintillator also increases as d increases, and therefore, more light photons are generated.

It is important to note from Figure 5.7 that although the *PPH* at 662 keV steadily decreases as h increases, the energy resolution at 662 keV for $h = 50.8$ mm is superior to that for $h = 38.1$ mm. This may be due to the fact that the light collection from different parts of the trapezoidal scintillator, especially from its bottom corners (see Figure 5.5), becomes more uniform for $h = 50.8$ mm than for $h = 38.1$ mm, because the transverse surfaces of the trapezoid are flatter for the former.

The results presented in this section are likely to vary if bulk absorption becomes significant and/or the reflection conditions change at the surfaces.

5.4 Simulation studies on the impact of presence *vis-a-vis* absence of light guide

As mentioned in Section 5.1, for an unchanged cross-sectional area of the light guide throughout its length, it is theoretically possible to collect all the photons from a scintillator to a photodetector of equal cross-sectional area, provided there is no loss of optical photons in the bulk of the light guide and on its surfaces. In order to check to what extent this assumption is valid for the material properties and surface parameters of the modeled light guide, simulations were performed with the two geometries shown in Figure 5.8.

5.4.1 Simulation methodology

The area of the larger flat surface of the trapezoidal CsI(Tl) scintillator was 35×35 mm², whereas that of the smaller flat surface was 18×18 mm². The height of the trapezoid was fixed at 50 mm. In Figure 5.8 (a), the scintillator is directly coupled to the $18 \times 18 \times 0.3$ mm³ photodetector, whereas in Figure 5.8 (b), it is coupled through an $18 \times 18 \times 10$ mm³

cuboid shaped PMMA light guide. In each case, the entire assembly was coated with a 1 mm thick Teflon reflector. The outer enclosure to this assembly was made up of aluminum that had a thickness of 0.5 mm at the bottom surface and 1 mm elsewhere. The reflectors and the aluminum enclosures are not shown in Figure 5.8 for clarity. Both assemblies were placed in air. A parallel beam of gamma photons was modeled to be incident perpendicularly on the larger surface of the trapezoid and entirely covering this surface. The energies of the incident gamma photons were sampled according to the source at serial number 2 (^{137}Cs) of Table 3.1.

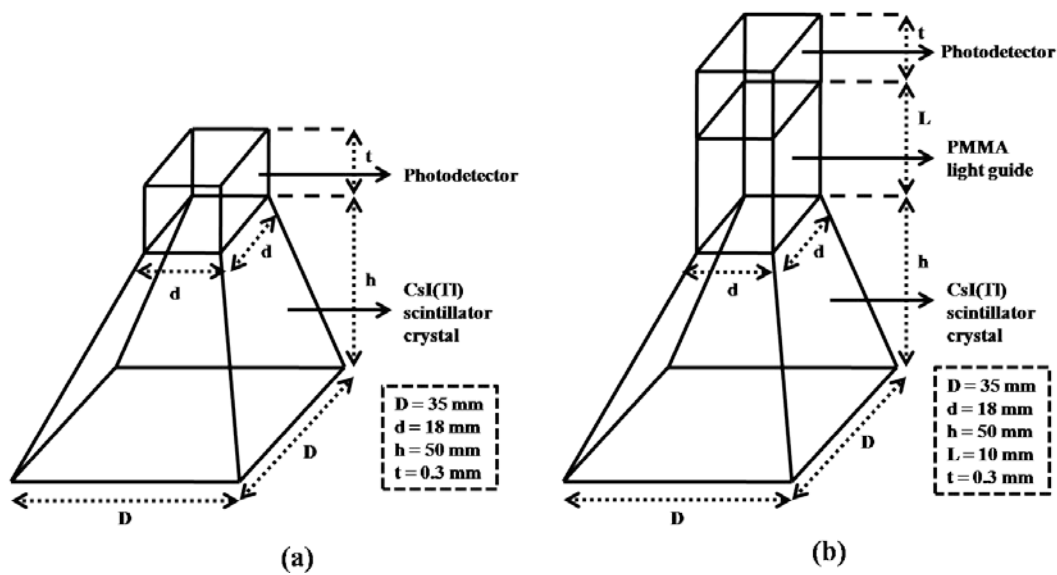


Figure 5.8: Schematic diagram of the simulation geometry consisting of a trapezoidal CsI(Tl) scintillator crystal, coupled (a) directly to a $18 \times 18 \times 0.3 \text{ mm}^3$ photodetector and (b) through a cuboid shaped PMMA light guide to the same photodetector. The Teflon reflectors and the outer aluminum enclosures in both the geometries are not shown for clarity (Figures not to scale).

Material properties, scintillation and optical properties, surface properties and procedure for scoring and generation of simulated spectra were same as those mentioned in Section 5.2.1.

5.4.2 Impact of presence *vis-a-vis* absence of light guide

Figure 5.9 depicts the two simulated spectra with ^{137}Cs with and without the light guide.

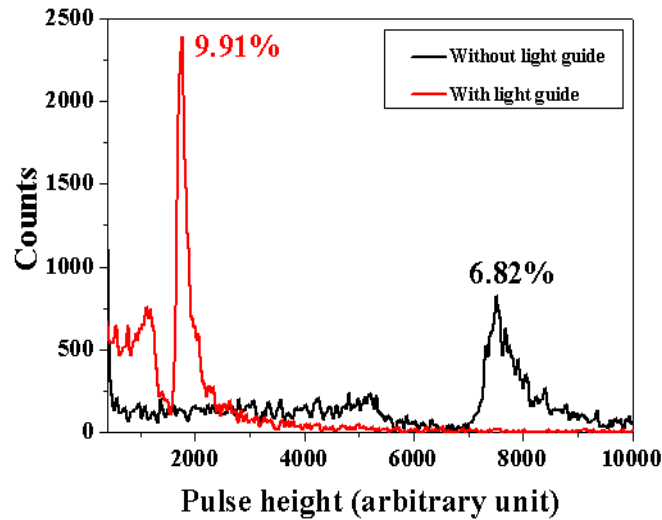


Figure 5.9: Comparison of the simulated spectra with ^{137}Cs with and without a 10 mm long cuboid shaped PMMA light guide in between a trapezoidal CsI(Tl) scintillator and a $18 \times 18 \times 0.3 \text{ mm}^3$ photodetector.

Clearly, the *PPH* at 662 keV is higher and also the energy resolution at 662 keV is superior for the case when the scintillator is directly coupled to the photodetector. In fact, the number of optical photons detected at the surface of the photodetector is seen to decrease by a factor of almost four when the 10 mm long light guide is introduced. This is due to two reasons. Firstly, the difference in refractive indices of CsI(Tl) (1.79) and PMMA (~ 1.49) results in loss some of the optical photons. Secondly, the introduction of the light guide increases the distance between the scintillator and the photodetector. Therefore, the optical photons must travel greater distances, and consequently, undergo more number of reflections before reaching the photodetector.

In general, the impact of introduction of the light guide would change depending on the refractive indices of the scintillator and the light guide, the overall geometry, the surface properties, etc.

5.5 Conclusion

PMMA light guide was included in the GEANT4 based simulation model. Optical transport through PMMA light guide was incorporated. Simulations were performed for various assemblies including scintillators and light guides of different shapes and sizes. The results indicate that the exact geometry affects the resulting pulse-height spectra in the most dominant way. For each particular shape and size of the scintillator and the photodetector, an optimized design of light guide can be identified from simulation. The developed simulation model can be helpful in *a priori* optimization of the design of future application specific light guides. Also, other light guide materials (e.g., fused silica or quartz) can be accommodated in the same model if the appropriate parameters are substituted.

DEVELOPMENT OF GAMMA SPECTROMETRY SYSTEMS

6.1 CsI(Tl) based environmental gamma spectrometry system (EGSS)

6.1.1 Introduction

Real-time spectroscopic identification of gamma emitting radionuclides present in open environment can be achieved by field-installed gamma spectrometry systems. A continuously operating automated system of this type with online data communication can provide valuable information about the radionuclides during routine releases from nuclear installations or during any radiological or nuclear emergency. Such information can be helpful in timely implementation of radionuclide-specific countermeasures from an emergency preparedness point of view [221]–[227]. This is important for reducing the overall radiation dose delivered to radiation workers, members of public, and the environment [16].

The pros and cons of the three major types of detectors used for gamma spectrometry, namely, inorganic scintillators, HPGe and CZT, have been discussed in Section 1.3.3 [1], [148], [149]. HPGe offers the best energy resolution and is available in large volumes, but it has to operate at LN₂ temperature. The associated LN₂ containing dewar requiring regular manual refilling cannot be afforded in systems meant for automated open field gamma spectrometry [1], [16]. CZT overcomes this problem and is the second best among the three detectors in terms of energy resolution offered, but it is available in small sizes and therefore, has low overall gamma absorption efficiency [150], [151]. Inorganic scintillators, although having the poorest energy resolution among the three detector types, offers a good combination of properties, e.g., high overall as well as photopeak efficiency, decent energy resolution, and suitability of operation at ambient temperatures [1]. Therefore, for the present application, inorganic scintillators were chosen as the detectors. Specifically,

the in-house grown CsI(Tl) single crystal scintillators, as described in Section 2.1.4.3, were used.

There are several challenges towards the development of a standalone, field-deployable EGSS. Firstly, the system needs to be battery operated in order to eliminate the requirement of AC mains supply, which cannot be guaranteed for open field installation locations. Secondly, referring to Figure 1.12, it can be seen that for laboratory based gamma spectrometry, the amplified and shaped pulses from the amplifier are sent to a MCA that require a dedicated personal computer (PC) for its operation. For standalone, battery operated systems, as in the present case, however, the PC needs to be eliminated because it increases the power consumption and also requires frequent manual maintenance. The increase in power requirement, on the other hand, also increases the overall size of the system by virtue of requiring batteries with higher capacities, which are heavier, bulkier, and need larger solar panels to charge them, in case the standalone system is targeted to be run on solar energy [16].

The CsI(Tl) scintillator was optically coupled to a PMT. The anode pulses of the PMT were fed to a preamplifier, whose output was sent to an in-house developed field programmable gate array (FPGA) based MCA board having a serial output. A microcontroller received the spectral data from the MCA over serial link. A global system for mobile communications (GSM) modem was used to transmit the data from the microcontroller to a central data receiving station in the form of short message service (SMS) packets. The use of the FPGA based MCA, therefore, eliminated the requirement of the PC. This, in turn, reduced the overall power requirement as well as size of the system and eliminated the dependence on the AC mains supply, thereby making it feasible to develop a standalone, solar-powered and battery operated EGSS [16].

A GM counter based gross gamma dose rate measurement circuit was also implemented into the system. The otherwise hibernating spectrometer is turned-on only when this circuit detects an ambient gamma dose rate level beyond a pre-set threshold value. This resulted in further reduction in the overall power consumption of the system [16].

Energy calibration of a gamma spectrometer is performed in order to convert the acquired spectra from channel numbers scale to energy scale (see Sections 3.5 and 4.2.4). However, this conversion is typically done at a particular temperature, whereas, for continuous on-field measurements, the overall gain of the spectrometer keeps on changing with variation in ambient temperature. This results in shifting of the recorded pulse-height spectra along their abscissa (channel number scale) with respect to the reference spectrum recorded at the calibration temperature [15], [228]. This leads to misidentification of peaks in the recorded spectra. To restore the shifted spectra, a mathematical methodology [15] was implemented at the central receiving station [16].

Section 6.1.2 describes the details about the design of various sub-components of the developed standalone, solar-powered, battery operated, field-deployable EGSS with online, real-time GSM based wireless data communication. The results of field-testing of the developed system are presented in Section 6.1.3.

6.1.2 Design of the system

6.1.2.1 The CsI(Tl)-PMT assembly

The scintillator-PMT assembly was similar to that described in Section 3.4. A 2" $\phi \times$ 2" L cylindrical sample was cut from an in-house grown CsI(Tl) single crystal ingot (see Section 2.1.4.3) [159]–[161]. One flat surface of the sample was hand-polished to clear optical finish. All other surfaces were ground. The polished surface was optically coupled to a 2" ϕ PMT (Hamamatsu R1306) [200]. The crystal was wrapped with Teflon reflector as described in Section 3.4. A HV generator module with a provision to control the HV through a

potentiometer, a voltage divider circuit, and a charge sensitive preamplifier were integrated in a small PCB. The power supply to the PMT was provided from this PCB and the output pulses of the PMT were fed to the preamplifier [16].

6.1.2.2 The FPGA based MCA board

The output tail pulses from the preamplifier were fed to an in-house developed FPGA based MCA PCB. Spectra were built by DPP. Trapezoidal pulse shaping was implemented. Communication between the MCA and the microcontroller was over USB and universal asynchronous receiver-transmitter (UART) at recommended serial communication standard 232 (RS-232) and complimentary metal-oxide-semiconductor (CMOS) logic levels. After the end of each user programmable acquisition interval, the spectrum built in the MCA was transferred to the microcontroller [16].

6.1.2.3 GM counter based environmental radiation monitor (ERM)

A GM counter based gamma dose rate measurement circuit (Figure 6.1) was integrated into the system [16]. This circuit works continuously as the ERM [229]. The microcontroller automatically turns-on the spectrometer via an in-house developed spectrometer triggering circuit when the dose rate sensed by the ERM crosses a pre-defined threshold value.

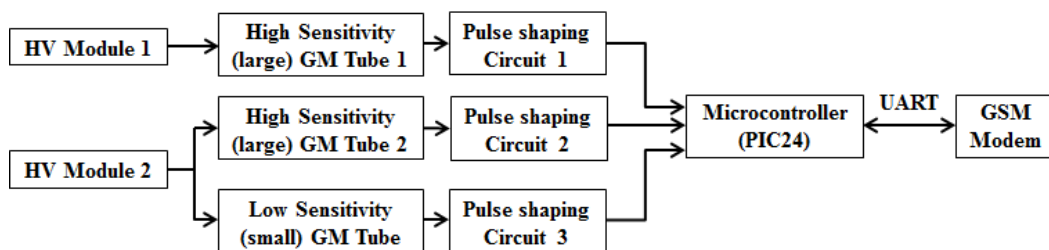


Figure 6.1: Block diagram of the GM counter based ERM [16].

The ERM consists of three energy compensated GM tubes, two (redundant) with high sensitivity (160 cps/(mR/h) relative to ^{60}Co) for measurement of natural background dose rate levels, and one with low sensitivity (0.26 cps/(mR/h) relative to ^{60}Co) for

measurement of elevated dose rate levels. The GM tubes have Ne as the fill gas and halogen as the quench gas. The recommended supply voltage of all the GM tubes is 500 V.

One high sensitivity GM tube is powered by one HV module. Another HV module powers the remaining two GM tubes. This ensures availability of at least one high sensitivity GM tube even in the case when one of the HV modules fails.

The three GM tubes, their individual pulse shaping circuits, the two HV modules, a PIC24 microcontroller and a GSM modem were all integrated in a PCB with dimensions $8.5 \times 45 \text{ cm}^2$. The pulse shaping circuits convert the output pulses of the GM tubes into transistor-transistor-logic (TTL) pulses. The TTL pulses are counted by the microcontroller. Based on conversion equations obtained from calibration of the GM tubes, the accumulated counts after each interval of 5 min are converted to dose rates by the microcontroller.

The dose rate response of the ERM was measured using a setup that consisted of standard collimated ^{60}Co sources with known activities as well as an automated distancing system and a laser based alignment system for accurate detector positioning. Figure 6.2 shows the measured dose rate response [16].

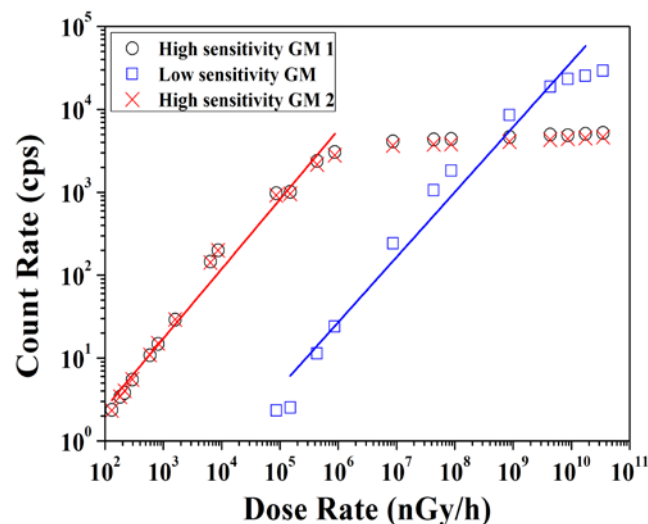


Figure 6.2: Dose rate response of the GM counter based ERM for ^{60}Co source [16].

It is clear from Figure 6.2 that the two high sensitivity GM tubes have almost identical response. Their response is seen to be linear in the range 130 nGy/h-870 μ Gy/h. The response saturates above this level. On the other hand, the response of the low sensitivity GM tube is seen to be linear in the range 150 μ Gy/h-17.39 Gy/h. The measurement range of the ERM is therefore 130 nGy/h-17.39 Gy/h. It needs to be mentioned here that the minimum dose rate (130 nGy/h) was achieved by placing the ERM as far away from the source (having the lowest activity) as was allowed in the calibration setup. Furthermore, the measurements were carried out in a room having a background radiation level of approximately 60-70 nGy/h. Therefore, the lower detection limit can be reduced further by carrying out measurements in a lower background area and by using a calibration setup that can produce lower standard dose rates. However, as this was beyond scope, the measurement range was assumed to extend down to 50 nGy/h.

The low sensitivity GM tube remains inactive under normal background conditions because its operating range starts from well beyond these dose rate levels. The dose rates recorded by the two high sensitivity GM tubes are averaged. The threshold for triggering was set on this average dose rate value. If the threshold is crossed, the power supply to the spectrometer is switched-on by the microcontroller. The average dose rate (from all three GM tubes if the low sensitivity GM tube shows non-zero values and from the two high sensitivity GM tubes, otherwise) is transmitted to the central receiving station along with the acquired spectra. If the average dose rate falls below the threshold, the microcontroller switches-off the power supply to the spectrometer. However, the hourly average of dose rate is calculated from the values recorded in each of the twelve 5 min intervals. 12 such hourly average dose rate values are communicated through a single SMS to the central receiving station after the end of 12 h. This communication happens twice a day [16].

6.1.2.4 Spectrometer triggering circuit and dual supply for spectrometer

As soon as the dose rate detected by the ERM crosses the threshold, the microcontroller generates an 'MCA ON' signal, which is passed to a transistor based triggering circuit having a fast switching power MOSFET [230]. The triggering circuit immediately switches on the dual power supply of the spectrometer. The dual power supply consists of a DC-DC converter module [231] that can source 200 mA current at ± 5 V [16].

6.1.2.5 GSM based data communication

The dose rate values measured by the ERM are transmitted via text mode SMSs to the central receiving station. When the spectrometer is switched on, a handshaking between the microcontroller and the MCA is established. The contents of the 512 channels of the MCA are received by the microcontroller at the end of each 5 min acquisition interval. The received data is encoded by the microcontroller. The encoded spectral data is sent as protocol description unit (PDU) mode SMSs by the GSM modem to the central receiving station. The PDU mode is used for sending compressed hex-coded binary information. Each channel of the MCA has 2 bytes of information. Therefore, a spectrum of 512 channels contains $512 \times 2 = 1024$ bytes of information. On the other hand, 140 bytes can be transmitted by one PDU mode SMS. Therefore, a total of at least eight SMSs are required for transmitting each spectrum. The first seven of these SMSs each carries the contents of 67 channels, i.e., $67 \times 2 = 134$ bytes of information. The contents of total $67 \times 7 = 469$ channels are transmitted in this way. The eighth (and the last) SMS carries the contents of the remaining $512 - 469 = 43$ channels as well as the dose rate values recorded by the ERM. Additionally, each of the eight SMSs contains a sequencing tag and an acquisition timestamp [16].

6.1.2.6 Power supply

The system runs on solar energy. It contains an 18 V/75 W polycrystalline silicon photovoltaic based solar panel. The panel charges a 12 V/42 Ah rechargeable, sealed

maintenance free (SMF), lead-acid battery. A relay based charge controller prevents overcharging and deep discharge of the battery. The total current consumed by the system when the spectrometer is powered on is nearly 600 mA. The rating of the solar panel is chosen such that it can fully charge the battery in nearly 6 h. The battery capacity is chosen such that once it is fully charged, it can drive the system continuously for nearly 3 days, considering that the spectrometer is on throughout. Therefore, after nearly 6 h of solar charging, the system can run for nearly another 3 days even in absence of sunlight. This running time extends to nearly 15 days when the spectrometer is hibernating and only the ERM works [16].

6.1.2.7 Functional block diagram of the system

Figure 6.3 shows the functional block diagram of the system [16].

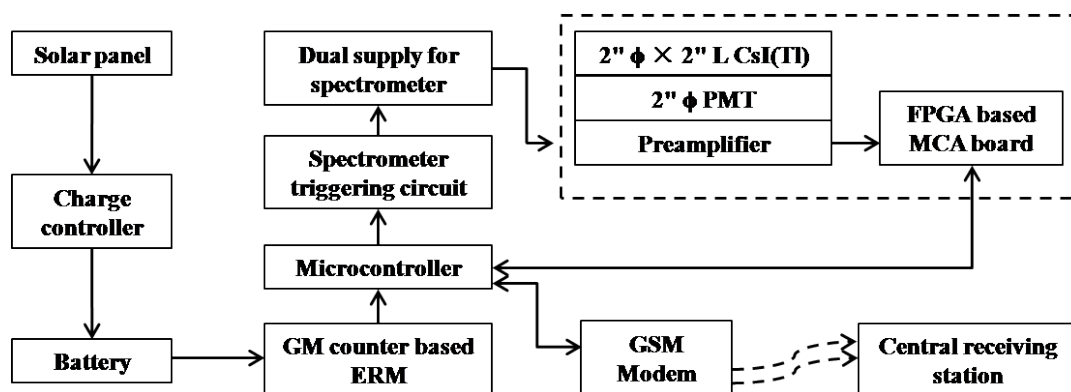


Figure 6.3: Functional block diagram of EGSS [16].

A CsI(Tl) scintillator is optically coupled to a PMT. The output pulses of the PMT are fed to a preamplifier, whose output is fed to an FPGA based MCA. The spectral data from the MCA is transferred via serial communication to a microcontroller. A GSM modem picks up the data from the microcontroller and sends it to a central receiving station in the form of SMS packets. When a GM counter based ERM detects a dose rate level above a pre-set threshold (usually set at three times the background radiation level at the installation location), the microcontroller switches on the dual power supply to the spectrometer via a spectrometer

triggering circuit. The entire system runs on a rechargeable SMF battery. The battery is charged by a solar panel. The presence of the charge controller between the solar panel and the battery prevents overcharging and deep discharge of the battery [16].

6.1.2.8 Mechanical housing of the system

An aluminum based hermetically sealed enclosure was fabricated for the system. The enclosure also contained the mounting arrangements for the solar panel. This made the system fit for permanent installation at open environment. Aluminum was chosen because it causes minimal attenuation of gamma radiation owing to its low atomic number ($Z = 13$) and also offers required structural ruggedness. Figure 6.4 shows a photograph of the complete system [16].



Figure 6.4: Photograph of EGSS (height: 92 cm, base area: $35 \times 35 \text{ cm}^2$, weight: 28 kg) [16].

The solar panel is fixed on a rotatable clamp which is mounted on an arm attached to the bottom chamber of the system. The bottom chamber houses the battery and the charge controller. It is made from 3 mm thick aluminum. The top chamber, on the other hand, is made from 2 mm thick aluminum for further reduction in attenuation of the incident gamma rays. This chamber houses the scintillator-PMT assembly, the PCB containing the

preamplifier, the HV generator module and the voltage divider circuit for the PMT, the PCB of the GM counter based ERM that also contains the microcontroller and the GSM modem, and the PCBs of the FPGA based MCA, the spectrometer triggering circuit and the dual supply for the spectrometer [16].

6.1.2.9 Spectrum reconstruction at central receiving station

The eight PDU mode SMSs corresponding to each spectrum are received by a GSM modem at the central receiving station. A Python based application reads the SMSs from this GSM modem and stores them in a MySQL based database. It also arranges the SMSs according to the sequencing tag and reconstructs the spectrum. The reconstructed spectrum is displayed over a Qt designer based user interface on a PC at the central receiving station. The screenshot presented in Figure 6.5 shows a reconstructed spectrum [16]. This spectrum was recorded by the system when it was intentionally triggered-on by introducing a ^{137}Cs test source.

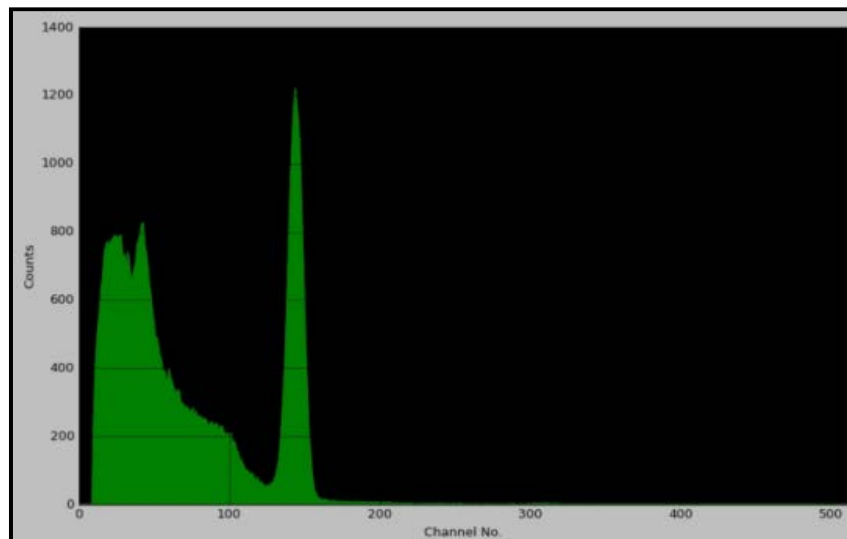


Figure 6.5: A screenshot of a spectrum displayed at the central receiving station. The spectrum was recorded by the system upon triggering-on by introduction of a ^{137}Cs test source [16].

6.1.2.10 Restoration of shifted spectra

As mentioned in Section 6.1.1, the overall gain of any scintillator based gamma spectrometer varies with temperature. For laboratory measurements, most often carried out under

controlled temperature environments, the effect of gain drift is usually negligible [15], [228]. However, for continuous measurements in open environment by field-installed systems, as in the present case, the gain drift can lead to misidentification of radionuclides when the channel number to energy conversion is done at a reference temperature and the gain of the spectrometer has significantly changed at the measurement temperature [15], [228], [232], [233].

The gain drift is caused by the temperature dependence of scintillation yield [18]–[20] and decay time constants [18], [20], [116], [234] of the scintillator, the fluctuations of the overall gain of the PMT with varying temperature [116], [235], [236], as well as the temperature dependence of the electronic components [237]. The most dominant among these is the gain drift of the PMT [232]. Furthermore, the gain does not stabilize during spectrum acquisition times of typically a few minutes [236]. Therefore, the peak-position versus temperature curve shows some kind of hysteresis when the temperature is continuously varied, as in open field [228]. A feedback signal generated based on the temperature value measured by an installed temperature sensor, therefore, does not help in online gain stabilization. There are various methodologies reported in literature to counter for this problem [15], [232], [233], [238]–[241].

A computer program was developed to calculate the shift in the energy scale between a reference and a shifted spectrum, by using the mathematical methodology described in [15]. The same program back-transformed the energy scale of the shifted spectrum to that of the reference spectrum. When the spectrometer gets triggered-on, the first recorded spectrum is taken as the reference, and all successive spectra are restored with respect to this reference spectrum. This program was implemented into a PC at the central receiving station and could restore the shifted spectra correctly, thereby helping in correct identification of the radionuclides. It is important to mention that the mathematical

methodology is such that it does not require the knowledge about the temperature values at which the spectra are recorded. Also, the methodology, although initially tested for NaI(Tl) [15], is applicable irrespective of the chosen scintillator, and therefore, could be applied for the present case involving CsI(Tl) as the scintillator [16].

6.1.2.11 Comparison with commercially available systems

The developed system is a cost-effective substitute to other commercially available instruments of similar type [242], [243]. In the developed system, the necessities of on-site PC and AC mains supply have been eliminated. The acquired spectra are not analyzed on-site. Instead, they are transmitted online to the central receiving station and the spectra are reconstructed at the central receiving station. The power consumption is thereby reduced. The conditional triggering of the spectrometer by the ERM ensures that the power consumption is further minimized. Real-time, on-line, wireless data transmission from remotely installed systems has been realized. Therefore, there is no need of any cabling for data transmission [16].

6.1.3 Results of field experiments

6.1.3.1 Performance testing under open environment conditions

The developed system was installed in open environment in Mumbai, India (~ 19.0760 °N, 72.8777 °E) and tested for almost a year. It performed uninterruptedly and unattended throughout. The mechanical housing could withstand normal ambient temperature cycles (~ 18-40 °C) as well as heavy rainfall (annual average ~ 1800 mm), and ensured proper functioning of the system. In the temperature regime of ~ 18-40 °C, the 512 channels' spectra shifted by less than 20 channels. The spectrum restoration program yielded satisfactory results in this temperature regime, thereby helping in proper identification of radionuclides.

Under normal background conditions, the system worked as a simple ERM and regularly sent the measured dose rate values, as per the scheme presented in Section 6.1.2.3.

The normal background radiation level at the installation site was nearly 60-70 nGy/h. It is known that this value varies from one installation site to another depending on the latitude, elevation, as well as the geophysical conditions [1]. The spectrometer could be intentionally triggered-on by introducing a gamma emitting radioactive source, as described in Section 6.1.3.2. Also, it automatically triggered-on when the ambient dose rate rose above the pre-set threshold of nearly three times the normal background, i.e., 200 nGy/h, as described in Section 6.1.3.3.

It is important to mention that the spectrometer is not being used here for quantification of dose rates. It is used only to identify the radionuclides that result in the elevation of dose rate levels. Hence, no efficiency calibration of the spectrometer was performed. The calibrated ERM (see Section 6.1.2.3) measures the dose rate levels. The CsI(Tl) scintillator has higher Z_{eff} and higher density than the gas-filled GM tubes. Therefore, the efficiency of the former is also much higher than that of the latter. The 2" $\phi \times 2$ " L CsI(Tl) scintillator, on the average, yielded a count rate of nearly 100 cps in the background of approximately 60-70 nGy/h. On the other hand, the high sensitivity GM tubes yielded about 1 cps in the same background. As the minimum detectable amount (MDA) of activity is nearly proportional to the square root of counts acquired for a particular counting time under background radiation conditions [1], the same of the scintillator should be approximately 10 times smaller than that of the high sensitivity GM tubes. However, in order to minimize power consumption, the spectrometer is not used for measurement of low dose rates. It is triggered-on for radionuclide identification only when the ERM detects a dose rate above nearly three times the background radiation level [16].

6.1.3.2 Intentional triggering-on of the spectrometer and energy calibration

When a small test source of ^{137}Cs was stuck with an adhesive tape on the outer surface of the top chamber of the system, the spectrometer triggered-on because the ERM detected a dose

rate level above 200 nGy/h. The recorded dose rate levels as well as the acquired spectra at the end of each 5 min interval were transmitted to the central receiving station. One such spectrum received at the central receiving station is shown in Figure 6.6, along with the energy resolution value (7.8%) at 662 keV.

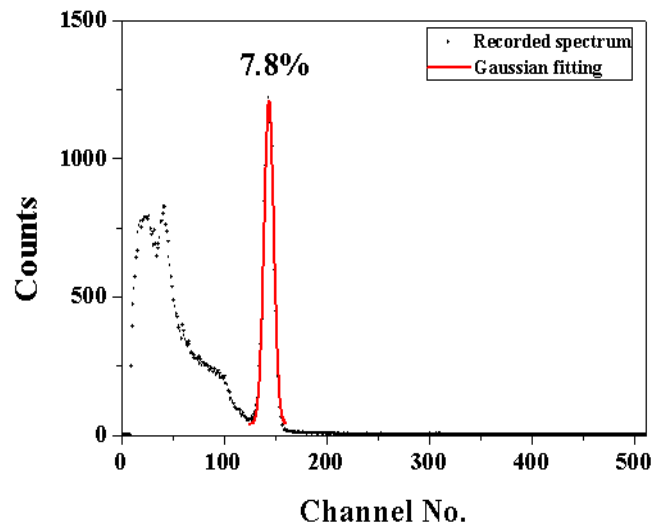


Figure 6.6: A typical pulse-height spectrum recorded by EGSS when a ^{137}Cs test source was introduced [16].

Figure 6.5 shows the screenshot of the same spectrum [16]. The spectrum of Figure 6.6 shows significant counts in the Compton and backscatter regions. This is due to scattered low energy gamma photons that are incident on the detector. The scattering from ground, mechanical enclosure of the system, detector's mounting support, etc., all contribute to this. The cosmic and terrestrial radiation also adds to this low energy background. This high background at low energies is a common feature for gamma spectra recorded at open environment by field-installed systems [1], [131], [221], [222], [226], [227], [244], [245].

Subsequently, the spectrometer was triggered-on by introducing a ^{137}Cs and a ^{60}Co test source together. One of the spectra recorded for 5 min and transmitted to the central receiving station is shown in Figure 6.7 (a), along with the derived energy calibration by

following the procedure described in Section 3.5. The same spectrum, converted to energy scale, is shown in Figure 6.7 (b).

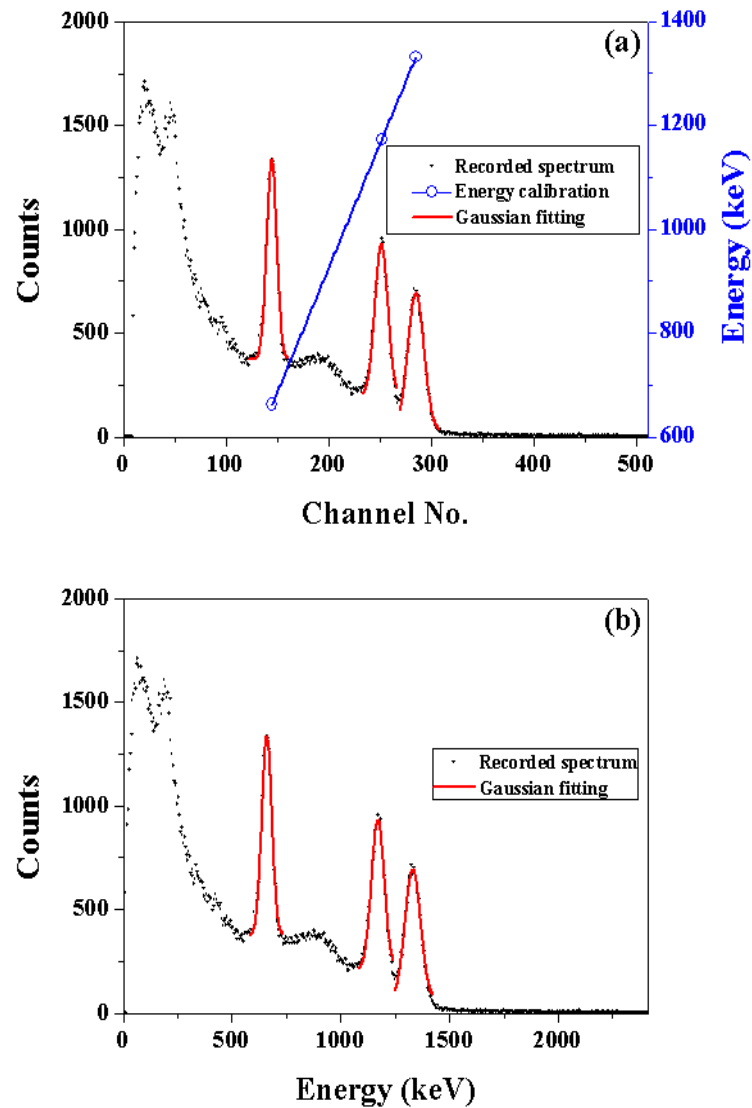


Figure 6.7: (a) Pulse-height spectrum recorded by EGSS when a ^{137}Cs and a ^{60}Co test source were introduced together, along with the derived energy calibration, (b) the same spectrum converted to energy scale.

6.1.3.3 Detection of atmospheric release of ^{41}Ar

Near the installation site of the system, there is an operational research reactor named Dhruva. The shutoff rods of this reactor are cooled by circulating ambient air. The ^{40}Ar present in this air gets partially converted to ^{41}Ar due to neutron activation. The stack of the

reactor routinely releases this ^{41}Ar containing air in the atmosphere well within regulatory limits. Dispersion of this ^{41}Ar containing plume has been previously studied [246] by employing GM counter based gross gamma dose rate monitors. The developed system (EGSS) could automatically trigger-on itself upon arrival of the ^{41}Ar containing plume. Spectra were automatically recorded upon triggering and sent after each acquisition interval of 5 min to the central receiving station. Figure 6.8 [16] shows one such sample spectrum, wherein the abscissa is converted to energy scale by using the energy calibration of Figure 6.7 (a).

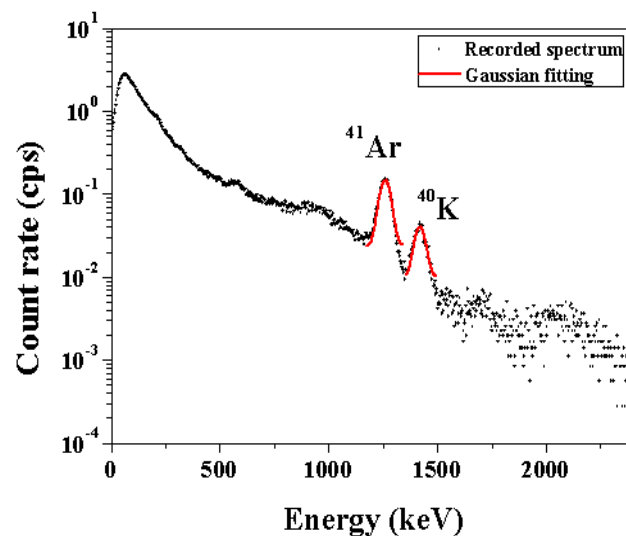


Figure 6.8: Pulse-height spectrum recorded during passing of ^{41}Ar containing plume over EGSS [16].

The peak due to ^{41}Ar (1293 keV) in Figure 6.8 is clearly resolved from that due to ^{40}K (1460 keV). The latter peak arises due to terrestrial radioactivity. The spectrum of Figure 6.8 is shown in logarithmic scale because the low energy background has increased even more than those present in Figures 6.6 and 6.7. This is because the spectra of Figures 6.6 and 6.7 are recorded by introduction of small test sources, whereas the spectrum of Figure 6.8 is recorded when a dispersed radioactive plume passes over the spectrometer. This

dispersed source resulted in a larger scattered component of gamma radiation being incident on the spectrometer.

It is to be mentioned that the acquisition time of 5 min was chosen for prompt identification of the radionuclides in case of their release to the environment. Upon initial identification, the acquisition time can be suitably increased for acquiring spectra with better statistics. This can be done by sending a command SMS from the central receiving station to the system. Four consecutive spectra, each recorded for 1 h during the passing of the ^{41}Ar containing plume, are presented in Figure 6.9 [16]. The gradual rise of the peak due to ^{41}Ar on the left of the nearly constant peak due to ^{40}K can be easily observed from Figure 6.9. Therefore, EGSS is proven to have the capability of identifying and tracking radioactive plumes. Such identification and tracking of radioactive plumes by a field-installed continuously operating gamma spectrometer during an accidental release of radionuclides into the environment can be really helpful in radiological emergency.

6.1.4 Conclusion

A standalone, solar-powered, battery operated EGSS having online wireless GSM based data communication was designed and developed. The in-house grown CsI(Tl) single crystal scintillator was used as the detector. Requirements of AC mains supply and on-site PC were eliminated by using an FPGA based MCA. The system was designed in such a way that the spectrometer gets automatically triggered-on only when a GM counter based ERM detects an ambient dose rate level beyond a pre-set threshold. Otherwise, it operates as a simple ERM. This resulted in further reduction of overall power requirement of the system. Results of field-testing showed encouraging performance of the system. It proved to be especially useful for tracking and identifying of radionuclides present in plumes dispersing in the atmosphere [16].

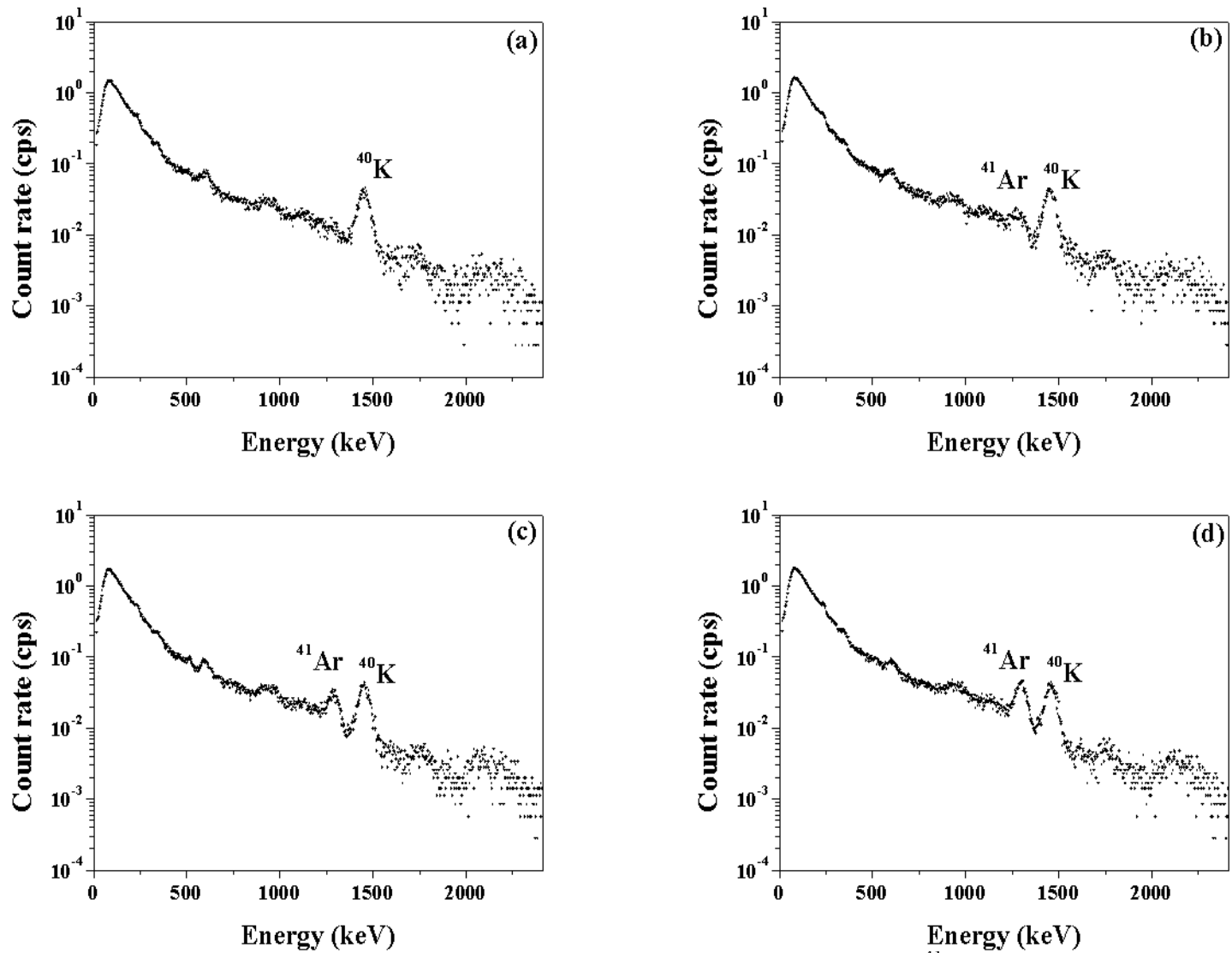


Figure 6.9: Four consecutive 1 h spectra recorded by EGSS during passing of ^{41}Ar containing plume [16].

6.2 Compact gamma spectrometer with a GGAG:Ce,B scintillator coupled to a photodiode

6.2.1 Introduction

The GGAG:Ce,B scintillator, owing to its scintillation emission spectrum (peaking at nearly 530 nm, as shown in Figure 2.9) that matches well with the spectral response of silicon based photodetectors, can be efficiently read-out by silicon photodiodes. This makes it possible to design photodiode based compact gamma spectrometers with this scintillator [93], [94], [157]. These spectrometers have many advantages over the conventional PMT based ones, e.g., compactness and mechanical robustness, insensitivity to magnetic fields, operation at comparatively much lower voltages, lower cost, etc. These compact spectrometers are well suited for many applications like baggage scanning, explosive detection, physics experiments, quick radionuclide identification, medical imaging, geological exploration, etc. [93], [157].

Another scintillator that is well suited for design of compact photodiode based spectrometers is CsI(Tl), because of its similar emission spectrum to that of GGAG:Ce,B, as shown in Figure 2.8 [94], [166]. However, GGAG:Ce,B has comparatively higher density and higher Z_{eff} , faster decay times and non-hygroscopic nature, thereby resulting in higher total and photoelectric absorption efficiency, suitability for higher counting rate applications, and ease of operation [93].

In addition to the replacement of the bulky PMT by a small photodiode, the development of a compact gamma spectrometer also involves miniaturization of the electronic components like the preamplifier, the amplifier, the MCA as well as the stable low voltage bias supply for the photodiode and the dual supply voltages of all the electronic components. In laboratory based gamma spectrometry, usually the nuclear instrument module (NIM) standard based electronic components are used. Their designs are standardized and

they usually provide optimized performance. Furthermore, their parameters are usually tunable, therefore enabling easy adaptation into different detector systems. However, they are bulky, and therefore, cannot be afforded in the design of a compact gamma spectrometer. Instead, smaller electronic components have to be employed and their performances have to be optimized before finalizing the overall design. Also, the bulky, NIM based power supplies that usually provide stable performance, cannot be afforded. Instead, a battery operated or USB powered system needs to be designed.

It is, however, understood that there may be some compromise in performance when the standard electronic components and power supplies are replaced by miniaturized components. Also, the deterioration of SNR when the PMT is replaced by a photodiode may result in some deterioration of performance. However, the aim is to design a compact gamma spectrometer with optimized performance, and therefore, this performance degradation, although cannot be fully eliminated, must be reduced to the extent possible.

Section 6.2.2 presents the details about the design and development of a compact, low power, USB based gamma spectrometer based on a small GGAG:Ce,B single crystal scintillator coupled to a small photodiode. The results of parametric investigation and spectroscopic performance evaluation of the system are also described.

6.2.2 Design and optimization of the spectrometer

6.2.2.1 Crystal growth and sample preparation

A single crystal ingot of GGAG:Ce,B was grown by the CZ technique, as described in Section 2.1.3.4 [157]. A $10 \times 10 \times 10 \text{ mm}^3$ sample was saw-cut from the ingot. Subsequently, the sample was annealed in air at 1000 °C for 10 h. Oxygen vacancies are present in the as-grown crystals because they are grown in an Ar-environment (see Section 2.1.3.4). The post-growth annealing treatment is known to reduce the oxygen vacancies in the crystal. This, in turn, increases the scintillation yield, reduces the decay times and improves the energy

resolution of the crystal [98], [157]. After annealing, one surface of the sample was polished to clear optical finish. No further surface treatment was applied to the other surfaces [93].

6.2.2.2 PMT based setup for initial characterization

The polished surface of the sample was optically coupled to the center of a 2" ϕ Hamamatsu R1306 PMT [200] using an optical grease (Dow Corning). The output of the PMT was fed to a preamplifier (Make: CAEN). The preamplifier's output was sent to a NIM-based spectroscopy amplifier. The amplified and shaped pulses were handled by an 8k MCA (Make: Tukan), which generated the pulse-height spectra.

6.2.2.3 Study on the impact of time after exposure to visible light on the recorded spectra

It has been reported earlier [98] that the light output of GGAG:Ce,B scintillators decreases if they are kept in the dark for a long time. This is due to the emptying of room temperature trap centers. In order to check how this affects the acquired spectra, after exposing the crystal (coupled with the PMT, as mentioned in Section 6.2.2.2) to white fluorescent light, it was immediately covered with a hemispherical Spectralon reflector, enclosed in a black chamber, and four consecutive 5 min spectra were acquired with a ^{137}Cs test source. Figure 6.10 shows the comparison of the four recorded spectra. It can be seen from Figure 6.10 that the 662 keV peak is farthest to the right in the first spectrum, indicating that the light output is highest during this time. Subsequently, the spectra shift to the left, and after nearly 10-15 min, the spectra become stable. Therefore, it can be inferred that the light output stabilizes after about 10-15 min, and therefore, all spectroscopic measurements need to be started after this waiting time. All measurements reported hereafter were, therefore, made following this principle.

6.2.2.4 Study on reflectors

Three different reflector materials were studied: (i) a hemispherical Spectralon, which is a diffuse reflector with high reflectivity, considered to be a white reflection standard [204], (ii)

standard Teflon tape wrapping of sufficient thickness of at least ten layers, and (iii) various number of coatings with a reflective paint (EJ-510, Eljen Technology[247]). The spectra recorded for 1200 s with these reflectors and a ^{137}Cs test source is shown in Figure 6.11.

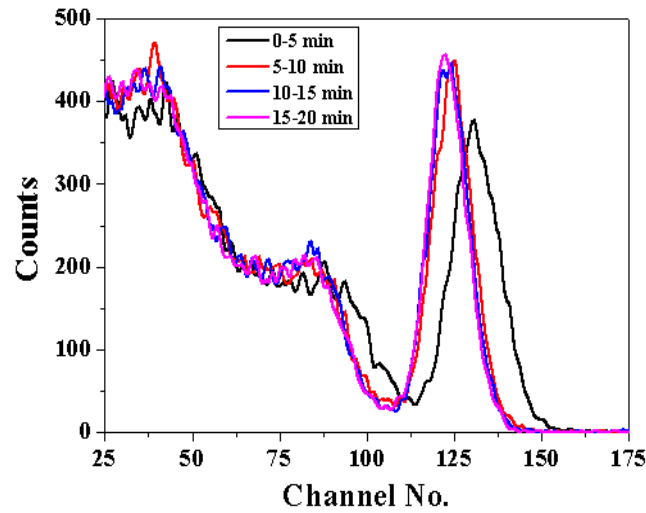


Figure 6.10: Comparison of four consecutive 5 min spectra of ^{137}Cs recorded with a $10 \times 10 \times 10 \text{ mm}^3$ GGAG:Ce,B scintillator (with Spectralon reflector) coupled to a PMT, after exposure to visible light.

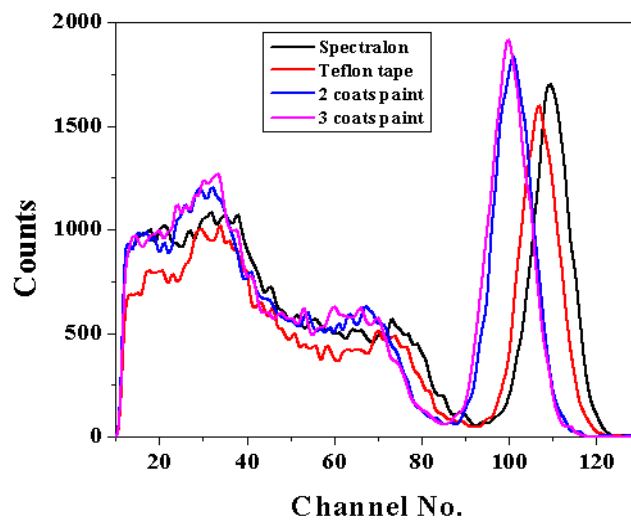


Figure 6.11: Comparison of pulse-height spectra of ^{137}Cs for different reflectors on a $10 \times 10 \times 10 \text{ mm}^3$ GGAG:Ce,B scintillator coupled to a PMT [93].

It can be seen from Figure 6.11 that the 662 keV peak is farthest to the right for Spectralon. Therefore, this reflector results in the most efficient light collection from the scintillator to the photocathode of the PMT. The position of the peak for Teflon tape wrapping is seen to be slightly to the left of that for Spectralon. This indicates that the light collection with Teflon tape wrapping is only slightly less than that with the Spectralon standard. On the other hand, the pulse-height values for the reflective paint, with both 2- and 3- coats, are significantly less. This indicates that the light collection with this paint is poorer than those with Teflon tape wrapping and Spectralon. Also, the fact that the peak position is nearly unchanged for both 2- and 3- coats of the paint indicates that the light collection with only two coats is almost saturated, and therefore, there is no visible improvement with the third coat. Based on the result of this study, Teflon tape was chosen as the reflector over the reflective paint for development of the compact gamma spectrometer [93].

It needs to be pointed out here that the reflectivity, reflection type and refractive index of the reflector, the uniformity of its coating thickness, as well as the presence or absence of air gaps between the scintillator and the reflector, can, in principle, contribute to the resulting light collection efficiency, and consequently, the pulse-height (see Sections 2.3.2.2.3.2 and 3.7).

6.2.2.5 Optical coupling with photodiode

After completing the studies mentioned in Sections 6.2.2.3 and 6.2.2.4, the scintillator was removed from the PMT. Its polished surface was then optically coupled to a Hamamatsu S3590-08 photodiode [191] (active area $10 \times 10 \text{ mm}^2$, thickness 0.3 mm, see Section 3.7.1) by using an optical grease (Dow Corning). The chosen reflector, i.e., Teflon tape, was wrapped tightly around the scintillator-photodiode assembly. At least ten layers of Teflon tape were used and care was taken to avoid the formation of air pockets in between the crystal and the reflector, as mentioned previously in Section 3.4 [93].

6.2.2.6 Setup of the compact photodiode based system for optimization studies

In order to miniaturize the electronics, compact electronic components were selected. The output of the photodiode was AC-coupled through a 10 nF coupling capacitor to a compact (0.85" × 0.88") charge sensitive preamplifier (Model: CR-110, Make: Cremat [248]). The preamplifier output was amplified by two cascaded stages of an AC-coupled (cutoff frequency: 20 Hz) non-inverting broadband (500 MHz-3 dB) amplifier. The broadband amplifier ensured effective amplification of the high frequency content of the signal, and its two stages together provided a gain of nearly 44. The output of the second stage of the broadband amplifier was amplified and shaped by a compact (0.85" × 0.88") Gaussian shaping amplifier (Model: CR-200, Make: Cremat [249]). Gaussian shaping is known to minimize noise power in the signal (considering the typical bath-tub type noise spectrum associated with photodiode instrumentation). The shaping amplifier CR-200 is available with various shaping times. Experiments were conducted to study the effect of the shaping time on the recorded spectra, and the optimized shaping time was identified. A 200 kΩ potentiometer was used for pole zero correction. The output from the shaping amplifier was sent to a buffer amplifier. A small (9 × 6 cm²) PCB (as shown in Figure 6.12) of the pulse processing electronics, along with the ±9 V to ±6 V conversion circuit, was designed and fabricated. The ±9 V was supplied from battery and the ±6 V was required to drive the electronic components. The output of the PCB was sent to an 8k MCA (Make: Tukan) [93].

6.2.2.7 Optimization of the reverse bias voltage of the photodiode

The reverse bias to the photodiode was provided by connecting various number of 9 V batteries in series. The impact of the bias voltage on the energy resolution at 662 keV was studied by recording the spectra with a ¹³⁷Cs test source for different values of the reverse bias voltage in the range 9-93 V. Each spectrum was recorded for 300 s.

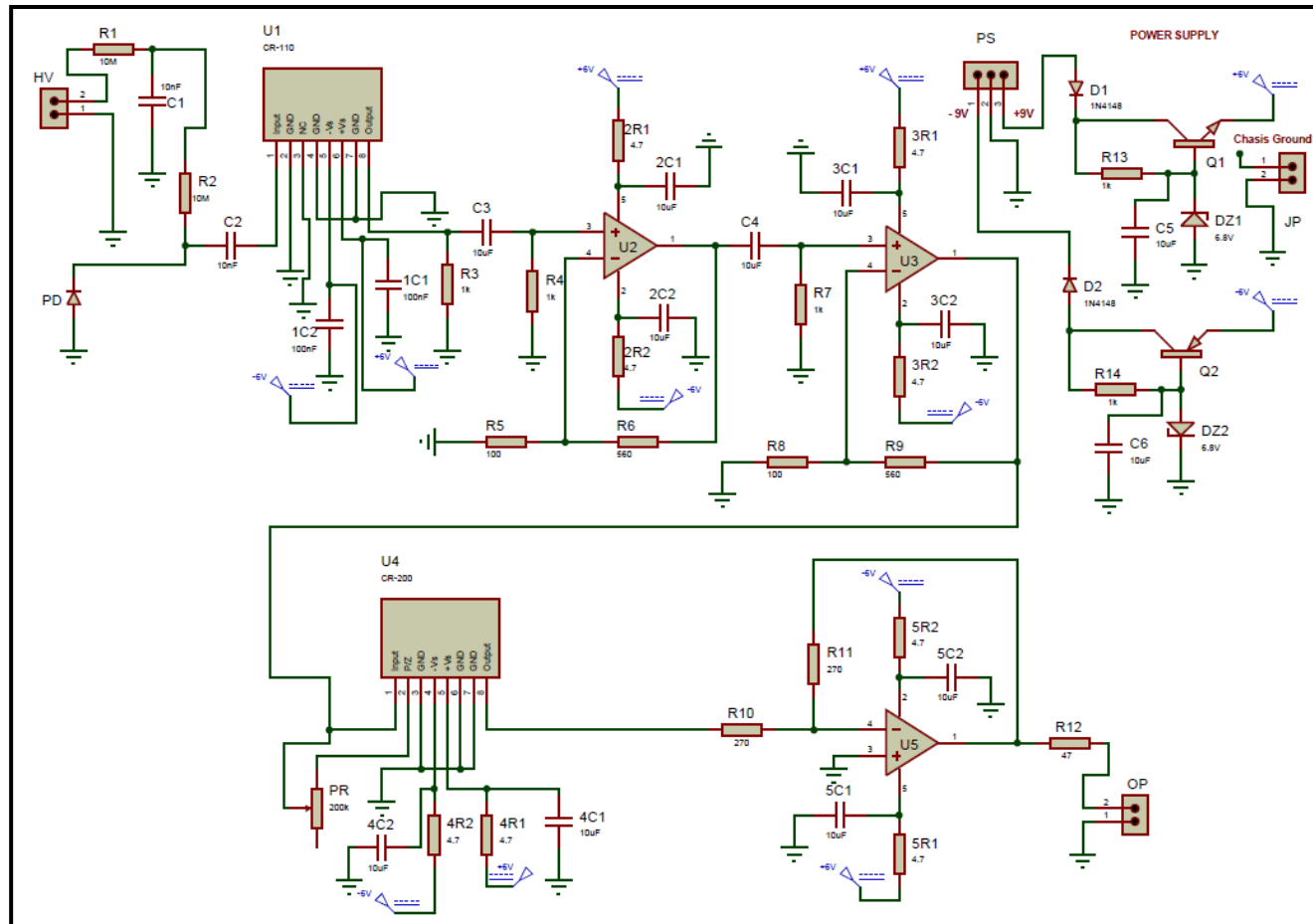


Figure 6.12: The pulse processing circuit of the compact gamma spectrometer with a GGAG:Ce,B scintillator coupled to a photodiode [93].

The energy resolution values, obtained by fitting Gaussian functions to the peak at 662 keV of each spectrum, are shown in Figure 6.13 as a function of the reverse bias voltage of the photodiode [93]. It can be seen from Figure 6.13 that the energy resolution remains more or less constant to within experimental uncertainties in the range of bias voltages studied. The uncertainties in the values of energy resolution depend on the choices of the ROIs and the accuracies of the Gaussian fitting. From the datasheet of the photodiode [191], it may be found that its full depletion voltage is nearly 70 V. Theoretically, the energy resolution is expected to improve for bias voltages above this full depletion voltage, because of minimization of the capacitance of the photodiode, and therefore, that of the associated series noise (see Section 1.2.3.1.3). However, this effect is most likely masked by the more dominant deterioration of the energy resolution by other factors [1], [91], as mentioned in Section 1.3.3.2.1.

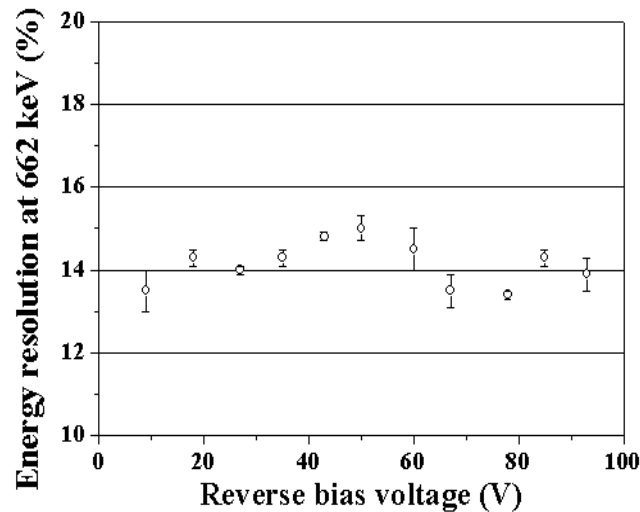


Figure 6.13: Energy resolution of the GGAG:Ce,B-photodiode based gamma spectrometer as a function of reverse bias voltage of the photodiode [93].

It was observed that the spectrum recorded with 0 V photodiode bias voltage was highly unstable and noisy. Also, it was seen that when the bias voltage was supplied by

batteries, the resulting spectra always had less noise and better energy resolution, than when the same was provided by a regulated power supply with a stability of better than ± 0.1 V.

Therefore, it was decided to design the system for operation with 9 V reverse bias voltage provided by a single battery. This ensured that the system would be compact as well as less noisy [93].

6.2.2.8 Optimization of the shaping time of the Gaussian shaping amplifier

As described in Section 1.2.3.1.3, as the shaping time is increased, the series noise of the photodiode decreases but the parallel noise increases. Overall noise is minimized at a particular choice of the shaping time [1]. Also, the shaping time must be longer than the decay time of the scintillator for complete charge collection, and, at the same time, short enough to minimize pulse pile-up.

In order to see the effect of the shaping time of the Gaussian shaping amplifier on the energy resolution at 662 keV, spectra were recorded by employing CR-200 shaping amplifiers with various shaping times in the range 25 ns-8 μ s. Each spectrum was recorded for 300 s. The recorded spectra with the 1, 2 and 4 μ s shaping times are shown in Figure 6.14 [93]. Spectra with the other shaping times (25, 50, 100, 250, 500 ns and 8 μ s) were noisier and had poorer energy resolution. Therefore, these spectra are not shown. Clearly, the best energy resolution is obtained with the shaping time of 2 μ s. Therefore, it was decided to design the final system with this fixed optimized shaping time. Hence, the CR-200-2 μ s shaping amplifier was chosen [93].

6.2.2.9 Energy calibration

Pulse-height spectra were recorded using the setup of Section 6.2.2.6 including the CR-200-2 μ s shaping amplifier with ^{137}Cs (662 keV), ^{60}Co (1173 and 1332 keV), ^{22}Na (511 and 1274.5 keV) and ^{152}Eu (344 and 1408 keV) test sources. Each spectrum was recorded for 300 s.

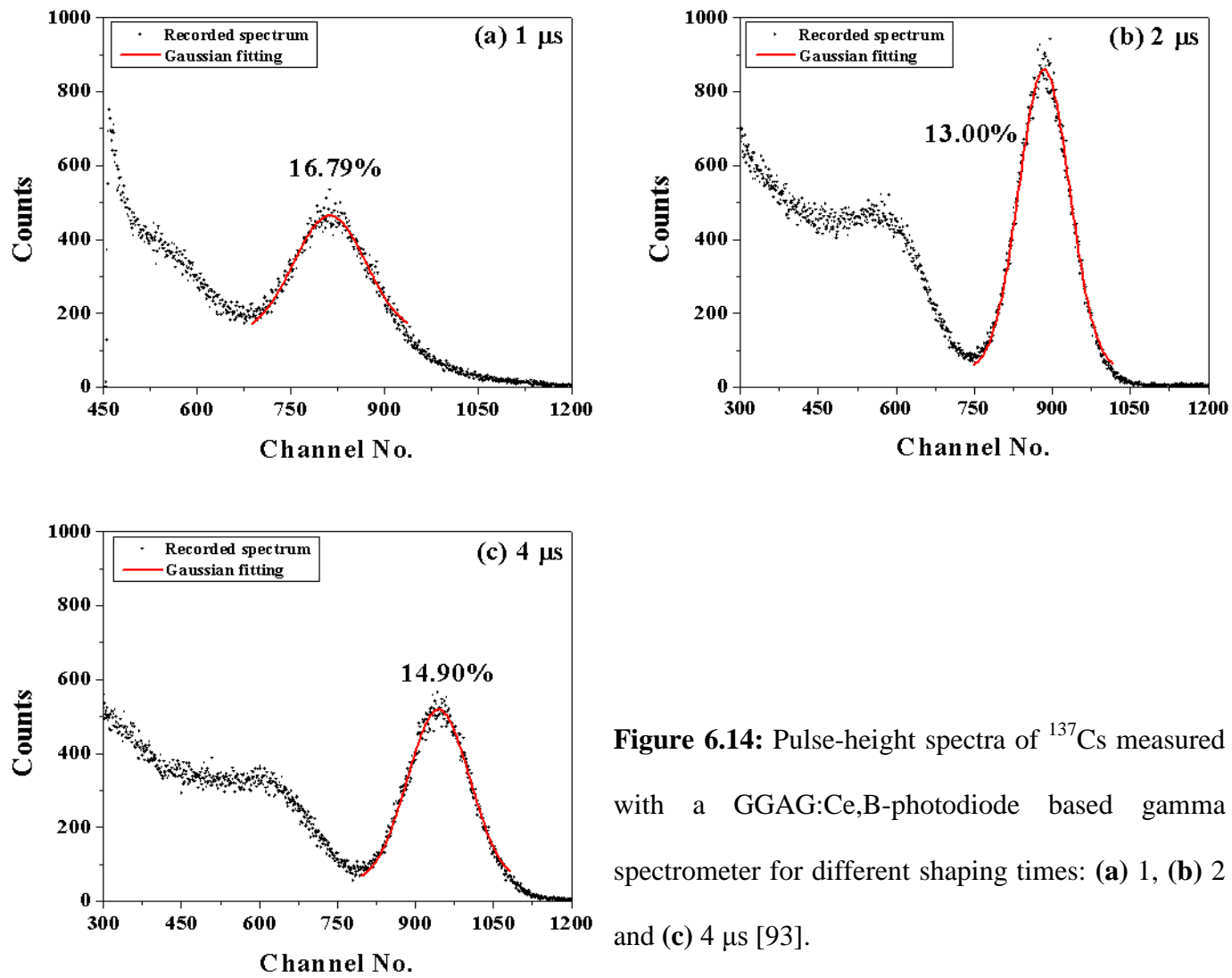


Figure 6.14: Pulse-height spectra of ^{137}Cs measured with a GGAG:Ce,B-photodiode based gamma spectrometer for different shaping times: (a) 1, (b) 2 and (c) 4 μs [93].

The energy calibration using these seven gamma energies is presented in Figure 6.15. Excellent energy linearity is observed in the studied energy range, i.e. 344-1408 keV [93].

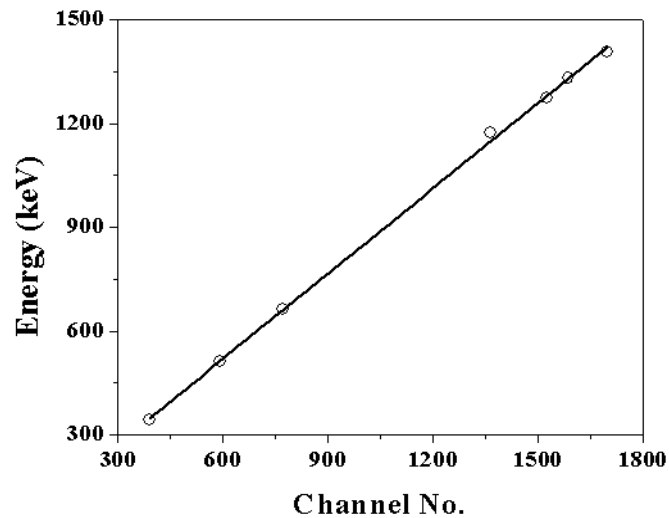


Figure 6.15: Energy calibration of the GGAG:Ce,B-photodiode based gamma spectrometer [93].

6.2.2.10 Factors affecting energy resolution of the GGAG:Ce,B-photodiode based gamma spectrometer

It is to be mentioned that the best energy resolution at 662 keV, obtained with the GGAG:Ce,B-photodiode based spectrometer, is nearly 13% (with shaping time 2 μ s and photodiode reverse bias 9 V). On the other hand, when the same scintillator is wrapped with Teflon tape, coupled to the Hamamatsu R1306 PMT, and the bulkier electronics of Section 6.2.2.2 is used, the energy resolution, as calculated from Figure 6.11, improves to nearly 9.4%. Therefore, although there is a huge improvement of the quantum efficiency when the photodiode is used (nearly 83%) as opposed to the PMT (only about 5%), the energy resolution with the former is still poorer. This is because of the small SNR and the resulting much higher noise of the photodiode (Gain = 1) based spectrometer, as compared to the PMT (Gain = 2.7×10^5) based one [93]. This argument is in line with the results presented in [144].

6.2.2.11 Development of the USB powered GGAG:Ce,B-photodiode based compact gamma spectrometer

The PCB of Figure 6.12 and that of a USB based 1k MCA, were together put inside an aluminum box with dimensions $137 \times 86 \times 84 \text{ mm}^3$ and thickness 1.5 mm. The DC-DC converter integrated circuit (IC), IA0509S, was used to convert the 5 V from USB to $\pm 9 \text{ V}$ required as the input to the $\pm 9 \text{ V}$ to $\pm 6 \text{ V}$ conversion circuit of Figure 6.12. The aluminum housing also enclosed the 9 V battery required to bias the photodiode. This completed the design of the compact USB based spectrometer. A photograph of the developed spectrometer is depicted in Figure 6.16 [93]. This spectrometer is portable and only needs a PC for connecting its USB. The software of the MCA needs to be installed in the PC. The spectrometer can then be controlled from the PC. The USB provides power to the system as well as receives the recorded spectra.

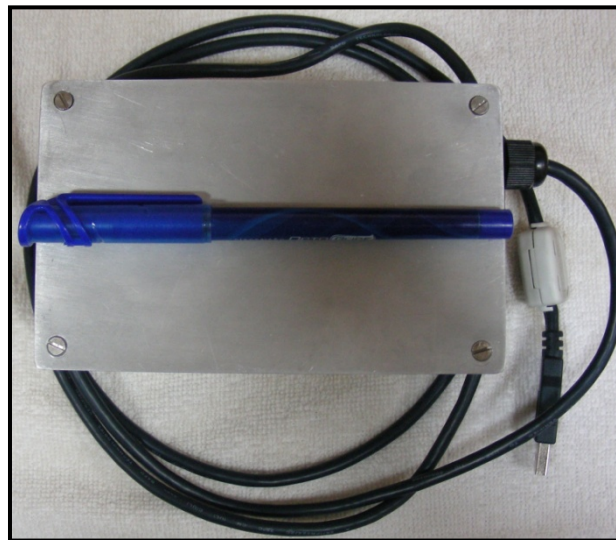


Figure 6.16: Photograph of the developed USB based compact ($137 \times 86 \times 84 \text{ mm}^3$) gamma spectrometer with a $10 \times 10 \times 10 \text{ mm}^3$ GGAG:Ce,B scintillator coupled to a $10 \times 10 \text{ mm}^2$ photodiode [93].

6.2.3 Conclusion

An in-house grown GGAG:Ce,B single crystal was coupled to a Hamamatsu S3590-08 photodiode. A compact, low power, USB based gamma spectrometer was designed and

developed using this scintillator-photodetector assembly. The biggest advantages of this spectrometer are its low voltage operation. It was optimized to work with a photodiode reverse bias voltage of only 9 V, provided by a single replaceable battery. Therefore, the need of the bulky high voltage electronics, typical for a PMT based system, was eliminated. Miniature hybrid preamplifier and shaping amplifier modules were chosen to provide compactness over the traditional NIM-based modules. The shaping time of the amplifier was optimized at 2 μ s. An optimum energy resolution of about 13% was achieved at 662 keV with the developed spectrometer. Excellent energy linearity was also observed over 344-1408 keV.

The developed photodiode based spectrometer offers a good alternative to a traditional PMT based spectrometer, albeit at the cost of some unavoidable deterioration in energy resolution. It is much more compact, rugged, low cost, and operates at much lower voltages. Furthermore, it can be used in strong magnetic field environments, where the PMT based systems might show some performance degradation [93].

CONCLUSION AND SCOPE FOR FUTURE WORK

7.1 Conclusion

In this thesis, Monte Carlo simulation as well as experimental studies were performed for two in-house grown single crystal inorganic scintillators, namely, CsI(Tl) and GGAG:Ce (as well as GGAG:Ce,B), to investigate their performance in gamma spectrometry in conjunction with different available photodetectors, viz. the PMTs and the silicon based photodetectors. CsI(Tl) is a widely used scintillator. However, GGAG:Ce (or GGAG:Ce,B) is a relatively new material with promising characteristics.

A GEANT4 based Monte Carlo simulation model including both radiation transport and optical photon transport was developed and experimentally validated for both of these scintillators. The model was subsequently used to study and identify the important parameters that influence the performance of these scintillators when they are coupled to photodetectors and employed for gamma spectrometry. The developed model can, therefore, be an important tool to evaluate the performance of scintillators-photodetector combinations in gamma spectrometry.

The simulation model was also shown to help in theoretical optimization of proposed designs of spectrometers that include light guides in between the scintillator and the photodetector. Light guides usually have to be custom made for each application. The developed model can help in this customization.

Starting from the as-grown single crystals, two gamma spectrometry systems were developed for possible field applications, one with the CsI(Tl)-PMT combination, and the other with the GGAG:Ce,B-photodiode combination.

A CsI(Tl) based standalone environmental gamma spectrometry system (EGSS) for continuous unattended operation in open environment was designed, developed and field-tested. The system was shown to be capable of identifying gamma emitting radionuclides in the environment including those present in dispersing gaseous plumes, a quality that can be immensely important from an emergency preparedness point of view.

A portable photodiode based USB powered gamma spectrometer was developed using a GGAG:Ce,B scintillator. It can be used for quick radionuclide identification for situations where a bulkier and costlier PMT based spectrometer cannot be afforded.

7.2 Scope for future work

Whereas some of the parameters required to drive the simulation model were incorporated from knowledge about the in-house grown scintillator crystals, and a few more from results of experimental studies conducted during this research work, the rest had to be incorporated from empirical data reported in literature. However, not all required parameters were available. These parameters, e.g., bulk absorption length for CsI(Tl) and GGAG:Ce scintillators as well as PMMA light guide, Birks' constant for GGAG:Ce, etc. were incorporated based on logical approximations. Also, for GGAG:Ce and GGAG:Ce,B, the scintillation yield is variously reported in literature. Wherever possible, the accurate theoretical or experimental evaluation of these parameters and their subsequent incorporation into the code would yield better results.

A more complete simulation model may be developed if the response of the photodetector can also be incorporated into the model. The fate of the generated charge carriers could then be simulated and this can give finer insights into the mechanisms leading to signal fluctuations and the associated deterioration of energy resolution.

An installed network of a large number of environmental gamma spectrometry systems can provide valuable data for studying radionuclide dispersion in the environment in case of a radiological or nuclear emergency.

An APD or SiPM based compact gamma spectrometer may be developed which may offer improved energy resolution compared to the presently developed photodiode based spectrometer, owing to the higher SNR achievable with APDs and SiPMs than with photodiodes.

REFERENCES

- [1] G. F. Knoll, *Radiation detection and measurement*, 4th ed. Hoboken, N.J: John Wiley, 2010.
- [2] F. H. Attix, *Introduction to radiological physics and radiation dosimetry*. Strauss GmbH, Morlenbach: Wiley-VCH, 2004.
- [3] H. Cember and T. E. Johnson, *Introduction to health physics*. New York: McGraw-Hill Medical, 2009.
- [4] N. R. Campbell and V. J. Francis, "A theory of valve and circuit noise," *J. Inst. Electr. Eng.* 3, vol. 93, no. 21, pp. 45, Jan. 1946.
- [5] B. B. Rossi and H. H. Staub, *Ionization Chambers and Counters*. New York: McGraw-Hill, 1949.
- [6] D. H. Wilkinson, *Ionization Chambers and Counters*. Cambridge: Cambridge University Press, 1950.
- [7] J. Sharpe, *Nuclear Radiation Detectors*, 2nd ed. London: Methuen and Co., 1964.
- [8] W. J. Price, *Nuclear Radiation Detection*, 2nd ed. New York: McGraw-Hill, 1964.
- [9] D. H. Wilkinson, "The Geiger discharge revisited Part I. The charge generated," *Nucl. Instrum. Methods Phys. Res. A*, vol. 321, no. 1, pp. 195–210, Sep. 1992, doi: 10.1016/0168-9002(92)90388-K.
- [10] J. B. Birks, *The Theory and Practice of Scintillation Counting*. Oxford: Pergamon Press, 1964.
- [11] P. Lecoq, A. Getkin, and M. Korzhik, *Inorganic Scintillators for Detector Systems*, 2nd ed. Switzerland: Springer, 2017.
- [12] R. Hofstadter, "Alkali Halide Scintillation Counters," *Phys. Rev.*, vol. 74, no. 1, pp. 100–101, Jul. 1948, doi: 10.1103/PhysRev.74.100.

- [13] R. Casanovas, J. J. Morant, and M. Salvadó, “Energy and resolution calibration of NaI(Tl) and LaBr₃(Ce) scintillators and validation of an EGS5 Monte Carlo user code for efficiency calculations,” *Nucl. Instrum. Methods Phys. Res. A*, vol. 675, pp. 78–83, May 2012, doi: 10.1016/j.nima.2012.02.006.
- [14] M. Moszyński, “Inorganic scintillation detectors in γ -ray spectrometry,” *Nucl. Instrum. Methods Phys. Res. A*, vol. 505, no. 1, pp. 101–110, Jun. 2003, doi: 10.1016/S0168-9002(03)01030-1.
- [15] P. Mitra *et al.*, “Application of spectrum shifting methodology to restore NaI(Tl)-recorded gamma spectra, shifted due to temperature variations in the environment,” *Appl. Radiat. Isot.*, vol. 107, pp. 133–137, Jan. 2016, doi: 10.1016/j.apradiso.2015.10.002.
- [16] P. Mitra *et al.*, “An environmental gamma spectrometry system with CsI(Tl) scintillator and FPGA based MCA for open field deployment,” *Appl. Radiat. Isot.*, vol. 172, p. 109677, Jun. 2021, doi: 10.1016/j.apradiso.2021.109677.
- [17] R. Kirkin, V. V. Mikhailin, and A. N. Vasil’ev, “Recombination of Correlated Electron–Hole Pairs With Account of Hot Capture With Emission of Optical Phonons,” *IEEE Trans. Nucl. Sci.*, vol. 59, no. 5, pp. 2057–2064, Oct. 2012, doi: 10.1109/TNS.2012.2194306.
- [18] C. L. Melcher and J. S. Schweitzer, “Gamma-ray detector properties for hostile environments,” *IEEE Trans. Nucl. Sci.*, vol. 35, no. 1, pp. 876–878, Feb. 1988, doi: 10.1109/23.12851.
- [19] R. Dayton, M. Mayhugh, M. Papp, P. Parkhurst, and R. Schreiner, “Performance results for scintillation detectors for high temperature environments including MWD,” *IEEE Trans. Nucl. Sci.*, vol. 35, no. 1, pp. 879–881, Feb. 1988, doi: 10.1109/23.12852.
- [20] W. C. Elmore and R. Hofstadter, “Temperature Dependence of Scintillations in Sodium Iodide Crystals,” *Phys. Rev.*, vol. 75, no. 1, pp. 203–204, Jan. 1949, doi: 10.1103/PhysRev.75.203.

- [21] “NaI(Tl) and Polyscin® NaI(Tl) Sodium Iodide | Products | Saint-Gobain Crystals.” <https://www.crystals.saint-gobain.com/products/nai-sodium-iodide> (accessed Jan. 10, 2021).
- [22] “NaI(Tl).” http://www.amcrys.com/details.html?cat_id=146&id=4278 (accessed Jan. 10, 2021).
- [23] “NaIL [NaI(Tl+Li)] Co-doped Sodium Iodide | Saint-Gobain Crystals.” <https://www.crystals.saint-gobain.com/products/nai-sodium-iodide-tl-lithium> (accessed Jan. 10, 2021).
- [24] M. Moszyński, W. Czarnacki, M. Kapusta, M. Szawlowski, W. Klamra, and P. Schotanus, “Energy resolution and light yield non-proportionality of pure NaI scintillator studied with large area avalanche photodiodes at liquid nitrogen temperatures,” *Nucl. Instrum. Methods Phys. Res. A*, vol. 486, no. 1–2, pp. 13–17, Jun. 2002, doi: 10.1016/S0168-9002(02)00668-X.
- [25] C. J. Crannell, R. J. Kurz, and W. Viehmann, “Characteristics of cesium iodide for use as a particle discriminator for high-energy cosmic rays,” *Nucl. Instrum. Methods*, vol. 115, no. 1, pp. 253–261, Feb. 1974, doi: 10.1016/0029-554X(74)90454-6.
- [26] I. Holl, E. Lorenz, and G. Mageras, “A measurement of the light yield of common inorganic scintillators,” *IEEE Trans. Nucl. Sci.*, vol. 35, no. 1, pp. 105–109, Feb. 1988, doi: 10.1109/23.12684.
- [27] J. D. Valentine, W. W. Moses, S. E. Derenzo, D. K. Wehe, and G. F. Knoll, “Temperature dependence of CsI(Tl) gamma-ray excited scintillation characteristics,” *Nucl. Instrum. Methods Phys. Res. A*, vol. 325, pp. 147–157, Feb. 1993.
- [28] S. Usuda, A. Mihara, and H. Abe, “Rise time spectra of α and $\beta(\gamma)$ rays from solid and solution sources with several solid scintillators,” *Nucl. Instrum. Methods Phys. Res. A*, vol. 321, pp. 247–253, 1992.

- [29] M. Moszynski, D. Wolski, T. Ludziejewski, S. E. Arnell, Ö. Skeppstedt, and W. Klamra, “Particle identification by digital charge comparison method applied to CsI(Tl) crystal coupled to photodiode,” *Nucl. Instrum. Methods Phys. Res. A*, vol. 336, pp. 587–590, 1993.
- [30] B. Ye *et al.*, “Development of a pulse shape discrimination circuit,” *Nucl. Instrum. Methods Phys. Res. A*, vol. 345, no. 1, pp. 115–119, Jun. 1994, doi: 10.1016/0168-9002(94)90979-2.
- [31] W. Skulski and M. Momayezi, “Particle identification in CsI(Tl) using digital pulse shape analysis,” *Nucl. Instrum. Methods Phys. Res. A*, vol. 458, no. 3, pp. 759–771, Feb. 2001, doi: 10.1016/S0168-9002(00)00938-4.
- [32] L. E. Dinca, P. Dorenbos, J. T. M. de Haas, V. R. Bom, and C. W. E. Van Eijk, “Alpha–gamma pulse shape discrimination in CsI:Ti, CsI:Na and BaF₂ scintillators,” *Nucl. Instrum. Methods Phys. Res. A*, vol. 486, no. 1–2, pp. 141–145, Jun. 2002, doi: 10.1016/S0168-9002(02)00691-5.
- [33] S. C. Wu *et al.*, “Near threshold pulse shape discrimination techniques in scintillating CsI(Tl) crystals,” *Nucl. Instrum. Methods Phys. Res. A*, vol. 523, no. 1–2, pp. 116–125, May 2004, doi: 10.1016/j.nima.2003.12.024.
- [34] S. Keszthelyi-Lándori and G. Hrehuss, “Scintillation response function and decay time of CsI(Na) to charged particles,” *Nucl. Instrum. Methods*, vol. 68, no. 1, pp. 9–12, Feb. 1969, doi: 10.1016/0029-554X(69)90682-X.
- [35] “LiI(Eu).” http://www.amcrys.com/details.html?cat_id=146&id=4285 (accessed Jan. 17, 2021).
- [36] G. Pausch and J. Stein, “Application of ⁶LiI(Eu) Scintillators With Photodiode Readout for Neutron Counting in Mixed Gamma-Neutron Fields,” *IEEE Trans. Nucl. Sci.*, vol. 55, no. 3, pp. 1413–1419, Jun. 2008, doi: 10.1109/TNS.2008.922836.

- [37] M. Moszyński, C. Gresset, J. Vacher, and R. Odru, “Timing properties of BGO scintillator,” *Nucl. Instrum. Methods Phys. Res.*, vol. 188, no. 2, pp. 403–409, Sep. 1981, doi: 10.1016/0029-554X(81)90521-8.
- [38] M. Kobayashi, M. Ishii, Y. Usuki, and H. Yahagi, “Cadmium tungstate scintillators with excellent radiation hardness and low background,” *Nucl. Instrum. Methods Phys. Res. A*, vol. 349, no. 2–3, pp. 407–411, Oct. 1994, doi: 10.1016/0168-9002(94)91203-3.
- [39] D. R. Kinloch, W. Novak, P. Raby, and I. Toepke, “New developments in cadmium tungstate,” *IEEE Trans. Nucl. Sci.*, vol. 41, no. 4, pp. 752–754, Aug. 1994, doi: 10.1109/23.322800.
- [40] T. Fazzini *et al.*, “Pulse-shape discrimination with CdWO₄ crystal scintillators,” *Nucl. Instrum. Methods Phys. Res. A*, vol. 410, no. 2, pp. 213–219, Jun. 1998, doi: 10.1016/S0168-9002(98)00179-X.
- [41] S. Ph. Burachas *et al.*, “Large volume CdWO₄ crystal scintillators,” *Nucl. Instrum. Methods Phys. Res. A*, vol. 369, no. 1, pp. 164–168, Jan. 1996, doi: 10.1016/0168-9002(95)00675-3.
- [42] Yu. G. Zdesenko *et al.*, “Scintillation properties and radioactive contamination of CaWO₄ crystal scintillators,” *Nucl. Instrum. Methods Phys. Res. A*, vol. 538, no. 1–3, pp. 657–667, Feb. 2005, doi: 10.1016/j.nima.2004.09.030.
- [43] M. Moszyński *et al.*, “Characterization of CaWO₄ scintillator at room and liquid nitrogen temperatures,” *Nucl. Instrum. Methods Phys. Res. A*, vol. 553, no. 3, pp. 578–591, Nov. 2005, doi: 10.1016/j.nima.2005.07.052.
- [44] “ZnS:Ag PHOSPHOR POWDER EJ-600.” <https://eljentechnology.com/23-products/zinc-sulfide-coated> (accessed Jan. 17, 2021).
- [45] “CaF₂(Eu) - Calcium Fluoride(Eu) Scintillator Crystal.” https://www.advatech-uk.co.uk/caf2_eu.html (accessed Jan. 17, 2021).

- [46] C. Plettner *et al.*, “CaF₂(Eu): an ‘old’ scintillator revisited,” *J. Inst.*, vol. 8, no. 06, pp. P06010–P06010, Jun. 2013, doi: 10.1088/1748-0221/8/06/P06010.
- [47] N. J. Cherepy *et al.*, “Strontium and barium iodide high light yield scintillators,” *Appl. Phys. Lett.*, vol. 92, no. 8, pp. 083508, Feb. 2008, doi: 10.1063/1.2885728.
- [48] E. V. van Loef *et al.*, “Crystal Growth and Scintillation Properties of Strontium Iodide Scintillators,” *IEEE Trans. Nucl. Sci.*, vol. 56, no. 3, pp. 869–872, Jun. 2009, doi: 10.1109/TNS.2009.2013947.
- [49] P. Schotanus, C. W. E. van Eijk, R. W. Hollander, and J. Pijpelink, “Temperature dependence of BaF₂ scintillation light yield,” *Nucl. Instrum. Methods Phys. Res. A*, vol. 238, no. 2–3, pp. 564–565, Aug. 1985, doi: 10.1016/0168-9002(85)90503-0.
- [50] P. Schotanus, C. W. E. Van Eijk, R. W. Hollander, and J. Pijpelink, “Photoelectron production in BaF₂-TMAE detectors,” *Nucl. Instrum. Methods Phys. Res. A*, vol. 259, no. 3, pp. 586–588, Sep. 1987, doi: 10.1016/0168-9002(87)90845-X.
- [51] P. Dorenbos, J. T. M. de Haas, R. Visser, C. W. E. van Eijk, and R. W. Hollander, “Absolute light yield measurements on BaF₂ crystals and the quantum efficiency of several photomultiplier tubes,” *IEEE Trans. Nucl. Sci.*, vol. 40, no. 4, pp. 424–430, Aug. 1993, doi: 10.1109/23.256593.
- [52] M. Laval *et al.*, “Barium fluoride — Inorganic scintillator for subnanosecond timing,” *Nucl. Instrum. Methods Phys. Res.*, vol. 206, no. 1, pp. 169–176, Feb. 1983, doi: 10.1016/0167-5087(83)91254-1.
- [53] K. Wisshak and F. Käppeler, “Large barium fluoride detectors,” *Nucl. Instrum. Methods Phys. Res. A*, vol. 227, no. 1, pp. 91–96, Nov. 1984, doi: 10.1016/0168-9002(84)90105-0.

- [54] Y. C. Zhu *et al.*, “New results on the scintillation properties of BaF₂,” *Nucl. Instrum. Methods Phys. Res. A*, vol. 244, no. 3, pp. 577–578, Apr. 1986, doi: 10.1016/0168-9002(86)91088-0.
- [55] H. J. Karwowski, K. Komisarčík, C. Foster, K. Pitts, and B. Utts, “Properties of BGO and BaF₂ detectors,” *Nucl. Instrum. Methods Phys. Res. A*, vol. 245, no. 1, pp. 207–208, Apr. 1986, doi: 10.1016/0168-9002(86)90278-0.
- [56] S. Kubota, S. Sakuragi, S. Hashimoto, and J. Ruan, “A new scintillation material: Pure CsI with 10 ns decay time,” *Nucl. Instrum. Methods Phys. Res. A*, vol. 268, no. 1, pp. 275–277, May 1988, doi: 10.1016/0168-9002(88)90619-5.
- [57] S. Keszthelyi-Lándori, I. Földvári, R. Voszka, Z. Fodor, and Z. Seres, “Decay time measurements on ‘pure’ CsI scintillators prepared by different methods,” *Nucl. Instrum. Methods Phys. Res. A*, vol. 303, no. 2, pp. 374–380, Jun. 1991, doi: 10.1016/0168-9002(91)90804-Y.
- [58] P. Schotanus and R. Kamermans, “Scintillation characteristics of pure and Tl-doped CsI crystals,” *IEEE Trans. Nucl. Sci.*, vol. 37, no. 2, pp. 177–182, Apr. 1990, doi: 10.1109/23.106614.
- [59] C. Amsler *et al.*, “Temperature dependence of pure CsI: scintillation light yield and decay time,” *Nucl. Instrum. Methods Phys. Res. A*, vol. 480, no. 2, pp. 494–500, Mar. 2002, doi: 10.1016/S0168-9002(01)01239-6.
- [60] K. S. Shah *et al.*, “CeBr₃ scintillators for gamma-ray spectroscopy,” *IEEE Trans. Nucl. Sci.*, vol. 52, no. 6, pp. 3157–3159, Dec. 2005, doi: 10.1109/TNS.2005.860155.
- [61] “Cerium Bromide (CeBr₃) Scintillators | Berkeley Nucleonics.” <https://www.berkeley-nucleonics.com/cerium-bromide> (accessed Jan. 17, 2021).

- [62] A. A. Annenkov, M. V. Korzhik, and P. Lecoq, "Lead tungstate scintillation material," *Nucl. Instrum. Methods Phys. Res. A*, vol. 490, no. 1, pp. 30–50, Sep. 2002, doi: 10.1016/S0168-9002(02)00916-6.
- [63] P. Lecoq, "Ten years of lead tungstate development," *Nucl. Instrum. Methods Phys. Res. A*, vol. 537, no. 1, pp. 15–21, Jan. 2005, doi: 10.1016/j.nima.2004.07.223.
- [64] C. W. E. van Eijk, "Development of inorganic scintillators," *Nucl. Instrum. Methods Phys. Res. A*, vol. 392, no. 1, pp. 285–290, Jun. 1997, doi: 10.1016/S0168-9002(97)00239-8.
- [65] M. Moszynski, M. Balcerzyk, M. Kapusta, D. Wolski, and C. L. Melcher, "Large size LSO:Ce and YSO:Ce scintillators for 50 MeV range /spl gamma/-ray detector," *IEEE Trans. Nucl. Sci.*, vol. 47, no. 4, pp. 1324–1328, Aug. 2000, doi: 10.1109/23.872972.
- [66] M. Balcerzyk, M. Moszynski, M. Kapusta, D. Wolski, J. Pawelke, and C. L. Melcher, "YSO, LSO, GSO and LGSO. A study of energy resolution and nonproportionality," *IEEE Trans. Nucl. Sci.*, vol. 47, no. 4, pp. 1319–1323, Aug. 2000, doi: 10.1109/23.872971.
- [67] M. Dahlbom *et al.*, "Performance of a YSO/LSO phoswich detector for use in a PET/SPECT system," *IEEE Trans. Nucl. Sci.*, vol. 44, no. 3, pp. 1114–1119, Jun. 1997, doi: 10.1109/23.596974.
- [68] R. Lecomte *et al.*, "Investigation of GSO, LSO and YSO scintillators using reverse avalanche photodiodes," *IEEE Trans. Nucl. Sci.*, vol. 45, no. 3, pp. 478–482, Jun. 1998, doi: 10.1109/23.682430.
- [69] H. Ishibashi *et al.*, "Scintillation performance of large Ce-doped Gd₂SiO₅ (GSO) single crystal," *IEEE Trans. Nucl. Sci.*, vol. 45, no. 3, pp. 518–521, Jun. 1998, doi: 10.1109/23.682439.
- [70] K. Kurashige *et al.*, "Large GSO single crystals with a diameter of 100mm and their scintillation performance," *IEEE Trans. Nucl. Sci.*, vol. 51, no. 3, pp. 742–745, Jun. 2004, doi: 10.1109/TNS.2004.829606.

- [71] M. Kobayashi and M. Ishii, “Excellent radiation-resistivity of cerium-doped gadolinium silicate scintillators,” *Nucl. Instrum. Methods Phys. Res. B*, vol. 61, no. 4, pp. 491–496, Oct. 1991, doi: 10.1016/0168-583X(91)95327-A.
- [72] Shimura *et al.*, “Zr Doped GSO:Ce Single Crystals and Their Scintillation Performance,” *IEEE Trans. Nucl. Sci.*, vol. 53, no. 5, pp. 2519–2522, Oct. 2006, doi: 10.1109/TNS.2006.876006.
- [73] T. Ludziejewski *et al.*, “Advantages and limitations of LSO scintillator in nuclear physics experiments,” *IEEE Trans. Nucl. Sci.*, vol. 42, no. 4, pp. 328–336, Aug. 1995, doi: 10.1109/23.467826.
- [74] P. Dorenbos, J. T. M. de Haas, C. W. E. van Eijk, C. L. Melcher, and J. S. Schweitzer, “Nonlinear response in the scintillation yield of $\text{Lu}_2\text{SiO}_5:\text{Ce}^{3+}$,” *IEEE Trans. Nucl. Sci.*, vol. 41, no. 4, pp. 735–737, Aug. 1994, doi: 10.1109/23.322780.
- [75] D. W. Cooke *et al.*, “Crystal growth and optical characterization of cerium-doped $\text{Lu}_{1.8}\text{Y}_{0.2}\text{SiO}_5$,” *J. Appl. Phys.*, vol. 88, no. 12, pp. 7360–7362, Nov. 2000, doi: 10.1063/1.1328775.
- [76] S. Kawamura *et al.*, “Floating Zone Growth and Scintillation Characteristics of Cerium-Doped Gadolinium Pyrosilicate Single Crystals,” *IEEE Trans. Nucl. Sci.*, vol. 54, no. 4, pp. 1383–1386, Aug. 2007, doi: 10.1109/TNS.2007.902372.
- [77] L. Pidol *et al.*, “High efficiency of lutetium silicate scintillators, Ce-doped LPS, and LYSO crystals,” *IEEE Trans. Nucl. Sci.*, vol. 51, no. 3, pp. 1084–1087, Jun. 2004, doi: 10.1109/TNS.2004.829542.
- [78] L. Pidol *et al.*, “Scintillation properties of $\text{Lu}_2\text{Si}_2\text{O}_7:\text{Ce}^{3+}$, a fast and efficient scintillator crystal,” *J. Phys.: Condens. Matter*, vol. 15, no. 12, pp. 2091–2102, Mar. 2003, doi: 10.1088/0953-8984/15/12/326.

- [79] J. A. Mares *et al.*, “Scintillation and spectroscopic properties of Ce³⁺-doped YAlO₃ and Lu_x(RE)_{1-x}AlO₃ (RE=Y³⁺ and Gd³⁺) scintillators,” *Nucl. Instrum. Methods Phys. Res. A*, vol. 498, no. 1, pp. 312–327, Feb. 2003, doi: 10.1016/S0168-9002(02)01996-4.
- [80] M. Kapusta, J. Pawelke, and M. Moszyński, “Comparison of YAP and BGO for high-resolution PET detectors,” *Nucl. Instrum. Methods Phys. Res. A*, vol. 404, no. 2–3, pp. 413–417, Feb. 1998, doi: 10.1016/S0168-9002(97)01151-0.
- [81] A. Del Guerra, F. de Notaristefani, G. D. Domenico, R. Pani, and G. Zavattini, “Measurement of absolute light yield and determination of a lower limit for the light attenuation length for YAP:Ce crystal,” *IEEE Trans. Nucl. Sci.*, vol. 44, no. 6, pp. 2415–2418, Dec. 1997, doi: 10.1109/23.656445.
- [82] M. Moszyński *et al.*, “Properties of the new LuAP:Ce scintillator,” *Nucl. Instrum. Methods Phys. Res. A*, vol. 385, no. 1, pp. 123–131, Jan. 1997, doi: 10.1016/S0168-9002(96)00875-3.
- [83] A. Lempicki and J. Glodo, “Ce-doped scintillators: LSO and LuAP,” *Nucl. Instrum. Methods Phys. Res. A*, vol. 416, no. 2–3, pp. 333–344, Nov. 1998, doi: 10.1016/S0168-9002(98)00689-5.
- [84] M. Moszyński, T. Ludziejewski, D. Wolski, W. Klamra, and L. O. Norlin, “Properties of the YAG:Ce scintillator,” *Nucl. Instrum. Methods Phys. Res. A*, vol. 345, no. 3, pp. 461–467, Jul. 1994, doi: 10.1016/0168-9002(94)90500-2.
- [85] T. Ludziejewski, M. Moszyński, M. Kapusta, D. Wolski, W. Klamra, and K. Moszyńska, “Investigation of some scintillation properties of YAG:Ce crystals,” *Nucl. Instrum. Methods Phys. Res. A*, vol. 398, no. 2, pp. 287–294, Oct. 1997, doi: 10.1016/S0168-9002(97)00820-6.

- [86] J. A. Mares *et al.*, “Scintillation response of Ce-doped or intrinsic scintillating crystals in the range up to 1 MeV,” *Radiat. Meas*, vol. 38, no. 4, pp. 353–357, Aug. 2004, doi: 10.1016/j.radmeas.2004.04.004.
- [87] G. Hull *et al.*, “Ce-doped single crystal and ceramic garnet for γ -ray detection,” San Diego, CA, Sep. 2007, p. 670617, doi: 10.1117/12.738961.
- [88] C. W. E. van Eijk, J. Andriessen, P. Dorenbos, and R. Visser, “Ce³⁺ doped inorganic scintillators,” *Nucl. Instrum. Methods Phys. Res. A*, vol. 348, no. 2, pp. 546–550, Sep. 1994, doi: 10.1016/0168-9002(94)90798-6.
- [89] K. Kamada *et al.*, “Composition Engineering in Cerium-Doped (Lu,Gd)₃(Ga,Al)₅O₁₂ Single-Crystal Scintillators,” *Cryst. Growth Des.*, vol. 11, no. 10, pp. 4484–4490, Oct. 2011, doi: 10.1021/cg200694a.
- [90] K. Kamada *et al.*, “Crystal Growth and Scintillation Properties of Ce Doped Gd₃(Ga,Al)₅O₁₂ Single Crystals,” *IEEE Trans. Nucl. Sci.*, vol. 59, no. 5, pp. 2112–2115, Oct. 2012, doi: 10.1109/TNS.2012.2197024.
- [91] J. Iwanowska *et al.*, “Performance of cerium-doped Gd₃Al₂Ga₃O₁₂ (GAGG:Ce) scintillator in gamma-ray spectrometry,” *Nucl. Instrum. Methods Phys. Res. A*, vol. 712, pp. 34–40, Jun. 2013, doi: 10.1016/j.nima.2013.01.064.
- [92] S. Rawat *et al.*, “Pulse shape discrimination properties of Gd₃Ga₃Al₂O₁₂:Ce,B single crystal in comparison with CsI:Tl,” *Nucl. Instrum. Methods Phys. Res. A*, vol. 840, pp. 186–191, Dec. 2016, doi: 10.1016/j.nima.2016.09.060.
- [93] P. Mitra, S. Srivastava, M. Tyagi, A. V. Kumar, and S. C. Gadkari, “Development of a silicon photodiode-based compact gamma spectrometer using a Gd₃Ga₃Al₂O₁₂:Ce,B single crystal scintillator,” *Bull. Mater. Sci.*, vol. 42, no. 6, pp. 258, Dec. 2019, doi: 10.1007/s12034-019-1942-x.

- [94] S. B. Donald *et al.*, “The Effect of B^{3+} and Ca^{2+} Co-Doping on Factors Which Affect the Energy Resolution of $Gd_3Ga_3Al_2O_{12}:Ce$,” *IEEE Trans. Nucl. Sci.*, vol. 60, no. 5, Oct. 2013, doi: 10.1109/TNS.2013.2277862.
- [95] M. Tyagi, M. Koschan, H. E. Rothfuss, J. Hayward, and C. L. Melcher, “Effect of Ca^{2+} Co-Doping on the Temperature Dependence of $Gd_2SiO_5:Ce$ Photoluminescence,” *IEEE Trans. Nucl. Sci.*, vol. 60, no. 2, pp. 973–978, Apr. 2013, doi: 10.1109/TNS.2012.2228235.
- [96] M. Tyagi, H. E. Rothfuss, S. B. Donald, M. Koschan, and C. L. Melcher, “Effect of Ca^{2+} Co-Doping on the Scintillation Kinetics of Ce Doped $Gd_3Ga_3Al_2O_{12}$,” *IEEE Trans. Nucl. Sci.*, vol. 61, no. 1, pp. 297–300, Feb. 2014, doi: 10.1109/TNS.2013.2276101.
- [97] M. Tyagi, F. Meng, M. Koschan, A. K. Singh, C. L. Melcher, and S. C. Gadkari, “Effect of Co-doping On the Radiation Hardness of $Gd_3Ga_3Al_2O_{12}:Ce$ Scintillators,” *IEEE Trans. Nucl. Sci.*, vol. 62, no. 1, pp. 336–339, Feb. 2015, doi: 10.1109/TNS.2014.2387834.
- [98] M. Tyagi, F. Meng, M. Koschan, S. B. Donald, H. Rothfuss, and C. L. Melcher, “Effect of codoping on scintillation and optical properties of a Ce-doped $Gd_3Ga_3Al_2O_{12}$ scintillator,” *J. Phys. D: Appl. Phys.*, vol. 46, no. 47, pp. 475302, Nov. 2013, doi: 10.1088/0022-3727/46/47/475302.
- [99] M. Tyagi *et al.*, “Improvement of the scintillation properties of $Gd_3Ga_3Al_2O_{12}:Ce,B$ single crystals having tailored defect structure,” *Phys. Status Solidi-RRL*, vol. 9, no. 9, pp. 530–534, 2015, doi: <https://doi.org/10.1002/pssr.201510227>.
- [100] S. Rawat, M. Tyagi, G. A. Kumar, S. C. Gadkari, and H. J. Kim, “The Effect of Codoping on Pulse-Shape Discrimination Properties of $Gd_3Ga_3Al_2O_{12}:Ce$ Single Crystals,” *IEEE Trans. Nucl. Sci.*, vol. 66, no. 12, pp. 2440–2445, Dec. 2019, doi: 10.1109/TNS.2019.2954476.

- [101] E. V. D. van Loef, P. Dorenbos, C. W. E. van Eijk, K. Krämer, and H. U. Güdel, “High-energy-resolution scintillator: Ce^{3+} activated LaCl_3 ,” *Appl. Phys. Lett.*, vol. 77, no. 10, pp. 1467–1468, Aug. 2000, doi: 10.1063/1.1308053.
- [102] E. V. D. van Loef, P. Dorenbos, C. W. E. van Eijk, K. Krämer, and H. U. Güdel, “High-energy-resolution scintillator: Ce^{3+} activated LaBr_3 ,” *Appl. Phys. Lett.*, vol. 79, no. 10, pp. 1573–1575, Aug. 2001, doi: 10.1063/1.1385342.
- [103] M. Balcerzyk, M. Moszyński, and M. Kapusta, “Comparison of $\text{LaCl}_3:\text{Ce}$ and $\text{NaI}(\text{Tl})$ scintillators in γ -ray spectrometry,” *Nucl. Instrum. Methods Phys. Res. A*, vol. 537, no. 1–2, pp. 50–56, Jan. 2005, doi: 10.1016/j.nima.2004.07.233.
- [104] B. D. Milbrath, B. J. Choate, J. E. Fast, W. K. Hensley, R. T. Kouzes, and J. E. Schweppe, “Comparison of $\text{LaBr}_3:\text{Ce}$ and $\text{NaI}(\text{Tl})$ scintillators for radio-isotope identification devices,” *Nucl. Instrum. Methods Phys. Res. A*, vol. 572, no. 2, pp. 774–784, Mar. 2007, doi: 10.1016/j.nima.2006.12.003.
- [105] A. Iltis, M. R. Mayhugh, P. Menge, C. M. Rozsa, O. Selles, and V. Solovyev, “Lanthanum halide scintillators: Properties and applications,” *Nucl. Instrum. Methods Phys. Res. A*, vol. 563, no. 2, pp. 359–363, Jul. 2006, doi: 10.1016/j.nima.2006.02.192.
- [106] “Lanthinum Bromide $\text{LaBr}_3(\text{Ce})$ | Products | Saint-Gobain Crystals.” <https://www.crystals.saint-gobain.com/products/standard-and-enhanced-lanthanum-bromide> (accessed Jan. 23, 2021).
- [107] R. Nicolini *et al.*, “Investigation of the properties of a 1"×1" $\text{LaBr}_3:\text{Ce}$ scintillator,” *Nucl. Instrum. Methods Phys. Res. A*, vol. 582, no. 2, pp. 554–561, Nov. 2007, doi: 10.1016/j.nima.2007.08.221.
- [108] P. Mitra, A. K. Verma, S. Anilkumar, D. D. Rao, and A. V. Kumar, “Temperature Response and Intrinsic Background Radiation Studies of a $\text{LaBr}_3(\text{Ce})$ Scintillation Detector for its use in Environmental Gamma Spectrometry,” in *Proceedings of the DAE-BRNS Symp.*

on *Nucl. Phys.* 61 (2016), Kolkata, India, 2016, pp. 992–993, [Online]. Available: www.sympnp.org/proceedings.

[109] B. D. Milbrath *et al.*, “Characterization of alpha contamination in lanthanum trichloride scintillators using coincidence measurements,” *Nucl. Instrum. Methods Phys. Res. A*, vol. 547, no. 2–3, pp. 504–510, Aug. 2005, doi: 10.1016/j.nima.2004.11.054.

[110] A. Owens *et al.*, “ γ -ray performance of a 1242 cm³ LaCl₃:Ce scintillation spectrometer,” *Nucl. Instrum. Methods Phys. Res. A*, vol. 574, no. 1, pp. 110–114, Apr. 2007, doi: 10.1016/j.nima.2007.01.091.

[111] R. Bernabei *et al.*, “Performances and potentialities of a LaCl₃:Ce scintillator,” *Nucl. Instrum. Methods Phys. Res. A*, vol. 555, no. 1–2, pp. 270–281, Dec. 2005, doi: 10.1016/j.nima.2005.09.030.

[112] P. R. Menge, G. Gautier, A. Iltis, C. Rozsa, and V. Solovyev, “Performance of large lanthanum bromide scintillators,” *Nucl. Instrum. Methods Phys. Res. A*, vol. 579, no. 1, pp. 6–10, Aug. 2007, doi: 10.1016/j.nima.2007.04.002.

[113] W. J. Kernan, “Self-activity in lanthanum halides,” *IEEE Trans. Nucl. Sci.*, vol. 53, no. 1, pp. 395–400, Feb. 2006, doi: 10.1109/TNS.2006.869849.

[114] E.-J. Buis *et al.*, “Proton induced activation of LaBr₃:Ce and LaCl₃:Ce,” *Nucl. Instrum. Methods Phys. Res. A*, vol. 580, no. 2, pp. 902–905, Oct. 2007, doi: 10.1016/j.nima.2007.06.052.

[115] S. Normand, A. Iltis, F. Bernard, T. Domenech, and P. Delacour, “Resistance to γ irradiation of LaBr₃:Ce and LaCl₃:Ce single crystals,” *Nucl. Instrum. Methods Phys. Res. A*, vol. 572, no. 2, pp. 754–759, Mar. 2007, doi: 10.1016/j.nima.2006.11.060.

[116] M. Moszyński *et al.*, “Temperature dependences of LaBr₃(Ce), LaCl₃(Ce) and NaI(Tl) scintillators,” *Nucl. Instrum. Methods Phys. Res. A*, vol. 568, no. 2, pp. 739–751, Dec. 2006, doi: 10.1016/j.nima.2006.06.039.

- [117] C. Hoel, L. G. Sobotka, K. S. Shah, and J. Glodo, “Pulse-shape discrimination of La halide scintillators,” *Nucl. Instrum. Methods Phys. Res. A*, vol. 540, no. 1, pp. 205–208, Mar. 2005, doi: 10.1016/j.nima.2004.12.029.
- [118] Scionix, “High resolution LBC scintillators * Scionix,” *Scionix*, Feb. 20, 2019. <https://scionix.nl/high-resolution-lbc-scintillators/> (accessed Jan. 23, 2021).
- [119] E. V. D. van Loef, P. Dorenbos, C. W. E. van Eijk, K. W. Krämer, and H. U. Güdel, “Properties and mechanism of scintillation in $\text{LuCl}_3:\text{Ce}^{3+}$ and $\text{LuBr}_3:\text{Ce}^{3+}$ crystals,” *Nucl. Instrum. Methods Phys. Res. A*, vol. 496, no. 1, pp. 138–145, Jan. 2003, doi: 10.1016/S0168-9002(02)01634-0.
- [120] J. Glodo, K. S. Shah, M. Klugerman, P. Wong, B. Higgins, and P. Dorenbos, “Scintillation properties of $\text{LuI}_3:\text{Ce}$,” *Nucl. Instrum. Methods Phys. Res. A*, vol. 537, no. 1, pp. 279–281, Jan. 2005, doi: 10.1016/j.nima.2004.08.026.
- [121] M. D. Birowosuto, P. Dorenbos, C. W. E. van Eijk, K. W. Krämer, and H. U. Güdel, “High-light-output scintillator for photodiode readout: $\text{LuI}_3:\text{Ce}^{3+}$,” *J Appl Phys*, vol. 99, no. 12, pp. 123520, Jun. 2006, doi: 10.1063/1.2207689.
- [122] J. Glodo, E. V. D. van Loef, W. M. Higgins, and K. S. Shah, “Mixed Lutetium Iodide Compounds,” *IEEE Trans. Nucl. Sci.*, vol. 55, no. 3, pp. 1496–1500, Jun. 2008, doi: 10.1109/TNS.2008.922215.
- [123] “CLLB | Products | Saint-Gobain Crystals.” <https://www.crystals.saint-gobain.com/products/cllb> (accessed Jan. 24, 2021).
- [124] E. V. D. van Loef, J. Glodo, W. M. Higgins, and K. S. Shah, “Optical and scintillation properties of $\text{Cs}_2\text{LiYCl}_6:\text{Ce}^{3+}$ and $\text{Cs}_2\text{LiYCl}_6:\text{Pr}^{3+}$ crystals,” *IEEE Trans. Nucl. Sci.*, vol. 52, no. 5, pp. 1819–1822, Oct. 2005, doi: 10.1109/TNS.2005.856812.
- [125] M. D. Birowosuto, P. Dorenbos, J. T. M. de Haas, C. W. E. van Eijk, K. W. Kramer, and H. U. Gudel, “Li-Based Thermal Neutron Scintillator Research; $\text{Rb}_2\text{LiYBr}_6:\text{Ce}^{3+}$ and

Other Elpasolites,” *IEEE Trans. Nucl. Sci.*, vol. 55, no. 3, pp. 1152–1155, Jun. 2008, doi: 10.1109/TNS.2008.922826.

[126] T. Yanagida *et al.*, “Evaluation of properties of YAG(Ce) ceramic scintillators,” *IEEE Trans. Nucl. Sci.*, vol. 52, no. 5, pp. 1836–1841, Oct. 2005, doi: 10.1109/TNS.2005.856757.

[127] N. J. Cherepy *et al.*, “Cerium-doped single crystal and transparent ceramic lutetium aluminum garnet scintillators,” *Nucl. Instrum. Methods Phys. Res. A*, vol. 579, no. 1, pp. 38–41, Aug. 2007, doi: 10.1016/j.nima.2007.04.009.

[128] T. Yanagida *et al.*, “Improvement of ceramic YAG(Ce) scintillators to $(Y,Gd)_3Al_5O_{12}(Ce)$ for gamma-ray detectors,” *Nucl. Instrum. Methods Phys. Res. A*, vol. 579, no. 1, pp. 23–26, Aug. 2007, doi: 10.1016/j.nima.2007.04.173.

[129] L. M. Bollinger, G. E. Thomas, and R. J. Ginther, “Neutron detection with glass scintillators,” *Nucl. Instrum. Methods*, vol. 17, no. 1, pp. 97–116, Sep. 1962, doi: 10.1016/0029-554X(62)90178-7.

[130] P. Pavan, G. Zanella, R. Zannoni, and P. Polato, “Radiation damage and annealing of scintillating glasses,” *Nucl. Instrum. Methods Phys. Res. B*, vol. 61, no. 4, pp. 487–490, Oct. 1991, doi: 10.1016/0168-583X(91)95326-9.

[131] A. Helaly, J. Birchall, N. Videla, J. S. C. McKee, and W. D. Ramsay, “Design and performance of a liquid helium scintillation polarimeter,” *Nucl. Instrum. Methods Phys. Res. A*, vol. 241, no. 1, pp. 169–171, Nov. 1985, doi: 10.1016/0168-9002(85)90527-3.

[132] S. Kubota, M. Hishida, M. Suzuki, and J. Ruan, “Liquid and solid argon, krypton and xenon scintillators,” *Nucl. Instrum. Methods Phys. Res.*, vol. 196, no. 1, pp. 101–105, May 1982, doi: 10.1016/0029-554X(82)90623-1.

[133] T. Doke, K. Masuda, and E. Shibamura, “Estimation of absolute photon yields in liquid argon and xenon for relativistic (1 MeV) electrons,” *Nucl. Instrum. Methods Phys. Res. A*, vol. 291, no. 3, pp. 617–620, Jun. 1990, doi: 10.1016/0168-9002(90)90011-T.

- [134] R. Ruchti, “Tracking with scintillating fibers,” *Nucl. Phys. B, Proc. Suppl.*, vol. 44, no. 1, pp. 308–319, Nov. 1995, doi: 10.1016/S0920-5632(95)80049-2.
- [135] H. Leutz, “Scintillating fibres,” *Nucl. Instrum. Methods Phys. Res. A*, vol. 364, no. 3, pp. 422–448, Oct. 1995, doi: 10.1016/0168-9002(95)00383-5.
- [136] Hamamatsu Photonics K. K., “Photomultiplier Tubes Basics and Applications.” 2007, [Online]. Available: https://www.hamamatsu.com/resources/pdf/etd/PMT_handbook_v3aE.pdf.
- [137] RCA, “RCA Photomultiplier Manual Theory Design Application. Technical Series PT-61.” RCA Corporation, Electronic Components, Harrison, N. J., 1970, [Online]. Available: <http://www.decadecounter.com/vta/pdf/RCAPMT.pdf>.
- [138] R. Mao, L. Zhang, and R. Zhu, “Optical and Scintillation Properties of Inorganic Scintillators in High Energy Physics,” *IEEE Trans. Nucl. Sci.*, vol. 55, no. 4, pp. 2425–2431, Aug. 2008, doi: 10.1109/TNS.2008.2000776.
- [139] R. Mirzoyan *et al.*, “Enhanced quantum efficiency alkali photo multiplier tubes,” *Nucl. Instrum. Methods Phys. Res. A*, vol. 572, no. 1, pp. 449–453, Mar. 2007, doi: 10.1016/j.nima.2006.11.047.
- [140] R. Mirzoyan, M. Laatiaoui, and M. Teshima, “Very high quantum efficiency PMTs with alkali photo-cathode,” *Nucl. Instrum. Methods Phys. Res. A*, vol. 567, no. 1, pp. 230–232, Nov. 2006, doi: 10.1016/j.nima.2006.05.094.
- [141] M. Itaya *et al.*, “Development of a new photomultiplier tube with high sensitivity for a wavelength-shifter fiber readout,” *Nucl. Instrum. Methods Phys. Res. A*, vol. 522, no. 3, pp. 477–486, Apr. 2004, doi: 10.1016/j.nima.2003.11.201.
- [142] H. R. Krall, F. A. Helvy, and D. E. Persyk, “Recent Developments in GaP(Cs)-Dynode Photomultipliers,” *IEEE Trans. Nucl. Sci.*, vol. 17, no. 3, pp. 71–74, Jun. 1970, doi: 10.1109/TNS.1970.4325676.

- [143] M. Suffert, "Silicon photodiode readout of scintillators and associated electronics," *Nucl. Instrum. Methods Phys. Res. A*, vol. 322, no. 3, pp. 523–528, Nov. 1992, doi: 10.1016/0168-9002(92)91226-Y.
- [144] E. Sakai, "Recent Measurements on Scintillator-Photodetector Systems," *IEEE Trans. Nucl. Sci.*, vol. 34, no. 1, pp. 418–422, Feb. 1987, doi: 10.1109/TNS.1987.4337375.
- [145] D. P. Boyd, "Status of Diagnostic X-Ray CT: 1979," *IEEE Trans. Nucl. Sci.*, vol. 26, no. 2, pp. 2835–2839, Apr. 1979, doi: 10.1109/TNS.1979.4330545.
- [146] J. M. Markakis, "Mercuric iodide photodetector-cesium iodide scintillator gamma ray spectrometers," *IEEE Trans. Nucl. Sci.*, vol. 35, no. 1, pp. 356–359, Feb. 1988, doi: 10.1109/23.12742.
- [147] W. Mengesha, T. D. Taulbee, B. D. Rooney, and J. D. Valentine, "Light Yield Nonproportionality of CsI(Tl), CsI(Na), and YAP," *IEEE Trans. Nucl. Sci.*, vol. 45, no. 3, pp. 456–461, Jul. 1998.
- [148] K. Debertin and R. G. Helmer, *Gamma- and X-ray spectrometry with semiconductor detectors*. Amsterdam: North-Holland, 1988.
- [149] J. C. Philippot, "Automatic Processing of Diode Spectrometry Results," *IEEE Trans. Nucl. Sci.*, vol. 17, no. 3, pp. 446–488, Jun. 1970, doi: 10.1109/TNS.1970.4325723.
- [150] D. S. McGregor and H. Hermon, "Room-temperature compound semiconductor radiation detectors," *Nucl. Instrum. Methods Phys. Res. A*, vol. 395, no. 1, pp. 101–124, Aug. 1997, doi: 10.1016/S0168-9002(97)00620-7.
- [151] Z. He, G. F. Knoll, D. K. Wehe, and J. Miyamoto, "Position-sensitive single carrier CdZnTe detectors," *Nucl. Instrum. Methods Phys. Res. A*, vol. 388, no. 1–2, pp. 180–185, Mar. 1997, doi: 10.1016/S0168-9002(97)00318-5.

- [152] C. L. Melcher, “Perspectives on the future development of new scintillators,” *Nucl. Instrum. Methods Phys. Res. A*, vol. 537, no. 1–2, pp. 6–14, Jan. 2005, doi: 10.1016/j.nima.2004.07.222.
- [153] C. Bebek, “A cesium iodide calorimeter with photodiode readout for CLEO II,” *Nucl. Instrum. Methods Phys. Res. A*, vol. 265, no. 1–2, pp. 258–265, Mar. 1988, doi: 10.1016/0168-9002(88)91079-0.
- [154] C. Dujardin *et al.*, “Optical and scintillation properties of large $\text{LuAlO}_3:\text{Ce}^{3+}$ crystals,” *J. Phys.: Condens. Matter*, vol. 10, no. 13, pp. 3061–3073, Apr. 1998, doi: 10.1088/0953-8984/10/13/022.
- [155] B. E. Patt, J. S. Iwanczyk, C. Rossington Tull, N. W. Wang, M. P. Tornai, and E. J. Hoffman, “High resolution CsI(Tl)/Si-PIN detector development for breast imaging,” *IEEE Trans. Nucl. Sci.*, vol. 45, no. 4, pp. 2126–2131, Aug. 1998, doi: 10.1109/23.708319.
- [156] S. G. Singh, A. Singh, A. Topkar, and S. C. Gadkari, “Performance of Indigenously Developed CsI(Tl)-Photodiode Detector for Gamma-ray Spectroscopy,” *AIP Conf. Proc.*, vol. 1349, pp. 481–482, 2015.
- [157] M. Tyagi *et al.*, “Development of $\text{Gd}_3\text{Ga}_3\text{Al}_2\text{O}_{12}:\text{Ce}$ Single Crystal Scintillator and USB Based Portable Gamma-ray Spectrometer,” *BARC Newslett.*, vol. 343, pp. 33–38, 2015.
- [158] C. Dujardin *et al.*, “Needs, Trends, and Advances in Inorganic Scintillators,” *IEEE Trans. Nucl. Sci.*, vol. 65, no. 8, pp. 1977–1997, Aug. 2018, doi: 10.1109/TNS.2018.2840160.
- [159] S. G. Singh *et al.*, “Growth of CsI:Tl crystals in carbon coated silica crucibles by the gradient freeze technique,” *J. Cryst. Growth*, vol. 351, no. 1, pp. 88–92, Jul. 2012, doi: 10.1016/j.jcrysgro.2012.04.019.
- [160] S. G. Singh, “Effect of crystal growth processes on characteristics of some technologically important oxide and halide crystals,” Homi Bhabha National Institute, Mumbai, India, 2014.

- [161] S. G. Singh *et al.*, “Development of Crystal Growth System to Grow Tl Doped CsI and NaI Single Crystals for Applications in Nuclear Radiation Detection,” *BARC Newslett.*, vol. Founder’s Day Special Issue, pp. 228–236, 2015.
- [162] S. Agostinelli *et al.*, “Geant4—a simulation toolkit,” *Nucl. Instrum. Methods Phys. Res. A*, vol. 506, no. 3, pp. 250–303, Jul. 2003, doi: 10.1016/S0168-9002(03)01368-8.
- [163] J. Allison *et al.*, “Geant4 developments and applications,” *IEEE Trans. Nucl. Sci.*, vol. 53, no. 1, pp. 270–278, Feb. 2006, doi: 10.1109/TNS.2006.869826.
- [164] Geant4 Collaboration, “Geant4 User’s Guide for Application Developers, Release 10.4, Rev 1.0.” Dec. 2017.
- [165] Geant4 Collaboration, “Physics Reference Manual, Release 10.4.” Dec. 08, 2017.
- [166] P. Mitra, M. Tyagi, R. G. Thomas, A. V. Kumar, and S. C. Gadkari, “Optimization of Parameters for a CsI(Tl) Scintillator Detector Using GEANT4-Based Monte Carlo Simulation Including Optical Photon Transport,” *IEEE Trans. Nucl. Sci.*, vol. 66, no. 7, pp. 1870–1878, Jul. 2019, doi: 10.1109/TNS.2019.2918564.
- [167] P. Mitra, R. G. Thomas, M. Tyagi, and A. V. Kumar, “Dependence of gamma spectra from a CsI(Tl) scintillator on the quantum efficiency of the coupled photodetector: A GEANT4- based study,” in *Proceedings of the DAE Symp. on Nucl. Phys. 64 (2019)*, Lucknow, India, 2019, pp. 878–879, [Online]. Available: www.sympnp.org/proceedings.
- [168] P. Mitra, R. G. Thomas, M. Tyagi, A. V. Kumar, and S. C. Gadkari, “Size dependence for $Gd_3Ga_3Al_2O_{12}:Ce,B$ single crystal scintillator on pulse-height spectra generated by GEANT4 simulation with optical photon transport,” presented at the DAE International Symp. on Nucl. Phys. 63 (2018), Mumbai, India, [Online]. Available: <http://sympnp.org/snp2018/>.
- [169] M. Tyagi, “Growth and characterization of Scheelite crystals,” Homi Bhabha National Institute, Mumbai, India, 2010.

- [170] J. C. Brice and J. C. Brice, *Crystal Growth Processes*. Blackie, 1986.
- [171] J. Czochralski, “Ein neues Verfahren zur Messung der Kristallisationsgeschwindigkeit der Metalle,” *Z. Phys. Chem.*, vol. 92U, no. 1, pp. 219–221, Nov. 1918, doi: 10.1515/zpch-1918-9212.
- [172] P. W. Bridgman, “Certain Physical Properties of Single Crystals of Tungsten, Antimony, Bismuth, Tellurium, Cadmium, Zinc, and Tin,” *Proc. Am. Acad. Arts Sci.*, vol. 60, no. 6, pp. 305–383, 1925, doi: 10.2307/25130058.
- [173] K. P. N. Murthy, “Monte Carlo: Basics,” *arXiv:cond-mat/0104215*, Apr. 2001, Accessed: Jan. 31, 2021. [Online]. Available: <http://arxiv.org/abs/cond-mat/0104215>.
- [174] C. J. Werner *et al.*, “MCNP Version 6.2 Release Notes,” LA-UR--18-20808, 1419730, Feb. 2018. doi: 10.2172/1419730.
- [175] I. Kawrakow, E. Mainegra-Hing, D. W. O. Rogers, F. Tessier, and B. R. B. Walters, “The EGSnrc Code System: Monte Carlo Simulation of Electron and photon Transport,” *Technical Report PIRS-701, National Research Council Canada*, 2017, Accessed: Jan. 31, 2021. [Online]. Available: <https://ci.nii.ac.jp/naid/10010091291/>.
- [176] T. T. Böhlen *et al.*, “The FLUKA Code: Developments and Challenges for High Energy and Medical Applications,” *Nuclear Data Sheets*, vol. 120, pp. 211–214, Jun. 2014, doi: 10.1016/j.nds.2014.07.049.
- [177] A. Ferrari, P. R. Sala, A. Fasso, and J. Ranft, “FLUKA: A Multi-Particle Transport Code,” SLAC-R-773, 877507, Dec. 2005. doi: 10.2172/877507.
- [178] Nuclear Energy Agency, *PENELOPE 2018: A code system for Monte Carlo simulation of electron and photon transport: Workshop Proceedings, Barcelona, Spain, 28 January – 1 February 2019*. OECD, 2019.
- [179] M. W. J. Hubbard, “Light transport modelling of pulse shape discrimination within plastic scintillators.,” 2020, doi: 10.15126/THESIS.00857773.

- [180] J. Nilsson, V. Cuplov, and M. Isaksson, “Identifying key surface parameters for optical photon transport in GEANT4/GATE simulations,” *Appl. Radiat. Isot.*, vol. 103, pp. 15–24, Sep. 2015, doi: 10.1016/j.apradiso.2015.04.017.
- [181] A. Levin and C. Moisan, “A more physical approach to model the surface treatment of scintillation counters and its implementation into DETECT,” in *1996 IEEE Nuclear Science Symposium. Conference Record*, Nov. 1996, vol. 2, pp. 702–706 vol.2, doi: 10.1109/NSSMIC.1996.591410.
- [182] M. Janecek and W. W. Moses, “Simulating Scintillator Light Collection Using Measured Optical Reflectance,” *IEEE Trans. Nucl. Sci.*, vol. 57, no. 3, pp. 964–970, Jun. 2010, doi: 10.1109/TNS.2010.2042731.
- [183] M. Kandemir and A. Cakir, “Simulation and efficiency studies of optical photon transportation and detection with plastic antineutrino detector modules,” *Nucl. Instrum. Methods Phys. Res. A*, vol. 898, pp. 30–39, Aug. 2018, doi: 10.1016/j.nima.2018.04.059.
- [184] R. Hofstadter, “Properties of scintillation materials,” *Nucleonics*, vol. 6, no. 5, pp. 70–72, 1950.
- [185] “CsI(Tl) - Cesium Iodide (Tl) Scintillator Crystal.” https://www.advatech-uk.co.uk/csi_tl.html (accessed Feb. 06, 2021).
- [186] “CsI(Tl) Thallium activated Cesium Iodide | Products | Saint-Gobain Crystals.” <https://www.crystals.saint-gobain.com/products/csitl-cesium-iodide-thallium> (accessed Feb. 06, 2021).
- [187] J. D. Valentine, D. K. Wehe, G. F. Knoll, and C. E. Moss, “Temperature dependence of absolute CsI(Tl) scintillation yield,” *IEEE Trans. Nucl. Sci.*, vol. 40, no. 4, pp. 1267–1274, Aug. 1993.

- [188] M. Moszynski, M. Kapusta, M. Mayhugh, D. Wolski, and S. O. Flyckt, "Absolute light output of scintillators," *IEEE Trans. Nucl. Sci.*, vol. 44, no. 3, pp. 1052–1061, Jun. 1997, doi: 10.1109/23.603803.
- [189] Y. Wu *et al.*, "CsI:Tl⁺, Yb²⁺: ultra-high light yield scintillator with reduced afterglow," *CrystEngComm*, vol. 16, pp. 3312–3317, Apr. 2014.
- [190] R. Mao, L. Zhang, and R.-Y. Zhu, "Crystals for the HHCAL Detector Concept," *IEEE Trans. Nucl. Sci.*, vol. 59, no. 5, pp. 2229–2236, 2012.
- [191] "Si PIN photodiode S3590-08." <https://www.hamamatsu.com/eu/en/product/type/S3590-08/index.html> (accessed Feb. 06, 2021).
- [192] D. K. Akar, H. K. Patni, M. Y. Nadar, V. P. Ghare, and D. D. Rao, "Monte Carlo simulation of NaI(Tl) detector in a shadow-shield scanning bed whole-body monitor for uniform and axial cavity activity distribution in a BOMAB phantom," *Radiat. Prot. Dosimetry*, vol. 155, no. 3, pp. 292–299, Jul. 2013.
- [193] I. Mouhti, A. Elanique, M. Y. Messous, B. Belhorma, and A. Benahmed, "Validation of a NaI(Tl) and LaBr₃(Ce) detector's models via measurements and Monte Carlo simulations," *J. Radiat. Res. Appl. Sci.*, vol. 11, no. 4, pp. 335–339, Oct. 2018, doi: 10.1016/j.jrras.2018.06.003.
- [194] H. D. Tam, N. T. H. Yen, L. B. Tran, H. D. Chuong, and T. T. Thanh, "Optimization of the Monte Carlo simulation model of NaI(Tl) detector by Geant4 code," *Appl. Radiat. Isot.*, vol. 130, pp. 75–79, Dec. 2017.
- [195] H. D. Tam, H. D. Chuong, T. T. Thanh, and C. Van Tao, "study of the effect of Al₂O₃ reflector on response function of NaI(Tl) detector," *Radiat. Phys. Chem.*, vol. 125, no. 08/2016, pp. 88–93, 2016.

- [196] “Polytetrafluoroethylene,” *Wikipedia*. Feb. 05, 2021, Accessed: Feb. 06, 2021. [Online]. Available: <https://en.wikipedia.org/w/index.php?title=Polytetrafluoroethylene&oldid=1005086215>.
- [197] V. Avdeichikov, A. S. Fomichev, B. Jakobsson, A. M. Rodin, and G. M. Ter-Akopian, “Range-energy relation, range straggling and response function of CsI(Tl), BGO and GSO(Ce) scintillators for light ions,” *Nucl. Instrum. Methods Phys. Res. A*, vol. 439, pp. 158–166, 2000.
- [198] “List of refractive indices,” *Wikipedia*. Jan. 08, 2021, Accessed: Feb. 06, 2021. [Online]. Available: https://en.wikipedia.org/w/index.php?title=List_of_refractive_indices&oldid=999174005.
- [199] “Optical PTFE.” https://www.berghof-fluoroplastics.com/fileadmin/redaktion-bft/Download_Dateien/Broschueren/OpticalPTFE_en.pdf (accessed Feb. 06, 2021).
- [200] “Photomultiplier tube R1306 | Hamamatsu Photonics.” <https://www.hamamatsu.com/eu/en/product/type/R1306/index.html> (accessed Jan. 06, 2021).
- [201] “ROOT,” *ROOT*. <https://root.cern/> (accessed Feb. 06, 2021).
- [202] “Thread seal tape,” *Wikipedia*. Jan. 07, 2021, Accessed: Feb. 06, 2021. [Online]. Available: https://en.wikipedia.org/w/index.php?title=Thread_seal_tape&oldid=998831080.
- [203] “Digital Pulse Processor for Scintillation Detectors DP5G.” <https://www.amptek.com/-/media/ametekamptek/documents/resources/specs/dp5g-digital-pulse-processor-for-scintillation-detectors-specifications.pdf?dmc=1&la=en&revision=a1d3efae-e541-4f77-b224-8d5ff353d53e> (accessed Feb. 06, 2021).
- [204] M. Janecek, “Reflectivity Spectra for Commonly Used Reflectors,” *IEEE Trans. Nucl. Sci.*, vol. 59, no. 3, pp. 490–497, Jun. 2012.

- [205] M. Janecek and W. W. Moses, “Optical Reflectance Measurements for Commonly Used Reflectors,” *IEEE Trans. Nucl. Sci.*, vol. 55, no. 4, pp. 2432–2437, Aug. 2008, doi: 10.1109/TNS.2008.2001408.
- [206] V. Bora *et al.*, “Estimation of Fano factor in inorganic scintillators,” *Nucl. Instrum. Methods Phys. Res. A*, vol. 805, pp. 72–86, Jan. 2016, doi: 10.1016/j.nima.2015.07.009.
- [207] K. Kamada *et al.*, “2-inch size single crystal growth and scintillation properties of new scintillator; Ce:Gd₃Al₂Ga₃O₁₂,” in *2011 IEEE Nuclear Science Symposium Conference Record*, Valencia, Spain, Oct. 2011, pp. 1927–1929, doi: 10.1109/NSSMIC.2011.6154387.
- [208] S. Rawat, M. Tyagi, G. A. Kumar, and S. C. Gadkari, “Efficiency Studies on Gd₃Ga₃Al₂O₁₂:Ce Scintillators: Simulations and Measurements,” *IEEE Trans. Nucl. Sci.*, vol. 65, no. 8, pp. 2109–2113, Aug. 2018, doi: 10.1109/TNS.2018.2823749.
- [209] “GAGG:Ce crystal - GAGG ceramic scintillator - Epic Crystal.” <http://www.epic-crystal.com/oxide-scintillators/gagg-ce-scintillator.html> (accessed Feb. 07, 2021).
- [210] K. Kamada *et al.*, “2 inch diameter single crystal growth and scintillation properties of Ce:Gd₃Al₂Ga₃O₁₂,” *J. Cryst. Growth*, vol. 352, no. 1, pp. 88–90, Aug. 2012, doi: 10.1016/j.jcrysgro.2011.11.085.
- [211] M. Kobayashi, Y. Tamagawa, S. Tomita, A. Yamamoto, I. Ogawa, and Y. Usuki, “Significantly different pulse shapes for γ - and α -rays in Gd₃Al₂Ga₃O₁₂:Ce³⁺ scintillating crystals,” *Nucl. Instrum. Methods Phys. Res. A*, vol. 694, pp. 91–94, Dec. 2012, doi: 10.1016/j.nima.2012.07.055.
- [212] K. Kamada *et al.*, “2-inch size crystal growth of Ce:Gd₃Al₂Ga₃O₁₂ with various Ce concentration and their scintillation properties,” in *2012 IEEE Nuclear Science Symposium and Medical Imaging Conference Record (NSS/MIC)*, Anaheim, CA, USA, Oct. 2012, pp. 1698–1701, doi: 10.1109/NSSMIC.2012.6551401.

- [213] Y. Tamagawa, Y. Inukai, I. Ogawa, and M. Kobayashi, “Alpha–gamma pulse-shape discrimination in $\text{Gd}_3\text{Al}_2\text{Ga}_3\text{O}_{12}$ (GAGG): Ce^{3+} crystal scintillator using shape indicator,” *Nucl. Instrum. Methods Phys. Res. A*, vol. 795, pp. 192–195, Sep. 2015, doi: 10.1016/j.nima.2015.05.052.
- [214] V. I. Tretyak, “Semi-empirical calculation of quenching factors for ions in scintillators,” *Astropart. Phys.*, vol. 33, no. 1, pp. 40–53, Feb. 2010, doi: 10.1016/j.astropartphys.2009.11.002.
- [215] “DT5790 - Dual Digital Acquisition System for Charge Integration and Pulse Shape Discrimination,” *CAEN - Tools for Discovery*. <https://www.caen.it/products/dt5790/> (accessed Feb. 07, 2021).
- [216] “CoMPASS - Multiparametric DAQ Software for Physics Applications - CAEN - Tools for Discovery.” <https://www.caen.it/products/compass/> (accessed Feb. 07, 2021).
- [217] “Light Guides and Acrylic Plastic - Eljen Technology.” <https://eljentechnology.com/products/light-guides-and-acrylic-plastic> (accessed Feb. 07, 2021).
- [218] “Poly(methyl methacrylate),” *Wikipedia*. Feb. 05, 2021, Accessed: Feb. 07, 2021. [Online]. Available: [https://en.wikipedia.org/w/index.php?title=Poly\(methyl_methacrylate\)&oldid=1005084978](https://en.wikipedia.org/w/index.php?title=Poly(methyl_methacrylate)&oldid=1005084978).
- [219] “Si PIN photodiode S3204-08 | Hamamatsu Photonics.” <https://www.hamamatsu.com/us/en/product/type/S3204-08/index.html> (accessed Feb. 07, 2021).
- [220] “Refractive index of $(\text{C}_5\text{H}_8\text{O}_2)_n$ (Poly(methyl methacrylate), PMMA) - Szczurowski.” https://refractiveindex.info/?shelf=organic&book=poly%28methyl_methacrylate%29&page=Szczurowski (accessed Feb. 07, 2021).

- [221] R. Casanovas, J. J. Morant, and M. Salvadó, “Development and calibration of a real-time airborne radioactivity monitor using direct gamma-ray spectrometry with two scintillation detectors,” *Appl. Radiat. Isot.*, vol. 89, pp. 102–108, Jul. 2014, doi: 10.1016/j.apradiso.2014.01.026.
- [222] R. Casanovas, J. J. Morant, and M. Salvadó, “Development and Calibration of a Real-Time Airborne Radioactivity Monitor Using Gamma-Ray Spectrometry on a Particulate Filter,” *IEEE Trans. Nucl. Sci.*, vol. 61, no. 2, pp. 727–731, Apr. 2014, doi: 10.1109/TNS.2014.2299715.
- [223] R. Casanovas, J. J. Morant, M. López, I. Hernández-Girón, E. Batalla, and M. Salvadó, “Performance of data acceptance criteria over 50 months from an automatic real-time environmental radiation surveillance network,” *J. Environ. Radioact.*, vol. 102, no. 8, pp. 742–748, Aug. 2011, doi: 10.1016/j.jenvrad.2011.04.001.
- [224] H. K. Aage, U. Korsbech, and K. Bagholz, “Early detection of radioactive fallout by gamma spectrometry,” *Radiat. Prot. Dosimetry*, vol. 106, no. 2, pp. 155–164, Aug. 2003, doi: 10.1093/oxfordjournals.rpd.a006345.
- [225] W. Zhang, E. Korpach, R. Berg, and K. Ungar, “Testing of an automatic outdoor gamma ambient dose-rate surveillance system in Tokyo and its calibration using measured deposition after the Fukushima nuclear accident,” *J. Environ. Radioact.*, vol. 125, pp. 93–98, Nov. 2013, doi: 10.1016/j.jenvrad.2012.12.011.
- [226] Y.-Y. Ji, H.-Y. Choi, W. Lee, C.-J. Kim, H.-S. Chang, and K.-H. Chung, “Application of a LaBr₃(Ce) Scintillation Detector to an Environmental Radiation Monitor,” *IEEE Trans. Nucl. Sci.*, vol. 65, no. 8, pp. 2021–2028, Aug. 2018, doi: 10.1109/TNS.2018.2823322.
- [227] P. Kessler, B. Behnke, R. Dabrowski, H. Dombrowski, A. Röttger, and S. Neumaier, “Novel spectrometers for environmental dose rate monitoring,” *J. Environ. Radioact.*, vol. 187, pp. 115–121, Jul. 2018, doi: 10.1016/j.jenvrad.2018.01.020.

- [228] L. T. Tsankov and M. G. Mitev, "Response of a NaI(Tl) scintillation detector in a wide temperature interval," in *Proceedings of the 15th International Conference, ET, Sozopol, Book 2*, 2006, pp.138–143.
- [229] M. D. Patel *et al.*, "Multi-Detector Environmental Radiation Monitor with Multichannel Data Communication for Indian Environmental Radiation MONitoring Network (IERMON)," *BARC Newslett.*, no. 320, pp. 31, 2011.
- [230] "IRFR9120, IRFU9120, SiHFR9120, SiHFU9120." <https://www.vishay.com/docs/91280/91280.pdf> (accessed Feb. 07, 2021).
- [231] "Traco Power DC/DC Converter TMR 2 Series, 2 Watt." https://www.tracopower.com/sites/default/files/products/datasheets/tmr2_datasheet.pdf (accessed Feb. 07, 2021).
- [232] R. Casanovas, J. J. Morant, and M. Salvadó, "Temperature peak-shift correction methods for NaI(Tl) and LaBr₃(Ce) gamma-ray spectrum stabilisation," *Radiat. Meas.*, vol. 47, no. 8, pp. 588–595, Aug. 2012, doi: 10.1016/j.radmeas.2012.06.001.
- [233] G. Pausch, J. Stein, and N. Teofilov, "Stabilizing scintillation detector systems by exploiting the temperature dependence of the light pulse decay time," *IEEE Trans. Nucl. Sci.*, vol. 52, no. 5, pp. 1849–1855, Oct. 2005, doi: 10.1109/TNS.2005.856616.
- [234] J. S. Schweitzer and W. Ziehl, "Temperature Dependence of NaI(Tl) Decay Constant," *IEEE Trans. Nucl. Sci.*, vol. 30, no. 1, pp. 380–382, Feb. 1983, doi: 10.1109/TNS.1983.4332293.
- [235] W. P. Ball, R. Booth, and M. Macgregor, "Temperature coefficients of scintillating systems," *Nucl. Instrum.*, vol. 1, no. 2, pp. 71–74, Mar. 1957, doi: 10.1016/0369-643X(57)90052-X.

- [236] R. E. Rohde, “Gain vs temperature effects in NaI(Tl) photomultiplier scintillation detectors using 10 and 14 stage tubes,” *Nucl. Instrum. Methods*, vol. 34, pp. 109–115, Apr. 1965, doi: 10.1016/0029-554X(65)90268-5.
- [237] “ICRU 53 Gamma-ray spectrometry in the environment.” International Commission on Radiation Units and Measurements, 1994.
- [238] K. Saucke, G. Pausch, J. Stein, H.- Ortlepp, and P. Schotanus, “Stabilizing scintillation detector systems with pulsed LEDs: a method to derive the LED temperature from pulse height spectra,” *IEEE Trans. Nucl. Sci.*, vol. 52, no. 6, pp. 3160–3165, Dec. 2005, doi: 10.1109/TNS.2005.862929.
- [239] R. Shepard, S. Wawrowski, M. Charland, H. Roberts, and M. Moslinger, “Temperature stabilization of a field instrument for uranium enrichment measurements,” *IEEE Trans. Nucl. Sci.*, vol. 44, no. 3, pp. 568–571, Jun. 1997, doi: 10.1109/23.603712.
- [240] L. Loska, “A computer method of γ -ray spectra stabilization,” *Appl. Radiat. Isot.*, vol. 46, no. 9, pp. 949–953, Sep. 1995, doi: 10.1016/0969-8043(95)00189-K.
- [241] L. T. Tsankov and M. G. Mitev, “A simple method for stabilization of arbitrary spectra,” in *Proceedings of the Sixteen International Scientific and Applied Science Conference ELECTRONICS ET*, 2007, pp. 19–21.
- [242] “Spectroscopic Detection SARA - ENVINET GmbH.” <https://envinet.com/en/products/spectroscopy-sara.html> (accessed Mar. 01, 2021).
- [243] “SpectroTRACER - Environmental radiation monitoring | Bertin Instruments.” <https://www.bertin-instruments.com/product/environmental-radiation-monitoring/spectrotracer-air-soil-water/> (accessed Mar. 01, 2021).
- [244] H. K. Aage, U. Korsbech, K. Bargholz, and J. Hovgaard, “A new technique for processing airborne gamma ray spectrometry data for mapping low level contaminations,”

Appl. Radiat. Isot., vol. 51, no. 6, pp. 651–662, Dec. 1999, doi: 10.1016/S0969-8043(99)00087-1.

[245] H. K. Aage and U. Korsbech, “Search for lost or orphan radioactive sources based on NaI gamma spectrometry,” *Appl. Radiat. Isot.*, vol. 58, no. 1, pp. 103–113, Jan. 2003, doi: 10.1016/S0969-8043(02)00222-1.

[246] M. K. Chatterjee, J. K. Divkar, S. S. Patil, R. Singh, K. S. Pradeepkumar, and D. N. Sharma, “Study on enhanced atmospheric dispersion of ^{41}Ar at the Trombay site,” *Radiat. Prot. Dosimetry*, vol. 155, no. 4, pp. 483–496, Aug. 2013, doi: 10.1093/rpd/nct020.

[247] “EJ-510, EJ-520 - Reflective Paint - Eljen Technology.” <https://eljentechnology.com/products/accessories/ej-510-ej-520> (accessed Feb. 07, 2021).

[248] “CR-110-R2.1 charge sensitive preamplifier: application guide.” <https://www.cremat.com/CR-110-R2.1.pdf> (accessed Feb. 07, 2021).

[249] “CR-200-X shaper modules – Cremat Inc.” <https://www.cremat.com/home/cr-200-x-shaper-modules/> (accessed Feb. 07, 2021).